EXPERIMENTAL AND THEORETICAL DEVELOPMENTS IN EXTENDED X-RAY ABSORPTION FINE STRUCTURE (EXAFS) SPECTROSCOPY

Thesis by

John James Boland

In Partial Fulfillment of the Requirements

for the Degree of

Doctor of Philosophy

California Institute of Technology

Pasadena, California

1985

(Submitted June 4, 1984)

This Thesis is Dedicated to

My Parents

ACKNOWLEDGEMENTS

I have enjoyed my stay at Caltech and I would like to take this opportunity to thank those who made it such a pleasant experience. To my thesis advisor, Dr. John D. Baldeschwieler, I owe a great debt of gratitude for his support and encouragement throughout my years at Caltech. John has given me an insight into the worlds of science and business which I will take with me through life. I would also like to thank the members of the JDB group with whom I have worked with over the years. In particular, I would like to thank Dr. Folim G. Halaka who worked closely with me on the EXAFS project. Thanks is also due to our secretary Susan Shaar who typed many boring manuscripts and also to the staffs of the electronics and machine shops for their assistance in times of difficulty.

Finally, I would like to thank my wife Noeleen, whose love and support has been a great comfort throughout my graduate studies.

ABSTRACT

To obtain accurate information from a structural tool it is necessary to have an understanding of the physical principles which govern the interaction between the probe and the sample under investigation. In this thesis a detailed study of the physical basis for Extended X-ray Absorption Fine Structure (EXAFS) spectroscopy is presented. A single scattering formalism of EXAFS is introduced which allows a rigorous treatment of the central atom potential. A final state interaction formalism of EXAFS is also discussed. Multiple scattering processes are shown to be significant for systems of certain geometries. The standard single scattering EXAFS analysis produces erroneous results if the data contain a large multiple scattering contribution. The effect of thermal vibrations on such multiple scattering paths is also discussed. From symmetry considerations it is shown that only certain normal modes contribute to the Debye-Waller factor for a particular scattering path. Furthermore, changes in the scattering angles induced by thermal vibrations produces additional EXAFS components called modification factors. These factors are shown to be small for most systems.

A study of the physical basis for the determination of structural information from EXAFS data is also presented. An objective method of determining the background absorption and the threshold energy is discussed and involves

Gaussian functions. In addition, a scheme to determine the nature of the scattering atom in EXAFS experiments is introduced. This scheme is based on the fact that the phase intercept is a measure of the type of scattering atom. A method to determine bond distances is also discussed and does not require the use of model compounds or calculated phase shifts. The physical basis for this method is the absence of a linear term in the scattering phases. Therefore, it is possible to separate these phases from the linear term containing the distance information in the total phase.

TABLE OF CONTENTS

TABLE OF CONTENTS (continued)

TABLE OF CONTENTS (continued)

LIST OF ILLUSTRATIONS AND FIGURES

LIST OF ILLUSTRATIONS (continued) Page

LIST OF ILLUSTRATIONS (continued) Page

LIST OF ILLUSTRATIONS (continued) Page

CHAPTER I

INTRODUCTION TO EXTENDED X-RAY ABSORPTION FINE STRUCTURE (EXAFS) SPECTROSCOPY

The term extended x-ray absorption fine structure (EXAFS) refers to the modulations in the x-ray absorption coefficient which occur on the high energy side of an absorption edge. The first experimental observation of these oscillations was made by Fricke[1] and Hertz[2] in 1920. The observed structure was confined to the near edge region[3], however, and thus could be readily explained by the theory of Kossel.[4] As experimental measurements improved, the structure was seen to extend many hundreds of electron volts past the edge with an amplitude of approximately 10% of the edge itself. Accordingly, a new description of this phenomenon was required.

An explanation of the physical basis of the EXAFS effect in condensed matter was first proposed by Kronig.[5] In this case, the EXAFS was described in terms of a modification of the final state photoelectron or Bloch wave due to scattering at the boundary of the Brillouin zone. Since this description depends explicitly on the periodicity of the solid such an explanation became known as a long range (LRO) theory of EXAFS. To explain the observation of EXAFS in molecules Kronig also proposed[6] a short range order (SRO) theory, in which the final state photoelectron wave is scattered by neighboring atoms. Apparently, Kronig never

realized that the same basic physics could be used to explain the observation of EXAFS in both solids and molecules. Indeed, as late as 1963, there was still a great deal of confusion as to which theory was the most appropriate description of EXAFS.[7] A major source of this confusion was the lack of quantitative comparison between theory and experiment.

It is now generally accepted that, in most instances, a single scattering SRO theory is an adequate description of EXAFS. The normalized oscillatory component of the absorption coefficient above a K-edge may be expressed as:

$$\chi(k) = \sum_j \frac{(\hat{e}\cdot\hat{r}_j)^2 N_j |f_j(k,\pi)|}{kr_j} \sin(2kr_j + \theta_j) \qquad (1.1.1)$$

This equation describes the modification of the photoelectron wave, which originates from an absorbing atom which is situated at the origin, and is scattered by N_j neighboring atoms at a radial distance r_j away. The amplitude of the EXAFS oscillations is dependent on the ability $|f_j(\pi,k)|$ of these atoms to backscatter the photoelectron. Note that the EXAFS is expressed in terms of the photoelectron wavenumber k which is defined by $k=[2m(\hbar\omega - E_o)]^{1/2}/\hbar$, where $\hbar\omega$ is the x-ray energy and E_o is the threshold energy. The argument of the sine wave in Eq. (1.1.1) is the total phase difference between the scattered and unperturbed photoelectron waves. This phase difference has a contribution due to the path difference ($2kr_j$) together with a phase function[8] $\theta_j(k)$ which represents the

phase shift due to scattering off both the absorbing and neighboring atoms. As suggested by Schmidt,[9] a term to account for thermal vibrations and static disorder should be appended to Eq. (1.1.1). Furthermore, since electrons which suffer inelastic losses may not contribute to the EXAFS, a mean-free path damping term must also be included in Eq. (1.1.1).[10]

The present interest in EXAFS began with the work of Sayers, Stern and Lytle[11] who realized that if Eq. (1.1.1) is a valid description of the EXAFS, then it should be possible to invert this expression to obtain the distances r_j. In particular, they showed that a Fourier transform of Eq. (1.1.1) is a form of radial distribution function in which the absorbing atom is located at the origin. Accordingly, there is a peak in the transform associated with each shell of atoms surrounding the central atom. These peaks do not occur at the true shell distances due to the presence of the phase function $\theta_j(k)$ in the argument of each sine wave. Therefore, to obtain distance information from EXAFS the k dependence of these phase functions must be known. If in addition, coordination numbers are to be determined, some information on the scattering amplitudes is required, together with a knowledge of the Debye-Waller and inelastic damping factors. In practice, however, model compounds[12] and theoretical calculations[13] are used extensively to extract structural information from EXAFS data.

The increased understanding of the physical basis of the EXAFS effect has been paralleled by a rapid development in the instrumentation used to measure EXAFS spectra. In particular, the advent of synchrotron radiation sources has provided a major impetus for the development of EXAFS as a structural tool.[14] Furthermore, high flux laboratory spectrometers, which utilize rotating anode sources and large crystal monochromators, are now available . These advances allow high signal to noise EXAFS spectra to be obtained in an acceptable period of time.

In view of these developments, it has been our objective to carefully re-examine the physical basis for the EXAFS effect. In Chapter II we have introduced a rigorous scattering formalism for EXAFS, which accounts for the presence of the central atom potential in a quantitative manner. The formalism also demonstrates the close relationship between EXAFS and the modulations observed in electron yield experiments. The contribution of multiple scattering processes to the observed EXAFS, which was neglected by earlier workers, is shown to be significant for systems of certain geometries . In such instances, the standard single scattering analysis methods are shown to be no longer valid. However, a careful study of such multiple scattering data should allow bond angles to be determined.

A formalism, which does not explicitly involve a scattering description of EXAFS, is introduced in Chapter III. This scheme allows an intuitive description of the

EXAFS in terms of the overlap between the initial and final states. At sufficiently high energies this description reduces to the standard EXAFS expression, Eq. (1.1.1). Unlike earlier theories, this formalism is valid over the complete energy range and may be used to describe both bound state transitions and shape resonances. Furthermore, the expression for the final state structure is an analytic function of k, and hence, may be used to calculate the damped or imaginary component of the photoelectron wave.

Since multiple scattering effects may contribute significantly to the EXAFS, the simple treatment of the thermal vibration given by Schmidt[9] is no longer valid. In Chapters IV and V of this thesis we discuss in detail the effects of thermal vibrations on EXAFS. The correlated motion of the atoms involved in the scattering process is explicitly calculated. The manner in which one should analyze such data is also discussed.

The remaining chapters of this thesis are concerned with the physical basis for the determination of structural information from EXAFS data. All the experiments described in this thesis were performed with the laboratory spectrometer which is discussed in Chapter VI. An objective method of determining the background absorption and the threshold energy is presented in Chapter VII. A novel scheme to establish the nature of the scattering atom is presented in Chapter VIII. Finally, Chapter IX demonstrates that it is possible, contrary to current belief, to obtain

bond distances from EXAFS data without the use of model compounds or calculated phase functions.

References

1. H. Fricke, Phys. Rev. **16**, 202 (1920).

2. G. Hertz, Zeit. f. Physik, **3**, 19 (1920).

3. A.E. Lindh, Zeit. f. Physik, **6**, 303 (1920).

4. W. Kossel, Zeit. f. Physik, **1**, 119 (1920).

5. R.L. Kronig, Z. Physik, **70**, 317 (1931).

6. R.L. Kronig, Z. Physik, **75**, 468 (1932).

7. L.V. Azaroff, Rev. Mod. Phys. **35**, 1012, (1963).

8. H. Peterson, Zeit. f. Physik, **80**, 528 (1933).

9. V.V. Schmidt, Bull. Acad. Sci. USSR, Ser. Phys. **25**, 998 (1961); **27**, 392 (1963).

10. M. Sawada, Rep. Sci. Works Osaka Univ. 7, 1 (1959).

11. D.E. Sayers, E.A. Stern and F.W. Lytle, Phys. Rev. Lett. **27**, 1204 (1971).

12. P.H. Citrin, P. Eisenberger and B.M. Kincaid, Phys. Rev. Lett. **36**, 1346 (1976).

13. P.A. Lee and G. Beni, Phys. Rev. **B 15**, 2862 (1977).

14. B.M. Kincaid and P. Eisenberger, Phys. Rev. Lett. **34**, 1361 (1975).

CHAPTER II

THEORY OF EXTENDED X-RAY ABSORPTION FINE STRUCTURE: SINGLE AND MULTIPLE SCATTERING FORMALISMS*

2.1 Introduction

Beginning with Kronig in 1932, a number of short range order theories[1-11] have been proposed to explain the post-edge fine structure--the extended x-ray absorption fine structure or EXAFS--of the x-ray absorption edge (see reviews of this subject by Lee et al.,[12] Stern[13] and Azaroff[14]). With the exception of Lee's recent work[10], all these studies suffer from difficulties in their treatment of the outgoing photoelectron wave, the scattering potential, or the central atom phase shift. Nevertheless, each study arrives at essentially the same expression for the oscillatory component of the K-edge x-ray absorption cross section:

$$\chi(k) \equiv \frac{\mu - \mu_0}{\mu_0} = -\sum_j (\hat{e}\cdot\hat{r}_j)^2 \frac{|f(\pi,k)|}{kr_j^2} \times \sin[2kr_j + 2\delta_1(k) + \phi(k)] \,. \qquad (2.1.1)$$

where the symbols have the following meanings: $k=[2m(\hbar\omega - E_o)]^{1/2}/\hbar$ is the photoelectron wavenumber. E_o is the threshold or binding energy of the K-shell and $\hbar\omega$ is the energy of the incident x-ray photon which is polarized in the direction $\hat{e}$. The backscattering amplitude associated with atom j is given by the expression $f_j(\pi,k) = |f_j(\pi,k)|$.

$\exp[i\phi_j(k)]$. The phase shift due to the central atom potential is $2\delta_1$, and $\mu(k)$ and $\mu_o(k)$ represent the absorption coefficients in the presence and absence of neighboring atoms in the final state.

In the case of polycrystalline samples, the geometric factor $(\hat{e}.\hat{r}_j)^2$, averages to a constant. Additional terms, to account for thermal effects[15] and losses due to inelastic scattering[5], may also be appended to Eq. (2.1.1)

Equation (2.1.1) embodies, among other assumptions, the single scattering approximation. That is, the photoelectron ejected upon absorption of an x-ray photon, is assumed to scatter off of only one neighboring atom. This description was recognized, by Lee and Pendry[9] and Ashley and Doniach[8], as being inadequate for the study of non-nearest neighbor atoms. These authors considered multiple scattering processes with pathlengths similar to those of single scattering processes but involving more distant atoms. The effect was noted to be of particular importance for multiple scattering involving the first and fourth shells in metallic copper, which are colinear with the absorbing atom. As the scattering amplitudes of all elements are strongly peaked in the forward direction, the presence of the first shell atom causes a significant amplification of the EXAFS at a frequency corresponding to the fourth shell distance. More recently, Teo[28] demonstrated the need to consider multiple scattering effects in a variety of situations. No attempt, however, was made to introduce a rigorous multiple

scattering formalism. In fact, the form of the EXAFS expression assumed by Teo[28] is incorrect, since it neglects a geometrical factor which does not average out in polycrystalline materials (see Section 2.5).

In this chapter we discuss an approach which separates the single and multiple scattering contributions of the general problem, and develops computational methods applicable to both. A general three-atom formalism is developed and employed in the discussion of two physically significant model systems.

2.2 The General Formalism

The x-ray absorption cross section in the dipole and the one-electron approximations is given by:[16]

$$\sigma_a = 4\pi^2\alpha\hbar\omega\,|\langle f|\hat{\epsilon}\cdot\mathbf{r}|i\rangle|^2 N(\omega)\,, \qquad (2.2.1)$$

where α is the hyperfine constant, ω is the angular photon frequency, and $N(\omega)$ is the density of final states for the photoelectron. The initial and final states of the system (i and f) are both eigenfunctions of an approximate unperturbed Hamiltonian H:

$$H = -\frac{\hbar^2}{2m}\nabla_r^2 - \frac{Ze^2}{r} + V\,, \qquad (2.2.2)$$

where V is the total final-state potential seen by the photoelectron. V is represented by a sum of non-overlapping, spherically symmetric, finite range potentials centered around each atomic site in the system, including

the absorbing or central atom c. A schematic representation of this final-state potential is shown in Fig. 1. The potential energy between the atomic sites is assumed to be constant and represents the zero of energy in the system.

In order to calculate the matrix element in Eq. (2.2.1), it is necessary to find the appropriate eigenfunctions of H. At energies corresponding to bound K-shell electrons (the only initial state considered here), the potentials of the neighboring atoms may be ignored, and the eigenfunction of the resulting Hamiltonian is the usual hydrogenlike wavefunction:

$$\langle r|i\rangle = \pi^{-1/2}\left(\frac{Z}{a_0}\right)^{3/2}\exp(-Zr/a_0) \qquad (2.2.3)$$

Two factors influence the nature of the final state: the potentials of the neighboring atoms and that due to the central or absorbing atom. For photoelectrons of sufficiently high energy (approximately three times the plasma frequency[6]), the attractive potential of the central atom's nucleus, together with the influence of the other bound electrons (though these are not explicitly considered here), becomes negligible, and the Schrodinger equation reduces to:

$$(E - H^0)|f\pm\rangle = V|f\pm\rangle\,, \qquad (2.2.4)$$

where H^o is the free-particle Hamiltonian. This equation may be inverted to give the Lippmann-Schwinger equation[17]

$$|f\pm\rangle = |k\rangle + G_0^{\pm}V|f\pm\rangle = |k\rangle + G_0^{\pm}T^{\pm}|k\rangle\ , \qquad (2.2.5)$$

where <r|k> are the normalized eigenfunctions of H^o. We shall use the minus form of Green's and T operators, so that <r|k> corresponds to the outgoing asymptote of the scattering process described by <r|f>. The description of the EXAFS phenomenon is thus expressed in terms of the state of the photoelectron after the scattering process is complete. Furthermore, this choice of asymptote most clearly illustrates the close relationship between EXAFS and the modulations observed in electron-yield type experiments.[29]

The full T operator may now be expanded in terms of the operators t_j associated with the individual scattering centers located at $\mathbf{r}=\mathbf{r}_j$[18]

$$T = \sum_i t_i + \sum_{i\neq j} t_i G_0 t_j + \sum_{i\neq j,\, j\neq k} t_i G_0 t_j G_0 t_k + \cdots\ . \qquad (2.2.6)$$

Note that successive scattering by the same potential is not permitted.

Substitution of the first two terms of Eq. (2.2.6) into the Eq. (2.2.5) yields an expression which may be represented graphically as shown in Fig. 2. The first diagram in this figure represents the simplest single scattering case: a photoelectron ejected in the direction $\hat{r}_j$, and scattered in some direction $\hat{R}$ by the atomic potential at $\mathbf{r}=\mathbf{r}_j$. A similar interpretation applies to the second diagram. The remaining diagrams represent double

scattering processes in which the photoelectron is scattered successively by two atomic potentials.

In particular, the third and fourth diagrams in Fig. 2 represent processes for which the second scattering center is the absorbing atom potential. In such instances the scattering path length is identical with that in the corresponding single scattering process. Accordingly, such terms must also be considered within our single scattering theory. The term corresponding to secondary scattering by the absorber was first discussed by Lee[10] and allows a rigorous treatment of the effect of the central atom potential. The approach adopted, however, was not sufficiently general to be readily extended to multiple scattering problems.

2.3 The Single Scattering Formalism

The two single scattering terms of Eq. (2.2.6) may now be substituted into the matrix element in Eq. (2.2.1):

$$\langle f - | \hat{e} \cdot \mathbf{r} | i \rangle = \langle k | \hat{e} \cdot \mathbf{r} | i \rangle + \sum_j \langle k | t_j^{\dagger} G_0^{\dagger} \hat{e} \cdot \mathbf{r} | i \rangle + \sum_j \langle k | t_c^{\dagger} G_0^{\dagger} t_j^{\dagger} G_0^{\dagger} \hat{e} \cdot \mathbf{r} | i \rangle , \tag{2.3.1}$$

where we have taken the complex conjugate of Eq. (2.2.5) and have noted that $t(z^*)=[t(z)]^{\dagger}$.

The first matrix on the right-hand side of Eq. (2.3.1) is responsible for the usual unperturbed photoelectric effect (i.e., for μ_o), and is evaluated in Appendix A with the result:

$$\langle k|\hat{e}\cdot\mathbf{r}|i\rangle = M(k,Z)\hat{k}\cdot\hat{e}\ ,$$

$$M(k,Z) = -\frac{(2)^{1/2}i}{\pi}\frac{8k\left(\frac{Z}{a_0}\right)^{5/2}}{\left(\frac{Z^2}{a_0}+k^2\right)^3}\ . \tag{2.3.2}$$

The remaining terms in Eq. (2.3.1) may be expanded in a complete set of states to obtain:

$$\sum_j \langle k|t_j^* G_0^* \hat{e}\cdot\mathbf{r}|i\rangle = \sum_j \int \langle k|t_j^*|r_1\rangle\langle r_1|G_0^*|r\rangle\,\hat{e}\cdot\mathbf{r}\langle r|i\rangle\,d\mathbf{r}\,d\mathbf{r}_1 \tag{2.3.3}$$

and

$$\sum_j \langle k|t_c^* G_0^* t_j^* G_0^* \hat{e}\cdot\mathbf{r}|i\rangle = \sum_j \int \langle k|t_c^*|r_3\rangle\langle r_3|G_0^*|r_2\rangle \times\langle r_2|t_j^*|r_1\rangle\langle r_1|G_0^*|r\rangle\,\hat{e}\cdot\mathbf{r}\langle r|i\rangle\,d\mathbf{r}\,d\mathbf{r}_1\,d\mathbf{r}_2\,d\mathbf{r}_3\ . \tag{2.3.4}$$

The EXAFS effect may be viewed as arising from a difference in phase at the origin between the unperturbed photoelectron and one that has scattered off of a neighboring atom. This occurs because the initial state is highly localized at the origin while the final state is a photoelectron which interacts with the neighboring atom potentials. To insure intensity for the EXAFS effect,the initial and final states in Eq.(2.2.1) must overlap, and hence, only the component of the scattered wave which is directed toward the origin is important. The simplest description of such a phenomenon is thus one in which all the matrix elements are expressed in terms of their effective values at the origin. The coordinate system, was chosen accordingly (see Fig. 3).

All that remains now is to evaluate matrix elements of the forms:

$$\langle r'|G_0^+|r\rangle \text{ and } \langle r'|t_j^+|r\rangle .$$

The configuration-space matrix element of the Green's operator are given by the corresponding free-particle Green's function:

$$\langle r'|G_0^+|r\rangle = -\frac{m}{2\pi\hbar^2}\frac{e^{ik|\mathbf{r}'-\mathbf{r}|}}{|\mathbf{r}'-\mathbf{r}|} . \tag{2.3.5}$$

Note that $|\mathbf{r}|$ in Eq. (2.3.5) is of the order of a_o/Z or less while $\mathbf{r}'$ is restricted to a domain of radius a_j around $\mathbf{r}_j$ (see Fig. 3). Hence $\mathbf{r}' \approx \mathbf{r}_j$ and $|\mathbf{r}'-\mathbf{r}|$ may be expanded as:[19]

$$|\mathbf{r}'-\mathbf{r}| = r_j + \hat{r}_j \cdot (\mathbf{r}'-\mathbf{r}_j-\mathbf{r}) + O(a_j/r_j) \tag{2.3.6}$$

Therefore, the Green's function in Eq. (2.3.5) may be approximated by:

$$\langle r'|G_0^+|r\rangle \approx -\frac{m}{2\pi\hbar^2}\frac{1}{r_j}\exp[i\mathbf{k}_j\cdot(\mathbf{r}'-\mathbf{r})] , \tag{2.3.7}$$

where $\mathbf{k}_j = k\hat{r}_j$ is the direction of propagation of the photoelectron. The error in making this approximation, a_j/r_j, is small since the core electrons of the neighboring atoms are responsible for most of the scattering in the EXAFS energy regime.[12]

Substituting the approximate Green's function Eq. (2.3.7) into the matrix elements Eqs. (2.3.3) and (2.3.4) permits us to perform the space integrals in the manner

described in Appendix A, with the results:

$$\sum_j \langle k|t_j^+ G_0 \vec{e}\cdot\mathbf{r}|i\rangle = -\sum_j \frac{m(2\pi)^2}{\hbar^2}\frac{1}{r_j}M(k,Z)(\hat{e}\cdot\hat{r}_j)\langle k|t_j^+|k_j\rangle\,, \tag{2.3.8}$$

$$\sum_j \langle k|t_c^+ G_0 t_j^+ G_0 \vec{e}\cdot\mathbf{r}|i\rangle = \sum_j \frac{m^2(2\pi)^4}{\hbar^4}\frac{1}{r_j^2}M(k,Z)(\hat{e}\cdot\hat{r}_j) \times\langle k|t_c^+|k_j'\rangle\langle k_j'|t_j^+|k_j\rangle\,, \tag{2.3.9}$$

where $\mathbf{k}_j' = -k\hat{r}_j$ is the direction of propagation of the back-scattered photoelectron.

We may now relate the matrix elements of $t_j^+(r_j)$ to those of $t_j^0(0)$ which represent the identical scattering problem, but centered about the origin[20]

$$\langle k|t_j^+|k_j\rangle = \exp[i(\mathbf{k}_j-\mathbf{k})\cdot\mathbf{r}_j]\langle k|t_j^0|k_j\rangle\,. \tag{2.3.10}$$

Since only elastic scattering events (i.e., $|\mathbf{k}|=|\mathbf{k}_j|$) are of interest, the matrix elements of $t_j^0(0)$ form an on-shell T matrix which may be expressed in terms of the scattering amplitude $f_j(\theta_j)$:[21]

$$\langle k|t_j^0|k_j\rangle \equiv \frac{-\hbar^2}{m(2\pi)^2}f_j(\theta_j)\,, \tag{2.3.11}$$

where $\cos\theta_j = R\cdot R_j = R\cdot\hat{r}_j$.

Equations (2.3.8) and (2.3.9) may now be rewritten as:

$$(3.8)=\sum_j M(k,Z)\frac{1}{r_j}(\hat{e}\cdot\hat{r}_j)f_j(\theta_j) \times\exp[ikr_j(1-\cos\theta_j)]\,, \tag{2.3.12}$$

and

$$(3.9)=\sum_j M(k,Z)\frac{1}{r_j^2}(\hat{e}\cdot\hat{r}_j)f_j(\pi) \times f_c(\pi-\theta_j)\exp(2ikr_j)\,, \tag{2.3.13}$$

where $\cos(\pi-\theta_j)=\mathbf{R}.\mathbf{R}_j=-\hat{\mathbf{R}}.\hat{\mathbf{r}}_j$.

The complete matrix element in Eq. (2.3.1) is the sum of three terms corresponding to the unperturbed photoelectric effect Eq. (2.3.2); simple scattering by the atom at $\mathbf{r}=\mathbf{r}_j$ Eq. (2.3.12); and secondary scattering by the absorbing atom Eq. (2.3.13):

$$\begin{aligned}\sigma_a(k) &\propto |\langle f|\hat{e}\cdot\mathbf{r}|i\rangle|^2 \\ &= |M(k,Z)\hat{k}\cdot\hat{e}+(3.12)+(3.13)|^2\,.\end{aligned} \tag{2.3.14}$$

The above treatment describes the absorption of a single x-ray photon by an absorber-scatterer atom pair. In an EXAFS experiment, however, a large number of such events will occur and the ejected photoelectrons will be scattered into many different directions $\hat{\mathbf{R}}$. In order to compute the average cross section of such a macroscopic system, it is necessary to average over all such directions $\hat{\mathbf{R}}$ in Eq. (2.3.14)

$$\int |\langle f - |\hat{e}\cdot\mathbf{r}|i\rangle|^2 \frac{d\Omega_k}{4\pi} = \int |M(k,Z)(\hat{k}\cdot\hat{e}) + (3.12) + (3.13)|^2 \frac{d\Omega_k}{4\pi}\,. \tag{2.3.15}$$

The four lowest order terms in r_j in this spherical average are evaluated in Appendix B with the results:

$$\int |M(k,Z)|^2 (\hat{k}\cdot\hat{e})^2 \frac{d\Omega_k}{4\pi} = \tfrac{1}{3}|M(k,Z)|^2\,, \tag{2.3.16}$$

$$\int 2\,\mathrm{Re}[M^*(\hat{k}\cdot\hat{e})\times(3.12)]\frac{d\Omega_k}{4\pi} = -|M|^2 \sum_j \frac{(\hat{e}\cdot\hat{r})^2}{kr_j^2}\,\mathrm{Im}[\exp(2ikr_j)f_j(\pi) + f_j(0)]\,, \tag{2.3.17}$$

$$\int |(3.12)|^2 \frac{d\Omega_k}{4\pi} = |M|^2 \sum_j \frac{(\hat{e}\cdot\hat{r}_j)^2}{r_j^2} \int |f_j(\theta_j)|^2 \frac{d\Omega_k}{4\pi}\,. \tag{2.3.18}$$

$$\int 2\,\mathrm{Re}[M^*(\hat{k}\cdot\hat{e})\times(3.13)]\frac{d\Omega_k}{4\pi} = -|M|^2 \sum_j \frac{(\hat{e}\cdot\hat{r}_j)^2}{kr_j^2} \times \mathrm{Im}\{[\exp(2i\delta_1) - 1] f_j(\pi)\exp(2ikr_j)\}\,. \tag{2.3.19}$$

Note that in summing the above expressions, the forward scattering term $f_j(0)$ in Eq. (2.3.17) cancels with Eq. (2.3.18) by virtue of the optical theorem.[22] The

macroscopic absorption coefficient $\mu = n\sigma_a$ is proportional to

$$\mu = n\sigma_a \propto \tfrac{1}{3}|M|^2 - \sum_j |M|^2 (\hat{e}\cdot\hat{r}_j)^2 \frac{1}{kr_j^2} \times \mathrm{Im}\{f_j(\pi)\exp[2i(kr_j+\delta_1)]\}, \tag{2.3.20}$$

where n is the number density of absorbing atoms. By convention, the oscillatory component of the EXAFS is normalized to μ_o.[23] Thus, the final expression for the single scattering EXAFS is obtained:

$$\chi(k) \equiv \frac{\mu-\mu_0}{\mu_0} = -\frac{3}{kr_j^2}(\hat{e}\cdot\hat{r}_j)^2 |f_j(\pi,k)| \times \sin[2kr_j + 2\delta_1(k) + \phi(k)], \tag{2.3.21}$$

where $f_j(\pi,k) = |f_j(\pi,k)|.\exp[i\phi(k)]$. We must append, onto Eq. (2.3.21), a term which describes the effects of thermal vibrations, the Debye-Waller factor; and also an additional term which accounts for the finite mean-free path of the photoelectron in the bulk. These Debye-Waller factors are discussed at length in Chapters IV and V.

2.4 The Multiple Scattering Formalism

The requirement that the final state photoelectron must scatter back to the central atom severely restricts the depth of penetration into the bulk. This is the origin of the short-range sensitivity of the EXAFS effect, the photoelectron can travel only a finite distance before it will inelastically scatter. Accordingly, the significance of multiple scattering events is limited by the total

scattering path length. In certain instances, however, the path length may be comparable to that associated with observable single scattering channels, in which case the multiple scattering contribution will dominate due to the additional scattering amplitudes involved. In general, the important multiple scattering events involve only a small number of atoms in which scattering occurs in the near forward direction. In this work we shall limit our discussion to systems which contain three atoms, the formalism developed, however, may be readily extended to study more complicated systems.

The three-atom system to be considered is shown in Fig. 4. Various scattering paths among these atoms are represented graphically in Fig. 5. Each path corresponds to a term in the expansion of the full Lippmann-Schwinger equation:

$$T = \sum_j t_j + \sum_{i \neq j} t_j G_0 t_i + \sum_{i \neq j, j \neq k} t_j G_0 t_i G_0 t_k + \cdots \qquad (2.4.1)$$

Low probability-amplitude processes involving long path lengths and/or large scattering angles have been omitted from Fig. 5, but may be treated in a manner similar to that discussed below.

The complete matrix element for the three-atom system, assuming the dipole approximation, may be written as:

$$\langle f - | \hat{e} \cdot \mathbf{r} | i \rangle = \langle k | \hat{e} \cdot \mathbf{r} | i \rangle + \sum_{n=i,j} \langle k | t_n^* G_0^* \hat{e} \cdot \mathbf{r} | i \rangle + \sum_{n=i,j} \langle k | t_c^* G_0^* t_n^* G_0^* \hat{e} \cdot \mathbf{r} | i \rangle \qquad (2.4.2)$$

$$+\langle k|t_j^{\dagger}G_0^{\dagger}t_i^{\dagger}G_0^{\dagger}\hat{e}\cdot\mathbf{r}|i\rangle+\langle k|t_i^{\dagger}G_0^{\dagger}t_j^{\dagger}G_0^{\dagger}\hat{e}\cdot\mathbf{r}|i\rangle+\langle k|t_c^{\dagger}G_0^{\dagger}t_j^{\dagger}G_0^{\dagger}t_i^{\dagger}G_0^{\dagger}\hat{e}\cdot\mathbf{r}|i\rangle \qquad (2.4.2)$$
$$+\langle k|t_c^{\dagger}G_0^{\dagger}t_i^{\dagger}G_0^{\dagger}t_j^{\dagger}G_0^{\dagger}\hat{e}\cdot\mathbf{r}|i\rangle+\langle k|t_j^{\dagger}G_0^{\dagger}t_i^{\dagger}G_0^{\dagger}t_j^{\dagger}G_0^{\dagger}\hat{e}\cdot\mathbf{r}|i\rangle+\langle k|t_c^{\dagger}G_0^{\dagger}t_j^{\dagger}G_0^{\dagger}t_i^{\dagger}G_0^{\dagger}t_j^{\dagger}G_0^{\dagger}\hat{e}\cdot\mathbf{r}|i\rangle$$

The first term in Eq. (2.4.2) corresponds to the unperturbed photoelectric effect, and the subsequent two terms correspond to the single-scattering contributions from atoms i and j. These terms have been treated in detail in the previous section and will not be discussed further here. The remaining terms in Eq. (2.4.2) involve scattering by both neighboring atoms. Of these, the fourth and fifth terms [those corresponding to diagrams (e) and (f) in Fig. 5] are identical by virtue of time reversal symmetry, as are those corresponding to diagrams (g) and (h). The multiple-scattering terms in Eq. (2.4.2) may thus be written as:

$$2\langle k|t_i^{\dagger}G_0^{\dagger}t_j^{\dagger}G_0^{\dagger}\hat{e}\cdot\mathbf{r}|i\rangle+2\langle k|t_c^{\dagger}G_0^{\dagger}t_i^{\dagger}G_0^{\dagger}t_j^{\dagger}G_0^{\dagger}\hat{e}\cdot\mathbf{r}|i\rangle$$
$$+\langle k|t_j^{\dagger}G_0^{\dagger}t_i^{\dagger}G_0^{\dagger}t_j^{\dagger}G_0^{\dagger}\hat{e}\cdot\mathbf{r}|i\rangle+\langle k|t_c^{\dagger}G_0^{\dagger}t_j^{\dagger}G_0^{\dagger}t_i^{\dagger}G_0^{\dagger}t_j^{\dagger}G_0^{\dagger}\hat{e}\cdot\mathbf{r}|i\rangle\,. \qquad (2.4.3)$$

Each term in Eq. (2.4.3) may now be expanded in complete states and the resulting Green's functions evaluated in the manner described in Section 2.3, where

$$\langle r'|G_0^{\dagger}|r\rangle\approx-\frac{m}{2\pi\hbar^2}\frac{1}{r_j}\exp[i\mathbf{k}_j\cdot(\mathbf{r}'-\mathbf{r})]\,, \qquad (2.4.4)$$

Note that the vector r is localized about the origin, $\mathbf{r}'$ is restricted to a radius a_j about $\mathbf{r}_j$, and $\mathbf{k}_j=k\hat{r}_j$. Those Green's functions which represent free propagation between two neighboring atom potentials may be evaluated by placing

one or the other of these atoms at the origin for the purposes of the calculation.

Equation (2.4.3) may now be written as:

$$
\begin{aligned}
&2\frac{M(k,Z)(\hat{e}\cdot\hat{r}_j)}{r_j r_{ij}}\frac{m^2(2\pi)^4}{\hbar^4}\langle k|t_i^+|k_{ij}\rangle\langle k_{ij}|t_j^+|k_j\rangle \\
&+2\frac{M(k,Z)(\hat{e}\cdot\hat{r}_j)}{r_i r_j r_{ij}}\frac{m^3(2\pi)^6}{\hbar^6}\langle k|t_c^+|k'_i\rangle\langle k'_i|t_i^+|k_{ij}\rangle\langle k_{ij}|t_j^+|k_j\rangle \\
&+\frac{M(k,Z)(\hat{e}\cdot\hat{r}_j)}{r_j r_{ij}^2}\frac{m^3(2\pi)^6}{\hbar^6}\langle k|t_j^+|k'_{ij}\rangle\langle k'_{ij}|t_i^+|k_{ij}\rangle\langle k_{ij}|t_j^+|k_j\rangle \\
&+\frac{M(k,Z)(\hat{e}\cdot\hat{r}_j)}{r_j r_{ij}^2}\frac{m^4(2\pi)^8}{\hbar^8}\langle k|t_c^+|k'_j\rangle\langle k'_j|t_j^+|k'_{ij}\rangle\langle k'_{ij}|t_i^+|k_{ij}\rangle\langle k_{ij}|t_j^+|k_j\rangle
\end{aligned}
\tag{2.4.5}
$$

where $\mathbf{k}_{ij} = k(\mathbf{r}_i-\mathbf{r}_j)/|\mathbf{r}_i-\mathbf{r}_j| = -\mathbf{k}'_{ij}$; $\mathbf{k}_n = k\hat{\mathbf{r}}_n = -\mathbf{k}'_n$; n=i,j and M(k,Z) has been defined in Appendix A.

The matrix elements of $t_n^+(r_n)$ associated with the atomic potential at $\mathbf{r}=\mathbf{r}_n$ may be related to those of $t_n^o(0)$ as described in Section 2.3.

$$
\langle k|t_n^+|k_n\rangle = \exp[i(\mathbf{k}_n-\mathbf{k})\cdot\mathbf{r}_n]\langle k|t_n^0|k_n\rangle \ . \tag{2.4.6}
$$

Furthermore, these matrix elements may be expressed in terms of their respective scattering amplitudes:

$$
\langle k|t_n^0|k_n\rangle = -\frac{\hbar^2}{m(2\pi)^2}f_n(\theta_n) \ , \tag{2.4.7}
$$

where $\cos\theta_n=\hat{\mathbf{k}}\cdot\hat{\mathbf{k}}_n=\hat{\mathbf{k}}\cdot\hat{\mathbf{r}}_n$. Substituting Eqs. (2.4.6) and (2.4.7) into Eq. (2.4.5) and rearranging terms gives:

$$
\begin{aligned}
&\frac{2M(k,Z)}{r_j r_{ij}}(\hat{e}\cdot\hat{r}_j)\exp(-i\mathbf{k}\cdot\mathbf{r}_i)\exp(ik|\mathbf{r}_i-\mathbf{r}_j|)f_i(\theta_{k,k_{ij}})\exp(ikr_j)f_j(\alpha) \\
&+\frac{2M(k,Z)}{r_i r_j r_{ij}}(\hat{e}\cdot\hat{r}_j)f_c(\theta_{k,k'_i})\exp(ikr_i)\exp(ik|\mathbf{r}_i-\mathbf{r}_j|)f_i(\beta)\exp(ikr_j)f_j(\alpha)
\end{aligned}
\tag{2.4.8}
$$

$$+\frac{M(k,Z)}{r_j r_{ij}^2}(\hat{e}\cdot\hat{r}_j)\exp(-i\mathbf{k}\cdot\mathbf{r}_j)f_j(\theta_{k,\kappa_{ij}})\ \exp(2ik|\mathbf{r}_i-\mathbf{r}_j|)f_i(\pi)\exp(ikr_j)f_j(\alpha) \tag{2.4.8}$$

$$+\frac{M(k,Z)}{r_j^2 r_{ij}^2}(\hat{e}\cdot\hat{r}_j)f_c(\theta_{k,\kappa_j})\exp(2ik|\mathbf{r}_i-\mathbf{r}_j|)f_i(\pi)\exp(2ikr_j)f_j^2(\alpha)\ .$$

The average x-ray absorption cross section for the three-atom system is proportional to the matrix element in Eq. (2.4.2) averaged over all possible directions $\hat{R}$ of the photoelectron:

$$\int|\langle f-|\hat{e}\cdot\mathbf{r}|i\rangle|^2\frac{d\Omega_k}{4\pi}=\int\Big|M(k,Z)(\hat{e}\cdot\hat{k})+\sum_{n=i,j}\frac{M(k,Z)(\hat{e}\cdot\hat{r}_n)}{r_n}f_n(\theta_n)$$

$$\times\exp[2ikr_n(1-\cos\theta_n)]\Big| \tag{2.4.9}$$

$$+\sum_{n=i,j}\frac{M(k,Z)(\hat{e}\cdot\hat{r}_n)}{r_n}f_n(\pi)f_c(\pi-\theta_n)\exp(2ikr_n)+(4.8)\Big|^2\frac{d\Omega_k}{4\pi}\ .$$

The first three terms in Eq. (2.4.2) were evaluated in Section 2.3, and the results appear in the integrand on the right-hand side of Eq. (2.4.9).

The methods required for the evaluation of the integrals in Eq. (2.4.9) have been developed in Appendix B. The results for the lowest order terms in r are:

$$\int|M(k,Z)|^2(\hat{e}\cdot\hat{k})^2\frac{d\Omega_k}{4\pi}=\tfrac{1}{3}|M(k,Z)|^2=\mu_0\ , \tag{2.4.10}$$

$$2\sum_{n=i,j}\frac{|M|^2(\hat{e}\cdot\hat{r}_n)}{r_n}\int\mathrm{Re}\{\exp[ikr_n(1-\cos\theta_n)]f_n(\theta_n)(\hat{e}\cdot\hat{k})\}\frac{d\Omega_k}{4\pi}$$

$$=-\sum_{n=i,j}\frac{|M|^2(\hat{e}\cdot\hat{r}_n)^2}{kr_n^2}\,\mathrm{Im}[\exp(2ikr_n)f_n(\pi)+f_n(0)]\ , \tag{2.4.11}$$

$$2\sum_{n=i,j}\frac{|M|^2(\hat{e}\cdot\hat{r}_n)}{r_n^2}\int \mathrm{Re}[f_n(\pi)f_c(\pi-\theta_n)\exp(2ikr_n)(\hat{e}\cdot\hat{k})]\frac{d\Omega_k}{4\pi}$$

$$=-\sum_{n=i,j}\frac{|M|^2(\hat{e}\cdot\hat{r}_n)^2}{kr_n^2}\,\mathrm{Im}\{[\exp(2i\delta_1)-1]f_n(\pi)\exp(2ikr_n\}\,, \qquad (2.4.12)$$

$$\frac{4|M|^2(\hat{e}\cdot\hat{r}_j)}{r_jr_{ij}}\int \mathrm{Re}[\exp(ikr_j)\exp(ik|\mathbf{r}_i-\mathbf{r}_j|)f_j(\alpha)\exp(-i\hat{k}\cdot\hat{r}_i)(\hat{e}\cdot\hat{k})f_i(\theta_{k,k_{ij}})]\frac{d\Omega_k}{4\pi}$$

$$=-\frac{2|M|^2(\hat{e}\cdot\hat{r}_i)(\hat{e}\cdot\hat{r}_j)}{kr_ir_jr_{ij}}\,\mathrm{Im}\{\exp(ikr_j)\exp(ik|\mathbf{r}_i-\mathbf{r}_j|)f_j(\alpha) \qquad (2.4.13)$$

$$[\exp(ikr_i)f_i(\beta)+\exp(-ikr_i)f_i(\pi-\beta)]\}\,,$$

$$\frac{4|M|^2(\hat{e}\cdot\hat{r}_j)}{r_ir_jr_{ij}}\int \mathrm{Re}[\exp(ikr_i)\exp(ikr_j)\exp(ik|\mathbf{r}_i-\mathbf{r}_j|)f_i(\beta)f_j(\alpha)f_c(\theta_{k,k_i'})(\hat{e}\cdot\hat{k})]\frac{d\Omega_k}{4\pi}$$

$$=-\frac{2|M|^2(\hat{e}\cdot\hat{r}_i)(\hat{e}\cdot\hat{r}_j)}{kr_ir_jr_{ij}}\,\mathrm{Im}\{\exp(ikr_i)\exp(ikr_j) \qquad (2.4.14)$$

$$\exp(ik|\mathbf{r}_i-\mathbf{r}_j|)f_i(\beta)f_j(\alpha)[\exp(2i\delta_1)-1]\}\,,$$

$$\frac{2|M|^2(\hat{e}\cdot\hat{r}_j)}{r_jr_{ij}^2}\int \mathrm{Re}[\exp(ikr_j)\exp(2ik|\mathbf{r}_i-\mathbf{r}_j|)f_i(\pi)f_j(\alpha)\exp(-i\mathbf{k}\cdot\mathbf{r}_j)(\hat{e}\cdot\hat{k})f_j(\theta_{k,k_{ij}'})]\frac{d\Omega_k}{4\pi}$$

$$=-\frac{|M|^2(\hat{e}\cdot\hat{r}_j)^2}{kr_j^2r_{ij}^2}\,\mathrm{Im}\{\exp(ikr_j)\exp(2ik|\mathbf{r}_i-\mathbf{r}_j|)f_i(\pi)f_j(\alpha) \qquad (2.4.15)$$

$$[\exp(ikr_j)f_j(\alpha)+\exp(-ikr_j)f_j(\pi-\alpha)]\}\,,$$

$$\frac{2|M|^2(\hat{e}\cdot\hat{r}_j)}{r_j^2r_{ij}^2}\int \mathrm{Re}[\exp(2ikr_j)\exp(2ik|\mathbf{r}_i-\mathbf{r}_j|)f_i(\pi)f_j^2(\alpha)f_c(\theta_{k,k_j'})(\hat{e}\cdot\hat{k})]\frac{d\Omega_k}{4\pi} \qquad (2.4.16)$$

$$=-\frac{|M|^2(\hat{e}\cdot\hat{r}_j)^2}{kr_j^2r_{ij}^2}\,\mathrm{Im}\{\exp(2ikr_j)\exp(2ik|\mathbf{r}_i-\mathbf{r}_j|)f_i(\pi)f_j^2(\alpha)[\exp(2i\delta_1)-1]\}$$

Several cancellations occur in the summation of the terms in Eq. (2.4.9). The non-oscillatory term containing $f_n(0)$ in Eq. (2.4.11) cancels with the spherically averaged squared term $|f_n(0)|^2$, by virtue of the optical theorem. The second term in Eq. (2.4.13) is cancelled by the average of the single scattering cross term arising from atoms i and j. The corresponding term in Eq. (2.4.15) also cancels, but, in this instance, with the average cross terms from the scattering processes shown in diagrams (a) and (e) of Fig. 5.

The expression obtained upon summation of the remaining terms in Eqs. (2.4.10) to (2.4.16) is proportional to the absorption coefficient of the system, and may be normalized to $\mu_o = 1/3\ |M(k,Z)|^2$, to yield the expression for the EXAFS:

$$\chi(k) = -\sum_{n=i,j} \frac{3(\hat{e}\cdot\hat{r}_n)^2}{kr_n^2} |f_n(\pi,k)| \sin[2kr_n + 2\delta_1(k) + \phi_n(k)]$$

$$- \frac{6(\hat{e}\cdot\hat{r}_i)(\hat{e}\cdot\hat{r}_j)}{kr_i r_j r_{ij}} |f_i(\beta,k)|\,|f_j(\alpha,k)| \sin[k(r_i + r_j + r_{ij}) + 2\delta_1(k) + \phi_i(k) + \phi_j(k)] \qquad (2.4.17)$$

$$- \frac{3(\hat{e}\cdot\hat{r}_j)^2}{kr_j^2 r_{ij}^2} |f_i(\pi,k)|\,|f_j(\alpha,k)|^2 \sin[2k(r_j + r_{ij}) + 2\delta_1(k) + \phi_i(k) + 2\phi_j(k)]\,,$$

where $f_n(\theta_n) = |f_n(\theta_n)|.\exp(i\phi_n)$ and n=i,j. Note that we have assumed that the phase of the scattering amplitude is independent of the scattering angle (i.e., $\arg[f_n(\theta_1)] = \arg[f_n(\theta_2)]$ where n=i,j). This assumption is not strictly valid,[28] but may be used to gain some understanding of the physical significance of these multiple scattering

processes.

In the case of polycrystalline materials an average over all possible polarization direction must be performed. The x-ray polarization directions in the dot products in Eq. (2.4.17) may be spherically averaged, with the results:

$$\int(\hat{e}\cdot\hat{r}_n)^2\frac{d\Omega_e}{4\pi}=\frac{1}{3}\quad,$$
$$\int(\hat{e}\cdot\hat{r}_j)(\hat{e}\cdot\hat{r}_i)\frac{d\Omega_e}{4\pi}=\frac{\hat{r}_j\cdot\hat{r}_i}{3}\,. \tag{2.4.18}$$

2.5 Results and Discussion

A straightforward derivation of the basic EXAFS equation has been presented. The simplicity of our approach lies in the expansion of the scattering amplitudes of neighboring atoms about the origin. Accordingly, the phase factor reflecting the difference in path length between unperturbed photoemission and various scattering processes arises in a natural manner.

The form of the Lippmann-Schwinger equation is of particular significance. In our scheme, <r|k> represents the outgoing asymptote and corresponds to the state of the photoelectron after the scattering process. This form has permitted us to describe the scattering in a simple diagrammatic fashion (Fig. 2). It also emphasizes the interference nature of the EXAFS effect, expressed in Eq. (2.3.1), in which the probability amplitude for x-ray absorption is given by the sum of three independent

scattering processes. Such a sum is required due to the indistinguishability of the individual events: the ejection of a photoelectron in some direction $\hat{R}$ upon ionization is completely indistinguishable from a process in which the ejected electron scatters off an adjacent atom and is subsequently scattered into the same direction $\hat{R}$ by the central atom.

Within our formalism, the central atom phase shift cancels in the interference terms since the direct and scattered photoelectron waves are both outgoing in nature. It is thus necessary to include the secondary scattering term in order to retrieve this phase shift. In the alternative form of the Lippmann-Schwinger equation [i.e., the use of $\langle r|f+\rangle$ in Eq. (2.2.5)], however, the term corresponding to the scattered photoelectron is an incoming wave, and no such cancellation occurs. In this latter approach, $\langle r|k\rangle$ corresponds to the incoming asymptote of the scattering process, and the phase does not explicitly occur within the formalism.

An expression for the oscillatory component of the absorption for the three-atom system has been given in Eq. (2.4.17). The first term corresponds to the independent single scattering events by atoms i and j. The second term results from scattering from atoms i and j, and vica versa. Note that this term retains a geometrical dependence even for experiments involving polycrystalline samples [see Eq. (2.4.18)]. The double scattering term vanishes when the

angle θ is 90^{o}. The expression assumed by earlier workers[28] omits this geometrical factor and hence overestimates the contribution of this term to the total EXAFS. The neglection of this factor, however, greatly facilitates the analysis of multiple scattering data. The third term in Eq. (2.4.17) results from a more complex scattering path: the photoelectron scatters sequentially off of atoms j and i, and then off of atom j once again (where we have assumed that $|r_j| < |r_i|$).

The cancellation of terms which occurred in Eq. (2.4.9) is of particular significance, since it insures that each term in the EXAFS expression is dependent on the sum of the interatomic distances that it represents. These processes are shown diagrammatically in Fig. 6: the first term in Eq. (2.4.17) corresponds to the sum of the diagrams 6(a) and 6(b), and the second and third terms correspond to diagrams 6(c) and 6(d), respectively. These diagrams are analogous to those of Fig. 5, but each is the spherically averaged sum of several of the latter diagrams. Note that no scattering is shown by the central atom, since the spherical average of Eq. (2.4.9) projects out the return path to the origin (shown as a straight line in Fig. 6).

In order to examine the relative importance of the various terms in Eq. (2.4.17), two model systems, Fe-O-Fe and Cu-S-Cu, were considered. The respective metal atoms were taken to be the absorbing atoms and the bond lengths fixed at 1.76 Å for the iron system {the distance found in

the binuclear complex μ-oxo-bis[tetraphenylporphine-iron(III)] and similar compounds} and 2.3 Å for the copper system. The scattering amplitudes were taken from the International Tables for X-Ray Crystallography, Vol. IV,[25] and the phase shift functions from the parametrizations of Lee et al.[26] These scattering amplitudes were calculated using the Born approximation. While this is an over-simplification it does not, however, significantly affect the results presented below.

The calculated contribution of each term to the EXAFS at a particular value of the bridging angle (140°) are shown in Figs. 7 and 8. The relative amplitudes of the various terms may be seen from the Fourier transforms in Fig. 9. No corrections were made for damping at large r due to inelastic scattering, but any such correction would affect the three terms involving the second-shell atom almost equally (the first shell peak would be relatively higher, however). Compared to the second-shell single scattering term, multiple scattering is significant in systems in which the ratio of the scattering power of the first- and second-shell-nearest neighbors is large or when the three atoms are nearly colinear.

Note also the relative linewidths of the various terms. The peaks due to multiple scattering processes are broader, primarily because of the additional scattering amplitudes involved. Scattering amplitudes in the Born approximation, decrease as a function of k in an approximate exponential

manner, and hence the effect on the Fourier transform is similar to that of a Debye-Waller factor.

Figures 10 and 11 show the variations of the peak positions and amplitudes in the Fourier transform as a function of bridging angle for both the iron and copper systems. Note that, in Figs. 10(a) and 10(b), there is a point where the additional phase shift incurred during the multiple scattering process is exactly offset by the additional path length involved in that process. This occurs because, the effect of the scattering phases in the sine argument of Eq. (2.4.17), is to shift the peaks in the Fourier transform to smaller distances, since these phase are largely monotonically decreasing functions of k.[26]

The condition required for this crossover point is given by:

$$|r_i| - |r_j| - |r_i - r_j| = \Delta r(\phi_j) \qquad (2.5.1)$$

where $\Delta r(\phi_j)$ is the effective displacement of the peak in the Fourier transform due to the phase of the scattering amplitude associated with atom j. This quantity, $\Delta r(\phi_j)$, is independent of the geometry of the system (provided the phase of the scattering amplitude is independent of the scattering angle, as discussed earlier), and varies over a limited range for different atom types j. The primary dependence of the crossover point is on the bond lengths; as the distances in the system increase, the crossover point occurs at larger bridging angles.

At bridging angles greater than the crossover point,

the multiple scattering terms are of particular importance. As shown in Fig. 11 these terms have large amplitudes at high angles and, above the crossover point, the corresponding peaks in the Fourier transform occur at smaller distance values than does the second-shell single scattering peak. In general, the three peaks involving the second-shell atom will be close enough to overlap in the transform. The presence of the multiple scattering components will then cause an apparent increase in the amplitude of the second-nearest neighbor peak in addition to shifting this peak to anomalously small distances. Therefore, if an analysis of EXAFS data which contain a significant multiple scattering contribution, is attempted using single scattering theory, one would overestimate the coordination number of the second-shell and underestimate the distance to that shell. Recently, Co *et al.*[27] studied a series of μ-oxo bridged iron systems using single scattering theory; their results are shown in Fig. 12. For a linear system, Co *et al.* predict an error in the coordination number of a factor of four and an underestimation of the distance by 0.2 Å. These results may be compared directly with the calculations for the μ-oxo system shown in Figs. 10(a) and 11(a). Since, when the system is linear, both multiple scattering components have comparable amplitudes and clearly dominate the second-shell EXAFS, the position of the composite second-shell peak may be taken as the average of the positions of the double and triple scattering peaks.

Therefore, we calculate from Fig. 10(a) that the average of the multiple scattering peak positions is smaller than that of second-shell single scattering peak by an amount of 0.21 Å. This is in excellent agreement with the observations of Co *et al*. A similar analysis when applied to the peak amplitudes in Fig. 11(a) yields an overestimation of the second-shell coordination number by a factor of eight. The calculated peak amplitudes are clearly inconsistent with the experimental observations.[27] The origin of this discrepancy is the omission of both the Debye-Waller and inelastic damping factors from the theoretical calculations. Chapters IV and V present a detailed study of the nature of the Debye-Waller factors in EXAFS.

At bridging angles which are smaller than the crossover point, the composite second-shell peak will occur at a larger distance than the second-shell single scattering peak; the effect is less significant, however, since the multiple scattering components have smaller amplitudes in this region.

In conclusion, multiple scattering effects need to be considered in many problems in which non-nearest neighbor shells are of interest. If such considerations are not made, serious errors may be incurred in the analysis of the data. Careful analysis of these effects, however, may allow the elucidation of geometrical information, such as bond angles, which is not otherwise available from the single scattering theory.

Appendix A

We wish to evaluate the integral

$$I = \int \langle k | r \rangle \, \hat{e} \cdot \mathbf{r} \langle r | i \rangle \, d\mathbf{r} \tag{A1}$$

which appears in Eq. (3.1); where $\langle r | k \rangle = (2\pi)^{-3/2} \times \exp(i\mathbf{k} \cdot \mathbf{r})$ and $\langle r | i \rangle = (\pi)^{-1/2}(Z/a_0)^{3/2} \exp(-Zr/a_0)$.

Expanding Eq. (A1) in terms of spherical harmonics, I may be rewritten as

$$I = (2\pi)^{-3/2} 4(\pi)^{1/2} \left(\frac{Z}{a_0}\right)^{3/2} \sum_l \sum_m \int (-i)^l j_l(kr) \times \exp(-Zr/a_0) r^2 \, dr \int Y_l^{*m}(\Omega_k) Y_l(\Omega_r)(\mathbf{r} \cdot \hat{e}) \, d\Omega_r \, , \tag{A2}$$

where $d\mathbf{r} = r^2 \, dr \, d\Omega_r$.

The angular integration in Eq. (A2) may be performed using the additional theorem for spherical harmonics:

$$\sum_l \sum_m \int Y_l^{*m}(\Omega_k) Y_l^m(\Omega_r)(\mathbf{r} \cdot \hat{e}) \, d\Omega_r = \frac{4\pi r}{3} \sum_l^{\infty} \sum_{m=-l}^{l} \sum_{s=-1}^{1} Y_1^s(\Omega_e) Y_l^{*m}(\Omega_k) \int Y_1^{*s}(\Omega_r) Y_l^m(\Omega_r) \, d\Omega_r = \frac{4\pi r}{3} \sum_{s=-1}^{1} Y_1^s(\Omega_e) Y_l^{*m}(\Omega_k) \delta_{m,s} \delta_{l,1} = r(\hat{k} \cdot \hat{e}) \, . \tag{A3}$$

Substituting Eq. (A3) into Eq. (A2), the expression for I becomes

$$I = (2\pi)^{-3/2} 4(\pi)^{1/2} (-i) \left(\frac{Z}{a_0}\right)^{3/2} (\hat{k} \cdot \hat{e}) \times \int_0^{\infty} j_1(kr) \exp(-Zr/a_0) r^3 \, dr \, , \tag{A4}$$

where $j_1(kr) = (kr)^{-2} \sin kr - (kr)^{-1} \cos kr$. Making use of the definite integral,

$$\int_0^{\infty} x^n e^{-\mu x} \, dx = n! \, \mu^{-(n+1)} \, , \quad \mathrm{Re}\, \mu > 0$$

the radial integration in Eq. (A4) may be performed to obtain

$$I = M(k, Z)(\hat{k} \cdot \hat{e}) \, ,$$

where $M(k, Z) = -i[(2)^{1/2}/\pi] \, [8k(Z/a_0)^{5/2}/(Z^2/a_0^2 + k^2)^3]$.

Appendix B

In this appendix, the angular integrals in Eq. (3.16), (3.17), and (3.19) are evaluated.

The first of these corresponds to μ_0, the hypothetical absorption coefficient in the absence of neighboring atoms. Placing $\hat{e}$ along the z direction:

$$\mu_0 \propto \frac{1}{4\pi}\int |M|^2 \hat{k}\cdot\hat{e}\, d\Omega_k$$

$$= \frac{|M|^2}{4\pi}\int \cos^2\theta_k \sin\theta_k\, d\theta_k\, d\phi_k = \tfrac{1}{3}|M(k,Z)|^2 \ .$$

The following result is required in Eq. (3.17):

$$I = \int (\hat{e}\cdot\hat{k}) \exp(-i\mathbf{k}\cdot\mathbf{r}_j) f(\theta_j)\frac{d\Omega_k}{4\pi} \ .$$

$(\hat{e}\cdot\hat{k})$ may be expanded in spherical harmonics, and setting $\mathbf{r}_j$ along the z axis, the azimuthal integration yields the $m=0$ component in the expansion. Hence:

$$I = -(\hat{e}\cdot\hat{r}_j)\frac{1}{2}\int d(\cos\theta_k)\cos\theta_k \exp(-i\mathbf{k}\cdot\mathbf{r}_j) f(\theta_j) \ , \qquad \text{(B1)}$$

where $\cos\theta_k = (\hat{k}\cdot\hat{r}_j)$. $\exp(-i\mathbf{k}\cdot\mathbf{r}_j)$ and $f(\theta_j)$ may be expressed in terms of Legendre polynomials:

$$\exp(-i\mathbf{k}\cdot\mathbf{r}_j) = \sum_l (2l+1)(-i)^l j_l(kr_j) P_l(\cos\theta_k) \ , \qquad \text{(B2)}$$

$$f(\theta_j) = \sum_{l'} f_{l'} P_{l'}(\cos\theta_k) \ , \qquad \text{(B3)}$$

and

$$P_l(\cos\theta_k) = \left(\frac{4\pi}{2l+1}\right)^{1/2} Y_l^0(\Omega_k) \ . \qquad \text{(B4)}$$

Substituting the above into Eq. (B1) yields

$$I = \sum_{l,l'} (\hat{e}\cdot\hat{r}_j)\tfrac{1}{2}(2l+1)(-i)^l \left(\frac{4\pi}{2l+1}\right)^{1/2}\left(\frac{4\pi}{2l'+1}\right)^{1/2}\left(\frac{4\pi}{3}\right)^{1/2}$$

$$\times j_l(kr_j) f_{l'} \int Y_{l'}^0(\Omega_k) Y_1^0(\Omega_k) Y_l^0(\Omega_k) d(-\cos\theta_k) \ , \qquad \text{(B5)}$$

where $d\Omega_k = d(-\cos\theta_k)d\phi_k$, and $\int_0^{2\pi}(d\phi_k/2\pi) = 1$. The angular integral in Eq. (B5) may be evaluated using the properties of Clebsch–Gordan coefficients[24]:

$$\int Y_{l'}^0(\Omega_k) Y_1^0(\Omega_k) Y_l^0(\Omega_k)\, d\Omega_k$$

$$= \left[\frac{(2l'+1)}{4\pi}\frac{3}{(2l+1)}\right]^{1/2} [C(l',1,l;0,0,0)]^2 \ ,$$

where $|l-l'| \le 1 \le |l+l'|$ and $l+l'+1=2n$ (n an integer). The summation over l and l' may be replaced by a single sum that has two components $l \pm 1$. Using the explicit forms of the Clebsch–Gordan coefficients above,

$$I = \sum_l (\hat{e}\cdot\hat{r}_j) f_l \left[(-i)^{l+1}\left(\frac{l+1}{2l+1}\right) j_{l+1}(kr_j) + (-1)^{l-1}\left(\frac{l}{2l+1}\right) j_{l-1}(kr_j)\right] = \sum_l (\hat{e}\cdot\hat{r}_j) f_l \left[\frac{l}{2l+1}\ j_{l-1}(kr_j) - \left(\frac{l+1}{2l+1}\right) j_{l+1}(kr_j)\right](-i)^{l-1} \ . \tag{B6}$$

Using the asymptotic form of the spherical Bessel function:

$$I = (\hat{e}\cdot\hat{r}_j)\frac{1}{kr_j}\tfrac{1}{2}i[\exp(ikr_j)f(\pi) + \exp(-ikr_j)f(0)] \ .$$

Hence:

$$\int 2\,\mathrm{Re}[M^*(\hat{k}\cdot\hat{e})(3.12)]\frac{d\Omega_k}{4\pi} = -\sum_j |M|^2 \frac{1}{kr_j^2}(\hat{e}\cdot\hat{r}_j)^2\,\mathrm{Im}[\exp(2ikr_j)f(\pi)+f(0)] \ .$$

The third angular integration necessary is given in Eq. (3.19):

$$I' = \int (\hat{e}\cdot\hat{k}) f_c(\pi-\theta_j)\frac{d\Omega_k}{4\pi} \ , \tag{B7}$$

where $f_c(\pi-\theta_j) = (-1)^l f_c(\theta_j)$

$$= \sum_l \sum_{m=-l}^{l} \frac{(-1)^l}{2ik}(4\pi)[\exp(2i\delta_l)-1]Y_l^m(\Omega_k)Y_l^{*m}(\Omega r_j) \ .$$

Expanding $(\hat{e}\cdot\hat{k})$ in spherical harmonics:

$$(\hat{e}\cdot\hat{k}) = \frac{4\pi}{3}\sum_{m'=-1}^{1} Y_1^{m'}(\Omega_e)Y_1^{*m'}(\Omega_k) \ .$$

Equation (B7) may be written:

$$I' = \frac{(-1)^l}{2ik}\frac{4\pi}{3}\sum_l \sum_{m=-l}^{l}\sum_{m'=-1}^{1}[\exp(2i\delta_l)-1]Y_l^{*m}(\Omega r_j)Y_1^{m'}(\Omega_e) \times \int Y_l^m(\Omega_k)Y_1^{*m'}(\Omega_k)d\Omega_k = -\frac{1}{2ik}[\exp(2i\delta_1)-1](\hat{e}\cdot\hat{r}_j)$$

due to the orthogonality of spherical harmonics. Hence:

$$\int 2\,\mathrm{Re}[M^*(k,Z)(\hat{e}\cdot\hat{k})(3.13)]\frac{d\Omega_k}{4\pi} = -|M|^2\sum_j \frac{(\hat{e}\cdot\hat{r}_j)^2}{kr_j^2}\,\mathrm{Im}\{[\exp(2i\delta_1)-1]f_j(\pi)\exp(2ikr_j)\} \ ,$$

References

*This chapter is based on: J.J. Boland, S.E. Crane and J.D. Baldeschwieler, J. Chem. Phys. **77**, 142 (1982).

1. R. de L. Kronig, Z. Phys. **80**, 317 (1931); **75**, 191 (1932); **75**, 468 (1932).

2. H. Petersen, Z. Phys. **80**, 258 (1933).

3. A.I. Kosterev, Zh. Eksp. Teor. Fiz. **19**, 413 (1949).

4. T. Shiraiwa, T. Ishimura and M. Sawada, J. Phys. Soc. Jpn. **138**, 848 (1958).

5. D.E. Sayers, F.W. Lytle and E.A. Stern, Adv. X-ray Anal. **13**, 248 (1970).

6. W.L. Schaich, Phys. Rev. **B 8**, 4028 (1973).

7. E.A. Stern, Phys. Rev. **B 10**, 3027 (1974).

8. C.A. Ashley and S. Doniach, Phys. Rev. **B 11**, 1279 (1975).

9. P.A. Lee and J.B. Pendry, Phys. Rev. **B 11**, 2795 (1975).

10. P.A. Lee, Phys. Rev. **B 13**, 5261 (1976).

11. P.A. Lee and G. Beni, Phys. Rev. **B 15**, 2862 (1977).

12. P.A. Lee, P.H. Citrin, P. Eisenberger and B.M. Kincaid, Rev. Mod. Phys. **53**, 769 (1981).

13. E.A. Stern, Contemp. Phys. **18**, 289 (1978).

14. L.V. Azaroff, Rev. Mod. Phys. **35**, 1012 (1963).

15. V.V. Schmidt, Bull. Acad. Sci. USSR, Ser. Phys. **25**, 988 (1961).

16. E. Merzbacher, Quantum Mechanics, 2nd ed. (Wiley, New York) p. 466.

17. J.R. Taylor, Scattering Theory (Wiley, New York, 1972) p. 168.

18. P. Lloyd and P.V. Smith, Adv. Phys. **21**, 69 (1972).

19. L.I. Schiff, Quantum Mechanics, 3rd ed. (McGraw-Hill, New York, 1968), p. 338.

20. M. Lax, Rev. Mod. Phys. **23**, 287 (1951).

21. J.R. Taylor, Ref. 19, p. 43.

22. J.R. Taylor, Ref. 19, p. 54.

23. B.K. Teo, P.A. Lee, A.L. Simons, P. Eisenberger and B.M. Kincaid, J. Am. Chem. Soc. **99**, 3854 (1977).

24. E. Merzbacher, Ref. 16, p. 396.

25. J.A. Ibers and W.C. Hamilton, International Tables for X-ray Crystallography (Kynoch, Birmingham, U.K., 1974), Vol. IV, p. 152.

26. P.A. Lee, B.K. Teo and A.L. Simons, J. Am. Chem. Soc. **99**, 3856 (1977).

27. M.S. Co, W.A. Hendrickson, K.O. Hodgson and S. Doniach J. Am. Chem. Soc. **105**, 1144 (1983).

28. B.K. Teo, J. Am. Chem. Soc. **103**, 3990 (1981).

29. J.J. Barton, C.C. Bahr, Z. Hussain, S.W. Robey, J.G. Tobin, L.E. Klebanoff and D.A. Shirley, Phys. Rev. Lett. 51, 272 (1983).

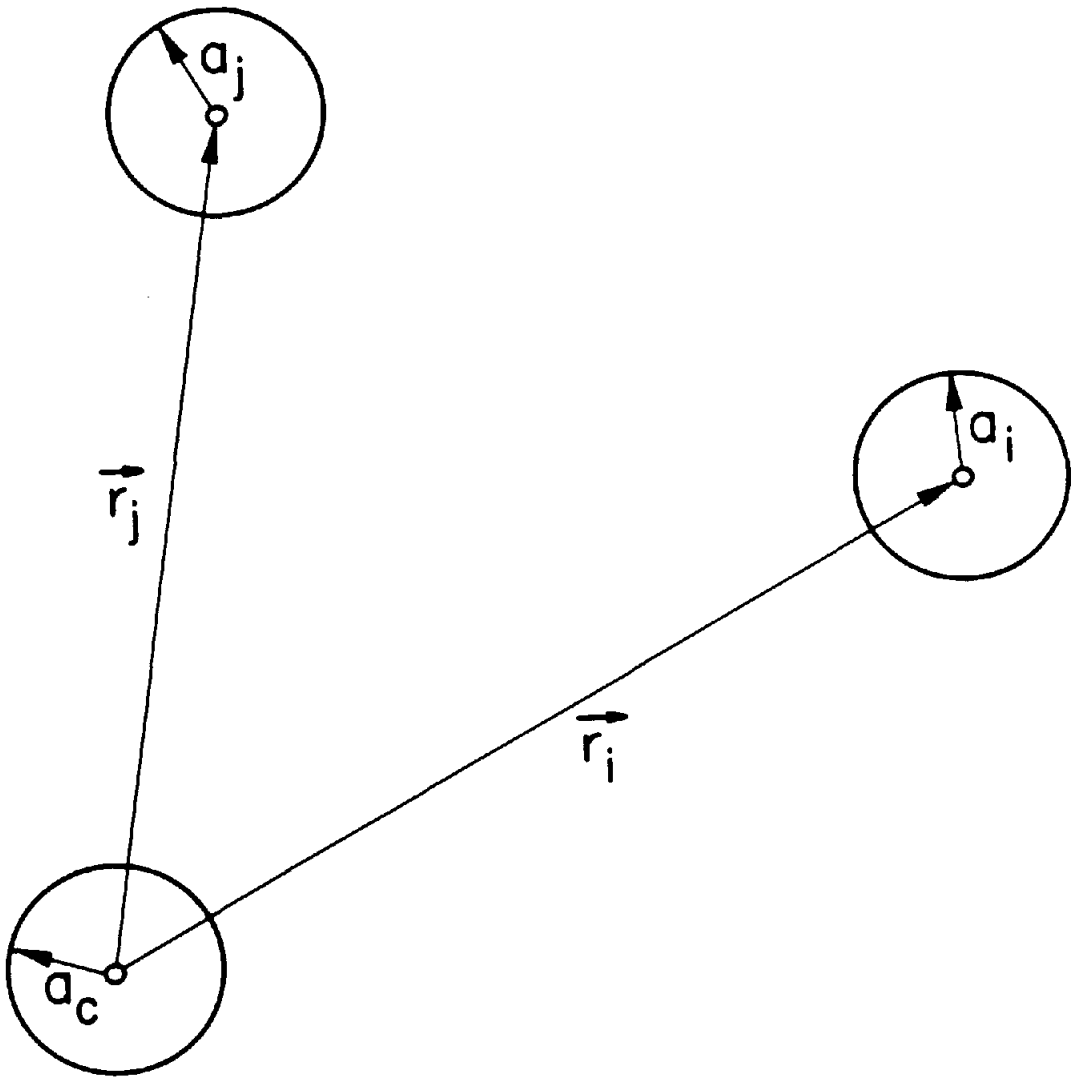

Figure 1.
Schematic representation of the final state potential V. About each atomic site, including the central atom c, there exists a sphere of radius $\underline{a}$ beyond which no scattering will occur. The atomic potentials are assumed to be spherically symmetric.

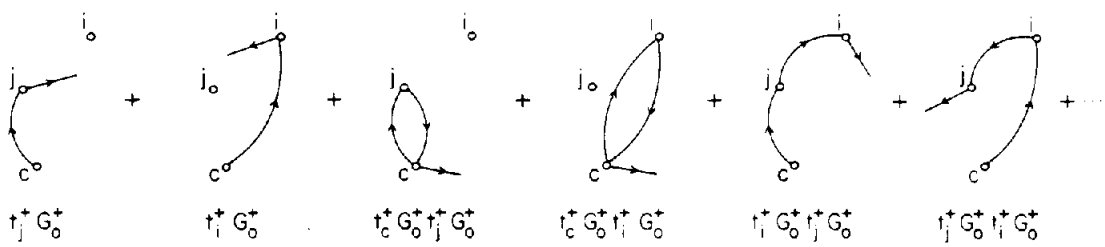

Figure 2.
Diagrammatic representation of the first and second order terms in the expansion of the full T operator in Eq. (2.2.6). The scattering paths shown are those that occur in a system with two neighboring atoms i and j.

Figure 3.
The vectors pertaining to the evaluation of the Green's function shown in Eq. (2.3.5). Upon absorption of an x-ray photon, the photoelectron propagates freely from $\mathbf{r}$, within a domain of radius a_c, to $\mathbf{r}'$, within a domain of radius a_j about the atom at $\mathbf{r}=\mathbf{r}_j$.

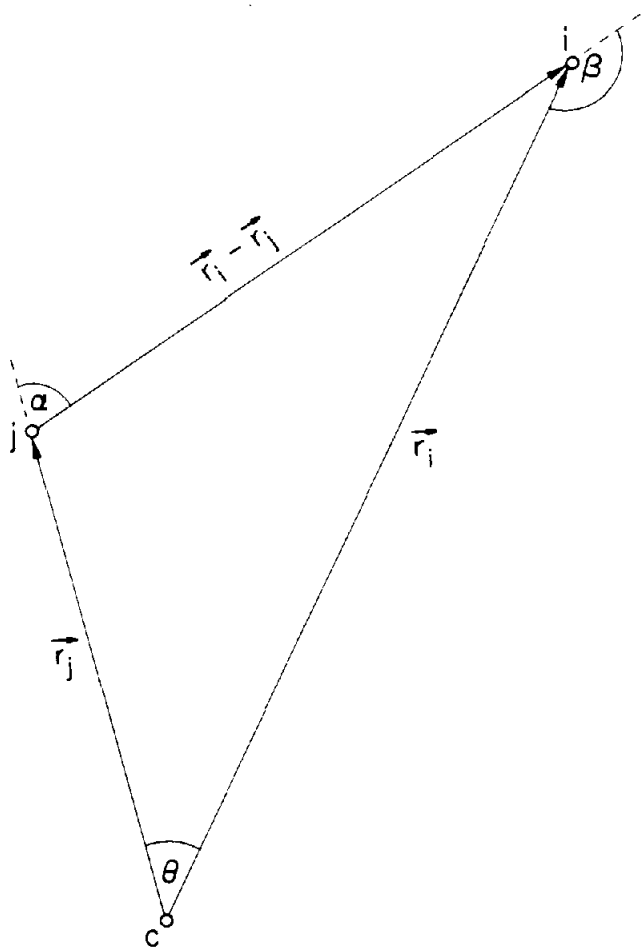

Figure 4.
The three-atom system. The central or absorbing atom is c. There are two neighboring atoms, i and j, where it is assumed that $|r_j| \leq |r_i|$. The bridging angle is given by $\pi - \alpha$.

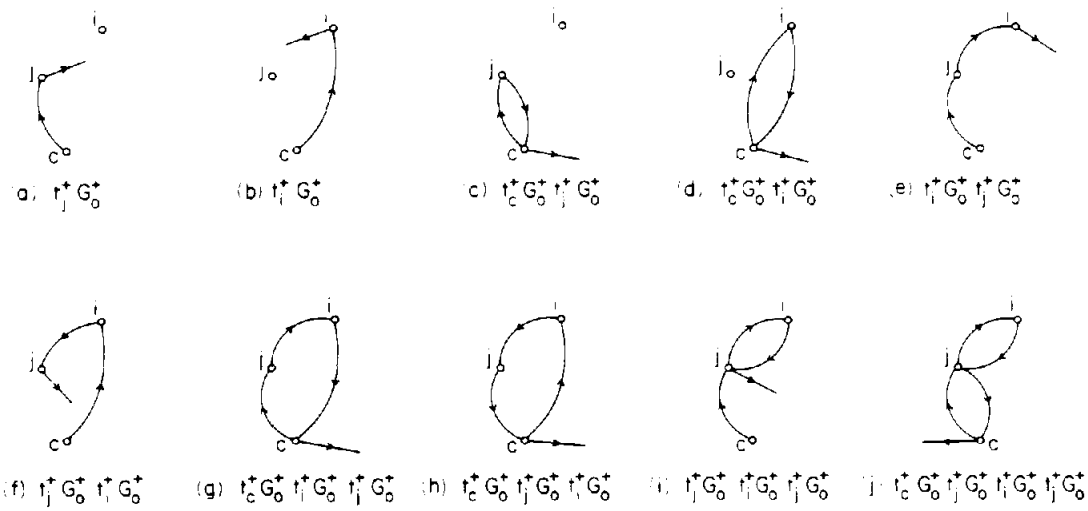

Figure 5.
The most significant scattering paths within the three-atom system. The operators shown with each diagram represent the corresponding term in the expansion of the full T operator in the Lippmann-Schwinger equation [Eq. (2.4.1)].

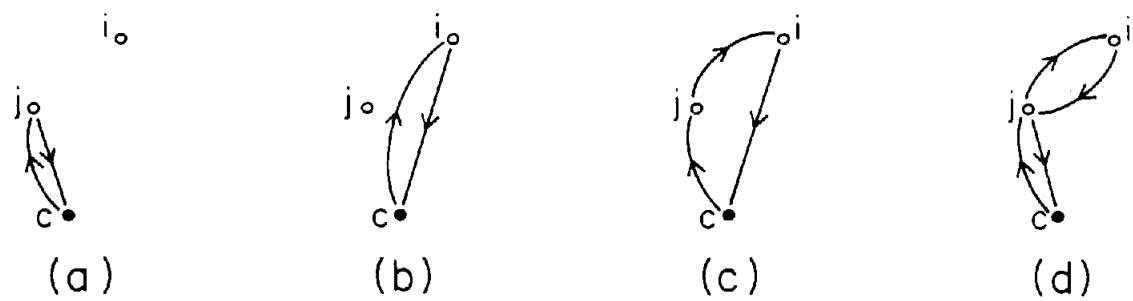

Figure 6.
Schematic representation of the terms in the EXAFS expression for the three-atom system. Note that no scattering is shown by the central atom since the spherical average in Eq. (2.4.9) projects out the return path to the origin (shown as a straight line).

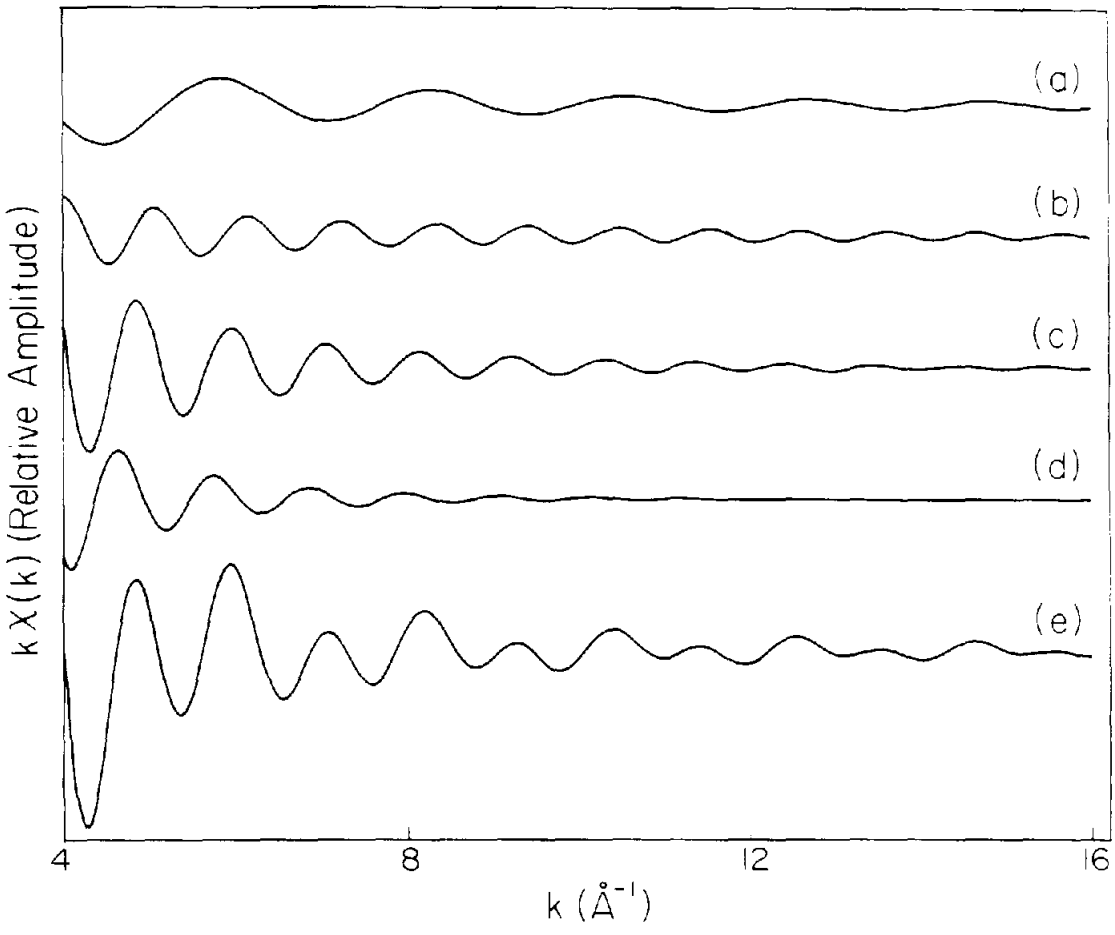

Figure 7.
Calculated EXAFS spectra for the Fe-O-Fe system. The bridging angle is 140° and the bond distances $r_{ij}=r_{ji}=1.76$ Å. Curves (a) and (b) are the single scattering contributions from the oxygen and iron atoms. Curves (c) and (d) are the double and triple scattering contributions. Curve (e) is the sum of all the above an represents the total EXAFS of the three-atom system.

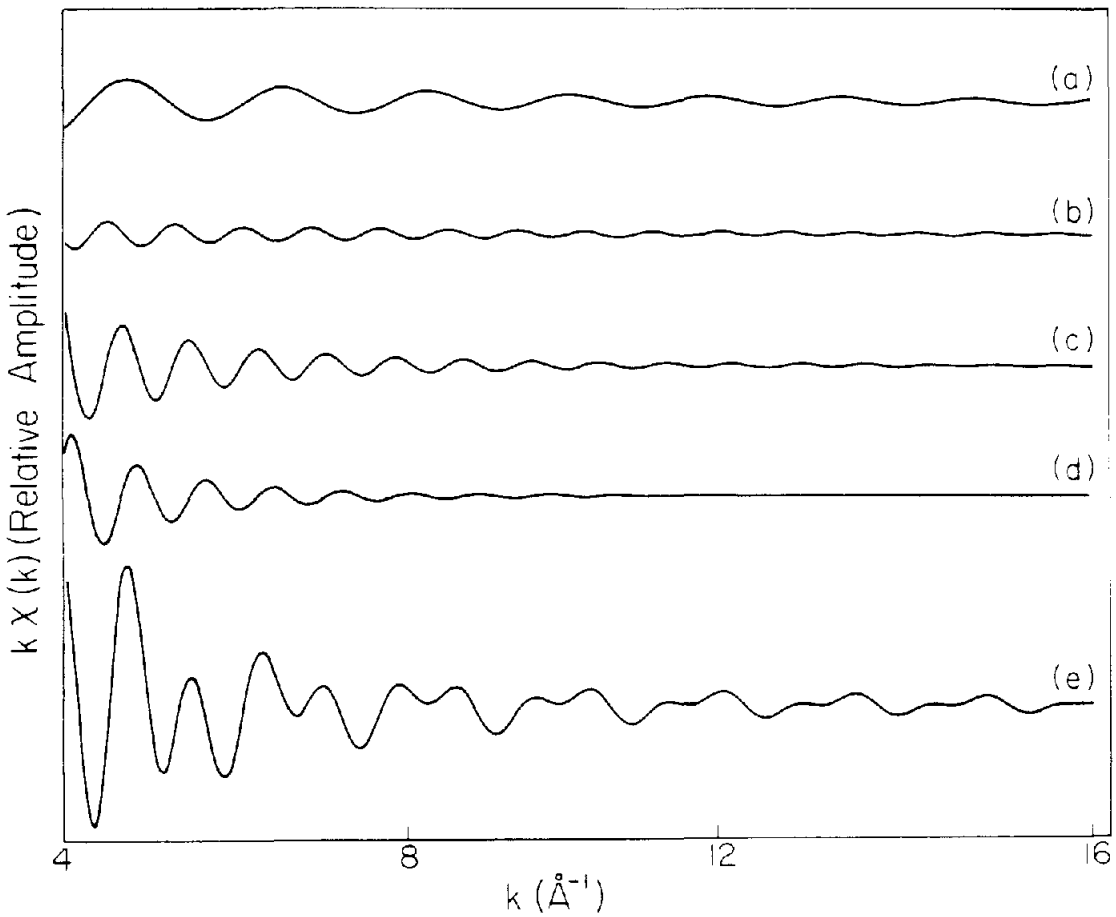

Figure 8.
Calculated EXAFS spectra for the Cu-S-Cu system. The bridging angle is 140° and the bond distances $r_j=r_{ij}=2.3$ Å. The individual curves are analogous to those shown in Fig. 7.

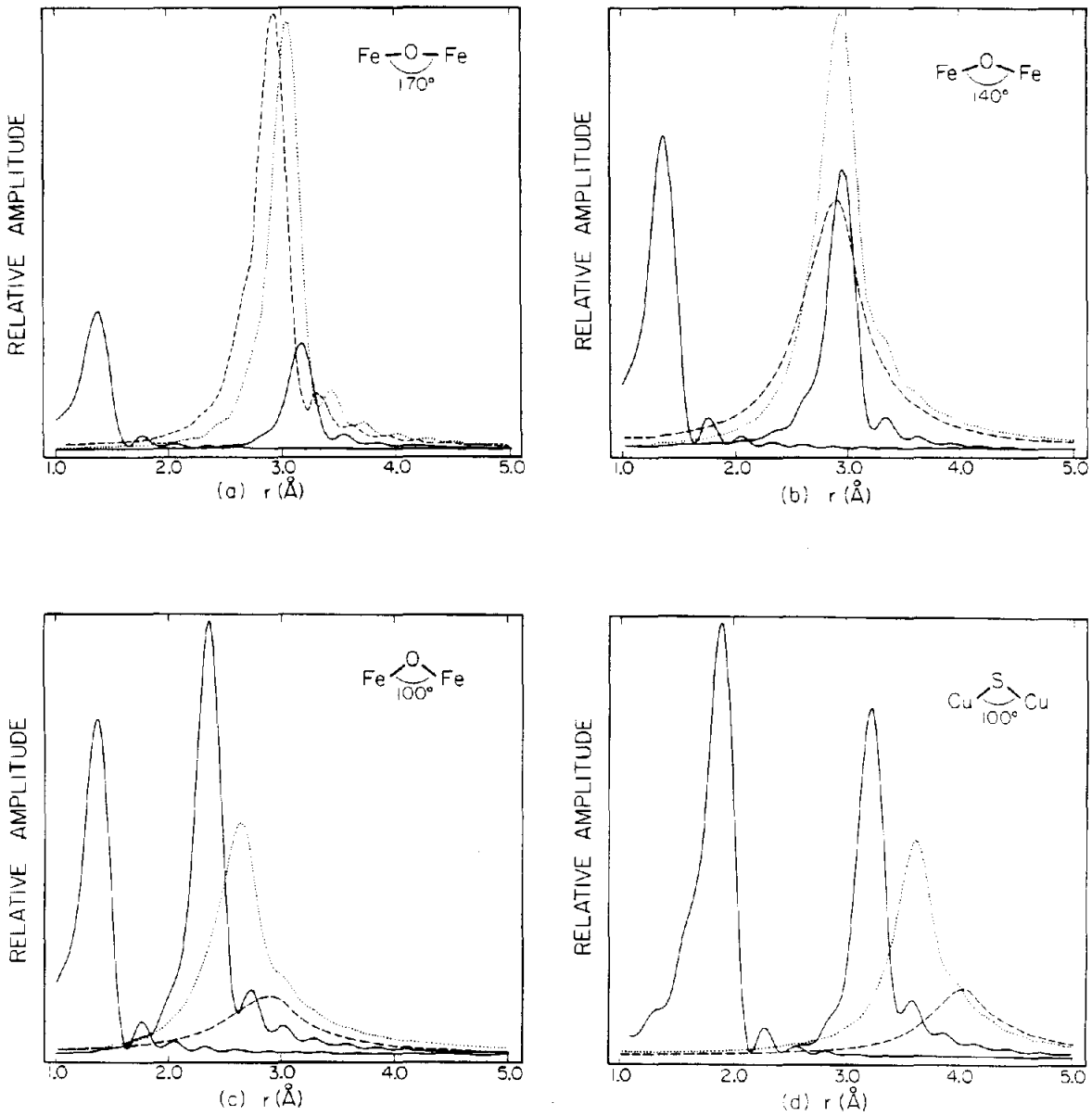

Figure 9.

Representative Fourier transforms of the bridged iron and copper systems at a series of bridging angles. The bond distances are the same as those in Figs. 7 and 8. Solid curves are the single scattering contributions. The dotted and dashed curves are the double and triple scattering contributions, respectively.

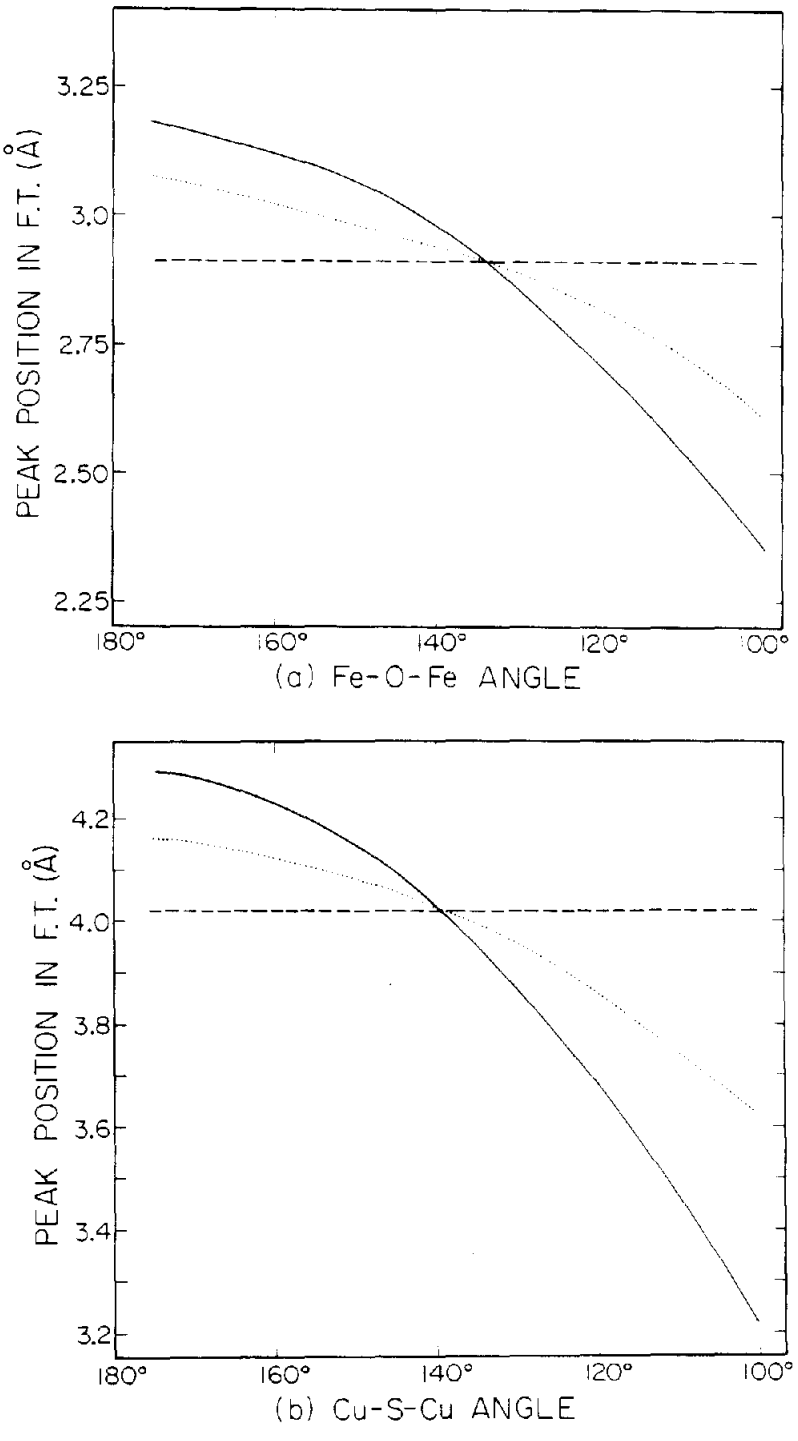

Figure 10.
Peak positions in the Fourier transform as a function of bridging angle. The solid curve is the second shell single scattering, while the dotted and dashed curves are the double and triple scattering pathways. (a) Fe system. (b) Cu system.

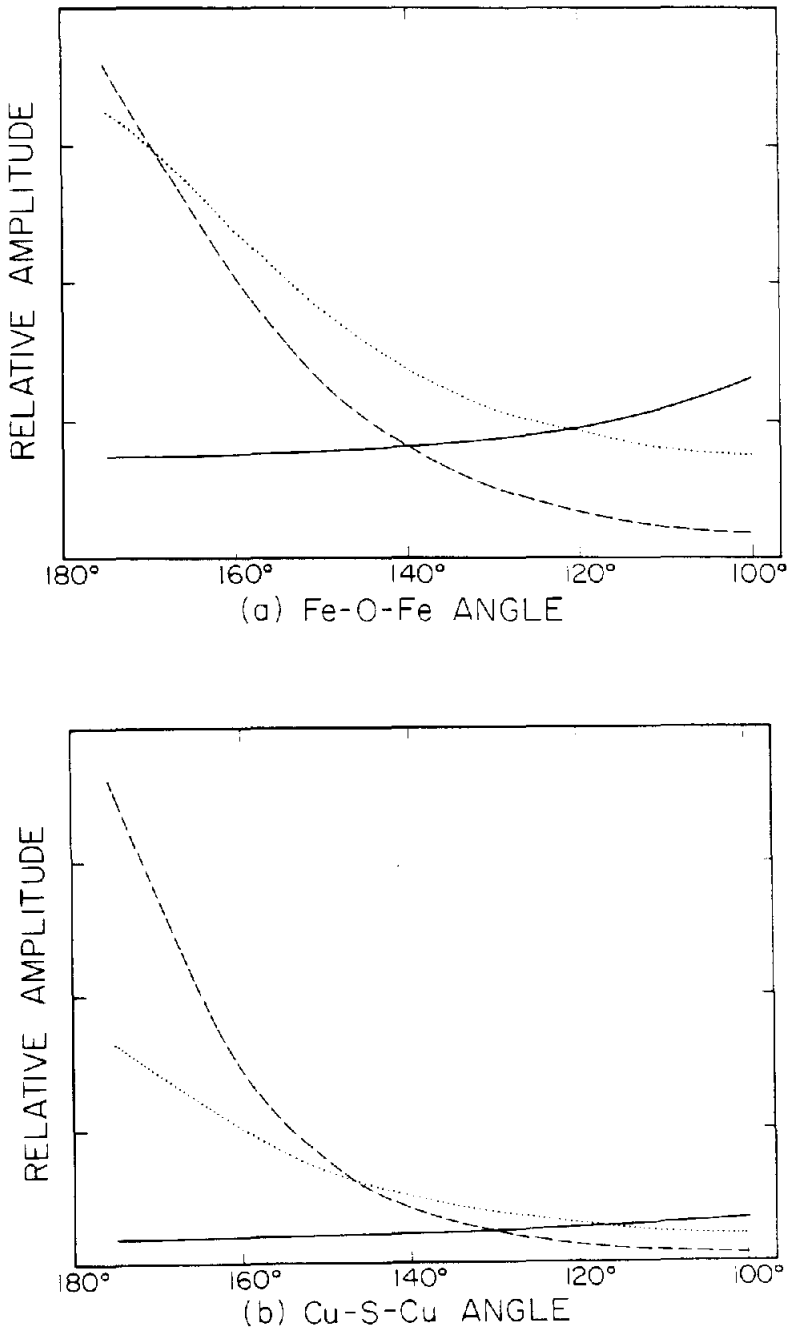

Figure 11.
Relative amplitudes of the peaks in the Fourier transform as a function of bridging angle. The solid, dotted and dashed curves represent the single, double and triple scattering pathways, respectively. (a) Fe system. (b) Cu system.

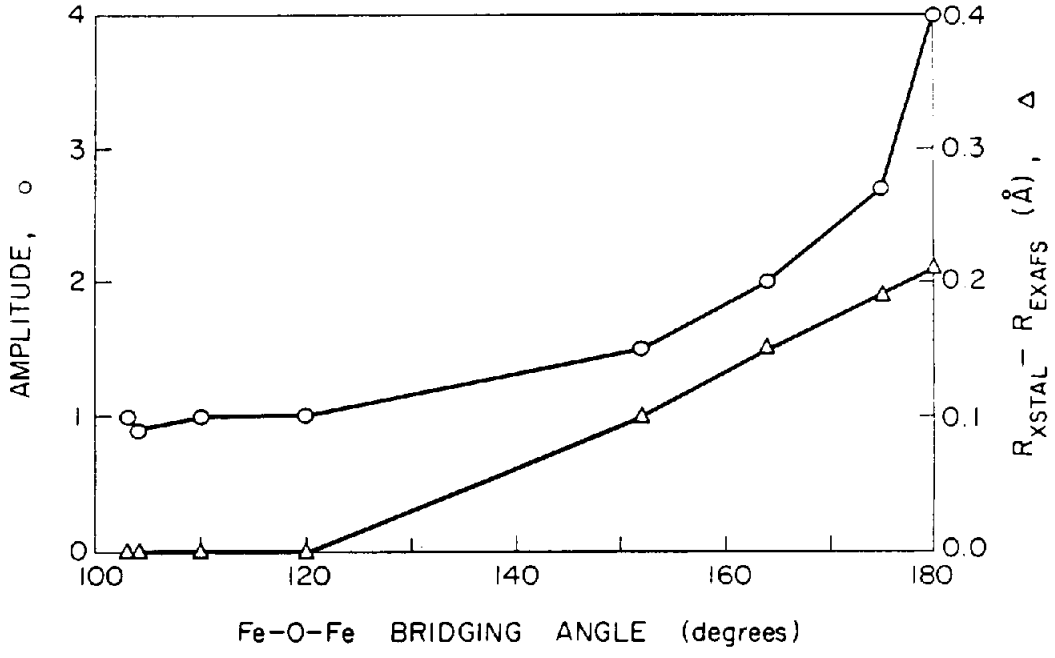

Figure 12.
A plot of the amplitude enhancement of the iron EXAFS in a series of Fe-O-Fe systems together with the error in the distance which is predicted by a single scattering EXAFS analysis.[27]

CHAPTER III

THEORY OF EXTENDED X-RAY ABSORPTION FINE STRUCTURE: FINAL STATE INTERACTION FORMALISM

3.1 Introduction

It is now well established that the EXAFS observed on the high frequency side of an x-ray absorption edge is due to an interference phenomenon in which the outgoing photoelectron wave is scattered by neighboring atom potentials. In this picture, the initial probability of the electron absorbing the photon is independent of the nature of the final state. After absorption occurs, however, the outward propagating photoelectron wave encounters the neighboring atoms and is scattered by them. This scattering process is then understood to interfere with the initial absorption probability, and in this manner, produces the observed modulations in the absorption coefficient. This description is unsatisfactory, however, since it involves a time evolution which is absent from the formalism which is used to calculate the EXAFS. Furthermore, since the radiation field is quantized, either the electron absorbs the whole quantum of energy or it does not absorb at all; there can be no fractional absorption. Therefore, it is difficult to imagine how such a spatially localized scattering phenomenon can bring about an increase or decrease in the macroscopic absorption coefficient.

It is important to note that our criticism lies with

the current interpretation of the EXAFS formalism. The formalism itself is a completely accurate description of the EXAFS phenomenon. In this chapter we introduce a new formalism which allows an intuitive description of the EXAFS in terms of a modulated overlap between the initial and final states. This description is valid over a wide energy range, and at sufficiently high energies it reduces to the standard EXAFS expression.

3.2 Final State Interactions

A comprehensive treatment of the theory and application of final state interactions has been given by Gillespie.[1] In this section we will restrict ourselves to a brief introductory discussion of the theory. Final state interaction theory is most readily applicable when the total potential may be conveniently split into two components one of which is considered to be the primary interaction. The second potential is then seen to modify the reaction caused by the primary potential. This latter potential is called the final state interaction potential. Thus, in general, the total potential may be written as:

$$V = V_p + V_f \tag{3.2.1}$$

where V_p and V_f are the primary and final state potentials, respectively.

To illustrate the qualitative features of final state interaction theory we shall now consider the simplest

possible example: the photoionization of atomic hydrogen. The primary interaction in this case is that between the electron and the electromagnetic radiation field while the final state interaction is the Coulomb potential between the proton and electron in the final state. It is particularly interesting to consider the back reaction in which the electron and proton recombine and emit a photon. Clearly, the initial state Coulomb interaction between the electron and proton increases the probability of hydrogen atom formation. By virtue of time-reversal invariance, however, the probability of the forward reaction must also be enhanced by the presence of the Coulomb interaction. Thus, the attractive interaction between the electron and proton actually increases the cross section for photoionization. This is a general result, and reflects the fact that, to first order in the vector potential describing the radiation field, a free particle cannot absorb or emit electromagnetic radiation. It is for this reason that the absorption cross section continually decreases beyond an x-ray absorption edge, since as the energy of the photon increases the electron effectively appears less tightly bound.

Let us now consider a process in which a particle incident in direction $\hat{k}$ is scattered into the direction $\hat{k}'$ by the full potential $V = V_p + V_f$. The full T matrix for this scattering event is given by:

$$T_{k',k} = \langle k'|V|k+\rangle \qquad (3.2.2)$$

where $\langle r|k'\rangle$ is the outgoing asymptote of the scattering process described by $\langle r|k+\rangle$. The Lippmann-Schwinger equation for V_f alone may be written as:

$$|k_f^{(-)}\rangle = |k'\rangle + G^o V_f |k_f^{(-)}\rangle \tag{3.2.3}$$

where G^o is the free particle Green's operator. Equation (3.2.3) may be substituted into Eq. (3.2.2) to yield

$$T_{k',k} = \langle k_f^{(-)}|V|k+\rangle - \langle k_f^{(-)}|V_f G^o V|k+\rangle \tag{3.2.4}$$

From the Lippmann-Schwinger equation of the full potential V, $G^o V|k+\rangle$ may be written as $|k+\rangle - |k\rangle$ to give

$$T_{k',k} = \langle k_f^{(-)}|V_p|k+\rangle + \langle k_f^{(-)}|V_f|k\rangle \tag{3.2.5}$$

But the last term in Eq. (3.2.5) is just $T^f_{k',k}$ the exact matrix element for the scattering process involving potential V_f alone. Thus the T matrix for the full scattering potential may be written as:

$$T_{k',k} = T^f_{k',k} + \langle k_f^{(-)}|V_p|k+\rangle \tag{3.2.6}$$

This is the celebrated two potential formula of Gell-Mann and Goldberger.[2] Equation (3.2.6) is exact, and merely represent an alternative means of expressing Eq. (3.2.2). However, as we shall see in the next section, by judiciously choosing the breakdown of the total potential into V_p and V_f, we can greatly simplify the description of the scattering process.

3.3 The Jost Function Formalism

In this section we shall develop a formalism to describe the process of x-ray absorption in the presence of neighboring atoms. The primary interaction is chosen to be that due to the interaction of the electromagnetic field with the K-shell electron which absorbs the incident photon.

$$V_p(\mathbf{r}) = -\frac{e}{mc}\,\mathbf{p}.\mathbf{A}(\mathbf{r}) \tag{3.3.1}$$

where $\mathbf{p}$ is the momentum operator of the electron whose position vector is $\mathbf{r}$ with respect to the origin (the center of mass of the absorbing atom). A(r) is the vector potential associated with the quantized radiation field. The final state interaction is assumed to be the potential seen by the photoelectron in the final state.

$$V_f(r) = \frac{Ze^2}{r} + \sum_j V_j(r-r_j) \tag{3.3.2}$$

where the first term represents the Coulomb interaction between the electron and the core hole while the second term represents the final state potential associated with the neighboring atoms located at $\mathbf{r} = \mathbf{r}_j$. Equations (3.3.1) and (3.3.2) may now be substituted into Eq. (3.2.6) to obtain the full T matrix for the absorption process. Note, however, that the initial state, $\langle r|k\rangle$, is a highly localized bound K-shell electron while the final state, $\langle r|k'\rangle$, is an electron which has absorbed a quantum of energy from the radiation field. Given the breakdown of the total potential

chosen above, it is clear that the matrix element, $T^{f}_{k',k}$, is identically zero; that is, the potential V_f in Eq. (3.3.2), cannot induce transitions between the initial and final states. The T matrix for the full potential is then given by:

$$T_{k',k} = \langle k_f^{-} | V_p | k+ \rangle \tag{3.3.3}$$

Note that the effect of V_f is still present in $\langle r | k_f^{-} \rangle$. This form of the T matrix is of little value since it still contains $\langle r | k+ \rangle$, which requires us to solve the Schrodinger equation in the presence of the full potential. Fortunately, we can approximate $\langle r | k+ \rangle$ by $\langle r | k_f+ \rangle$ and hence neglect the effect of the radiation field on the initial state. This approximation is equivalent to a first-order perturbation theory treatment of the problem.

An expression for the x-ray absorption cross section in the dipole approximation[3] may be obtained using Eqs. (3.3.3) and (3.3.1)

$$\sigma = 4\pi^2 \alpha \hbar\omega |\langle k- | \hat{e}.\mathbf{r} | i \rangle|^2 N(\omega) \tag{3.3.4}$$

where we have neglected the subscript f and replaced $\langle r | k_f'- \rangle$ and $\langle r | k_f+ \rangle$ by $\langle r | k- \rangle$ and $\langle r | i \rangle$, respectively, to demonstrate the relationship to the formalism developed in Chapter II. In Eq. (3.3.4) α is the hyperfine constant, ω is the frequency of the incident x-ray photon and $N(\omega)$ is the density of final states for the photoelectron.

The final state, $\langle r | k- \rangle$, is the distorted wave of the

photoelectron in the field of the final state potential. By analogy with the expansion of a plane wave in terms of spherical harmonics, the final state may be written as:[4]

$$\langle r|k-\rangle = (2\pi)^{3/2}\sum_{L}(2L+1)\,i^{L}\,\psi_{L}^{-}(k,r)\,P_{L}(\hat{r}\cdot\hat{R}) \qquad (3.3.5)$$

where $\psi_{L}^{-}(k,r)$ is the normalized radial solution of the Schrodinger equation containing the final state interaction potential. When the final state potential is zero, $\psi_{L}(k,r)$ reduces to the spherical Bessel function $j_{L}(kr)$. The boundary conditions:

$$\begin{aligned} &\psi_{L}(k,r) \longrightarrow \text{constant} \times j_{L}(kr) && r \to 0 \\ &\psi_{L}(k,r) \longrightarrow j_{L}(kr) + kf_{L}(k)h_{L}^{+}(kr) && r \to \infty \end{aligned} \qquad (3.3.6)$$

define $\psi_{L}(k,r)$ as the physically significant solution of the radial equation where $f_{L}(k)$ is the partial wave amplitude and $h_{L}^{+}(k)$ is a spherical Hankel function of the first kind.

Mathematically, however, it is more convenient to introduce another radial solution which is defined by the boundary condition at a single point:

$$\phi_{L}(k,r) \longrightarrow j_{L}(kr) \qquad r \to 0 \qquad (3.3.7)$$

This solution is called the regular solution and is obviously proportional to the physical solution, $\psi_{L}(k,r)$;

$$\phi_{L}(k,r) = F_{L}(k)\;\psi_{L}(k,r) \qquad (3.3.8)$$

where the coefficient of proportionality, $F_{L}(k)$, is called a

Jost function. The advantage of using the regular solution lies in the fact that the boundary condition, Eq. (3.3.7), is independent of k and thus $\phi_L(k,r)$ is an entire (or regular) function of k . In general, the physical solution defined by Eq. (3.3.6) is not an entire function of k.

The matrix element in Eq. (3.3.4) may now be conveniently calculated by substitution of Eq. (3.3.5) for the final state. Assuming the initial state, $\langle r|i\rangle$, to be a spherically symmetric 1s state, the angular integration may be performed.

$$\int \langle r|k\text{->}\rangle^* \hat{e}.r\langle r|i\rangle dr = \frac{C(Z)(\hat{R}.\hat{e})}{F_1(k)} \int \phi_1(k,r) e^{-Zr/a} r^3 dr \quad (3.3.9)$$

where C(Z) is a constant that depends on the atomic number Z of the absorbing atom and we have used the fact that the Jost function is not a function of the coordinate r [see Eq. (3.3.8)]. Since the initial state is highly localized about the origin it is permissible to replace $\phi_1(k,r)$ with $j_1(kr)$ in accordance with Eq. (3.3.7). The remaining radial integration in Eq. (3.3.9) may then be completed

$$\int \langle r|k\text{->}\rangle^* \hat{e}.r\langle r|i\rangle \, dr = M(k,Z)(\hat{R}.\hat{e})/F_1(k) \quad (3.3.10)$$

where $F_1(k)$ is the L=1 Jost function and M(k,Z) has been defined in Appendix A of Chapter II. But $\psi_L(k,r)$ reduces to $j_L(kr)$ only when the final state interaction potential vanishes [see Eq. (3.3.6)]. Consequently, the numerator in Eq. (3.3.10) is simply the amplitude for x-ray absorption in the absence of any final state interactions. In other

words, the sole effect of the final state interaction potential, V_f, is to modify the amplitude by a factor of $1/F_l(k)$.

The problem of calculating the x-ray absorption cross section is now reduced to the evaluation of $F_l(k)$ for the final state under consideration. Note that Eq. (3.3.10) is completely general, for at this point no assumptions have been made as to the exact nature of the final state interaction. An explicit expression for the Jost function may be obtained from Eqs. (3.3.6) through to (3.3.8) and is given by:[5]

$$F_L(k) = 1 + 2mk/h^2 \int h_L^+(kr) V_f(r)\ \phi_L(k,r)\ r^2 dr \qquad (3.3.11)$$

Clearly, as the final state potential, $V_f(r)$, becomes vanishingly small, $F_L(k)$ approaches unity and the amplitude in Eq. (3.3.10) reduces to that of the unperturbed system. For large values of k both $\phi_L(k,r)$ and $h_L^+(kr)$ vary as $1/k$; therefore, from Eq. (3.3.11), $F_L(k)$ also tends to unity as $|k|$ approaches infinity.

It may be readily shown from Eq. (3.3.11) that for a purely attractive final state potential [i.e., $V_f(r) < 0$ for all r] the associated Jost function has a modulus of less than or equal to one and attains the unity value only in the limit of large k. In this instance, the total amplitude is everywhere greater than that for the same process in the absence of final state interactions. Physically, this enhancement factor represents the increased amplitude for

finding the electron in the region where the primary interaction (x-ray absorption) takes place. For a wholly repulsive final state potential the corresponding Jost function has a modulus greater than or equal to unity and the total amplitude is reduced.

3.4 The EXAFS Regime

In this section we shall derive an expression for the EXAFS which is based on the Jost function formalism discussed above. Since the absorption coefficient is given by the square of the modulus of Eq. (3.3.10), all that remains is to calculate the Jost function $F_l(k)$ for the apropriate final state potential.

From Eqs. (3.3.11) and (3.3.8) we may write the reciprocal of this Jost function as:

$$1/F_l(k) = 1 - 2mk/\hbar^2 \int h_l^+(kr)\ V_f(r)\ [\psi_l^-(k,r)]^*\ r^2 dr \qquad (3.4.1)$$

Note that the physical solution in Eq. (3.4.1) has been written as $[\psi_l^-(k,r)]^*$ to emphasize the outgoing nature of the final state as described in Eqs. (3.3.5) and (3.3.10). It may be shown that the ingoing and outgoing asymptotes are related by:[6]

$$[\psi_l^-(k,r)]^* = \psi_l^+(k,r) \qquad (3.4.2)$$

Furthermore, from elementary scattering theory it may be shown that:[7]

$$\langle k|[T^-] = \langle k-|V \qquad (3.4.3)$$

where T^- is the T operator associated with the evolution of the scattering state $\langle r|k-\rangle$ into the outgoing asymptote $\langle r|k\rangle$. Using Eq. (3.4.2) and by analogy with Eq. (3.4.3) above, we may write:

$$V_f(r)\ \psi_1^+(k,r) = T^+\ j_1(kr) \qquad (3.4.4)$$

where we have noted that $[T^-]^\dagger = T^+$. This equation represents the L=1 partial wave radial component of Eq. (3.4.3). The T operator may now be expanded in terms of the individual operators associated with the different scattering atoms in the final state as described in the previous chapter [see Eq. (2.2.6)].

Now that we have expressed the final state potential in a convenient form we must write down an explicit expression for the Hankel function.

$$h_1^+(kr) = -i/kr\ e^{ikr} \qquad (3.4.5)$$

Furthermore, in the EXAFS energy range $kr>>1$ and the Bessel function in Eq. (3.4.1) may be expressed as a sum of ingoing and outgoing spherical waves:

$$j_1(kr) = -1/2kr[e^{ikr} + e^{-ikr}] \qquad (3.4.6)$$

Since the final state of interest is outgoing in nature we shall neglect the second term in Eq. (3.4.6). Using Eqs. (3.4.4), (3.4.5) and (3.4.6) we may write down an expression for the Jost function in Eq. (3.4.1) due to the final state

interaction which involves the neighboring atom j alone.

$$1/F_l^+(k) = 1 - imk/(4\pi\hbar^2)\int 1/kr\ e^{ikr}\ t_j^+\ 1/kr\ e^{ikr}\ dr \quad (3.4.7)$$

Note that we have included a factor of 4π in the denominator and converted the radial integration in Eq. (3.4.1) into a volume integral. Since t_j^+ is highly localized about $r=r_j$, the integral is non-zero only at this point. We may now make the plane wave approximation. This involves writing the spherical waves in Eq. (3.4.7) as:

$$e^{ikr} = (2\pi)^{3/2} \langle r|k\rangle = e^{ik.r} \quad (4.3.8)$$

where the factor $(2\pi)^{-3/2}$ is a normalization constant. With these approximations, the integration over r may be readily performed to yield:

$$1/F_l^+(k) = 1 - \frac{im(2\pi)^3 k}{4\pi\hbar^2 k^2 r_j^2} \langle -k_j|t_j^+|k_j\rangle \quad (3.4.9)$$

where $k_j=k\hat{r}_j$. As described in the previous chapter, this matrix element may be translated to the origin and then expressed in terms of its associated scattering amplitude. The final form of the Jost function is then given by:

$$1/F_l^+(k) = 1 - i/(2kr_j^2)\ f_j(\pi,k)\ e^{2ikr_j} \quad (3.4.10)$$

where $f_j(\pi,k)$ is the backscattering amplitude from atom j.

To obtain the central atom phase shift we must go to the next order in the T matrix as described in Chapter II. The contribution to the Jost function from this term may be

written as:

$$1/F_1^{\pi}(k) = -2mk/(4\pi\hbar^2)\int j_1(kr)\ t_c^+\ G_o^+\ t_j^+\ e^{ikr}/kr\ dr \quad (4.3.11)$$

where t_c^+ is the T matrix associated with the central atom potential. Note that it is no longer valid to write the Bessel function in the manner shown in Eq. (3.4.6) since kr is small, as r is restricted to the vicinity of the origin. Equation (4.3.11) may now be expanded in a complete set of states and the Hankel function may be approximated by a plane wave:

$$1/F_1^{\pi}(k) = \frac{2mk(2\pi)^6\ (-m)}{4\pi\hbar^2 3(\hat{r}_j\cdot\hat{R}_1)2\pi\hbar^2 kr_j^2}\langle k_1|t_c^+|-k_j\rangle\langle -k_j|t_j^+|k_j\rangle \quad (4.3.12)$$

where the configuration space matrix element of the Green's operator was calculated in the manner described in Chapter II. Note that $\langle r|k_1\rangle$ is the L=1 partial wave component of the plane wave. Therefore, the central atom scattering amplitude associated with the matrix element $\langle k_1|t_c^+|-k_j\rangle$ has only an L=1 component. Thus we may write [see Eq. (2.3.11)]

$$\langle k_1|t_c^+|-k_j\rangle = -\frac{\hbar^2}{m(2\pi)^2}[\exp(2i\delta_1) - 1]\frac{3}{2ik}(-\hat{r}_j\cdot\hat{R}_1) \quad (4.3.13)$$

where δ_1 is the L=1 partial wave phase shift. Furthermore, as described above, the t_j^+ matrix element may be expressed as:

$$\langle -k_j|t_j^+|k_j\rangle = -\hbar^2/[m(2\pi)^2]\ f_j(\pi,k)\ e^{2ikr_j} \quad (3.4.14)$$

Substituting Eqs. (3.4.13) and (3.4.14) into Eq. (3.4.12) yields the final form for this contribution to the Jost function.

$$1/F_l''(k) = i/(2kr_j^2)\ [\exp(2i\delta_l) - 1]\ f_j(\pi,k)\ e^{2ikr_j} \quad (3.4.15)$$

The complete Jost function may now be obtained by adding the contributions from $F_l'(k)$ and $F_l''(k)$, with the result:

$$1/F_l(k) = 1 + i/(2kr_j^2) f_j(\pi,k) \exp(2ikr_j + 2i\delta_l) \quad (3.4.16)$$

This equation may now be substituted into Eq. (3.3.10), which when squared, yields the standard EXAFS expression

$$\chi(k) = -\frac{3(\hat{e}\cdot R_j)^2}{kr_j^2} \mathrm{Im}\{f_j(\pi,k)\exp[2i(kr_j+\delta_l)]\} \quad (3.4.17)$$

Note that Eq. (3.4.17) has been normalized to 1/3 M(k,Z) as described in Chapter II.

3.5 Analytical Properties of the Jost Function

The analytical properties of radial wave functions has been discussed in detail by Newton.[8] It may be shown that the physically significant Jost function $F_L(k)$ (k positive and real) is continuously connected to the analytic function $F_L(k)$ in {Im k>0}. Under more restrictive assumptions concerning the asymptotic behaviour of the final state potential at large distances, $F_L(k)$ may be shown to be an entire function of k. Therefore, it is possible to expand

the Jost function in a Taylor series about a given point and study the behavior of the function in the neighborhood of this point. In particular, it is possible to move off the real axis and explore the imaginary component of the photoelectron's wavevector. In this manner,the damping characteristics of the photoelectron may be studied. Furthermore, the behaviour (i.e., k dependence) of the Jost function, and hence the absorption coefficient, may be predicted in the region of the threshold or in the vicinity of a bound state.[9]

Note that if the Jost function vanishes at given point the matrix element in Eq. (3.3.10) blows up. Let us suppose that this occurs at some point k' (Im k'>0). In accordance with the properties of the radial wavefunctions developed in Section 3.3 above, the asymptotic form of the regular solution may be written as:

$$\Phi_L(k,r) = -i/2\ F_L(-k')\ h_L^+(k'r) \qquad r \longrightarrow \infty \qquad (3.5.1)$$

where we have noted that $F_L(k)=[F_L(-k^*)]^*$ by virtue of the Schwartz reflection principle.[10] In the region Im k'>0, $h_L^+(k'r)$ is an exponentially decreasing function. Since the regular solution vanishes at r=0, Eq. (3.5.1) is a normalizable solution of the radial Schrodinger equation with energy $\hbar^2k'^2/2m$ and angular momentum L. Since the eigenvalues of the Hamiltonian must be real, k' must be pure imaginary, k'=ix, and the energy $-\hbar^2x^2/2m$ corresponds to that of a bound state.

In the case of x-ray absorption spectroscopy, the photoelectron wavenumber is defined as:

$$k = [2m(\hbar\omega - E_o)]^{1/2}/\hbar \qquad (3.5.2)$$

where E_o is the threshold energy of the absorption edge. When the energy of the x-ray photon is less than the binding energy E_o, then k as defined by Eq. (3.5.2), is pure imaginary. Therefore, if the system has a bound state of energy $\hbar^2k^2/2m$ with respect to the threshold, there will be a corresponding zero in the Jost function, and the absorption coefficient, defined by Eq. (3.3.10), will sharply increase. The cross section will not be infinite at this energy, however, due to damping and finite lifetime effects. If the initial state is a K (L=0) state, the dipole allowed transitions may be calculated from $F_1(k)$. On the other hand, the quadrupole allowed bound state transitions may be determined from $F_2(k)$. In this manner, the Jost function formalism is not restricted to describing the EXAFS region of the spectrum but may be used to calculate the absorption coefficient at any energy.

3.6 Discussion

In this chapter we have presented a novel formalism which may be used to describe the final state interactions which occur in x-ray absorption spectroscopy. At high energies this formalism was seen to reduce to the standard EXAFS expression. Furthermore, bound state transitions and the threshold behavior of the absorption coefficient could

be described using this scheme. If the final state potential may be accurately modeled, the inelastic damping of the photoelectron wave may be calculated.

The origin of the EXAFS phenomenon may be readily explained within the framework of the formalism. In Section 3.3 we showed that for a purely attractive potential, the associated Jost function has a modulus less than unity. Physically, this corresponds to an enhanced overlap between the initial and final states, since the amplitude of the photoelectron wave at the origin is increased by the attractive interaction. In this case, the absorption is greater at all energies than it would be in the absence of such an interaction. For a repulsive final state potential, the opposite is true, and the absorption is decreased everywhere. It is important to note that these conclusions are valid only if the final state potential is centered about the origin. In the case of EXAFS, however, the final state potential is centered on each of the neighboring atoms. To observe the effect of the presence of these atoms on an absorption process which occurs at the origin, the final state potential must be translated to the origin. In doing so, however, a phase factor e^{2ikr_j}, is incurred. Accordingly, the overlap between the initial and final states is modulated due to the presence of these atoms. As a result, there is no net increase in the integrated absorption since the modulated overlap simply results in a modulation of the absorption coefficient.

References

1. J. Gillespie, Final State Interactions (Holden-Day, San Francisco, 1964).

2. J.R. Taylor, Scattering Theory (Wiley, New York, 1972) p. 271.

3. E. Mertzbacher, Quantum Mechanics (Wiley, New York, 1970) p.466.

4. See for example; ref. 3, p. 185.

5. Reference 3, p. 206.

6. Reference 3, p. 209.

7. Reference 3, p. 169.

8. R.G. Newton, J. Math. Phys. 1, 319 (1960).

9. Reference 3, p. 229.

10. Reference 3, p. 219.

CHAPTER IV

THE EFFECT OF THERMAL VIBRATIONS ON EXTENDED X-RAY ABSORPTION FINE STRUCTURE: DEBYE-WALLER FACTORS*

4.1 Introduction

In recent years Extended X-Ray Absorption Fine Structure (EXAFS) spectroscopy has been used extensively as a structural tool. Although the existence of the extended structure has been known for many years, it was not until Sayers, Stern and Lytle[1] introduced a simple parameterization of the structure that the informational content of EXAFS was realized. In addition, the development of synchrotron and laboratory EXAFS facilities has made the technique available to a large number of investigators and provided a major impetus towards the development of EXAFS as a structural tool.

Much of the present interest in EXAFS stems from its short range nature which allows the technique to be applied in instances where other structural tools are not suitable. The sensitivity to short range order insures that the EXAFS contributions from distant shells are small, which in turn, greatly simplifies an analysis of the extended fine structure. The ability to change the x-ray frequency over a large energy range allows structural information to be obtained on the local environment about each absorbing atom in the sample. In principle, bond distances, coordination numbers and the types of neighboring atoms present may be

determined from an EXAFS study.[2]

The purpose of this paper is to provide a detailed study of the nature of the Debye-Waller factor in EXAFS. In general, the Debye-Waller factor has components due to static and vibrational disorder. This paper will address the problem of thermally excited vibrations and their effect on EXAFS spectra. Previous studies of the Debye-Waller factor in EXAFS were concerned solely with single scattering events.[3-6] Recently, however, there has been considerable interest in multiple scattering EXAFS processes and the determination of bond angles from an analysis of the extended structure.[7,8] The possibility of determining accurate bond angles from an EXAFS study is obviously dependent on an understanding of the relative motion of the atoms involved. This present work will discuss the nature of the Debye-Waller factor in EXAFS spectra which contain a significant multiple scattering component.

4.2 The General Formalism

The problem of thermal diffuse scattering is important in any structural tool which uses the difference in the phase of a scattered wave from different scattering sites to obtain structural information. The frequency of the incident wave is typically many orders of magnitude greater than the frequency of vibration of the scattering centers. The observed scattered intensity thus provides a measure of the instantaneous configuration of the scattering centers

averaged over all possible configurations. In general, the effects of thermal vibrations are included by setting the distance between the scattering sites to their equilibrium values and multiplying each term representing the scattered intensity by a factor of the form exp(-M), where M is the Debye-Waller factor for the scattering process. We present below a general formalism which may readily be applied to most scattering problems including the EXAFS effect.

Consider the following general scattering problem. Suppose we have an N-particle system with masses m_i(i = 1,...,N). Let $\mathbf{r}_i$ denote the position vector of the i^{th} atom in its equilibrium position with respect to some arbitrary origin. If $\mathbf{u}_i$ is the displacement vector of the i^{th} atom from its equilibrium position then the instantaneous position of this atom is given by:

$$\mathbf{r} = \mathbf{r}_i + \mathbf{u}_i. \tag{4.2.1}$$

Let us consider now the scattering process whereby a particle incident in the direction $\mathbf{k}$ is scattered by atom i into the direction $\mathbf{k}'$. The probability amplitude a_i for this event in the absence of thermal vibrations is:

$$a_i = \langle k' | T_i | k \rangle = a_i^0 e^{i(\mathbf{k} - \mathbf{k}')\cdot\mathbf{r}_i}, \tag{4.2.2}$$

where T_i is the T operator associated with the scattering potential at $\mathbf{r}=\mathbf{r}_i$. a_i^0 is the probability amplitude for the same scattering event but located at the origin.[10] At

finite temperatures, however, the position of the i^{th} atom is given by Eq. (4.2.1) so that the time dependent probability amplitude A_i may be written as:

$$A_i = a_i^0 e^{iK\cdot(r_i + u_i)} = a_i e^{iK\cdot u_i}, \tag{4.2.3}$$

where $\mathbf{K} = \mathbf{k}-\mathbf{k}'$ and $\hbar\mathbf{K}$ represents the momentum transferred to the scattering atom. The total probability amplitude is then the sum of the amplitudes A_i due to the individual scattering centers:

$$A = \sum_i A_i = \sum_i a_i e^{iK\cdot u_i}. \tag{4.2.4}$$

The total scattered intensity is then proportional to:

$$|A|^2 = \sum_i \sum_j a_i a_j^* e^{iK\cdot(u_i - u_j)}. \tag{4.2.5}$$

Throughout this present work the harmonic or quadratic approximation is assumed. While this approximation is strictly valid only for small displacement or amplitudes of vibration, it does however, provide a reasonably accurate description of most solids and molecules, particularly at low temperatures.[9] To study further the temperature dependence of the scattered intensity in the quadratic approximation, it is convenient to introduce the normal coordinates Q_n (n = 1,...,3N). These coordinates have the advantage that they diagonalize both the potential and

kinetic energy matrices of the system. The displacement vectors $\mathbf{u}_i$ may be expressed in this coordinate system as:

$$\mathbf{u}_i m_i^{1/2} = \sum_n \epsilon_i^n Q_n$$

or (2.4.6)

$$\mathbf{u}_i = \sum_n \mathbf{e}_i^n Q_n,$$

where $\mathbf{e}_i^n = \epsilon_i^n / m_i^{1/2}$ and represents the amplitude vector of the i^{th} atom in the n^{th} normal mode. The transformation between mass weighted and normal coordinates is orthogonal and therefore the amplitude vectors ϵ_i^n form an orthonormal set defined by:[11]

$$\sum_i \epsilon_i^n \cdot \epsilon_i^{n'} = \delta_{nn'}. \qquad (4.2.7)$$

This property of normal coordinates eliminates the interaction or cross-terms which occur in the potential and kinetic energies of the system. Equation (4.2.7) also serves to normalize the amplitudes of vibration of the atoms in each normal mode.

With the aid of Eq. (4.2.6) the expression for the scattered intensity, Eq. (4.2.5), may be rewritten as:

$$|A|^2 = \sum_i \sum_j a_i a_j^* \prod_n e^{i\mu_{ij}^n Q_n}, \qquad (4.2.8)$$

where $\mu_{ij}^n = \mathbf{K}.(\mathbf{e}_i^n - \mathbf{e}_j^n)$ and the sum in the exponent of Eq. (4.2.5) has been expressed as a product of exponential terms.

To obtain the experimentally observed intensity we must perform an ergodic average of Eq. (4.2.8) over a time period

which is short on a microscopic scale but which is long compared with the period of vibration of the atoms involved. In practice, however, it is more convenient to perform an ensemble average of Eq. (4.2.8) over a canonical ensemble defined by the Hamiltonian of the system. Classically, this average is understood to be a mean over all possible initial states weighted with the corresponding Boltzmann factor. Assuming that the vibration of the atoms may be described by a quadratic Hamiltonian it may be shown that[12]

$$\langle \exp(i\mu_{ij}^{n} Q_n) \rangle = \exp[-\tfrac{1}{2}(\mu_{ij}^{n})^2 \langle Q_n^2 \rangle], \qquad (4.2.9)$$

where the brackets <...> denote the ensemble or thermal average.

In the case of an harmonic oscillator the mean-square amplitude of vibration $\langle Q_n^2 \rangle$ may be related to the average energy of the oscillator $\langle E_n \rangle$,[13]

$$\langle Q_n^2 \rangle = \frac{\langle E_n \rangle}{\omega_n^2} = \frac{1}{\omega_n^2}\left[\frac{\hbar\omega_n}{\exp(\hbar\omega_n / k_B T) - 1} + \tfrac{1}{2}\hbar\omega_n\right], \qquad (4.2.10)$$

where ω_n is the frequency of the n^{th} normal mode and k_B is Boltzmann's constant. The expression for the thermally averaged scattered intensity may now be written as:

$$\langle |A|^2 \rangle = \sum_i \sum_j a_i a_j^* e^{-M_{ij}}, \qquad (4.2.11)$$

where $M_{ij} = 1/2 \sum_n (\mu^n_{ij})^2 \langle Q_n^2 \rangle$ and the product of exponential terms in Eq. (4.2.8) has been replaced by a sum in the exponent of Eq. (4.2.11). The exponent, M_{ij},

represents the Debye-Waller factor for the scattering process.

For computational purposes Eq. (4.2.10) may be conveniently written in terms of an hyperbolic cotangent

$$\langle Q_n^2 \rangle = \frac{\hbar}{2\omega_n} \coth\left(\frac{\hbar\omega_n}{2k_B T}\right). \tag{4.2.12}$$

For low frequency modes or at high temperature the mean-square amplitude of vibration may be approximated by:

$$\langle Q_n^2 \rangle \simeq k_B T/\omega_n^2 \tag{4.2.13}$$

and the Debye-Waller factor varies linearly with temperature. At low temperatures or for very high frequency modes the mean-square amplitude of vibration may be written as:

$$\langle Q_n^2 \rangle \simeq \tfrac{1}{2}\hbar/\omega_n \tag{4.2.14}$$

and the Debye-Waller factor is temperature independent.

4.3 The EXAFS Problem

While EXAFS is primarily a single scattering probe, in certain instances, low-order multiple scattering events contribute significantly to the extended structure. Teo[7] and Boland et al.[8] have shown that a three-atom system comprised of an absorbing atom and two neighboring atoms is sufficient to account for all significant multiple scattering effects in EXAFS. The phase and the amplitude of the multiple scattering components were shown to be a

function of the geometry of the triatomic system.[8] An EXAFS analysis based on a knowledge of these components will then allow bond angles to be determined.

To study the effect of thermal vibrations on these multiple scattering EXAFS components let us consider the three-atom system shown in Fig. 1. We shall first consider the general case in which the system has C_s symmetry. A photoelectron of energy 100 eV has a velocity of approximately 6×10^4 Å $psec^{-1}$ which justifies our assumption that the scattering process provides an instantaneous snapshot of the configuration of the system even for long scattering paths. The instantaneous positions of the atoms with respect to each other are also shown in Fig. 1. The expression for the EXAFS of the three-atom system in the absence of thermal vibrations is given by:[8]

$$\chi^0(k,\hat{e}) = \chi_S^0(k,\hat{e}) + 2\chi_D^0(k,\hat{e}) + \chi_T^0(k,\hat{e}). \qquad (4.3.1)$$

The superscript zero indicates the absence of thermal vibrations and k is the photoelectron wavenumber defined by $k=[2m(\hbar\omega-E_o)]^{1/2}/\hbar$ where ω is the photon frequency and E_o is the threshold energy. The subscripts S, D and T refer to single, double and triple scattering events, respectively, and $\hat{e}$ is the unit vector in the direction of polarization of the incident x-ray beam.

The single scattering EXAFS, $\chi_S^0(k,\hat{e})$, consists of two terms each corresponding to single scattering events involving the neighboring atoms at $\mathbf{r} = \mathbf{r}_j$ and $\mathbf{r} = \mathbf{r}_i$ (see

Fig. 2(a) and 2(b)). $\chi^{o}_{S}(k,\hat{e})$ may be expressed as:

$$\chi^{0}_{s}(k,\hat{e}) = \sum_{\alpha=i,j} \chi^{0}_{s_\alpha}(k,\hat{e}),$$

where (4.3.2)

$$\chi^{0}_{s_\alpha}(k,\hat{e}) = -\frac{3(\hat{r}_\alpha\cdot\hat{e})^2}{kr_\alpha^2}\left(\frac{-m(2\pi)^2}{\hbar^2}\right) \times \mathrm{Im}\left[\langle -k_\alpha|T_\alpha|k_\alpha\rangle e^{2ik_\alpha\cdot r_\alpha}e^{2i\delta_1}\right]$$

and $\mathbf{k} = k\hat{r}$. The T-matrix element represents the probability amplitude for scattering a photoelectron incident in direction $\mathbf{k}$ into direction $-\mathbf{k}$ and δ_1 is the phase shift due to the central atom potential. The double scattering EXAFS, $\chi^{o}_{D}(k,\hat{e})$, involves events in which the photoelectron successively scatters off one neighboring atom and then scatters off the other remaining neighboring atom. The order in which the scattering occurs does not affect the probability amplitude so that this term is counted twice in Eq. (4.3.1) [see Fig. 2(c) and 2(d)]. $\chi^{o}_{D}(k,\hat{e})$ may be written as:

$$\chi^{0}_{D}(k,\hat{e}) = \frac{-3(\hat{r}_i\cdot\hat{e})(\hat{r}_j\cdot\hat{e})}{kr_ir_jr_{ij}}\left(\frac{m^2(2\pi)^4}{\hbar^4}\right) \times \mathrm{Im}\{\langle -k_i|T_i|k_{ij}\rangle\langle k_{ij}|T_j|k_j\rangle \times \exp[i(\mathbf{k}_j\cdot\mathbf{r}_j + \mathbf{k}_{ij}\cdot\mathbf{r}_{ij} + \mathbf{k}_i\cdot\mathbf{r}_i)]e^{2i\delta_1}\}, \quad (4.3.3)$$

where $\mathbf{k}_{ij} = k\hat{r}_{ij} = k(\mathbf{r}_i - \mathbf{r}_j)/|\mathbf{r}_i - \mathbf{r}_j|$. The triple scattering EXAFS term, $\chi^{o}_{T}(k,\hat{e})$, describes a process in which the outgoing photoelectron first scatters off the nearest neighboring atom j then scatters off atom i and finally

scatters off atom j once again [see Fig. 2(e)]. $\chi^{o}_{T}(k,\hat{e})$ may be written as:

$$\begin{aligned}\chi^{0}_{T}(k,\hat{e}) = \frac{-3(\hat{r}_j\cdot\hat{e})^2}{kr_j^2 r_{ij}^2}\left(\frac{-m^3(2\pi)^6}{\hbar^6}\right)\mathrm{Im}\{\langle -k_j|T_j|-k_{ij}\rangle \\ \times\langle -k_{ij}|T_i|k_{ij}\rangle\langle k_{ij}|T_j|k_j\rangle \\ \times\exp[2i(\mathbf{k}_j\cdot\mathbf{r}_j+\mathbf{k}_{ij}\cdot\mathbf{r}_{ij})]e^{2i\delta_1}\}.\end{aligned} \tag{4.3.4}$$

An expression for the EXAFS due to the instantaneous configuration of three-atom system shown in Fig. 1 may be obtained by replacing the relative equilibrium position vectors of the atoms by their respective instantaneous position vectors. Retaining only the lowest order terms in the displacement, the EXAFS, $\chi(k,\hat{e})$, due to this configuration is given by:

$$\begin{aligned}\chi(k,\hat{e}) = \chi_s^0\exp[2ik\hat{r}_\alpha\cdot(\mathbf{u}_\alpha-\mathbf{u}_0)] + 2\chi_D^0 \\ \times\exp\{ik[\hat{r}_j\cdot(\mathbf{u}_j-\mathbf{u}_0)+\hat{r}_{ij}\cdot(\mathbf{u}_i-\mathbf{u}_j)]\} \\ \times\exp\{ik[\hat{r}_i\cdot(\mathbf{u}_i-\mathbf{u}_0)]\}+\chi^0_T \\ \times\exp\{2ik[\hat{r}_j\cdot(\mathbf{u}_j-\mathbf{u}_0)+\hat{r}_{ij}\cdot(\mathbf{u}_i-\mathbf{u}_j)]\},\end{aligned} \tag{4.3.5}$$

where α = i,j and $\mathbf{u}_i$, $\mathbf{u}_j$ and $\mathbf{u}_o$ are the displacement vectors of neighboring atoms i and j and the central atom from their respective equilibrium positions. Note that we have neglected any changes that occur in the scattering angles due to the displacement of the atoms. Such angular changes are a higher order effect and may be treated separately.[19] We may now proceed as described in the previous section by expressing the displacement vectors in terms of normal

coordinates. Thus

$$\mathbf{u}_i = \sum_n \mathbf{e}_i^n Q_n \tag{4.3.6}$$

and we may rewrite Eq. (4.3.5) as:

$$\begin{aligned}\chi(k,\hat{e}) = \chi_s^0 \exp\left(2ik \sum_n \mu_{\alpha 0}^n Q_n\right) \\ + 2\chi_D^0 \exp\left[ik \sum_n (\mu_{j0}^n + \mu_{ij}^n + \mu_{i0}^n) Q_n \right] \\ + \chi_T^0 \exp\left[2ik \sum_n (\mu_{j0}^n + \mu_{ij}^n) Q_n \right],\end{aligned} \tag{4.3.7}$$

where $\mu_{ij}^n = \hat{r}_{ij} \cdot (\mathbf{e}_i^n - \mathbf{e}_j^n)$ and represents the maximum effective change in the distance along the equilibrium internuclear axis between atoms i and j in the n^{th} normal mode of vibration. A similar interpretation applies to the terms μ_{jo}^n and μ_{io}^n. For the three-atom system under consideration there are in total nine degrees of freedom so that the sum over n above extends to three terms for non-linear systems and four terms for linear systems.

The experimentally observed EXAFS may be obtained by performing an ensemble average of Eq. (4.3.7) as described in Section 4.2. Using Eq. (4.2.9) above, the thermally averaged EXAFS for the general system of C_S symmetry is then given by:

$$\begin{aligned}\langle \chi(k,\hat{e}) \rangle = \chi_s^0 \exp\left[-2k^2 \sum_n (\mu_{\alpha 0}^n)^2 \langle Q_n^2 \rangle \right] \\ + 2\chi_D^0 \exp\left[-\tfrac{1}{2}k^2 \sum_n (\mu_{j0}^n + \mu_{ij}^n + \mu_{i0}^n)^2 \langle Q_n^2 \rangle \right] \\ + \chi_T^0 \exp\left[-2k^2 \sum_n (\mu_{j0}^n + \mu_{ij}^n)^2 \langle Q_n^2 \rangle \right].\end{aligned} \tag{4.3.8}$$

The exponential terms in Eq. (4.3.8) correspond to the Debye-Waller factors for each of the scattering processes. The Debye-Waller factor obtained for the single scattering EXAFS is identical to that found by previous investigators.[3,4]

4.4 Application to Model Systems

For our present purpose it is convenient to write out Eq. (4.3.8) in detail:

$$\begin{aligned}\langle\chi(k,\hat{e})\rangle = \chi_s^0 \exp\left\{-2k^2\sum_n\left[(\hat{r}_\alpha\cdot\mathbf{e}_\alpha^n)-(\hat{r}_\alpha\cdot\mathbf{e}_0^n)\right]^2\langle Q_n^2\rangle\right\}\\ + 2\chi_D^0\exp\left\{-\tfrac{1}{2}k^2\sum_n\left[(\hat{r}_j\cdot\mathbf{e}_j^n)-(\hat{r}_j\cdot\mathbf{e}_0^n)+(\hat{r}_{ij}\cdot\mathbf{e}_i^n)-(\hat{r}_{ij}\cdot\mathbf{e}_j^n)+(\hat{r}_i\cdot\mathbf{e}_i^n)-(\hat{r}_i\cdot\mathbf{e}_o^n)\right]^2\langle Q_n^2\rangle\right\}\\ + \chi_T^0\exp\left\{-2k^2\sum_n\left[\hat{r}_j\cdot\mathbf{e}_j^n)-(\hat{r}_j\cdot\mathbf{e}_0^n)+(\hat{r}_{ij}\cdot\mathbf{e}_i^n)-(\hat{r}_{ij}\cdot\mathbf{e}_j^n)\right]^2\langle Q_n^2\rangle\right\},\end{aligned} \tag{4.4.1}$$

where α = i,j. Now consider that the three-atom system is symmetric and bent with a bridging angle θ and belongs to the C_{2v} point group. The normal modes of vibration transform as:

$$\Gamma_{\text{vib}} = 2A_1 + B_1. \tag{4.4.2}$$

The two totally symmetric A_1 modes correspond to a symmetric stretching and bending mode of vibration. The B_1 mode is associated with the asymmetric stretch. A schematic representation of the normal modes of the three-atom system are shown in Fig. 3. Note that all displacement vectors are confined to the plane defined by the three atoms.

The symmetry of the system results in a simplification

of Eq. (4.4.1) which is dependent on the normal mode in question. All normal modes in the C_{2v} point group are subject to the following conditions:

$$\begin{array}{ll} \text{For all modes} & m_0 = m_i = m, \\ \text{in a } C_{2v} \text{ point group:} & |\mathbf{e}_0^n| = |\mathbf{e}_i^n|, \end{array} \tag{4.4.3}$$

where m_o and m_i are the masses of the central atom and neighboring atom i, respectively. In addition, a study of either Fig. 3(a) or 3(b) shows that the following restrictions apply to both A_1 type modes of vibration:

$$\begin{array}{ll} & (\hat{r}_j \cdot \mathbf{e}_0^{A_1}) = -(\hat{r}_{ij} \cdot \mathbf{e}_i^{A_1}), \\ A_1 \text{ mode:} & (\hat{r}_j \cdot \mathbf{e}_j^{A_1}) = -(\hat{r}_{ij} \cdot \mathbf{e}_j^{A_1}), \\ & (\hat{r}_i \cdot \mathbf{e}_0^{A_1}) = -(\hat{r}_i \cdot \mathbf{e}_i^{A_1}). \end{array} \tag{4.4.4}$$

An analogous set of conditions apply to the B_1 mode of vibration [see Fig. 3(c)]

$$\begin{array}{ll} & (\hat{r}_j \cdot \mathbf{e}_0^{B_1}) = (\hat{r}_{ij} \cdot \mathbf{e}_i^{B_1}), \\ B_1 \text{ mode:} & (\hat{r}_{ij} \cdot \mathbf{e}_j^{B_1}) = (\hat{r}_j \cdot \mathbf{e}_j^{B_1}), \\ & (\hat{r}_i \cdot \mathbf{e}_0^{B_1}) = (\hat{r}_i \cdot \mathbf{e}_i^{B_1}). \end{array} \tag{4.4.5}$$

With the aid of Eqs. (4.4.3), (4.4.4) and (4.4.5) the thermally averaged EXAFS, Eq. (4.4.1), for a three-atom system of C_{2v} symmetry may be reduced to:

$$\langle \chi(k,\hat{e}) \rangle_{C_{2v}} = \chi_{sj}^{0} \exp\left\{ -2k^2 \sum_{A_1} [(\hat{r}_j \cdot \mathbf{e}_j^{A_1}) - (\hat{r}_j \cdot \mathbf{e}_0^{A_1})]^2 \langle Q_{A_1}^2 \rangle \right\}$$

$$\exp\left\{ -2k^2 [(\hat{r}_j \cdot \mathbf{e}_j^{B_1}) - (\hat{r}_j \cdot \mathbf{e}_0^{B_1})]^2 \langle Q_{B_1}^2 \rangle \right\}$$

$$+ \chi_{si}^{0} \exp\left\{ -2k^2 \sum_{A_1} [2(\hat{r}_i \cdot \mathbf{e}_i^{A_1})]^2 \langle Q_{A_1}^2 \rangle \right\} \qquad (4.4.6)$$

$$+ 2\chi_{D}^{0} \exp\left\{ -\tfrac{1}{2}k^2 \sum_{A_1} [2(\hat{r}_{ij} \cdot \mathbf{e}_i^{A_1}) + 2(\hat{r}_j \cdot \mathbf{e}_j^{A_1}) + 2(\hat{r}_i \cdot \mathbf{e}_i^{A_1})]^2 \langle Q_{A_1}^2 \rangle \right\}$$

$$+ \chi_{T}^{0} \exp\left\{ -2k^2 \sum_{A_1} [2(\hat{r}_{ij} \cdot \mathbf{e}_i^{A_1}) + 2(\hat{r}_j \cdot \mathbf{e}_j^{A_1})]^2 \langle Q_{A_1}^2 \rangle \right\},$$

where χ_{Si} and χ_{Sj} are the single scattering contributions to the EXAFS from atoms i and j, in the absence ofthermal vibrations. The Debye-Waller factors in Eq. (4.4.6) have been factored into two terms to emphasize the separate contributions of the A_1 and B_1 type modes. Note that the double and triple EXAFS components receive no contribution to their Debye-Waller factors from the B_1 normal mode. The asymmetric B_1 mode contributes only to the single scattering Debye-Waller factor for the first shell atom. This fact may also be discerned from symmetry considerations. Since the B_1 mode is asymmetric with respect to reflection in the plane of symmetry which passes through atom j, any scattering path which crosses this plane will receive no contribution to its Debye-Waller factor from this mode. This occurs because the increase in pathlength on one side of this plane is exactly offset by a corresponding decrease on the other side.

A calculation of the Debye-Waller factors for the C_{2v} system requires a full normal mode analysis. Before doing

so it is interesting to consider a linear symmetric configuration as a limiting case of a system with C_{2v} symmetry. Suppose that the interatomic distances r_j and r_{ij} are equal and the terminal atoms are of the same kind. Then the system belongs to the $D_{\infty h}$ point group and the normal modes of vibration transform as:

$$\Gamma_{vib} = \Sigma_g^+ + \Sigma_u^+ + \Pi_u. \tag{4.4.7}$$

A schematic representation of the normal modes of the system are shown in Fig. 4. The bending modes Π_u are degenerate and may be interconverted by a rotation of 90° about the axis of the molecule.

The symmetry of the system requires that the following condition must always be satisfied:

$$\begin{aligned} & m_0 = m_i = m. \\ \text{For all modes:} \quad & \hat{r}_j = \hat{r}_i = \hat{r}_{ij}, \\ \text{in a } D_{\infty h} \text{ group} \quad & |\mathbf{e}_n^0| = |\mathbf{e}_i^n|. \end{aligned} \tag{4.4.8}$$

In addition, the following restrictions apply to each of the normal modes of vibration (see Fig. 4).

$$\begin{aligned} &\Sigma_g^+ \text{ mode:} (\hat{r}_j \cdot \mathbf{e}_0^{\Sigma_g^+}) = -(\hat{r}_{ij} \cdot \mathbf{e}_i^{\Sigma_g^+}), \quad |\mathbf{e}_j^{\Sigma_g^+}| = 0. \\ &\Pi_u \text{ mode:} \quad (\hat{r}_j \cdot \mathbf{e}_0^{\Pi_u}) = (\hat{r}_j \cdot \mathbf{e}_i^{\Pi_u}) = (\hat{r}_j \cdot \mathbf{e}_j^{\Pi_u}) = 0. \\ &\Sigma_u^+ \text{ mode:} (\hat{r}_j \cdot \mathbf{e}_0^{\Sigma_g^+}) = (\hat{r}_j \cdot \mathbf{e}_i^{\Sigma_u^+}). \end{aligned} \tag{4.4.9}$$

With the above conditions satisfied, the expression for the thermally averaged EXAFS in a three-atom system of

symmetry $D_{\infty h}$ is given by:

$$\begin{aligned}\langle\chi(k,\hat{e})\rangle_{D_{\infty h}} = {} & \chi^0_{s_j}\exp\{-2k^2(\hat{r}_j\cdot\mathbf{e}_0^{\Sigma_g^+})^2\langle Q^2_{\Sigma_g^+}\rangle\}\exp\{-2k^2\left[(\hat{r}_j\cdot\mathbf{e}_j^{\Sigma_u^+})-(\hat{r}_j\cdot\mathbf{e}_0^{\Sigma_u^+})\right]^2\langle Q^2_{\Sigma_u^+}\rangle\} \\ & + \chi^0_{s_i}\exp\{-2k^2\left[2(\hat{r}_i\cdot\mathbf{e}_i^{\Sigma_g^+})\right]^2\langle Q^2_{\Sigma_g^+}\rangle\} \\ & + \chi^0_T\exp\{-2k^2\left[2(\hat{r}_i\cdot\mathbf{e}_i^{\Sigma_g^+})\right]^2\langle Q^2_{\Sigma_g^+}\rangle\} \\ & + 2\chi^0_D\exp\{-\tfrac{1}{2}k^2\left[4(\hat{r}_i\cdot\mathbf{e}_i^{\Sigma_g^+})\right]^2\langle Q^2_{\Sigma_g^+}\rangle\}\end{aligned} \qquad (4.4.10)$$

The degenerate bending modes of vibration do not contribute to any of the Debye-Waller factors in Eq. (4.4.10). This occurs because the displacement vectors in these modes have no components along the axis of the three-atom system. Furthermore, the asymmetric stretching mode Σ_u^+ contributes only to the Debye Waller factor in the first shell single scattering EXAFS.

To analyze the normal modes of the C_{2v} three-atom system it is convenient to introduce the internal displacement coordinates R_1 and R_2 together with an angle bending coordinate δ_3. R_1 and R_2 represent the change in the bond lengths r_j and r_{ij} from their respective equilibrium values. The bending coordinate δ_3 represents the change in the bridging angle θ. For small amplitudes of vibration both the kinetic and potential energies of the system may be expressed as quadratic functions of these coordinates. In the instance of a C_{2v} three-atom system the potential energy may be written as:

$$2V = a_{11}(R_1^2 + R_2^2) + a_{33}\,\delta_3^2 + a_{12}R_1R_2 \qquad (4.4.11)$$

where the force constant $a_{11} = a_{22}$ and there is no interaction force constant between the displacement and bending coordinates.

For computational purposes it is more convenient to introduce the symmetry coordinates S_1, S_2 and S_3 shown in Fig. 5. Note that S_1 and S_2 transform as A_1 in the C_{2v} point group while S_3 transforms as B_1. The potential and kinetic energies may be written as:

$$2V = C_{11}S_1^2 + C_{22}S_2^2 + C_{33}S_3^2 + 2C_{12}S_1S_2 \qquad (4.4.12)$$

and

$$2T = d_{11}\dot{S}_1^2 + d_{22}\dot{S}_2^2 + d_{33}\dot{S}_3^2 + 2d_{12}\dot{S}_1\dot{S}_2. \qquad (4.4.13)$$

The two sets of force constants in Eqs. (4.4.11) and (4.4.12) are related to each other by:[15]

$$\begin{aligned} C_{11} &= 2\sin^2(\theta/2)[a_{11} + a_{12}] + 4\cos^2(\theta/2)a_{33}/r_j^2, \\ C_{12} &= [2a_{11}p - 4pa_{33}/r_j^2 + 2a_{12}p]\sin(\theta/2)\cos(\theta/2), \\ C_{22} &= 2p^2\cos^2(\theta/2)[a_{11} + a_{12}] + 4p^2\sin^2(\theta/2)a_{33}/r_j^2, \\ C_{33} &= 2r^2(a_{11} - a_{12}), \end{aligned} \qquad (4.4.14)$$

where $p = 1 + 2m/m_j$ and $r = 1 + [2m/m_j]\sin^2(\theta/2)$. The coefficients in the expansion of the kinetic energy, Eq. (4.4.13), may also be evaluated.

$$\begin{aligned} &d_{11} = 2m, \quad d_{22} = 2mp, \quad d_{33} = 2mr, \\ &d_{12} = d_{13} = d_{23} = 0. \end{aligned} \qquad (4.4.15)$$

The frequency of each normal mode of vibration may now be expressed in terms of the force constants a_{ij} and the bridging angle θ:

$$\lambda_3 = 4\pi^2 c^2 \nu_3^2 = \left[\frac{1}{m} + \frac{2}{m_j}\sin^2(\theta/2)\right](a_{11} - a_{12}),$$

$$\lambda_1 + \lambda_2 = 4\pi^2 c^2(\nu_1^2 + \nu_2^2) = \left[\frac{1}{m} + \frac{2}{m_j}\cos^2(\theta/2)\right] \times (a_{11} + a_{12}) + 2\left[\frac{1}{m} + \frac{2}{m_j}\sin^2(\theta/2)\right]\frac{a_{33}}{r_j^2}, \tag{4.4.16}$$

$$\lambda_1\lambda_2 = 16\pi^4 c^4 \nu_1^2 \nu_2^2 = 2\left(\frac{1}{m^2} + \frac{2}{mm_j}\right)(a_{11} + a_{12})\frac{a_{33}}{r_j^2}.$$

λ_1 and λ_2 are associated with the A_1 stretching and bending modes of vibration while λ_3 is associated with the asymmetric B_1 stretching mode. The normal modes of vibration may then be calculated from the secular equation defined by Eqs. (4.4.12) and (4.4.13).

$$\begin{aligned} Q_{A_1}(\lambda_1) &= (C_{22} - \lambda_1 d_{22})S_1 - (C_{21} - \lambda_1 d_{21})S_2, \\ Q_{A_1}(\lambda_2) &= (C_{22} - \lambda_2 d_{22})S_1 - (C_{21} - \lambda_2 d_{21})S_2, \\ Q_{B_1}(\lambda_3) &= [(C_{11} - \lambda_3 d_{11})(C_{22} - \lambda_3 d_{22}) \\ &\quad - (C_{21} - \lambda_3 d_{21})(C_{12} - \lambda_3 d_{12})]S_3. \end{aligned} \tag{4.4.17}$$

For the linear symmetric system of point group $D_{\infty h}$ the symmetry coordinates are identical to the normal coordinates shown in Fig. 4. The explicit form of the symmetrized force constants and the frequencies of the normal modes may be obtained by substituting a bridging angle of 180° in Eqs.

(4.4.14) and (4.4.16), respectively.

To perform a complete normal mode analysis of any system it is necessary to solve the secular equation. A solution of this equation, however, requires a knowledge of all the force constants in the system. In practice, the force constants are unknown and the only information available are the frequencies of the normal modes. As the number of force constants is typically greater than the number of normal modes, the secular equation is underdetermined. For systems which possess some symmetry the number of force constants will be reduced by symmetry considerations. In general, it is necessary to ignore some force constants or to measure the normal frequencies in an isotopically substituted system.

The approach we shall adopt in this present work is as follows. Given the normal modes of vibration for a linear symmetrical system we can calculate all the force constants from Eq. (4.4.16) when $\theta = 180^{o}$ is substituted for the bridging angle. These force constants are then used to calculate the frequencies of the normal modes and the symmetrized force constants in Eqs. (4.4.16) and (4.4.14) for a system of C_{2v} symmetry with a bridging angle θ. It is implicitly assumed that the force constants are independent of θ for the angular range of these calculations, $\theta = 100^{o} - 180^{o}$. This approximation is least valid for a description of the bending modes. Given this information, the explicit form of the normal modes may be calculated from the secular

equation in Eq. (4.4.17). The calculated frequency of each normal mode allows the mean-square amplitude of vibration to be determined [Eq. (4.2.12)]. The contribution of the Debye-Waller factors from each normal mode may then be summed to obtain the total factor in Eq. (4.3.6) for each scattering path.

The systems chosen for this study are shown in Table I. The Debye-Waller factor at $10^{o}K$ for each of these three-atom systems was calculated using Eq. (4.4.6) together with the normal modes calculated as described above. The results of these calculations are shown in Fig. 6. The calculated frequency of each of the normal modes of the $BeBr_2$ compound as a function of bridging angle are shown in Fig. 7. This compound was chosen for a detailed study as its mass ratio is typical of that encountered in instances where multiple scattering is significant. The temperature dependence of the Debye-Waller factor for the $BeBr_2$ system with three different bridging angles is shown in Fig. 8.

4.5 Discussion

We have presented a general description of the nature and origin of the Debye-Waller factor. The formalism developed is quite general and may be applied to any scattering problem. The form of the Debye-Waller factor in EXAFS was discussed in detail. An expression was obtained for the Debye-Waller factor in a general three-atom system. The form of this factor was shown to be dependent on the

geometry and symmetry of the system. The formalism as presented is readily applicable to multiple scattering events involving more than three atoms and may also be extended to describe systems of arbitrary symmetry.

The Debye-Waller factors for the series of three-atom systems described in Table I are shown in Fig. 6. Note that the double scattering factor has been divided by four so that the Debye-Waller factor for each scattering path has the standard form $\exp(-2k^2\sigma^2)$ [see Eq. (4.4.6)]. At all temperatures the Debye-Waller factors associated with the second shell single scattering, the double scattering and the triple scattering EXAFS components converge to a single value at a bridging angle of 180°. This convergence is required by Eq. (4.4.10) which describes the Debye-Waller factor for a linear system as a limiting case of that for a similar but bent system.

The relative magnitudes of the Debye-Waller factors associated with the various scattering paths deserves comment. A normal mode analysis of each system shown in Table I indicates that for all mass ratios (m/m_j), at a bridging angle of 100°, the displacement vectors of the terminal atoms in the A_1 stretch make an angle of about 40° with the base of the isosceles triangle which represents the system. As the system approaches linearity this angle decreases until it is zero when the bridging angle is 180°. In the case of the A_1 bend this angle depends on the mass ratio of the system. For small mass ratios the displacement

vectors of the terminal atoms make an angle of about 150° with the base of the triangle. When the mass ratio is larger this initial angle is closer to 180°. In both cases, as the system becomes less bent this angle decreases until it is 90° when a bridging angle of 180° is achieved.

The contribution of a given mode to the Debye-Waller factor for a particular scattering path is dependent on the frequency of the mode due to the presence of the Boltzmann factor in Eq. (4.2.10). In general, both the asymmetric stretch and symmetric bend increase in frequency as the system becomes less bent while the frequency of the symmetric stretch decreases (see Fig. 7). Furthermore, different scattering paths show different degrees of sensitivity to the displacements of the atoms that occur in a given normal mode. For instance, the triple scattering path receives a large contribution to its Debye-Waller factor from the A_1 stretching mode. This scattering path is, however, very insensitive to the A_1 bending mode except perhaps at small bridging angles (100°) where the frequency of the bend is low and the displacement vectors of the terminal atoms still have significant components along the internuclear axes. At large mass ratios the contribution to the triple scattering Debye-Waller factor from the A_1 stretch increases as the frequencies of the two A_1 modes become comparable (see Table I). On the other hand, the second shell single scattering Debye-Waller factor receives a large contribution from the A_1 bend. This is particularly

true at small bridging angles (where the frequency is low) and at high mass ratios where the displacement vectors of the terminal atoms have large components along the base of the isosceles triangle.

From Fig. 6 it is apparent that the first shell single scattering and the triple scattering Debye-Waller factors increase as the mass ratio increases. This occurs because both of these scattering paths are sensitive to the A_1 stretch whose frequency drops relative to the A_1 bend as the mass ratio increases. When the frequency of the A_1 bend is greater than the A_1 stretch, the magnitude of the triple scattering Debye-Waller factor surpasses that of the second shell single scattering [see Fig. 6(e)]. The double scattering factor, however, is sensitive to both A_1 type modes. At small angles this scattering path receives a large contribution to the Debye-Waller factor from the A_1 bend. As the system approaches linearity the frequency of the A_1 bend increases and the components of the displacement vectors of the terminal atoms diminish so that the contribution from this mode decreases. The contribution to the Debye-Waller factor from the A_1 stretch increases, however, due to the reduced frequency of this mode at large angles.

The temperature dependence of the Debye-Waller factors for the $BeBr_2$ system is shown in Fig. 8. The low frequency of the bending mode at small bridging angles (100°) causes the second shell single scattering Debye-Waller factor to

have the observed sharp temperature dependence. The interplay of both A_1 modes in determining the Debye-Waller factor for the double scattering path is evident from Fig. 8. At small bridging angles the temperature dependence of the double scattering term is more severe than that for the triple scattering term. This occurs because the double scattering path is sensitive to the A_1 bend which has a low frequency at these angles while the triple scattering path is most sensitive to the A_1 stretch which occurs at much higher frequencies (see Fig. 7). As the system approaches linearity, however, the temperature dependence of both the double and triple scattering paths become very similar due to the dominant contribution of the A_1 stretch to each Debye-Waller factor. In general, it is apparent that the Debye-Waller factors for each scattering path are strong functions of temperature. At sufficiently low temperatures each Debye-Waller factor is independent of temperature while at higher temperature the Debye-Waller factors vary linearly with temperature in agreement with Eqs. (4.2.13) and (4.2.14).

The purpose of this present study is to provide an understanding of the Debye-Waller factor in EXAFS so that accurate bond angles may be determined. A standard method of analysis for EXAFS data that contain a significant multiple scattering component has not yet been presented. Teo[7] has suggested that the terms involving the second shell atom in Eq. (4.3.1) may be combined and that the resulting

expression can be analyzed as though it described a single scattering EXAFS process with a modified amplitude and phase. This results in a considerable simplification of the data analysis. This approach, however, neglects the polarization terms in Eq. (4.3.3). In addition, it assumes that the Debye-Waller factors for all scattering paths involving the second shell atom are the same. To study the significance of this latter assumption the resulting modification in the amplitude of the double and triple EXAFS components in the $BeBr_2$ system were calculated and are shown in Fig. 9. All amplitude calculations were carried out at $k = 10\ \text{Å}^{-1}$, the amplitude modification is smaller and larger at smaller and larger values of k, respectively. The errors involved are clearly larger at small bridging angles and high temperatures. At low temperatures, the larger modification occurs in the amplitude of the double scattering component while at higher temperatures the amplitude of the triple scattering component is more sensitive. This observation is consistent with the above mentioned dependence of the triple scattering Debye-Waller factor on the A_1 stretching mode. For a bridging angle of 120° the amplitudes of the double and triple scattering terms are reduced by a factor of 11.1 and 19.4 respectively, at room temperature. The reductions in the amplitudes are considerably less for a system that is approximately linear, especially at low temperature [see Fig. 9(d)].

The calculations in Fig. 9, however, assume that both

the double and triple scattering paths contribute equally to the EXAFS. The ratio of the intrinsic amplitudes of the double and triple scattering terms is:

$$|2\chi_D^0/\chi_T^0| = \frac{2(\hat{r}_i\cdot\hat{r}_j)r_j r_{ij}|f_i(\beta,k)|}{r_i|f_j(\alpha,k)||f_i(\pi,k)|}, \qquad (4.5.1)$$

where α and β are the scattering angles at atoms j and i and the T-matrices in Eqs. (4.3.3) and (4.3.4) have been written in terms of their respective scattering amplitudes. In instances where multiple scattering is important, $120^\circ < \beta < 180^\circ$, we may approximate the scattering amplitude through angle β with the backscattering amplitude.[7] For symmetric systems $r_j = r_{ij}$ and $r_i = 2r_j(\hat{r}_i\cdot\hat{r}_j)$ so that the ratio is given by:

$$|2\chi_D^0/\chi_T^0| \sim r_j/|f_j(\alpha,k)|. \qquad (4.5.2)$$

The triple scattering EXAFS component will dominate when the bond distance r_j is small or when the scattering amplitude through an angle α is large for the intervening atom j. In general, the multiple term which dominates is dependent on the geometry of the system and the nature of the intervening atom. If one term completely dominates the EXAFS, then the other terms may be neglected and Teo's approximation is always valid. The errors shown in Fig. 9 are significant only if the both multiple scattering terms and the single scattering terms are comparable or if one multiple scattering term and the single scattering terms are

comparable while the remaining multiple scattering term is small. If both multiple scattering terms are comparable in magnitude and greater than the single scattering term, then we must compare the difference in the Debye-Waller factors of the multiple scattering terms to obtain the error in the amplitude. This error is typically smaller than those found in Fig. 9 (see Fig. 8).

A study of the temperature dependence of the Debye-Waller factors reveals that there exists a point at which the double and triple scattering factors are equal. This crossover point occurs because the triple scattering factor is less sensitive than the double scattering factor to the low frequency bend mode. Since the frequency of the bend mode increases as the system becomes less bent the temperature of the crossover point also increases (see Fig. 8). Provided the single scattering contribution to the EXAFS is small, an analysis of data collected at this temperature, and based on Teo's assumption, is rigorous and should yield accurate results.

Recently, Alberding and Crozier[18] discussed the analysis of EXAFS data which contained a significant amount of multiple scattering. They considered a μ-oxo system, Fe_2O, and a dihydroxy bridged system, $Fe_2(OH)_2$. The Fe_2O system is approximately symmetric with a bridging angle of 164° and an Fe-O bond length of 1.8 Å. Using an analysis similar to that described by Teo[7], Alberding and Crozier obtained a bridging angle of 180° and an Fe-Fe distance of

3.63 Å (compared to an actual distance of 3.55 Å). These results are not surprising since Teo's analysis is not strictly valid in this instance, especially at high temperatures [see Eq. (4.5.2) and Fig. 8]. A calculated bridging angle of 180° might be explained by the fact that the Debye-Waller factors associated with each scattering path, which are constrained to be equal by the analysis, are in fact, equal only at this bridging angle. A second model analysis involving a bending mode was also proposed. This latter method yielded a better Fe-Fe distance and bridging angle. The residual surface was broad and ill-defined. The physical basis for this method of analysis is discussed in the next chapter.

In conclusion, the Debye-Waller factors in EXAFS spectra which contain a significant multiple scattering component are sensitive to the geometry of the system. The accuracy of Teo's approximation depends on which term or terms dominate the EXAFS for the system in question. In general, there will be a significant discrepancy if any two or more of the scattering paths involving the second shell have comparable amplitudes. The magnitude of this error is smallest for systems with large bridging angles or at low temperature. In instances in which the contribution to the observed EXAFS from the single scattering path is small, there exists a range of temperatures over which the above approximation is very accurate.

References

*This chapter is based on: J.J. Boland and J.D. Baldeschwieler. J. Chem. Phys. **80**, 3005 (1984).

1. D.E. Sayers, E.A. Stern and F.W. Lytle. Phys. Rev. Lett. **27**, 1204, (1971).

2. P.A. Lee, P.H. Citrin, P. Eisenberger and B.M. Kincaid. Rev. Mod. Phys. **53**, 769 (1981).

3. V.V. Schmidt. Bull. Acad. Sci. USSR Phy. Ser. **25**, 988 (1961); **27**, 392 (1963)

4. G. Beni and P.M. Platzman. Phys. Rev. **B 14**, 1514 (1976).

5. R.B. Gregor and F.W. Lytle. Phys. Rev. **B 20**, 4902, (1979).

6. E. Sevillano, H. Meuth and J.J. Rehr. Phys. Rev. **B 20**, 4908 (1979).

7. B.K. Teo. J. Am. Chem. Soc. **103**, 3940 (1981).

8. J.J. Boland, S.E. Crane and J.D. Baldeschwieler. J. Chem. Phys. **77**, 142 (1982).

9. See for example, A.A. Maradudin, G.W. Montroll A.H. Weiss and I.P. Ipatova, Theory of Lattice Dynamics in the Quadratic Approximation (Academic, New York, 1971).

10. M. Lax. Rev. Mod. Phys. **23**, 287 (1951).

11. See for example, E.B. Wilson, J.C. Dicius and P.C. Cross, Molecular Vibrations (McGraw-Hill, New York, 1955).

12. M. Born and K. Sarginson. Proc. Roy. Soc. **A 179**, 69, (1941).

13. See for example, T.L. Hill Introduction to Statistical Thermodynamics (Addison-Wesley, Reading, 1960).

14. M. Born. Rep. Prog. Phys. **9**, 294, (1943).

15. See for example, G. Hertzberg. Infrared and Raman Spectra (Van Nostrand, New Jesey, 1945).

16. K. Nakamoto. Infrared Spectra of Inorganic and Coordination Compounds 3rd edition (Wiley, New York, 1970).

17. P.A. Lee and J.B. Pendry. Phys. Rev. **B 11**, 2795, (1975).

18. N. Alberding and E.D. Crozier. Phys. Rev. **B 27**, 3374 (1983).

19. J.J. Boland and J.D. Baldeschwieler. J. Chem. Phys. in press (1984).

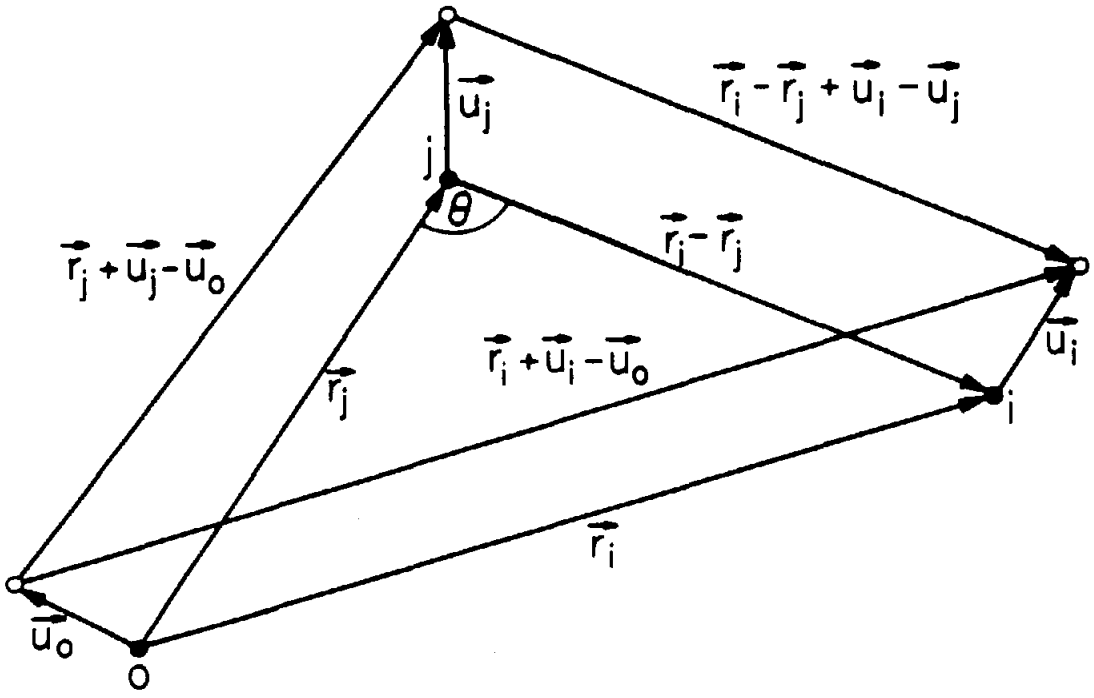

Figure 1.
The general three-atom system. The equilibrium positions of the central atom (O), first nearest-neighbor atom (j) and second nearest neighbor atom (i) are shown as filled circles. The displacement of these atoms from their respective equilibrium positions are shown as open circles. θ represents the equilibrium bridging angle. The equilibrium position of the central atom was chosen to represent the origin of the system.

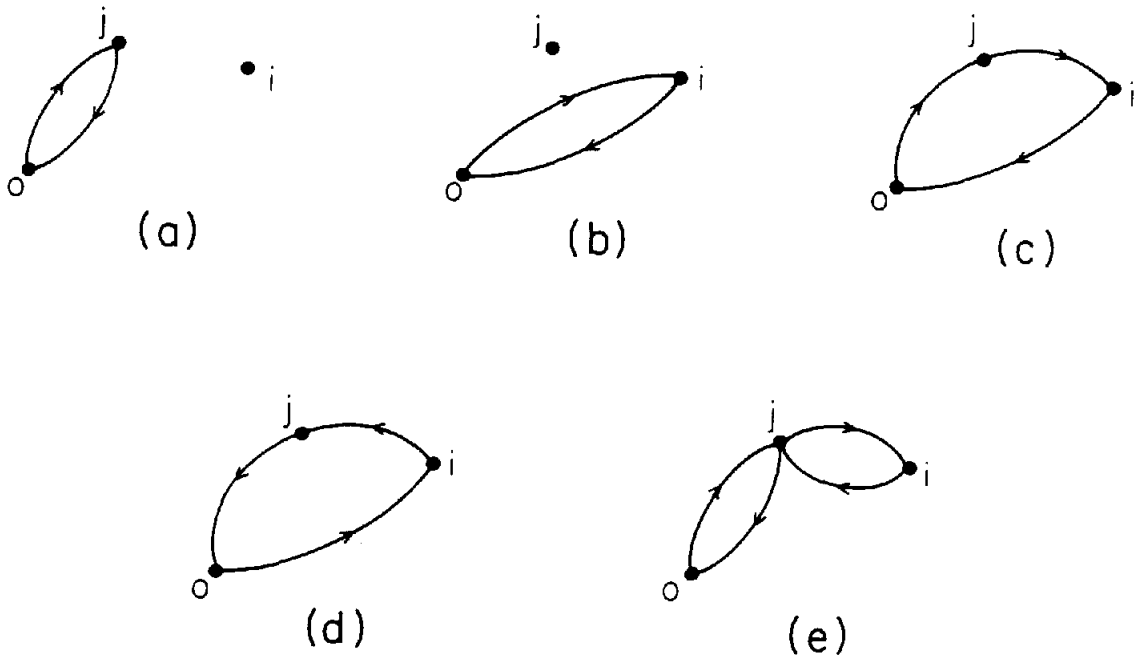

Figure 2.
The five significant scattering paths in a system of three atoms. (a) and (b) represent the single scattering paths from atoms i and j. The two double scattering paths (c) and (d) are identical by virtue of time-reversal symmetry. The triple scattering path is shown in (e).

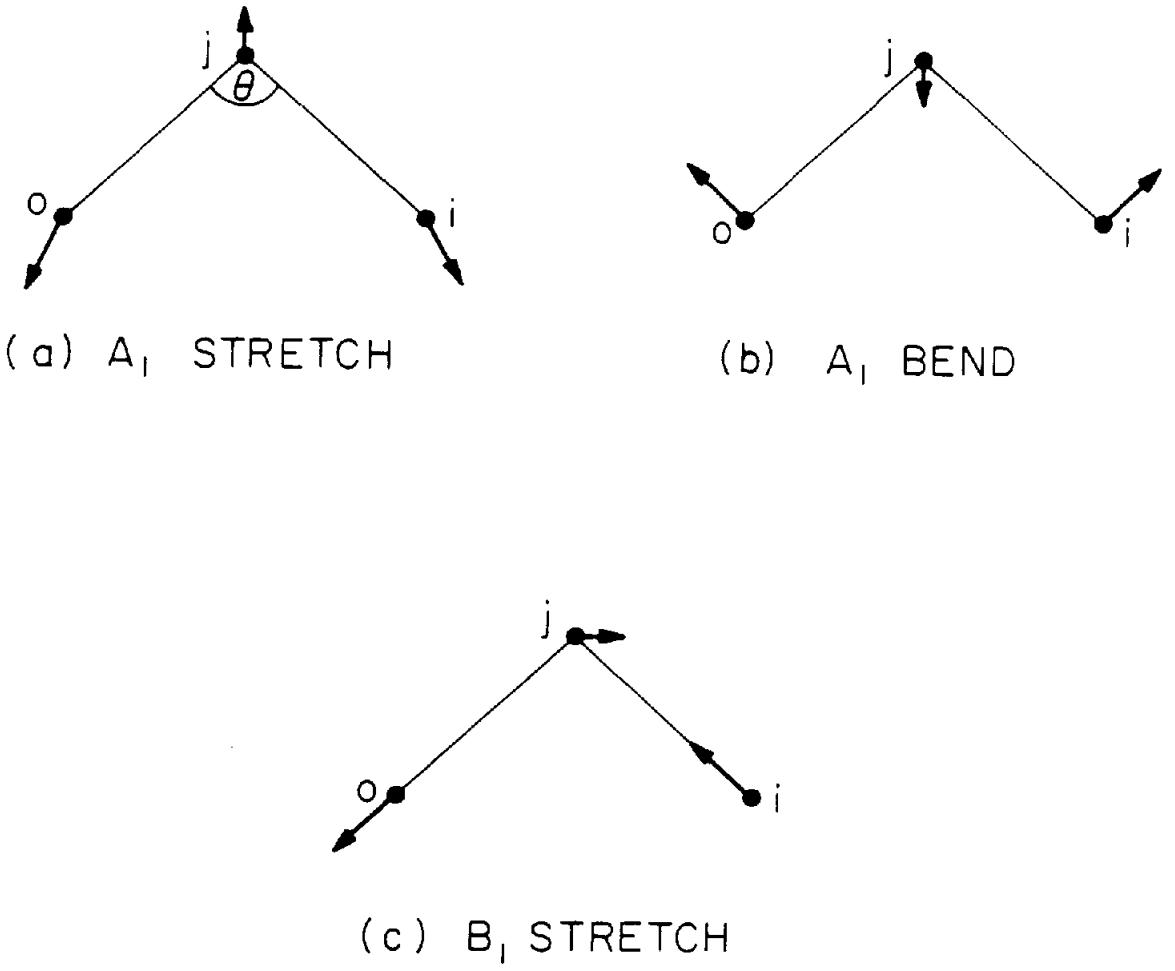

Figure 3.
Schematic of the normal modes in a three-atom system of C_{2v} symmetry. There are three normal mode two of A_1 type symmetry and a single B_1 mode.

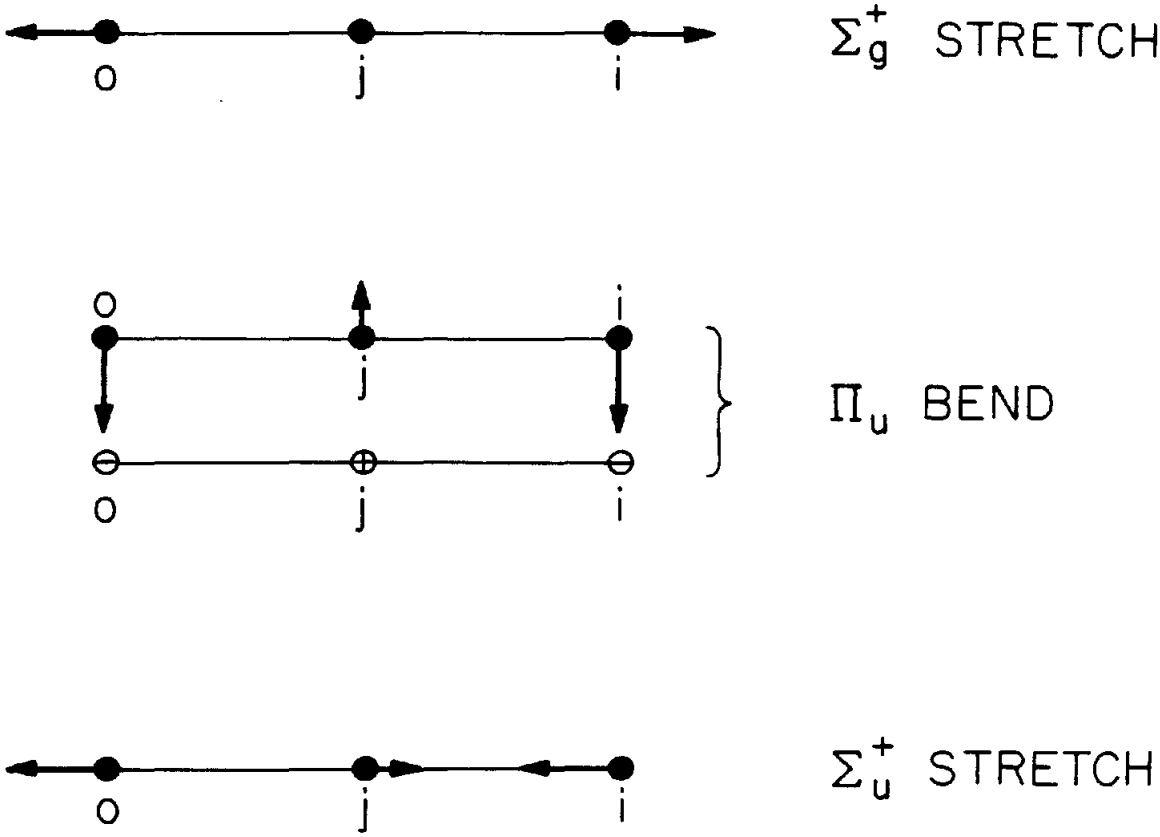

Figure 4.
Schematic of the normal modes in a three-atom system of $D_{\infty h}$ symmetry. The symmetric stretch, Σ_g^+, involves no motion of the intervening atom j. The degenerate bending modes, Π_u, may be interconverted by a rotation of 90° about the molecular axis. The asymmetric stretch, Σ_u^+, is the limiting case of the single B_1 mode in a C_{2v} system.

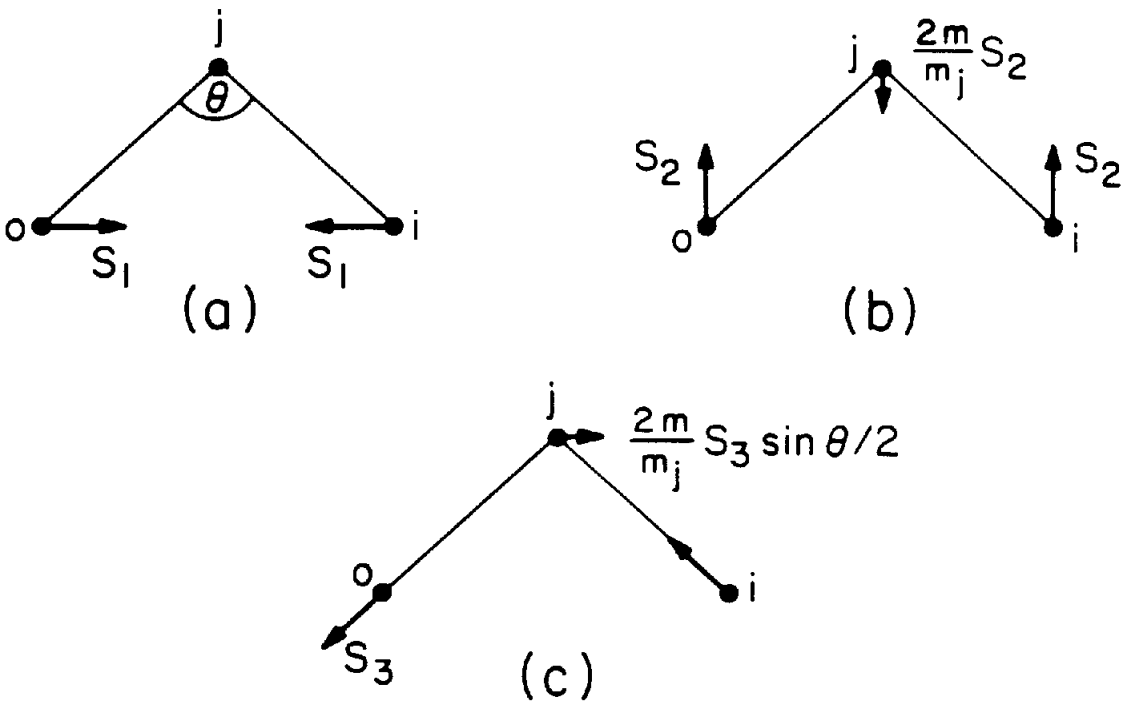

Figure 5.
The symmetrized coordinates used in a normal mode analysis of the three-atom system. S_1 and S_2 transform as A_1 in a C_{2v} system while S_3 transforms as B_1 and is identical, apart from a constant factor, to the asymmetric stretching mode.

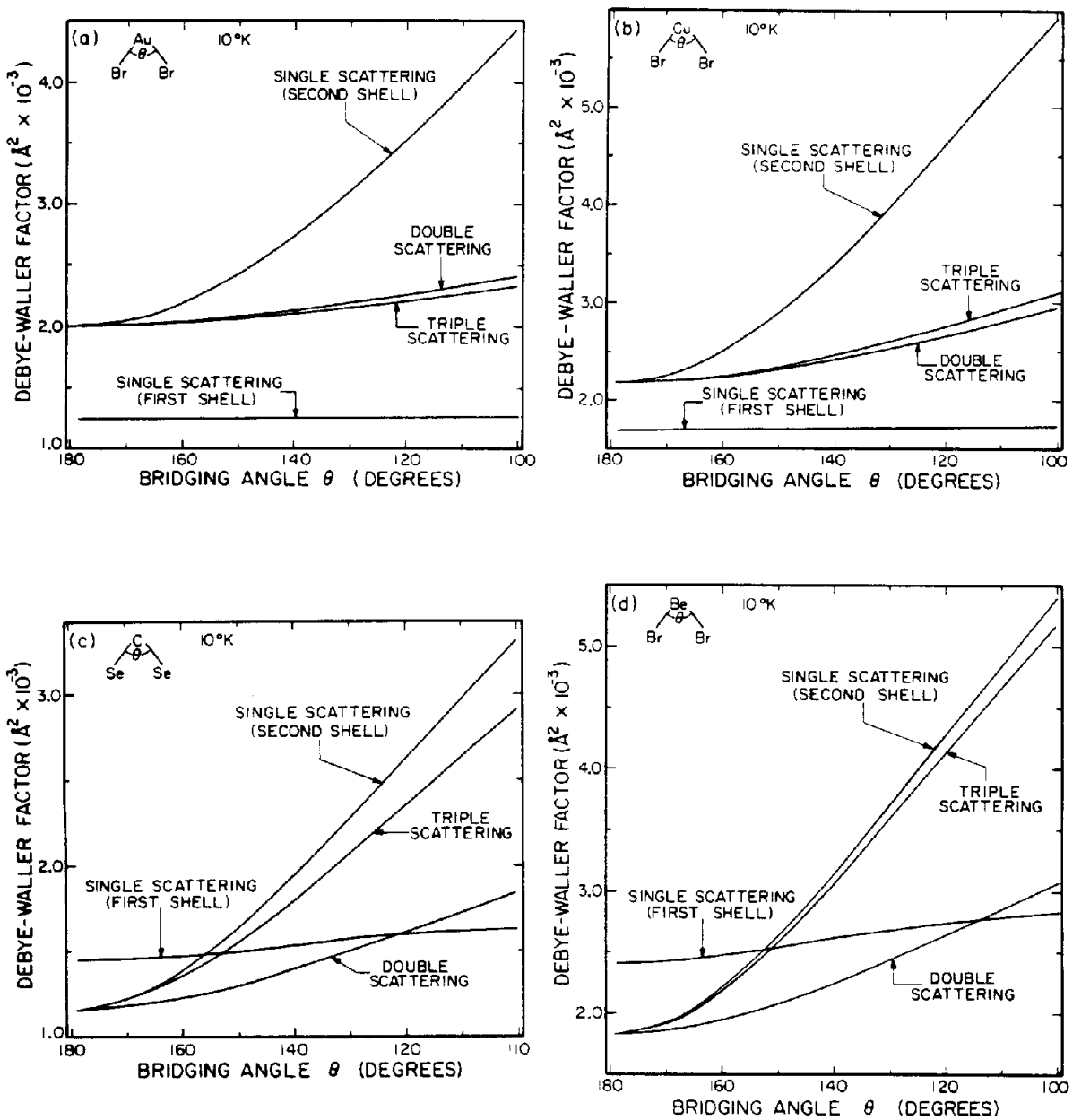

Figure 6.
Calculated Debye-Waller factors at 10°K as a function of bridging angle for a series of three atom systems. (a) $AuBr_2$. (b) $CuBr_2$. (c) CSe_2. (d) $BeBr_2$. (e) BeI_2.

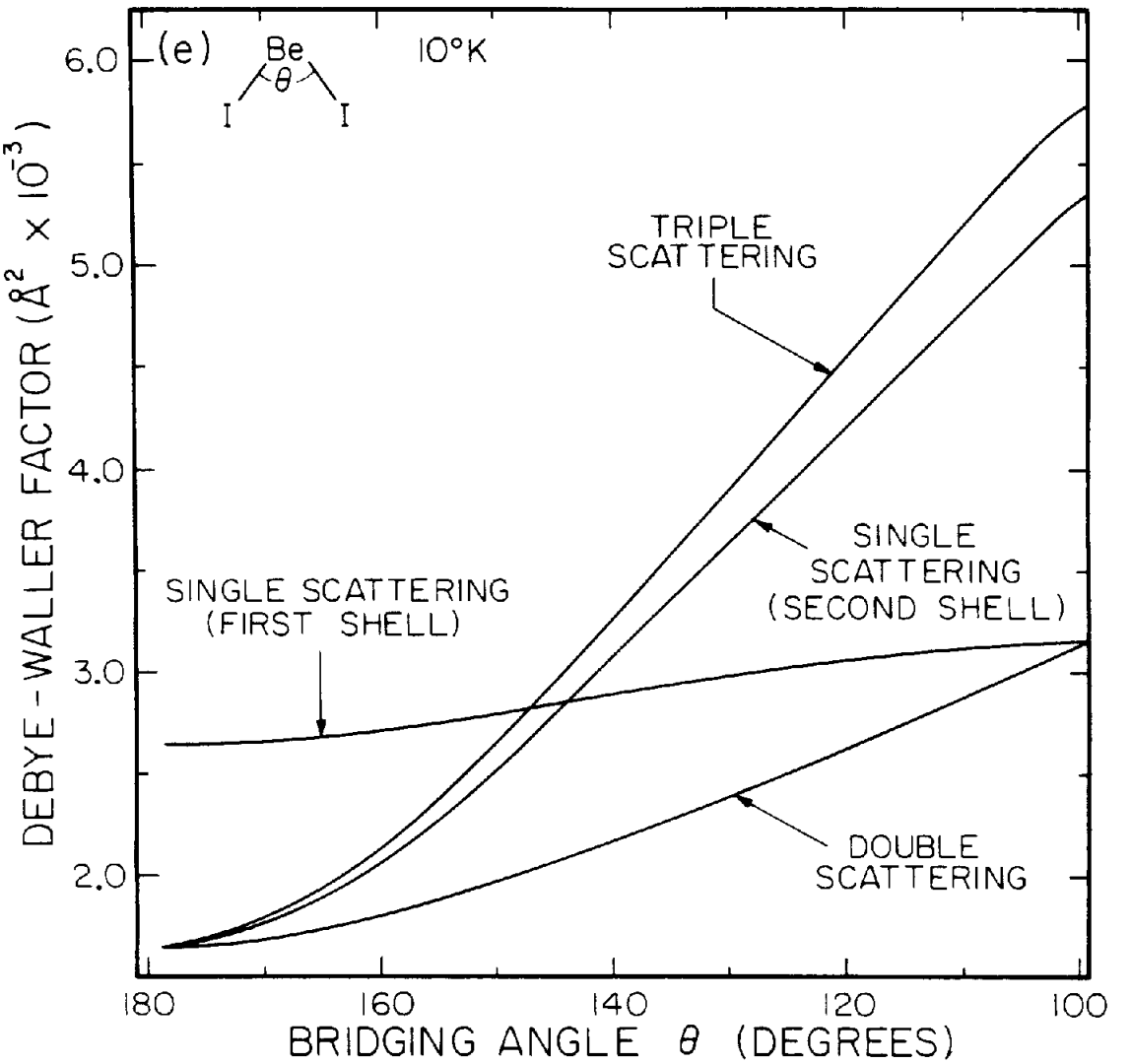

Figure 6, continued.

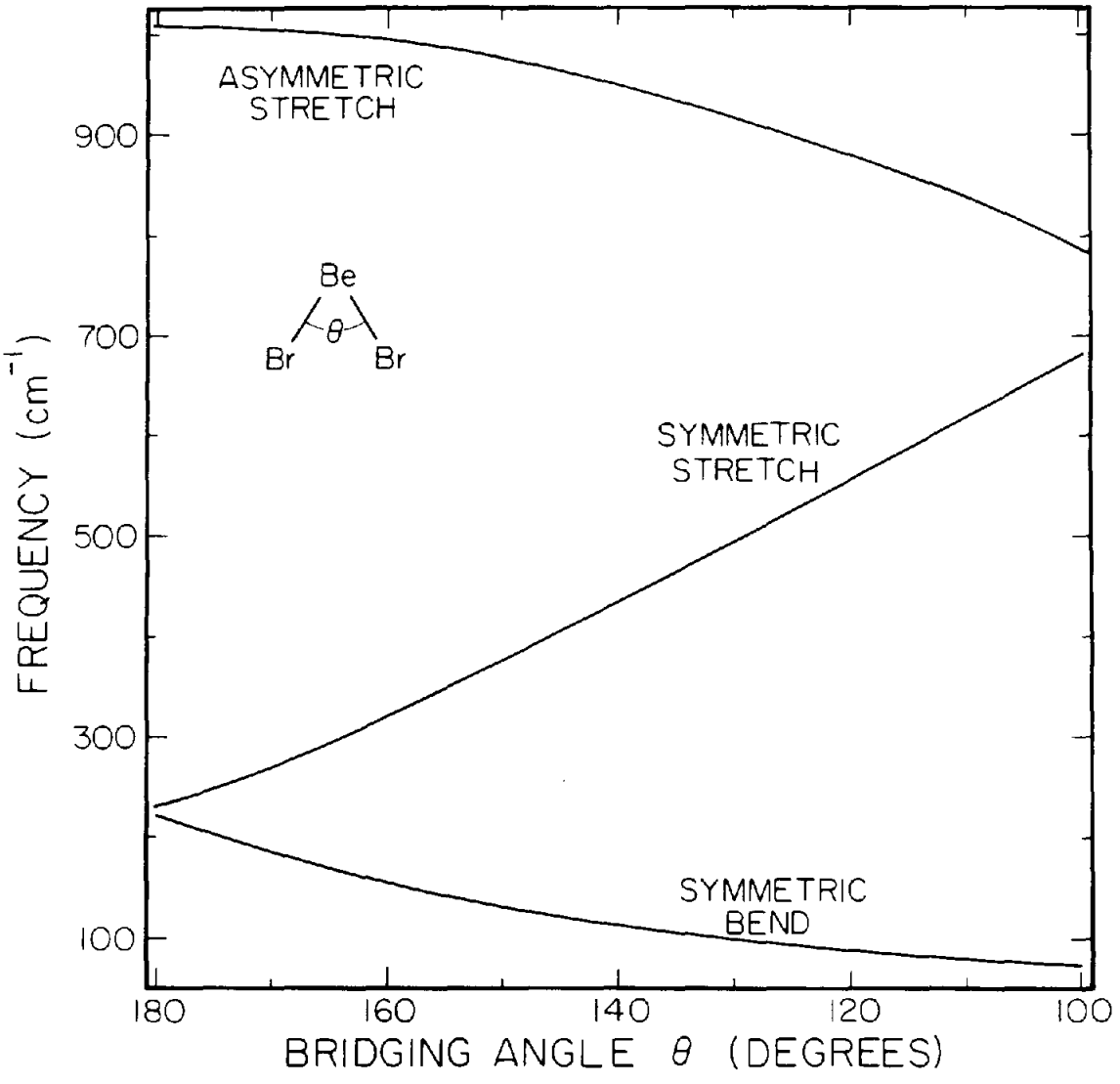

Figure 7.
Calculated frequencies of the normal modes of vibration for the $BeBr_2$ system as a function of bridging angle θ.

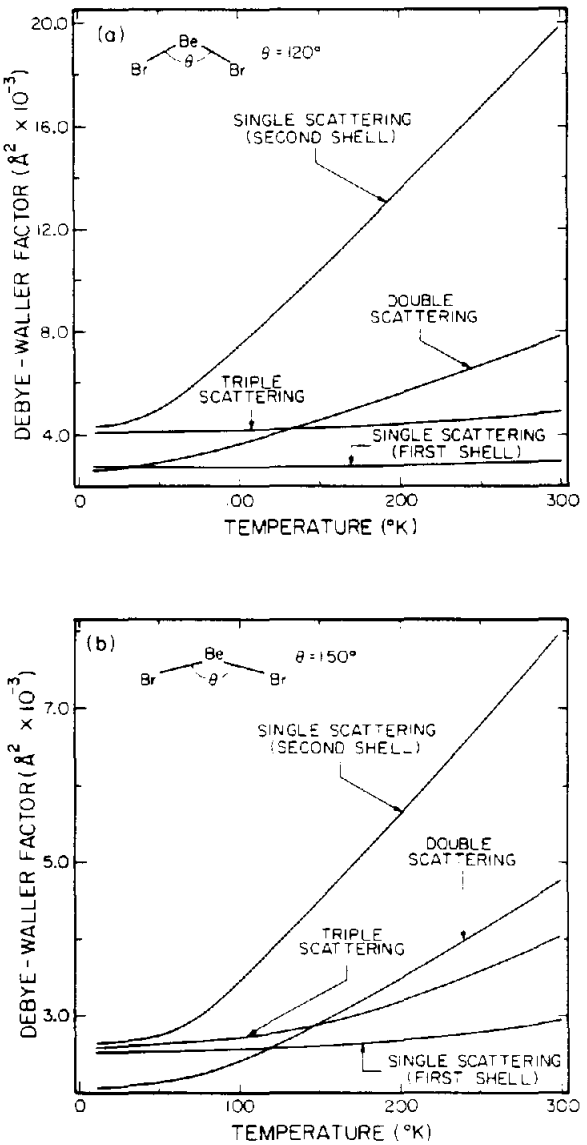

Figure 8.
Temperature dependence of the Debye-Waller factors for the $BeBr_2$ system at three different bridging angles. (a) 120°. (b) 150°. (c) 170°.

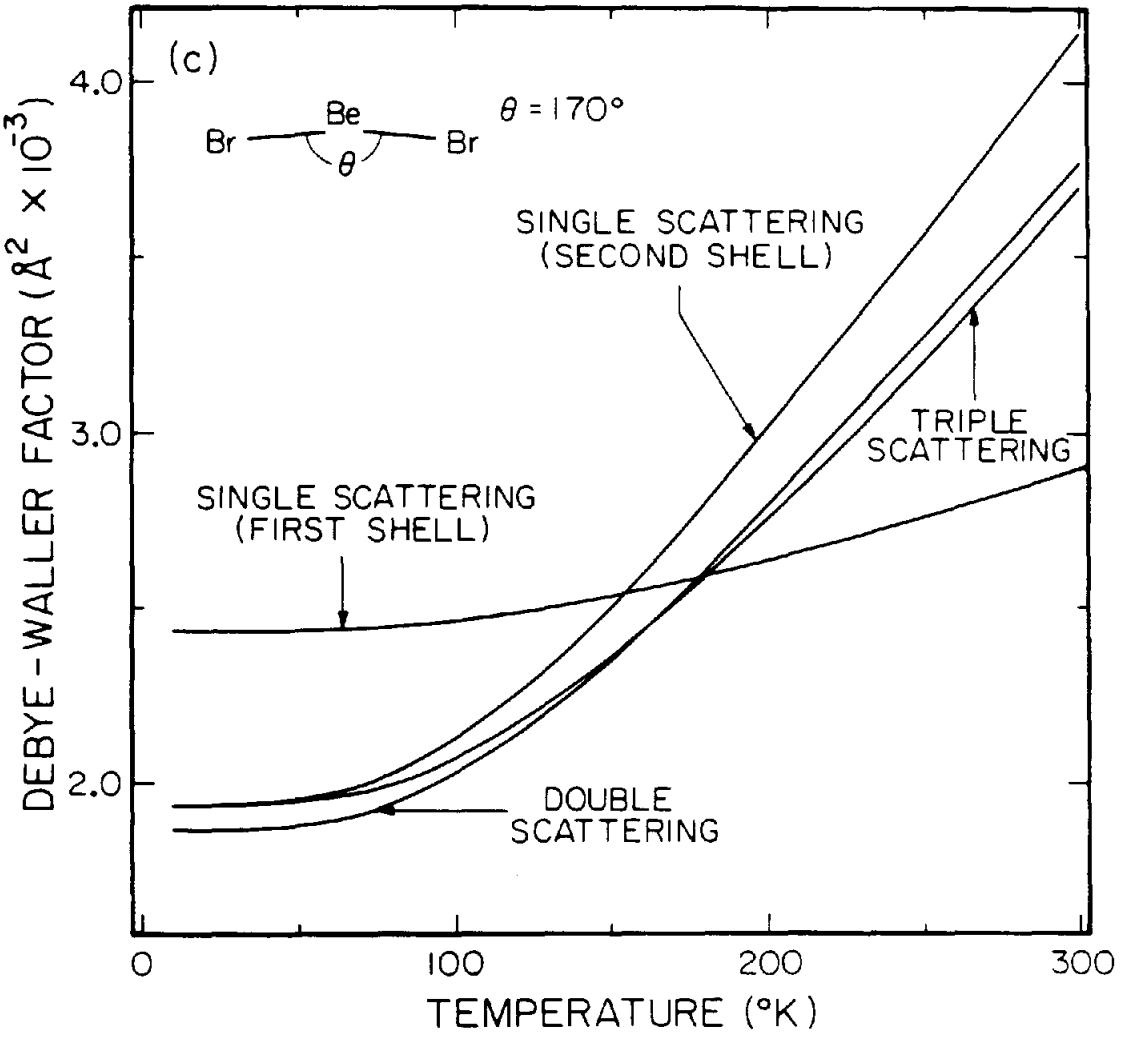

Figure 8, continued.

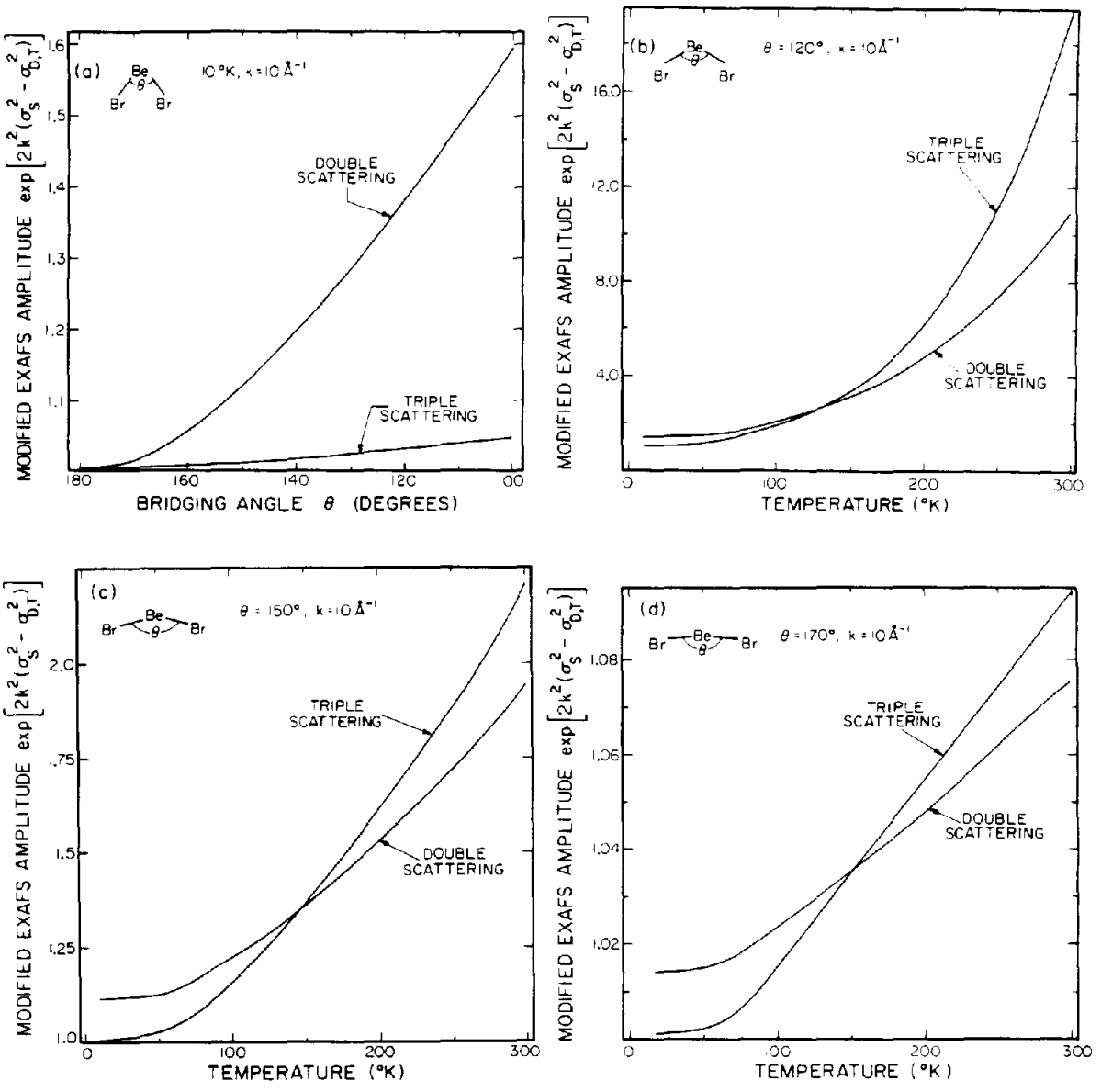

Figure 9.

Modification in the EXAFS amplitude of the double and triple scattering terms in the $BeBr_2$ system due to the assumption that the second shell single scattering Debye-Waller factor (σ_S) may be used to approximate the double (σ_D) and triple (σ_T) scattering Debye-Waller factors. All amplitudes were calculated at k = 10 $Å^{-1}$. (a) Modification in the amplitudes of the double and triple scattering terms at 10°K as a function of bridging angle θ. (b) temperature dependence at a bridging angle of 120°. (c) 150°. (d) 170°.

Table I. Normal frequencies of vibration for the linear model systems discussed in the text.[16] The mass ratio of the central to the intervening atom is also shown.

SYSTEM	$\nu_1(cm^{-1})$	$\nu_2(cm^{-1})$	$\nu_3(cm^{-1})$	m/m_j
$AuBr_2$	209	77	254	0.40
$CuBr_2$	193	81	322	1.26
CSe_2	364	313	1303	6.58
$BeBr_2$	230	220	1010	8.88
BeI_2	160	175	873	14.11

CHAPTER V

THE EFFECT OF THERMAL VIBRATIONS ON EXTENDED X-RAY ABSORPTION FINE STRUCTURE: MODIFICATION FACTORS*

5.1 Introduction

Extended X-Ray Absorption Fine Structure (EXAFS) refers to the modulations observed in the absorption coefficient on the high frequency side of an x-ray absorption edge. The origin of this structure was first explained by Kronig[1] who described the EXAFS in terms of a modification of the photoelectron's wave function due to the presence of neighboring atoms. Despite this early work, the potential of EXAFS to yield local structural information went unnoticed until Sayers, Stern and Lytle[2] presented a parameterization of the extended structure in terms of physically significant quantities. Since then EXAFS has emerged as an important structural tool with applications in many areas of physics, chemistry and biology.[3]

EXAFS yields structural information about the local environment of the atomic species which absorbs the x-ray photon. The modulations observed in the absorption coefficient are due to an interference phenomenon in which the outgoing photoelectron wave is scattered by neighboring atom potentials. The amplitude of the scattered wave returning to the absorption site is inversely proportional to the product of the individual scattering path lengths during which the photoelectron propagates freely. This

ensures that the contribution to the EXAFS from distant shells is small. In addition, the limited coherent path length due to inelastic scattering and the finite lifetime of the core hole further serve to restrict the depth of penetration of the photoelectron into the bulk. Since multiple scattering events necessarily involve large path lengths this contribution to the EXAFS was generally considered to be small. Exception was taken to the case in which the absorbing atom and two neighboring atoms lined up such that the large forward scattering amplitude of the intervening atom compensated for the decrease in flux due to the long scattering path.[4] The short range nature of the EXAFS effect thus facilitates an analysis of the extended structure. The predominance of single scattering and the relatively few distances involved make EXAFS amenable to the methods of Fourier analysis. The Fourier transform of an isolated EXAFS pattern yields a form of radial distribution function in which the central atom is located at the origin. The distribution function is distorted, however, due to the presence of phase shifts incurred by the photoelectron during the scattering process. From such an analysis it is possible to determine bond distances, coordination numbers and the types of neighboring atoms involved.

Recently, however, there has been considerable interest in multiple scattering events in EXAFS. Teo[5] and Boland *et al.*[6] have shown that a three-atom system comprised of an absorbing atom and two neighboring atoms is sufficient to

describe all significant multiple scattering effects. The amplitude and phase of the multiple scattering components were shown to be sensitive to the geometry of the system. When data analysis is based on a single scattering model, spectra which contain a significant degree of multiple scattering often appear to have anomalous Fourier coefficients. In such instances, however, a multiple scattering analysis should make possible a determination of the complete local geometry, including bond angles, about the absorbing atom. The frequency of the single and multiple scattering EXAFS components may be sufficiently similar that a Fourier analysis is unable to resolve the individual components. It is this problem which makes an accurate treatment of such EXAFS data difficult.

To develop a method of analysis for multiple scattering EXAFS data it is necessary to understand the factors which affect the amplitude and phase of each EXAFS component. Teo[5] has suggested that the scattering paths involving the second shell atom may be combined and analyzed as though they described a single scattering process with a modified amplitude and phase. This method results in a considerable simplification of the data analysis. More recently, Alberding and Crozier[7] discussed separately the effects on the observed EXAFS of changes in bond distances and scattering angles. This present paper will address the problem of thermal vibrations and their effect on EXAFS spectra. In a previous paper[8] (discussed in detail in

Chapter IV) we showed that, to lowest order, the Debye-Waller factor associated with changes in the internuclear distances may be treated separately from changes in scattering angles. The purpose of this present work is to describe the effects of changes in bond angles and the correlation that exists between such changes and the accompanying changes in bond distances.

5.2 Formal Considerations

To study the effects of thermal vibrations let us consider the general three-atom system shown in Fig. 1. Systems of this type have been discussed previously by Teo[5] and Boland et al.[6]. In the absence of thermal vibrations, the EXAFS for such a system may be described by:

$$\chi^{o}(k,\hat{e}) = \chi^{o}_{S}(k,\hat{e}) + 2\chi^{o}_{D}(k,\hat{e}) + \chi^{o}_{T}(k,\hat{e}) \qquad (5.2.1)$$

The superscript zero indicates the absence of thermal vibrations and k is the photoelectron wave number defined by the free electron dispersion relation:

$$k = [2m(\hbar\omega - E_{o})]^{1/2}/\hbar \qquad (5.2.2)$$

where $\hbar\omega$ is the energy of the x-ray photon and E_o is the threshold energy. The subscripts S, D and T refer to single, double and triple scattering events and $\hat{e}$ is the unit vector which specifies the direction of polarization of the incident x-ray beam.

A schematic representation of the scattering paths

within this three-atom system is shown in Fig. 2. The single scattering EXAFS, $\chi_S^o(k,\hat{e})$, consists of two terms each of which correspond to a single scattering event involving the neighboring atom located at $\vec{r} = \vec{r}_i$ or $\vec{r} = \vec{r}_j$. $\chi_S^o(k,\hat{e})$ may be expressed as:

$$\chi_S^o(k,\hat{e}) = \sum_{g=i,j} \chi_{S_g}^o(k,\hat{e})$$

where

$$\chi_{S_g}^o(k,\hat{e}) = \frac{-3(\hat{r}_g\cdot\hat{e})^2}{kr_g^2}\ \mathrm{Im}\left[f_g(\pi,k)\ e^{2i\vec{k}_g\cdot\vec{r}_g}\ e^{2i\delta_1}\right] \tag{5.2.3}$$

where $\vec{k}_g = k\vec{r}_g$ and $\chi_{S_g}^o(k,\hat{e})$ represents the contribution to the total single scattering from atom g. The probability amplitude of atom g scattering the incident photoelectron through an angle π is given by $f_g(\pi,k)$. The double scattering EXAFS, $\chi_D^o(k,\hat{e})$, involves events in which the photoelectron successively scatters of one neighboring atom and then off the other remaining neighboring atom. By virtue of time reversal invariance, the order in which this scattering sequence occurs does not affect the probability amplitude so that this term is counted twice in Eq. (5.2.1) [see Fig. 2(c) and 2(d)]. $\chi_D^o(k,\hat{e})$ may be written as:

$$\chi_D^o(k,\hat{e}) = \frac{-3(\hat{r}_i\cdot\hat{e})(\hat{r}_j\cdot\hat{e})}{kr_ir_jr_{ij}}\ \mathrm{Im}\Big[f_j(\alpha,k)f_j(\beta,k)\ e^{2i\delta_1}\ e^{i(\vec{k}_j\cdot\vec{r}_j + \vec{k}_{ij}\cdot\vec{r}_{ij} + \vec{k}_i\cdot\vec{r}_i)}\Big] \tag{5.2.4}$$

where $\vec{k}_{ij} = k\hat{r}_{ij} = k(\vec{r}_i - \vec{r}_j)/|\vec{r}_i - \vec{r}_j|$ and α and β are the scattering angles at atoms j and i, respectively. The triple scattering EXAFS term, $\chi_T^o(k,\hat{e})$, describes a process in which the outgoing photoelectron wave first scatters off the nearest neighboring atom j then scatters off atom i and finally scatters off atom j once again [see Fig. 2(e)]. $\chi_T^o(k,\hat{e})$ may be expressed as:

$$\chi_T^o(k,\hat{e}) = \frac{-3(\hat{r}_j\cdot\hat{e})^2}{kr_j^2 r_{ij}^2}\ \mathrm{Im}\Big[\big(f_j(\alpha,k)\big)^2\ f_i(\pi,k)\ e^{2i\delta_1}\ e^{2i\vec{k}(\vec{k}_j\cdot\vec{r}_j + \vec{k}_{ij}\cdot\vec{r}_{ij})}\Big] \tag{5.2.5}$$

To obtain an expression for the EXAFS corresponding to the configuration of the three atoms shown in Fig. 1 the relative equilibrium position vectors of the atoms must be replaced by their respective instantaneous position vectors. The EXAFS is then described in terms of the instantaneous bond angles and distances of the system. To describe the effect such configurations have on the observed EXAFS spectrum, it is necessary to express the instantaneous value of any factor in terms of its equilibrium value together with a time dependent expression describing the deviation of this factor from equilibrium. Consideration of Eqs. (5.2.3) through (5.2.5) shows that there are four such factors, common to all equations, which are sensitive to the instantaneous geometry of the system. We shall now identify and estimate the importance of each of these four factors.

First let us consider the polarization terms which are common to all EXAFS expressions. Note that there are essentially two types of polarization factors. The instantaneous values of these dot products may be expressed in terms of their equilibrium values by expanding the products in a Taylor series. Since we are primarily concerned with polycrystalline samples these dot products must be averaged over all possible polarization directions. It may be shown that to first order, changes in the position vectors of the atoms do not effect the spherically averaged polarization factor. These factors will not be discussed further, to the order of the present calculations they are sufficiently well approximated by their equilibrium values. When single crystal or directionally oriented samples (e.g., surfaces) are being studied, however, it is necessary to explicitly calculate each of the terms in the Taylor series.

The second factor to be considered is the exponential term representing the total scattering path length. Since each term of this type is similar, we shall focus on a given term and generalize the results. In single scattering events involving atom j the exponential term in Eq. (5.2.3) corresponding to the instantaneous configuration shown in Fig. 1 may be written as:

$$e^{2i\vec{k}'_j \cdot \vec{r}'_j} = e^{2ik|\vec{r}_j+\vec{u}_j-\vec{u}_o|} \qquad (5.2.6)$$

where $\vec{k}'_j = k\hat{r}'_j$ and $\vec{r}'_j$ is the instantaneous position vector corresponding to the equilibrium position vector $\vec{r}_j$. The

displacement vectors of the central atom and atom j are given by $\vec{u}_o$ and $\vec{u}_j$, respectively. The path length may be written as:

$$|\vec{r}_j+\vec{u}_j-\vec{u}_o| = (r_j^2+u_j^2+u_o^2+2\vec{r}_j.\vec{u}_j-2\vec{r}_j.\vec{u}_o-2\vec{u}_j.\vec{u}_o)^{1/2} \quad (5.2.7)$$

Retaining only the lowest order terms in the displacement, this distance may be approximated using a binomial expansion.

$$|\vec{r}_j+\vec{u}_j-\vec{u}_o| \approx r_j+\hat{r}_j.(\vec{u}_j-\vec{u}_o) \quad (5.2.8)$$

Substituting Eq. (5.2.8) into Eq. (5.2.6) reveals that the original exponential term is factored into the equilibrium separation of the atoms and the projection of the displacement vectors along the bond defined by these atoms.

$$e^{2ik|\vec{r}_j+\vec{u}_j-\vec{u}_o|} = e^{2ikr_j}\, e^{2ik\hat{r}_j.(\vec{u}_j-\vec{u}_o)} \quad (5.2.9)$$

A similar treatment may be applied to the remaining terms of this type.

The next quantity which must be discussed in our treatment of thermal vibrations is the effect of the instantaneous distances which occur in the denominator of each EXAFS component. Using the approximations developed in Eq. (5.2.8) above, it may be shown that such corrections are negligible and we may replace the instantaneous distances in the demoninator by their equilibrium values.

The remaining factor to be considered is the effect on the scattering amplitude of small changes in the directions

of the incident and scattered photoelectron wave induced by thermal vibrations. The instantaneous scattering amplitude of atom j may be expressed in a Taylor series about the equilibrium scattering angle α:

$$f_j(\alpha+\Delta\alpha,k) = f_j(\alpha,k) + \left(\frac{f_j(\alpha',k)}{\partial\alpha'}\right)_\alpha + O(\Delta\alpha^2) \qquad (5.2.10)$$

where $\Delta\alpha$ is the deviation from the equilibrium value. Note that in instances where the equilibrium scattering angle is π, the instantaneous angle is also π so that such scattering amplitudes need not be discussed further.

To estimate the magnitude of the lowest order term in Eq. (5.2.10) it is necessary to express the angular deviation in terms of the displacement vectors of the three atoms shown in Fig. 1. The scattering angle α may be written in terms of the unit vectors of the system

$$\cos\alpha = \hat{r}_j \cdot \hat{r}_{ij} \qquad (5.2.11)$$

Equation (5.2.11) may be differentiated to yield:

$$\Delta\cos\alpha = -\sin\alpha\,\Delta\alpha = \hat{r}_j \cdot \Delta\hat{r}_{ij} + \Delta\hat{r}_j \cdot \hat{r}_{ij} \qquad (5.2.12)$$

so that the change in the angle from its equilibrium value is given by:

$$\Delta\alpha = -\frac{\hat{r}_j \cdot \hat{r}_{ij} + \hat{r}_j \cdot \hat{r}_{ij}}{\sin\alpha} \qquad (5.2.13)$$

Noting that each unit vector may be written as $\hat{r}_j = \vec{r}_j/r_j$, an expression for the deviation in angle may be readily

obtained. Separating the contribution to $\Delta\alpha$ form each of the displacement vectors allows Eq. (5.2.13) to be written in the form

$$\Delta\alpha = \vec{a}_j.\vec{u}_o + \vec{b}_j.\vec{u}_i + \vec{c}_j.\vec{u}_j$$

where

$$\vec{a}_j = \frac{\hat{r}_{ij}-\hat{r}_j\cos\alpha}{r_j\sin\alpha}$$

$$\vec{b}_j = \frac{\hat{r}_{ij}\cos\alpha-\hat{r}_j}{r_{ij}\sin\alpha} \qquad (5.2.14)$$

$$\vec{c}_j = \frac{r_j(\hat{r}_j-\hat{r}_{ij}\cos\alpha) + r_{ij}(\hat{r}_j\cos\alpha-\hat{r}_{ij})}{r_j r_{ij}}$$

It is important to note that the vectors $\vec{a}_j$, $\vec{b}_j$ and $\vec{c}_j$ are functions only of the equilibrium geometry of the three atom system. An expression of this type also exists for $\Delta\beta$, the deviation in the scattering angle about atom i, in which

$$\vec{a}_i = -\frac{\hat{r}_{ij}-\hat{r}_j\cos\beta}{r_j\sin\beta}$$

$$\vec{b}_i = \frac{r_i(\hat{r}_i+\hat{r}_{ij}\cos\beta) + r_{ij}(\hat{r}_{ij}+\hat{r}_i\cos\beta)}{r_i r_{ij}\sin\beta} \qquad (5.2.15)$$

$$\vec{c}_i = -\frac{\hat{r}_i+\hat{r}_{ij}\cos\beta}{r_{ij}\sin\beta}$$

5.3 EXAFS Modification Factors

Our discussion of the significance of the four factors present in each EXAFS component is now complete. These factors represent the possible ways in which thermal vibrations may modify EXAFS spectra. With the above information in hand we may write out in detail an expression for the EXAFS due to the instantaneous configuration shown in Fig. 1. To obtain the experimentally observed EXAFS, however, we must perform an ensemble average of this expression over the canonical ensemble defined by the Hamiltonian of the three-atom system. Retaining only the lowest order terms in the angular displacement, this average may be written as:

$$\langle\chi(k,\hat{e})\rangle = \chi_S^o \langle e^{2ik\hat{r}_g\cdot(\vec{u}_g - \vec{u}_o)}\rangle + 2\chi_D^o \langle e^{ik[\hat{r}_j\cdot(\vec{u}_j - \vec{u}_o) + \hat{r}_{ij}\cdot(\vec{u}_i - \vec{u}_j)]}$$

$$\times e^{ik[\hat{r}_i\cdot(\vec{u}_i - \vec{u}_o)]}\rangle + \chi_T^o \langle e^{2ik[\hat{r}_j\cdot(\vec{u}_j - \vec{u}_o) + \hat{r}_{ij}\cdot(\vec{u}_i - \vec{u}_j)]}\rangle$$

$$- \frac{6(\hat{r}_j\cdot\hat{e})(\hat{r}_i\cdot\hat{e})}{kr_ir_jr_{ij}} \mathrm{Im}\left\{ f_i(\beta,k)\left(\frac{\partial f_j(\alpha',k)}{\partial\alpha'}\right)_\alpha e^{ik(r_j + r_{ij} + r_i)} e^{2i\delta_1}\right.$$

$$\left.\times \langle\Delta\alpha\, e^{ik[\hat{r}_j\cdot(\vec{u}_j - \vec{u}_o) + \hat{r}_{ij}\cdot(\vec{u}_i - \vec{u}_j) + \hat{r}_i\cdot(\vec{u}_i - \vec{u}_j)]}\rangle\right\} \qquad (5.3.1)$$

$$- \frac{6(\hat{r}_j\cdot\hat{e})(\hat{r}_i\cdot\hat{e})}{kr_ir_jr_{ij}} \mathrm{Im}\left\{ f_j(\alpha,k)\left(\frac{\partial f_i(\beta',k)}{\partial\beta'}\right)_\beta e^{ik(r_j + r_{ij} + r_i)} e^{2i\delta_1}\right.$$

$$\left.\times \langle\Delta\beta\, e^{ik[\hat{r}_j\cdot(\vec{u}_j - \vec{u}_o) + \hat{r}_{ij}\cdot(\vec{u}_i - \vec{u}_j) + \hat{r}_i\cdot(\vec{u}_i - \vec{u}_j)]}\rangle\right\}$$

$$- \frac{6(\hat{r}_j \cdot \hat{e})^2}{k r_j^2 r_{ij}^2} \; \mathrm{Im} \left\{ f_i(\pi,k) \; f_j(\alpha,k) \left(\frac{\partial f_j(\alpha' k)}{\partial \alpha'} \right)_\alpha \; e^{2ik(r_j + r_{ij})} \right. \tag{5.3.1}$$

$$\left. \times \, e^{2i\delta_1} \, \langle \Delta\alpha \; e^{2ik[\hat{r}_j \cdot (\vec{u}_j - \vec{u}_o) + \hat{r}_{ij} \cdot (\vec{u}_i - \vec{u}_j)]} \rangle \right\}$$

where the brackets <...> denote the ensemble or thermal average of the quantity enclosed. The first three terms in Eq. (5.3.1) above correspond to the case in which the only contribution to the Debye-Waller factor is due to changes in the interatomic distances. Note that these terms are described by the usual type of Debye-Waller factor in which the EXAFS expression in the absence of vibrations is multiplied by a damping term to account for the effects of thermal vibrations. These terms have been discussed previously in Chapter IV and they will not be discussed further in this present work. The remaining terms represent the combined effect of changes in both angles and distances. These variations are strongly correlated and this fact must be taken into account when the appropriate thermal averages are performed. Note that these latter terms involve only the double and triple scattering EXAFS components. Since these terms must be added to the damped EXAFS expression defined by the first three terms in Eq. (5.3.1) it is inappropriate to refer to these terms as Debye-Waller factors. For the purpose of the present discussion, we

shall call such terms modification factors, since each has a modified amplitude and phase when compared to the corresponding term in the damped EXAFS expression. An amplitude modification occurs due to the presence, in each of these factors, of a derivative of the scattering amplitude together with an angular variation term in the thermal average. The phase of each factor is modified because the phase of a derivative of the scattering amplitude may be different from the phase of the amplitude itself.

We shall now focus attention on the thermal averages which occur within each modification factor. To explicitly calculate such averages, it is necessary to know the potential energy surface governing the motion of the three atom system. Throughout this work the harmonic or quadratic approximation is assumed. This approximation consists of expanding the potential energy in a Taylor series about its equilibrium value and truncating the expansion after the first non-zero term. This is consistent with our expansion of the scattering amplitudes about the equilibrium scattering angle in which only the first order term was retained. Each of these approximations is then strictly valid only for small departures from equilibrium. Therefore, it is possible to approximate Eq. (5.2.14) by:

$$\Delta\alpha = 1/2i \left[\exp\{i(\vec{a}_j.\vec{u}_o+\vec{b}_j.\vec{u}_i+\vec{c}_j.\vec{u}_j)\} - \exp\{-i(\vec{a}_j.\vec{u}_o+\vec{b}_j.\vec{u}_i+\vec{c}_j.\vec{u}_j)\}\right] \qquad (5.3.2)$$

A similar expression may be obtained for $\Delta\beta$.

Since the form of the potential energy surface is harmonic it is convenient to express the displacement vectors in terms of the normal coordinates Q_n (n = 1,...,3N)

$$\vec{u}_j = \sum_n \vec{e}_j^n \, Q_n \qquad (5.3.3)$$

where N is the number of atoms in the system and $\vec{e}_j^n$ is the amplitude vector of the j^{th} atom in the n^{th} normal mode. The properties and advantages of this coordinate system have been discussed in Chapter IV. In the case of our three atom system there is a total of nine degrees of freedom so that the sum over n above extends to three terms for non-linear systems and four terms for linear systems. The remaining terms represent translation and rotation of the system as a whole and do not contribute to the EXAFS. For harmonic systems it may be shown that[9]

$$\langle \exp[if(n)Q_n] \rangle = \exp-\{1/2[f(n)]^2\langle Q_n^2 \rangle\} \qquad (5.2.4)$$

where f(n) is the some function of the normal mode n and $\langle Q_n^2 \rangle$ is the mean-square amplitude of vibration in the n^{th} normal mode. Furthermore, $\langle Q_n^2 \rangle$ may be written as:[10]

$$\langle Q_n^2 \rangle = (\hbar/2\omega_n) \coth(\hbar\omega_n/2k_BT) \qquad (5.3.5)$$

where ω_n is the frequency of the n^{th} normal mode and k_B is Boltzmann's constant.

The explicit form of the thermal averages may now be determined. For convenience of notation let us define $\langle \Delta\alpha \rangle_D$

to be the thermal average that occurs within the double scattering modification factor in which the angle α changes by $\Delta\alpha$. Substituting Eq. (5.3.3) into Eq. (5.3.2) and then into the appropriate term in Eq. (5.3.1) an expression for $\langle\Delta\alpha\rangle_D$ is obtained:

$$\langle\Delta\alpha\rangle_D = \frac{1}{2i}\left\langle e^{ik\sum_n[(\mu^n_{jo}+\mu^n_{ij}+\mu^n_{io})+\frac{1}{k}(\rho^n_{jo}+\rho^n_{ji}+\rho^n_{jj})]}\right\rangle Q_{n>}$$
$$-\frac{1}{2i}\left\langle e^{ik\sum_n[(\mu^n_{jo}+\mu^n_{ij}+\mu^n_{io})-\frac{1}{k}(\rho^n_{jo}+\rho^n_{ji}+\rho^n_{jj})]}\right\rangle Q_{n>} \qquad (5.3.6)$$

In the preceding equation, $\mu^n_{ij} = \hat{r}_{ij}\cdot(\vec{e}^n_i - \vec{e}^n_j)$ and represents the maximum effective change in the distance along the internuclear axis between atoms i and j in the n^{th} normal mode. The contribution to the change in the scattering angle at atom i due to the displacement of atom j in the n^{th} normal mode is given by $\rho^n_{ij} = \vec{c}_i\cdot\vec{e}^n_j$. A similar interpretation applies to the remaining terms of these types. Note that each of the two terms in Eq. (5.3.6) contains a summation in the exponent which may be replaced by a product of exponential terms. This product extends over all of the normal modes of the system. Since there is no correlation between the individual normal modes the average of each product is just the product of the averages. Using Eq. (5.3.4) we can determine the thermal average associated with each normal mode in Eq. (5.3.6), calculate the product of these averages and thus determine $\langle\Delta\alpha\rangle_D$.

$$\langle \Delta\alpha \rangle_D = ie^{-\frac{1}{2}k^2 \sum_n (\mu^n_{jo} + \mu^n_{ij} + \mu^n_{io})^2 \langle Q_n^2 \rangle} \times e^{-\frac{1}{2}\sum_n (\rho^n_{jo} + \rho^n_{ji} + \rho^n_{jj})^2 \langle Q_n^2 \rangle} \times \sinh\left[k \sum_n (\mu^n_{jo} + \mu^n_{ij} + \mu^n_{io})(\rho^n_{jo} + \rho^n_{ji} + \rho^n_{jj}) \langle Q_n^2 \rangle\right] \quad (5.3.7)$$

The remaining thermal averages, $\langle \Delta\beta \rangle_D$ and $\langle \Delta\alpha \rangle_T$, may be determined in a similar fashion.

Several features of this equation deserve comment. Equation (5.3.7) has been written in a manner which emphasizes the individual contributions to the thermal average due to changes in bond lengths and scattering angles. Note that the magnitude of the exponential damping term, which involves a change in scattering angle, is not dependent on the energy of the photoelectron. The physical reason for this is due to the fact that EXAFS involves the scattering of spherical waves, so that when the scattering angle varies the atoms are constrained to move along an arc of a spherical wavefront. Therefore, no dependence is expected on the wavelength of the photoelectron. In constrast, however, the motion of the atoms described by Debye-Waller type factors involve large displacements normal to the wavefront. Accordingly, such factors have a severe dependence on the wavelength of the photoelectron.

The hyperbolic sine term represents the fact that there is a correlation between a change in bond length and a change in scattering angle. Note also that the thermal

average is a pure imaginary quantity; this has the effect of shifting the phase of the EXAFS oscillations due to the modification factors by $\pi/2$. Therefore, the sine wave oscillations of the original EXAFS take the form of a cosine wave in the modification factors.

It is now possible to write down a complete expression for the averaged modification factors in Eq. (5.3.1)

$$
\begin{aligned}
\langle \chi_M(k,\hat{e}) \rangle = {} & \frac{-6(\hat{r}_j \cdot \hat{e})(\hat{r}_i \cdot \hat{e})}{k r_i r_j r_{ij}} \; e^{-\frac{1}{2}k^2 \sum_n (\mu_{jo}^n + \mu_{ij}^n + \mu_{io}^n)^2 \langle Q_n^2 \rangle} \\
& \times e^{-\frac{1}{2}\sum_n (\rho_{jo}^n + \rho_{ji}^n + \rho_{jj}^n)^2 \langle Q_n^2 \rangle} \\
& \times \sinh\left[k \sum_n (\mu_{jo}^n + \mu_{ij}^n + \mu_{ij}^n)(\rho_{jo}^n + \rho_{ji}^n + \rho_{jj}^n) \langle Q_n^2 \rangle\right] \\
& \times \mathrm{Re}\left\{ f_i(\beta,k) \left(\frac{\partial f_j(\alpha',k)}{\partial \alpha'} \right)_\alpha e^{ik(r_j + r_{ij} + r_i)} e^{2i\delta_1} \right\} \\
& \\
& \frac{-6(\hat{r}_j \cdot \hat{e})(\hat{r}_i \cdot \hat{e})}{k r_i r_j r_{ij}} \; e^{-\frac{1}{2}k^2 \sum_n (\mu_{jo}^n + \mu_{ij}^n + \mu_{io}^n)^2 \langle Q_n^2 \rangle} \\
& \times e^{-\frac{1}{2}\sum_n (\rho_{io}^n + \rho_{ii}^n + \rho_{ij}^n)^2 \langle Q_n^2 \rangle} \\
& \times \sinh\left[2k \sum_n (\mu_{jo}^n + \mu_{ij}^n)(\rho_{jo}^n + \rho_{ji}^n + \rho_{jj}^n) \langle Q_n^2 \rangle\right] \\
& \times \mathrm{Re}\left\{ f_i(\pi,k) f_j(\alpha,k) \left(\frac{\partial f_j(\alpha',k)}{\partial \alpha'} \right)_\alpha e^{2ik(r_j + r_{ij})} e^{2i\delta_1} \right\} \\
& \\
& \frac{-6(\hat{r}_j \cdot \hat{e})^2}{k r_j^2 r_{ij}^2} \; e^{-2k^2 \sum_n (\mu_{jo}^n + \mu_{ij}^n)^2 \langle Q_n^2 \rangle} \\
& \times e^{-\frac{1}{2}\sum_n (\rho_{jo}^n + \rho_{ji}^n + \rho_{jj}^n)^2 \langle Q_n^2 \rangle} \\
& \times \sinh\left[k \sum_n (\mu_{jo}^n + \mu_{ij}^n + \mu_{io}^n)(\rho_{io}^n + \rho_{ii}^n + \rho_{ij}^n) \langle Q_n^2 \rangle\right] \\
& \times \mathrm{Re}\left\{ f_j(\alpha,k) \left(\frac{\partial f_i(\beta',k)}{\partial \beta'} \right)_\beta e^{ik(r_j + r_{ij} + r_i)} e^{2i\delta_1} \right\}
\end{aligned}
\tag{5.3.8}
$$

The subscript M refers to that fact that Eq. (5.3.8) represents only the modified portion of the total EXAFS expression given in Eq. (5.3.1) for a general three-atom system of C_S symmetry.

5.4 Application to Model Systems

A series of model systems will be considered to determine the contribution of the modification factors in Eq. (5.3.8) to the observed EXAFS. To illustrate the symmetry properties of these factors, let us consider a three-atom system which is symmetric and bent with a bridging angle $\theta = \pi - \alpha$. A plane of symmetry of the molecule passes through atom j such that the central atom (o) and the second nearest-neighbor (i) are of the same type. This system then belongs to the C_{2v} point group and the normal modes of vibration transform as:

$$\Gamma_{vib} = 2A_1 + B_1 \qquad (5.4.1)$$

The two totally symmetric A_1 modes correspond to a symmetric stretching and bending mode of vibration. The single B_1 mode is associated with the asymmetric stretch. A schematic representation of the normal modes of the three-atom system is shown in Fig. 3.

The symmetry of the system allows us to simplify the modification factors in Eq. (5.3.8). All modes in a C_{2v} point group are subject to the following conditions:

For all modes in a C_{2v} point group:

$$m_o = m_i = m$$
$$|\vec{e}_o^n| = |\vec{e}_i^n| \qquad (5.4.2)$$

where m_o and m_i are the masses of the central atom and neighboring atom i, respectively. The symmetry properties of the terms μ_{ij}^n have been discussed fully in Chapter IV. In this present work we shall only consider the additional symmetry properties due to the terms ρ_{ij}^n. The properties of these latter terms, however, depend on the symmetry properties of the vectors $\vec{a}$, $\vec{b}$ and $\vec{c}$ in Eqs. (5.2.14) and (5.2.15). Note that for any system

$$\vec{a}_t + \vec{b}_t + \vec{c}_t = 0 \qquad t=i,j \qquad (5.4.3)$$

which represents the requirement that the center of mass is fixed during a pure vibration. The symmetry properties of ρ_{ij}^n are also dependent on the normal mode in question and the atom at which the scattering angles varies.

We shall consider first the case in which the angular variation occurs at atom j. For a symmetric system of the type being discussed, Fig. 4 shows that $\vec{c}_j$ bisects the bridging angle θ in all normal modes. Furthermore, $\vec{a}_j$ and $\vec{b}_j$ are equal in magnitude and the angle between them is also bisected by $\vec{c}_j$. Therefore, all A_1 type modes satisfy the following conditions (see Fig. 3):

$$\vec{a}_j \cdot \vec{e}_o^{A_1} = \vec{b}_j \cdot \vec{e}_i^{A_1}$$

or

$$\rho_{jo}^{A_1} = \rho_{ji}^{A_1}$$

A_1 modes: (5.4.4)

$$\vec{c}_j \cdot \vec{e}_j^{A_1} = \pm |c_j| \, |\vec{e}_j^{A_1}| = \rho_{jj}^{A_1}$$

The first part of Eq. (5.4.4) expresses the fact that displacement of atom i and the central atom in an A_1 mode produce the same change in the scattering angle at atom j. The sign of the second part of this equation is determined by whether the mode is a bend or a stretch. In the single B_1 mode, however, the contribution to the change in angle α due to the displacements of the central atom and atom i, cancel exactly. In addition, $\vec{c}_j$ is perpendicular to $\vec{e}_j^{B_1}$ so that the following conditions must be satisfied:

$$\rho_{jo}^{B_1} = - \rho_{ji}^{B_1}$$

B_1 mode: (5.5.5)

$$\vec{c}_j \cdot \vec{e}_j^{B_1} = \rho_{jj}^{B_1} = 0$$

Thus the B_1 mode does not contribute to a change in the scattering angle α.

No symmetry arguments may be applied to the modification factor which involves a change in the scattering angle β. This is because no symmetry element, other than the plane of the system, maps atom i onto itself. To determine this modification factor it is necessary to explicitly calculate all of the terms shown in Eq. (5.3.8).

There are essentially two separate calculations necessary to determine the modification factors in Eq.

(5.3.8). The first involves a calculation of the exponential and hyperbolic sine terms and requires a full normal mode analysis of the system. The details, and the manner in which such an analysis may be performed has been discussed in Chapter IV. The second calculation requires a determination of the contribution of the scattering amplitude to the amplitude and phase of the modification factors. This latter calculation requires a knowledge of the modulus and phase of the scattering amplitudes as a function of scattering angle and wavenumber k. Assuming a plane wave approximation the scattering amplitude may be written as:

$$f_j(\alpha,k) = F_j(\alpha,k)\ e^{i\phi(\alpha,k)} \tag{5.4.6}$$

where $F_j(\alpha,k)$ is the modulus of the scattering amplitude and $\phi(\alpha,k)$ is the phase of the amplitude. This approximation is valid for large bond distances or small scattering atoms. The derivatives in Eq. (5.3.8) now take the form:

$$\left(\frac{\partial f_j(\alpha',k)}{\partial\alpha'}\right)_\alpha = e^{i\phi(\alpha,k)} \left(\frac{F_j(\alpha',k)}{\partial\alpha'}\right)_\alpha + F_j(\alpha,k) \left(\frac{\partial e^{i\phi(\alpha',k)}}{\partial\alpha'}\right)_\alpha \tag{5.4.7}$$

Values of the modulus and phase of the scattering amplitude as a function of scattering angle have been reported only for carbon and oxygen atoms.[11] Since we are concerned with bridged systems in which the central atom and atom i are

heavy atoms we have insufficient information to calculate the modification factors in Eq. (5.3.8). However, Teo[5] has shown that the scattering amplitude at atom i may be approximated by:

$$f_i(\beta,k) \approx f_i(\pi,k) \qquad 120^o \leq \beta \leq 180^o \qquad (5.4.8)$$

which includes the angular range in which multiple scattering is most likely to be important. In this approximation, the rate of change of the scattering amplitude at atom i with respect to the scattering angle β is zero. Therefore, the modification factor involving a change in this angle β is also zero. Equation (5.3.8) then reduces to two terms corresponding to the double and triple scattering modification factors in which angle α changes by $\Delta\alpha$. In the case of heavy elements, structure tends to be developed in the angular range of Eq. (5.4.8) making the validity of this approximation questionable.[5] Despite this, we shall assume Eq. (5.4.8) to be valid since no information exists on the angular dependence of the scattering amplitudes for such elements.

The model system to be studied is Br_2O, which we shall consider to be representative of oxygen bridged systems. We shall assume that the symmetric stretch and bend occur at 250 cm^{-1} and 245 cm^{-1} in the linear system while the asymmetric stretch occurs at 800 cm^{-1}. The normal frequencies of the linear bridged system are then used to generate a set of force constants as described in Chapter

IV. These force constants are assumed to be independent of the geometry of the molecule and are used to calculate the normal frequencies at any bridging angle θ. This assumption is least valid for a description of the bending mode of vibration. The frequencies chosen above are typical of those found in linear oxygen bridged systems.[12]

The calculated frequency of each of the normal modes as a function of bridging angle is shown in Fig. 5. The angular-depersion of the normal frequencies agrees well with earlier calculations and observations of oxygen bridged systems.[12] The calculated Debye-Waller factors and angle-related amplitude factors are shown in Figs. 6 and 7, respectively. The modulus and phase of the scattering amplitudes together with their derivatives are shown in Figs. 8 and 9. Finally, Figs. 10 and 11 illustrate the angle and temperature dependence of the amplitude of the EXAFS corresponding to each scattering path including the associated modification factors.

5.5 Discussion

We have presented a general description of the effect of thermal vibrations on Extended X-Ray Absorption Fine Structure. The formalism developed is general and may be applied to any scattering problem in which there exists a correlation between a change in distance and a change in scattering angle. An expression was obtained for the EXAFS in a general three-atom system of C_S symmetry. Variations in the scattering angle were shown to give rise to additional

EXAFS terms which we called modification factors. The form of these modification factors was shown to be dependent on the geometry and symmetry of the system. The formalism, in its present form, is readily applicable to multiple scattering events involving more than three atoms. Systems of other than C_{2v} symmetry may be considered by determining the symmetry properties of the Debye-Waller and modification factors subject to the point group in question.

The Debye-Waller factors which reflect the damping of the EXAFS amplitude due to thermally induced changes in the internuclear distances of the system are shown in Fig. 6. The double scattering factor in Fig. 6 has been divided by four such that the Debye-Waller factors associated with each scattering path has the standard form $\exp(-2k^2\sigma^2)$ [see Eq. (5.3.8)]. It is important to note that there are two quantities which determine the contribution of a given normal mode to the Debye-Waller factor for a particular scattering path. The frequency of the normal mode determines the mean-square amplitude of vibration in accordance with Eq. (5.3.5). In addition, the amplitude and direction of the displacement vectors of the atoms in a given normal mode determine the projection of these vectors along the internuclear axes. From Fig. 6(a) it may be seen that the Debye-Waller factors associated with each scattering path increases as the bridging angle decreases. This increase can, in part, be attributed to a decrease in the frequency of the bending mode at these angles. The

three scattering paths involving the second shell atom, however, show different degrees of sensitivity to the A_1 bend. The triple scattering path is the least sensitive since a change in the bridging angle does not appreciably change the length of the scattering path. The second shell single scattering path, however, is very sensitive to this bending mode since it induces a large change in the bromine-bromine distance. The double scattering path, on the other hand, is sensitive to both A_1 type modes. At low bridging angles the A_1 bend dominates primarily due to the low frequency of this mode when compared to the A_1 stretch at these angles. As the system approaches linearity the frequencies of both A_1 modes become comparable but the displacement vectors in the bending mode tend to become orthogonal to the internuclear axes. In such instances, the A_1 stretch dominates the double scattering Debye-Waller factor.

The temperature dependence of the double and triple scattering Debye-Waller factors is shown in Fig. 6(b). The second shell single scattering factor [which is not shown in Fig. 6(b)] has the most severe temperature dependence due to the large contribution of the bending mode to this Debye-Waller factor. As described in the previous chapter, the double and triple scattering factors are equal in magnitude at all temperatures when the bridging angle is 180°. At high temperatures and low bridging angles the double scattering factor is dominant. This occurs because the

double scattering factor receives a large contribution from the A_1 bend which is a low frequency mode at these small angles. The triple scattering factor, however, is dominated by the higher frequency stretching mode. As the bridging angle increases the double scattering Debye-Waller factors, like the triple scattering factor, becomes dominated by the stretching mode such that both factors exhibit the same temperature dependence in the limiting case of a linear system.

The hyperbolic sine terms reflect the degree of correlation that exists between a change in scattering path-length and a change in scattering angle. Fig. 7(a) shows both the double and triple scattering hyperbolic sine terms together with the angular damping factor which is the exponent of the exponential term which represents the damping of the EXAFS due solely to a change in scattering angle. As described in the previous section, we shall only consider changes in the scattering angle α. Note that both the hyperbolic sine terms and the exponential damping term are dependent on the bond distance r_j. The magnitude of the hyperbolic sine terms is inversely proportional to the bond distance [see Eq. (5.3.14)]. The angular damping factor varies inversely as the bond distance squared. Throughout the present discussion a bond distance of 2.0 Å is assumed. Since the magnitude of each hyperbolic sine term may be approximated by its arguments at these angles, the effect of a change in bond distance may be readily calculated. Note

also that the argument of the hyperbolic sine terms increase linearly with k while the angular damping factor is independent of k.

An understanding of the functional form of the hyperbolic sine terms requires a knowledge of the degree of correlation that exists, within each normal mode, between a change in distance and a change in scattering angle. On the basis of qualitative considerations we may conclude that a positive correlation exist in the A_1 stretching mode; that is, an increase in the scattering path length is accompanied by an increase in the scattering angle α (see Fig. 3). In the A_1 bend mode a negative correlation exists whereby an increase in the path length results in a decrease in the scattering angle α. Both of these conclusions are confirmed by a rigorous normal mode anlaysis. Since the A_1 bend contributes significantly to the double scattering Debye-Waller factor, the total correlation due to both A_1 modes represented by the double scattering hyperbolic sine term, is negative. The triple scattering hyperbolic sine term is positive, however, due to the dominant contribution of A_1 stretch which has a positive correlation. Note that for comparison purposes both the double and triple scattering hyperbolic sine terms are shown to be positive in Fig. 7. From Fig. 7(a) it may be seen that the magnitudes of both the double and triple scattering hyperbolic sine terms decrease rapidly as the system approaches linearity. This behavior may be readily explained in terms of the normal

modes of a linear symmetric system. In this configuration the displacement vectors in the stretching mode produce no change in the scattering angle α. The displacement vectors of the atoms in the bending mode, however, produce a large change in α, but there is no change in distance as these vectors are orthogonal to the molecular axis. Therefore, both the double and triple hyperbolic sine terms tend to zero as the bridging angle of the system approaches 180°.

The angular damping factor increases as the three-atom system becomes less bent [see Fig. 7(a)]. As the bridging angle increases the contribution to this factor from the bending mode also increases. This occurs because the displacement vectors of the atoms in this mode tend to move increasingly perpendicular to the internuclear axes thereby inducing large changes in the scattering angle. The change in this angular damping factor as a function of angle is slow since the frequency of the bending mode increases as the bridging angle increases.

The temperature dependence of the double and triple scattering hyperbolic sine terms together with the angular damping factor is shown in Fig. 7(b)-(d). Note that the magnitude of the triple scattering hyperbolic sine term decreases with increasing temperature. The negative correlation due to the A_1 bend increases as the temperature rises thereby increasing the contribution of this mode to the hyperbolic sine terms. The contribution of the stretching mode also increases, but less sharply since the

frequency of the stretch is greater than that of the bend. Since the total correlation of the triple scattering path is positive an increase in temperature only serves to reduce the magnitude of the corresponding hyperbolic sine term. The opposite, of course, is true in the case of the double scattering term where the existing negative correlation is further enforced by an increase in temperature.

The modulus and phase of the scattering amplitude for oxygen as a function of scattering angle and k are shown in Fig. 8 and Fig. 9. All calculations in these figures are based on the reported values of the amplitude and phase.[10] A detailed description of these functions has been given by Teo.[5]

Figure 8(a) shows the modulus of the scattering amplitude for oxygen as a function of scattering angle for a series of k values. In this angular range, the modulus is well described by the Born amplitude for the scattering of fast electrons off atoms. The modulus in the forward direction is independent of k and becomes increasingly peaked in this direction at higher k values. Outside this angular range, however, the modulus tends to develop complex structure which is related to the sampling of the oxygen core by the photoelectron. Figures 8(c) and (d) show the derivative of the modulus with respect to scattering angle as a function of k and scattering angle. Since the the modulus has a local maximum at $\alpha = 0^{o}$ [see Fig. 8(a)] the derivative is zero at this angle for all energies. Note

that the sign of the derivative is negative while the derivative itself peaks at increasingly smaller scattering angles as the photoelectron wavenumber increases.

The phase of the scattering amplitude for oxygen as a function of k and a series of scattering angles is shown in Fig. 9(a). The derivative of the phase with respect to scattering angle as a function of scattering angle and k are are shown in Fig. 9(b) and (c), respectively. The sign of the derivative is positive at all scattering angles. The magnitude of the derivative is small in the near forward scattering direction but becomes appreciable at larger scattering angles and shows complex structures as a function of k and scattering angle. The peaks which occur in the derivative of the phase occur at smaller scattering angles as the photoelectron wavenumber increases. In addition, subsidiary maxima occur at larger scattering angles, the number of such maxima increases at higher k values.

Before discussing the contribution to the observed EXAFS due to the various amplitude terms described above, we must consider the effect these terms have on the phase of the EXAFS oscillations. As described in the previous section [see Eq. (5.3.7)] the phase of the oscillations in the modification factors is shifted by $\pi/2$ when compared to the oscillations of the original EXAFS. From Eq. (5.4.7) the derivative of the scattering amplitude in each modification factor may be written as:

$$\left(\frac{\partial f_j(\alpha',k)}{\partial \alpha'}\right)_\alpha = e^{i\phi(\alpha,k)} \left(\frac{\partial F_j(\alpha',k)}{\partial \alpha'}\right)_\alpha + iF_j(\alpha,k)\, e^{i\phi(\alpha,k)} \left(\frac{\partial \phi(\alpha',k)}{\partial \alpha'}\right)_\alpha \tag{5.5.1}$$

The first term on the right-hand side of Eq. (5.5.1) yields EXAFS oscillations that are shifted $\pi/2$ from the original. We shall refer to such terms as type I modification factors. The remaining term on the right-hand side gives rise to EXAFS oscillations that are π out of phase with the original and are called type II modification factors. Note that these latter factors serve to directly reduce the amplitude of the associated original EXAFS oscillations.

The amplitudes of the EXAFS oscillations for each scattering path, including the associated modification factors, are shown in Figs. 10 and 11. The amplitudes are calculated at three bridging angles and two temperatures. The parameterizations of Teo *et al.*[13] and Lee *et al.*[14] were used to describe modulus and phase of the backscattering amplitude for bromine. No damping terms reflecting the finite mean-free path of the photoelectron have been included in these calculations. Since the double scattering hyperbolic sine term is negative, and the derivative of the amplitude is also negative, the double scattering type I modification factor remains $\pi/2$ out of phase with respect to original double scattering EXAFS oscillations [see Eq. (5.3.8) and (5.5.1)]. However, since the derivative of the phase is positive the double scattering type II modification

factor is exactly in phase with the original double scattering EXAFS oscillations. The triple scattering modification factors have exactly the opposite behavior since the associated hyperbolic sine term is always positive. Thus the triple scattering type I modification factor is $3\pi/2$ out of phase while the type II factor is exactly out of phase with the original triple scattering EXAFS oscillations.

Figure 10 shows that the amplitude of the second shell single scattering EXAFS component increases gradually as the bridging angle increases. This increase is more pronounced at high k values and reflects the angular dependence of the Debye-Waller factor for this scattering path [see Fig. 6(a)]. The amplitudes of the double and triple scattering EXAFS components show a more dramatic increase with bridging angle and reflect a decrease in the Debye-Waller factor for these scattering paths together with an increased amplitude for scattering through small angles [see Fig. 8(a)]. At sufficiently large bridging angles the amplitudes of the double and triple scattering paths surpass that of the single scattering path.

The amplitudes of the modification factors are also shown in Fig. 10. The detailed structure observed in these factors may be attributed to the complex structures present in the amplitude and phase and their derivatives. The triple scattering modification factors increase in magnitude as the bridging angle increases due to the presence of the

oxygen scattering amplitude which is absent in the corresponding double scattering factors [see Eq.(5.3.8)]. Furthermore, the triple scattering hyperbolic sine term falls off more gradually than the double scattering term as the bridging angles increase [see Fig. 7(a)]. In general, the magnitude of each modification factor is substantially smaller than that of the original damped EXAFS. When the bridging angle is 180^{o} the amplitude of each modification factor is zero since both the correlation terms and the derivative of the scattering amplitude are zero at this angle.

A comparison of Figs. 10 and 11 reveals the temperature dependence of the EXAFS amplitude factors. Note that the magnitude of the second shell single scattering component is greatly diminished at higher temperatures. This is due primarily to the large dependence of this scattering path on the low frequency bending mode of vibration. The magnitude of the double and triple scattering components exhibit a less severe temperature dependence. The double and triple scattering modification factors show different temperature dependences. Both double scattering modification factors increase with temperature while the triple scattering factors decrease. As described earlier, the double scattering modification factors serve to increase the total amplitude of the double scattering EXAFS. The triple scattering modification factors, however, reduce the total triple scattering amplitude. Therefore in general, the

contribution to the total EXAFS due to the modification factors of both the double and triple scattering paths increases as the temperature increases.

Recently, Alberding and Crozier[7] introduced an integrated multiple scattering (IMS) approach to data analysis in which they explicitly considered variations in the scattering angle α. The authors, however, failed to recognize that such angular variations are a second order effect and that to lowest order only distance variations are important [see Eqs. (5.2.9) and (5.2.10)]. Furthermore, these second order terms are negligible due to the lack of correlation (particularly in the forward direction) between changes in the scattering path length and the scattering angle α. Accordingly, the physical basis for this approach is unclear. The authors[7] also introduced a mean multiple scattering (MMS) approach to the analysis of EXAFS data. The failure of this approach to yield satisfactory results was discussed earlier in Chapter IV.

In conclusion, a change in the scattering angle α, induced by thermal vibrations, produces a large change in the scattering amplitude, particularly in the near forward direction. However, the correlation that exists between such an angle change and the associated change in distance for a given scattering path is small, especially at large bridging angles. It is the degree of correlation which determines the contribution of the modification factors to the observed EXAFS. Since the degree of correlation is

small, the modification factors may be neglected in an analysis of multiple scattering EXAFS data. Accordingly, for systems of this type it is sufficient to use the multiple scattering analysis proposed by Teo[5] provided an adequate treatment is given to the Debye-Waller factors which involve a change in scattering pathlength.[8]

References

*This chapter is based on: J.J. Boland and J.D. Baldeschwieler, J. Chem. Phys. in press (1984).

1. R. de L. Kronig, Z. Phys. **80**, 317 (1931); **75**, 191 (1932).

2. D.E. Sayers, E.A. Stern and F.W. Lytle, Phys. Rev. Lett. **27**, 1204 (1974).

3. See for example, P.A. Lee, P.H. Citrin, P. Eisenberger and B.M. Kincaid, Rev. Mod. Phys. **53**, 769 (1981).

4. P.A. Lee and J.B. Pendry, Phys. Rev. **B 11**, 2795 (1975).

5. B.K. Teo, J. Am. Chem. **103**, 3990 (1981).

6. J.J. Boland, S.E. Crane and J.D. Baldeschwieler, J. Chem. Phys., **77**, 162 (1982).

7. N. Alberding and E.D. Crozier, Phys. Rev. **B 27**, 3374 (1983).

8. J.J. Boland and J. D. Baldeschwieler, J. Chem. Phys., **80**, 3005 (1984).

9. M. Born and K. Sarginson, Proc. Roy. Soc. **A 179**, 69 (1941).

10. See for example, T.L. Hill, Introduction to Statistical Thermodynamics (Addison-Wesley, Reading, 1960).

11. Supplementary material available from ref. 5.

12. R.M. Wing and K.P. Callahan, Inorg. Chem. **8**, 871 (1969);
See also K. Nakamoto, Infrared Spectra of Inorganic and Coordination Compounds, 3rd ed. (Wiley, New York, 1970).

13. B.K. Teo, P.A. Lee, A.L. Simons, P. Eisenberger and B.M. Kincaid, J. Am. Chem. **99**, 3854 (1977).

14. P.A. Lee, B.K. Teo and A.L. Simons, J. Am. Chem. **99**, 3856 (1977).

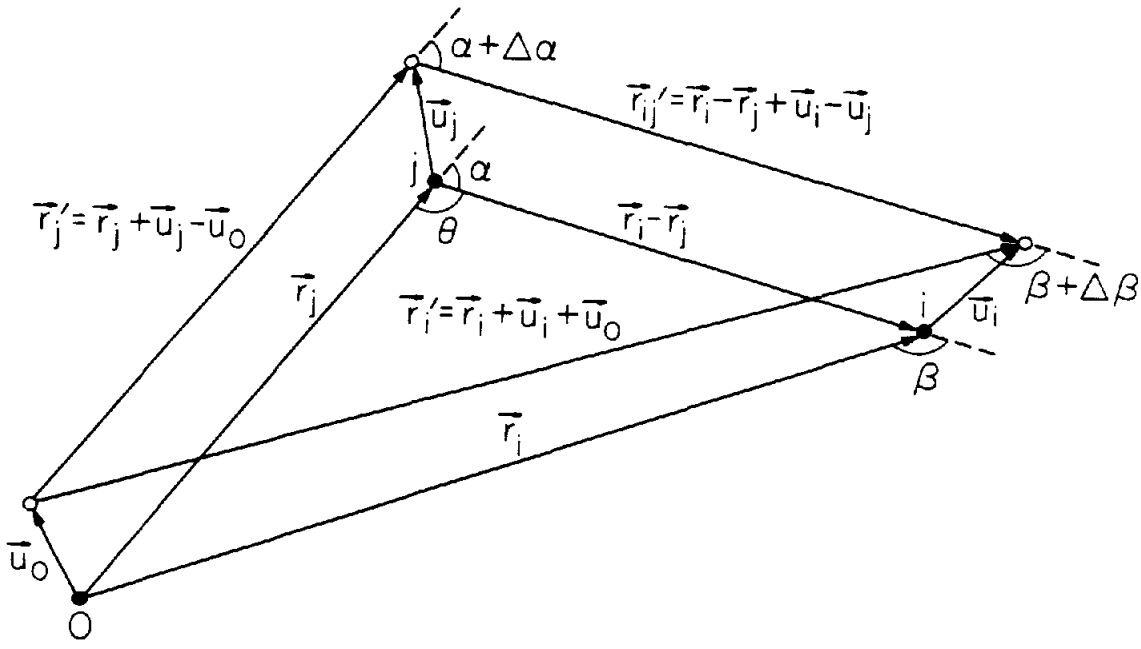

Figure 1.

The general three-atom system. The equilibrium positions of the central atom (o), first nearest-neighbor atom (j) and second nearest neighbor atom (i) are shown as filled circles. The displacement of these atoms from their respective equilibrium positions are shown as open circles. θ represents the equilibrium bridging angle. The equilibrium position of the central atom was chosen to represent the origin of the system.

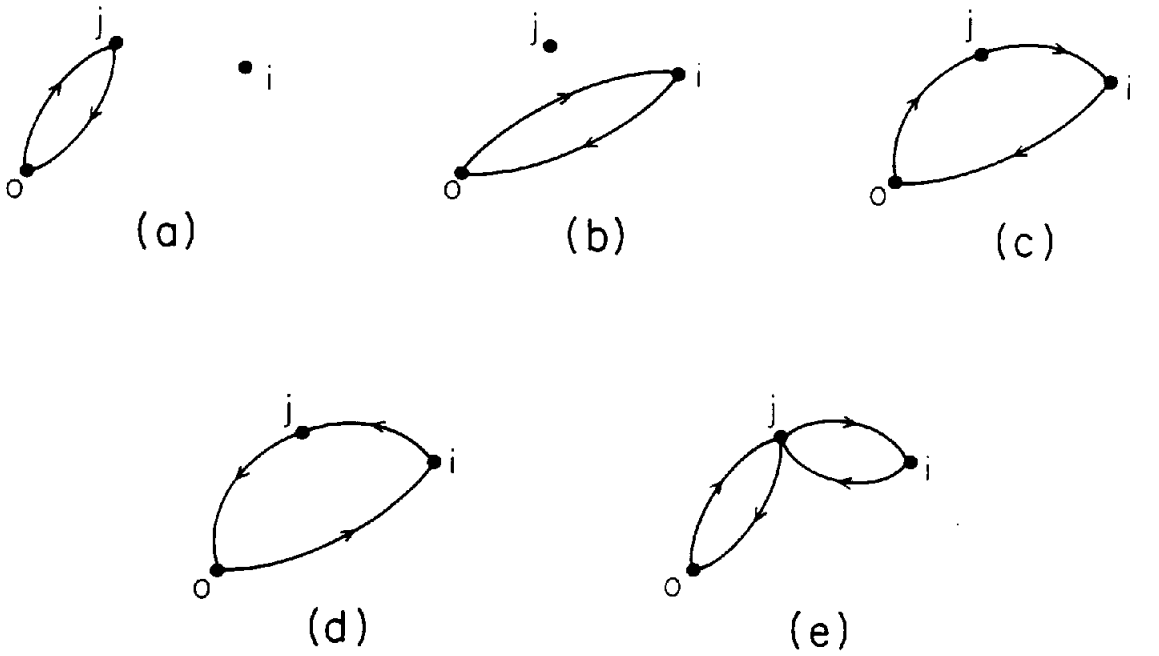

Figure 2.
The five significant scattering paths in a system of three atoms. (a) and (b) represent the single scattering paths from atoms i and j. The two double scattering paths (c) and (d) are identical by virtue of time-reversal symmetry. The triple scattering path is shown in (e).

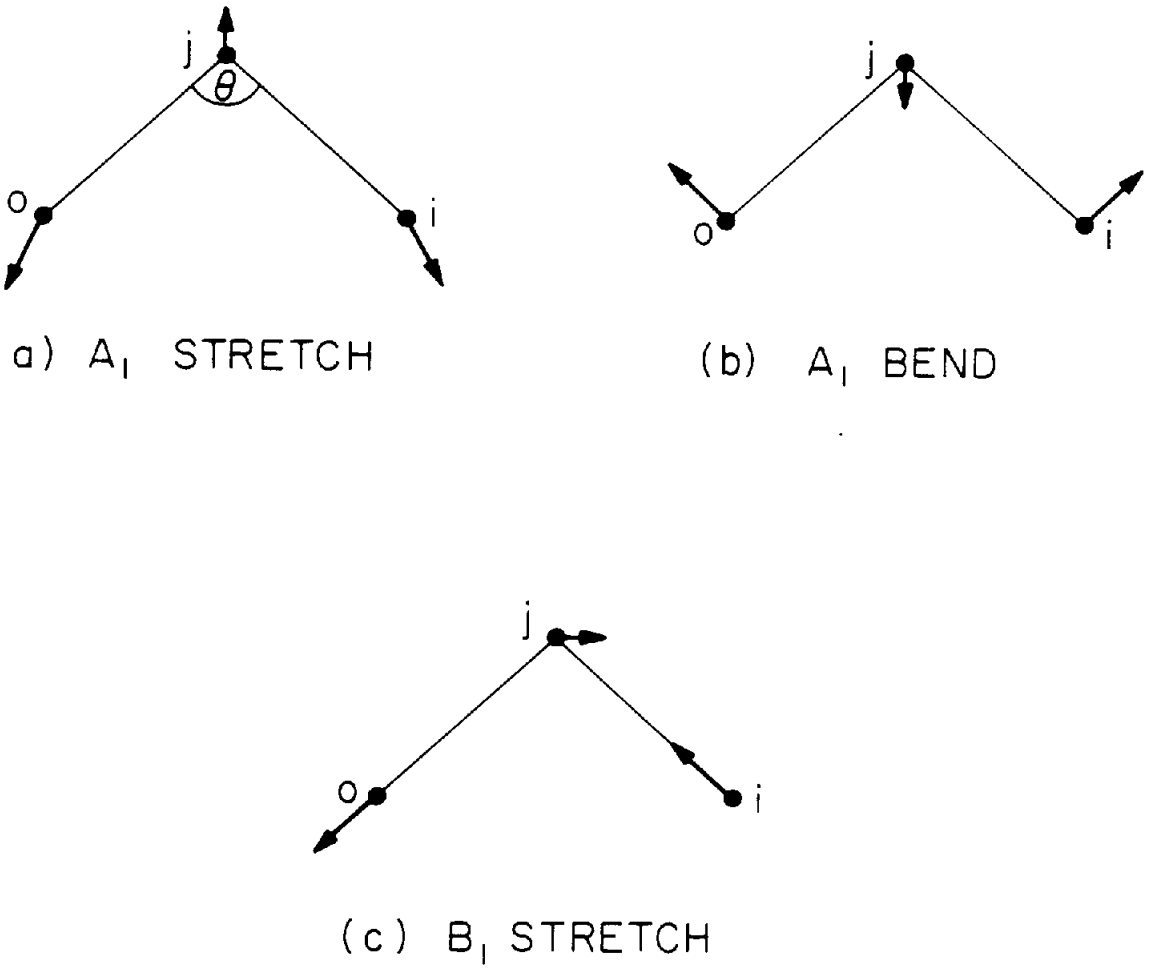

Figure 3.
Schematic of the normal modes in a three-atom system of C_{2v} symmetry. There are three normal modes, two of A_1 type symmetry and a single B_1 mode.

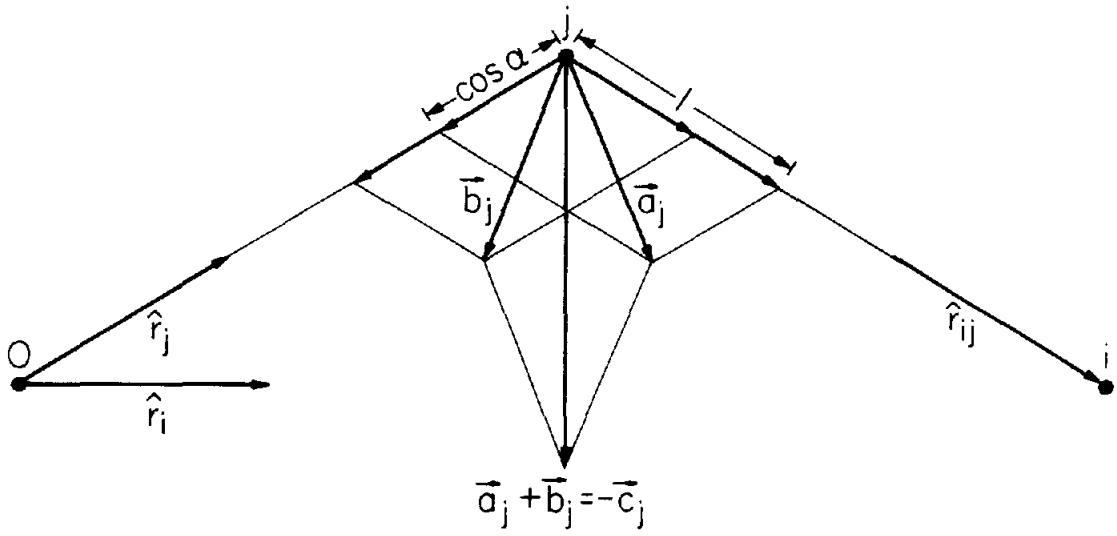

Figure 4.
Schematic representation of the vectors which determine the change in scattering angle α at atom j due to the displacement of all the atoms in a given normal mode [see Eq. (5.3.8)].

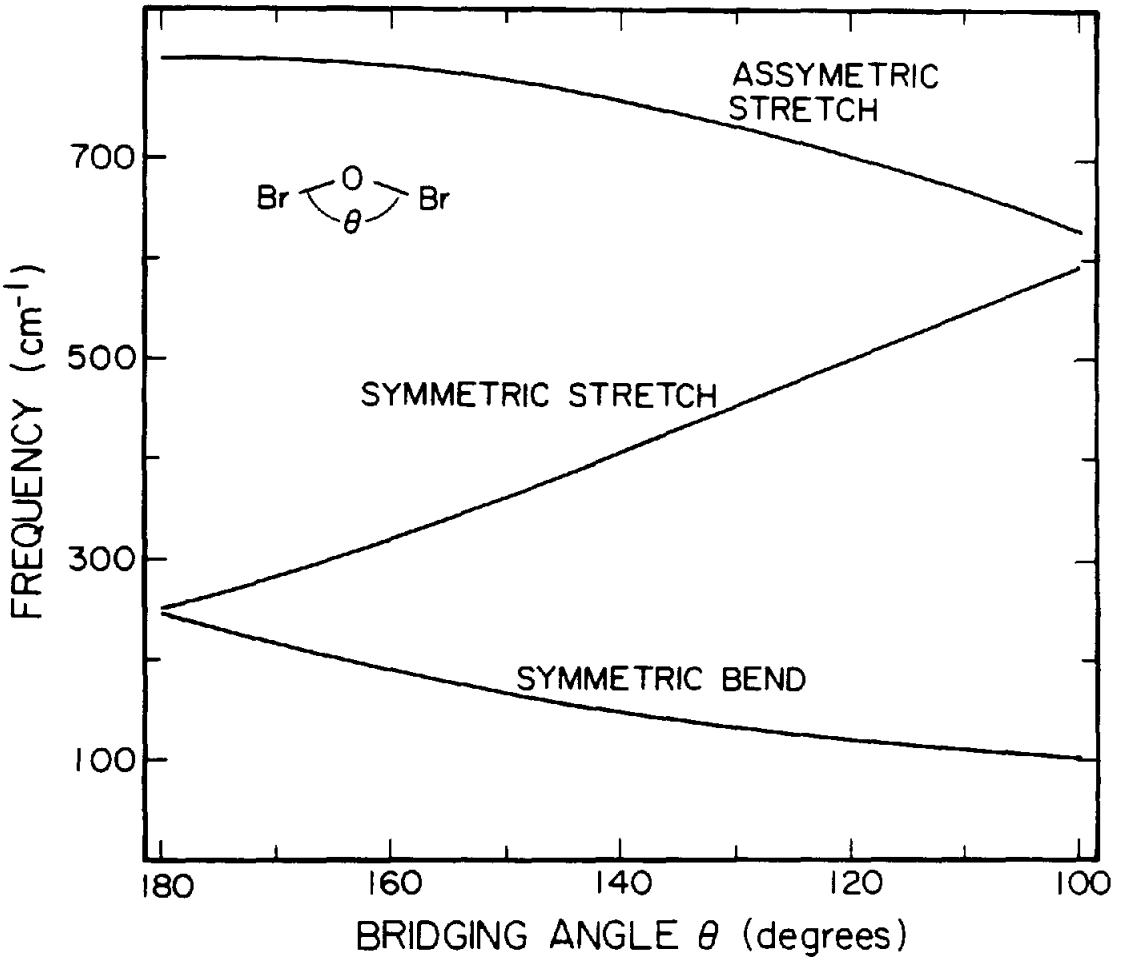

Figure 5.
Calculated frequencies of the normal modes of vibration for the Br_2O system as a function of bridging angle θ.

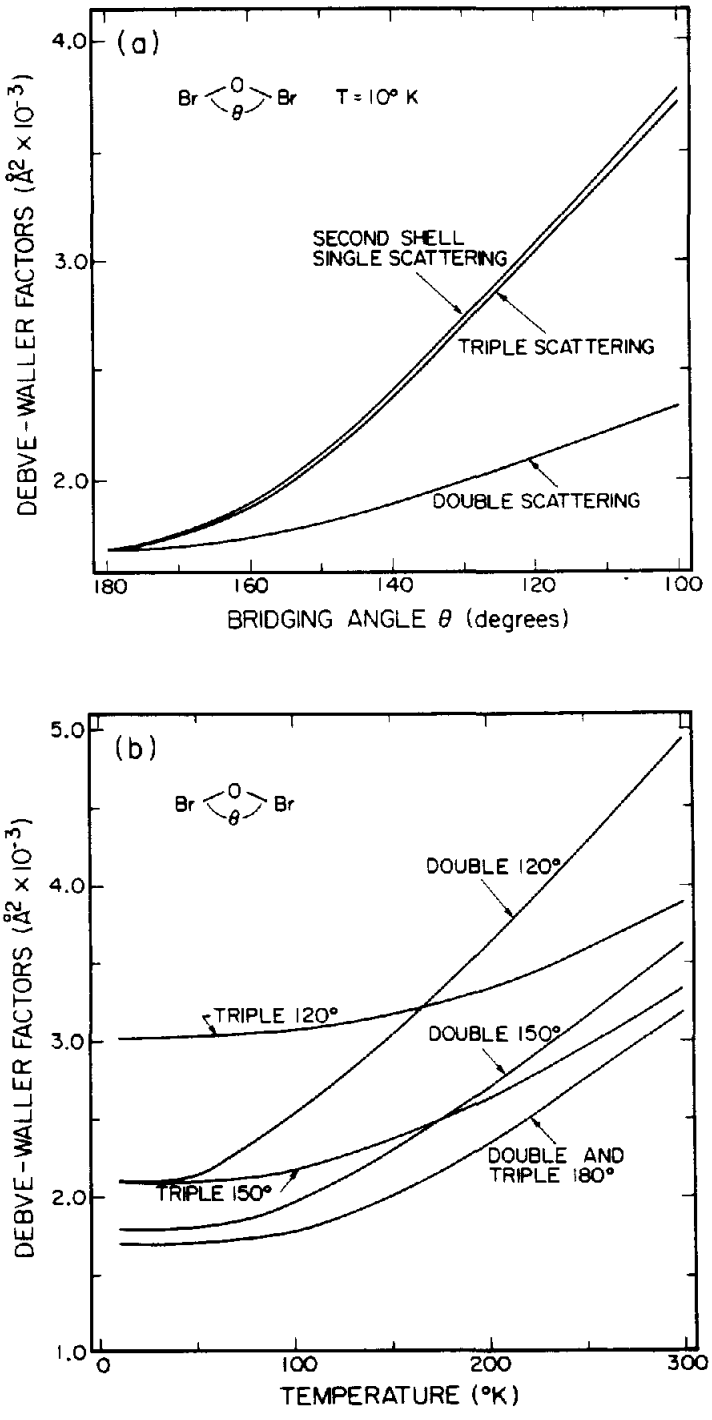

Figure 6.
Debye-Waller factors for the three-atom system. (a) Debye-Waller factor as a function of bridging angle at 10°K. (b) Debye-Waller factor as a function of temperature for bridging angles 120°, 150° and 180°.

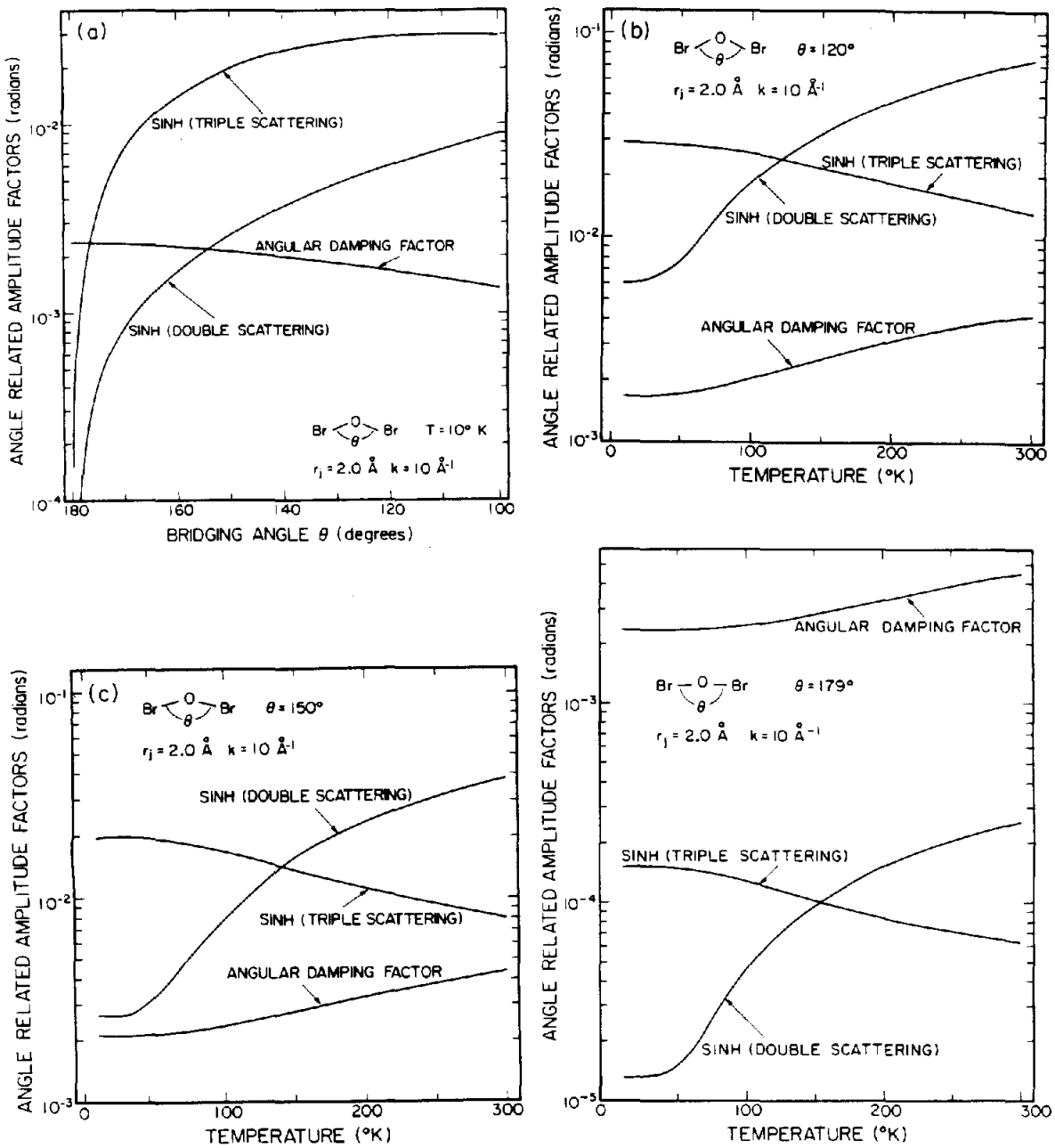

Figure 7.

The argument of the hyperbolic sine terms for the double and triple scattering paths. The angular damping factor is the exponent of the exponential terms which represent the damping of the EXAFS due to a change in the scattering angle α. The hyperbolic sine terms were calculated at k = 10 Å^{-1} and a bond distance of 2.0 Å was used throughout. Note that the sign of the double scattering hyperbolic term is negative. (a) These terms as a function of bridging angle at 10°K. (b) as a function of temperature at a bridging angle of 120°K. (c) 150°K (d) 179°.

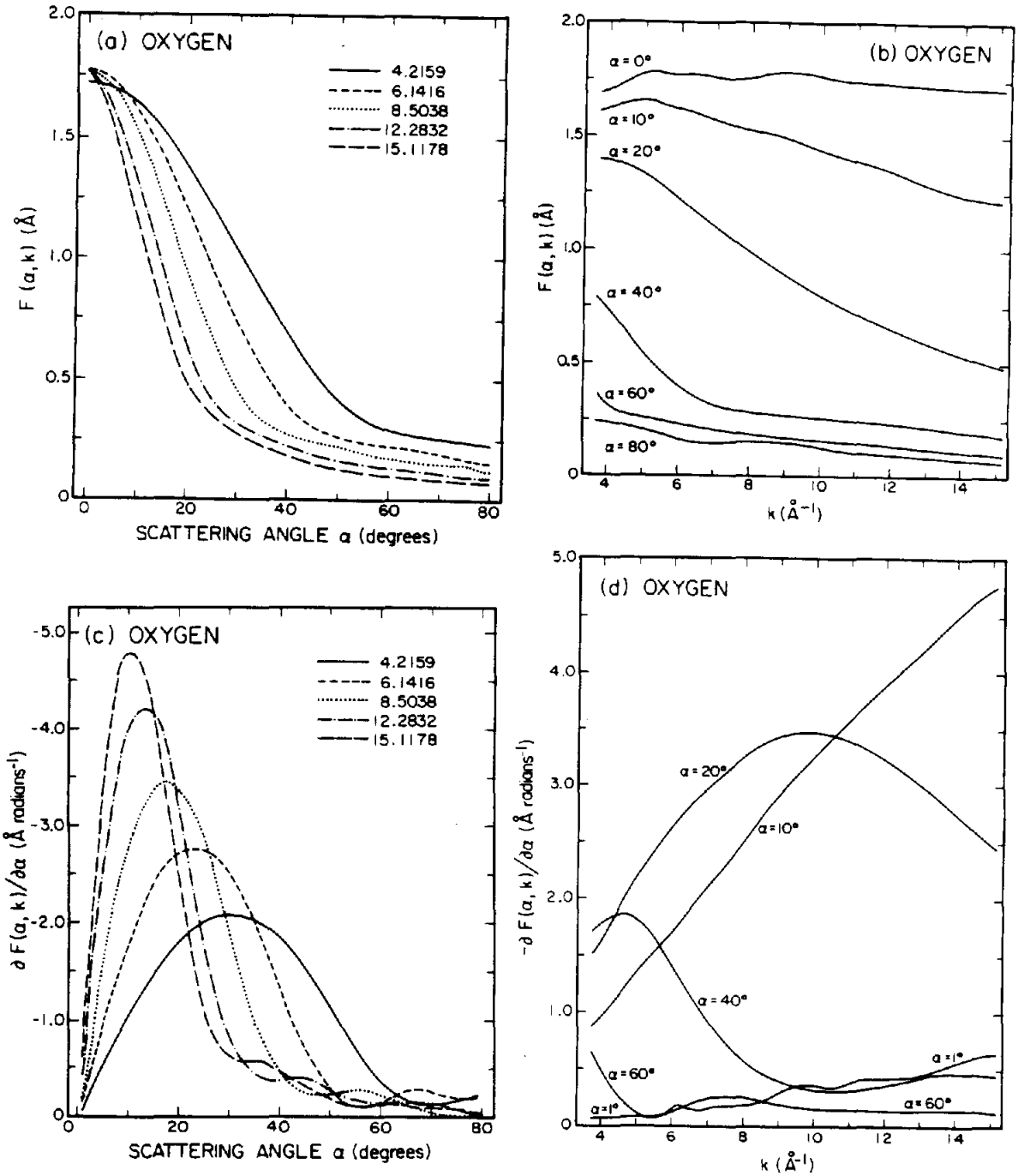

Figure 8.

Modulus of the scattering amplitude for oxygen. (a) As a function of scattering angle for various k values. (b) As a function of k for various scattering angles α. (c) Rate of change of the modulus as a function of scattering angle for various k values. (d) Rate of change as a function of k for various scattering angles α.

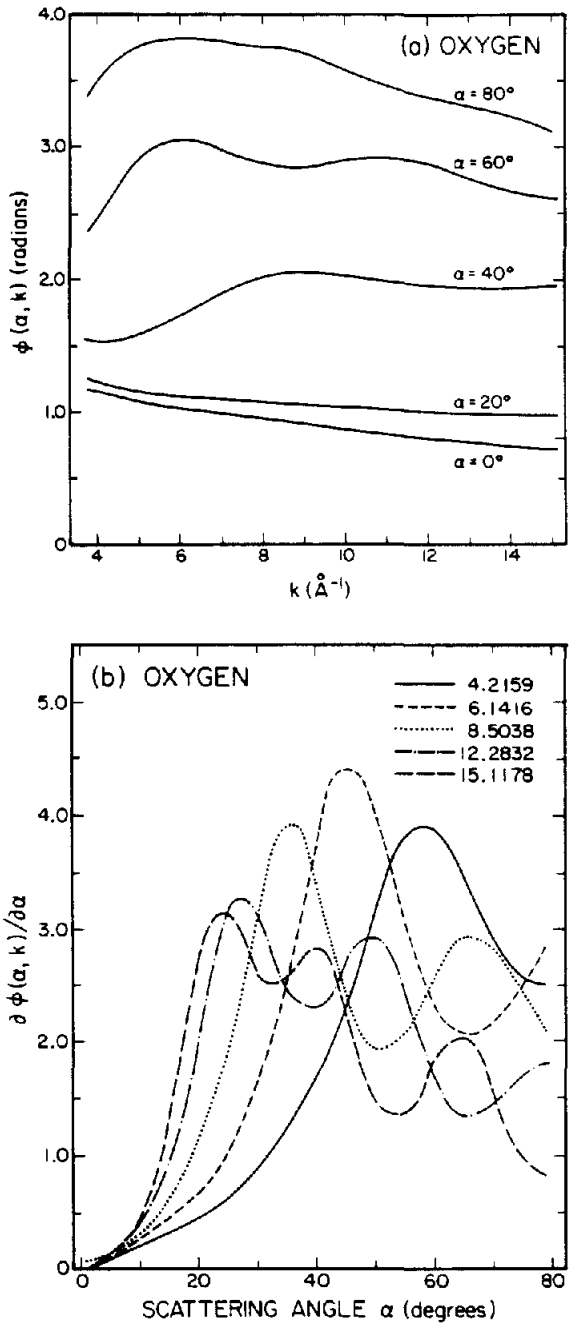

Figure 9.
Phase of the scattering amplitude for oxygen (a) as a function of k for various scattering angles α. (b) Rate of change of the phase as a function of scattering angle for various k values. (c) Rate of change as a function of k for various scattering angles α.

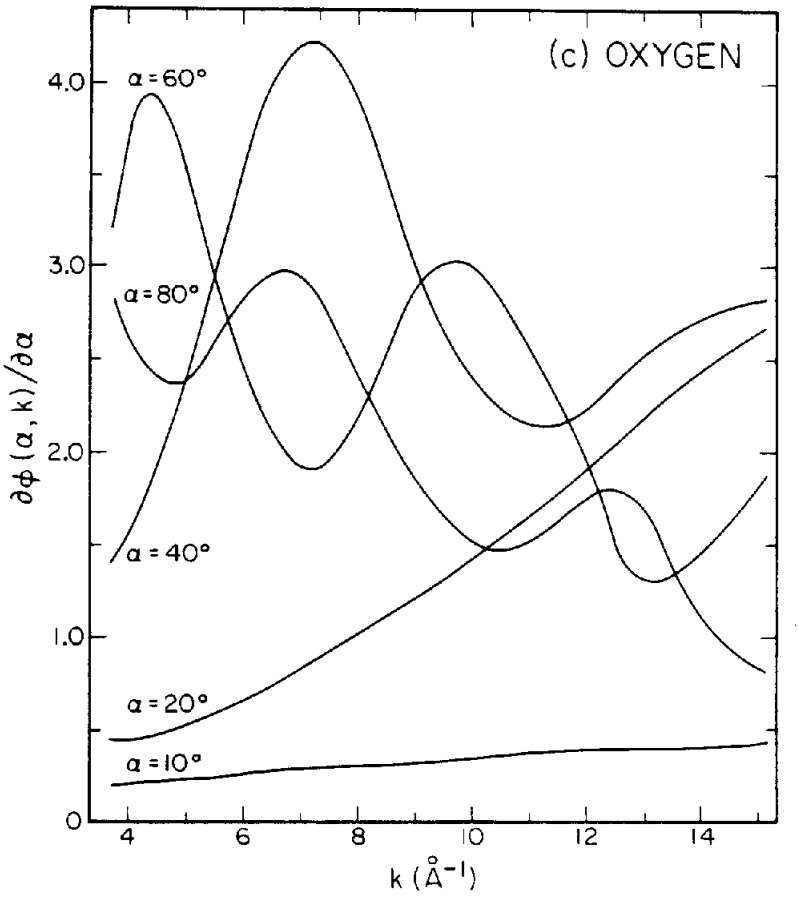

Figure 9, continued.

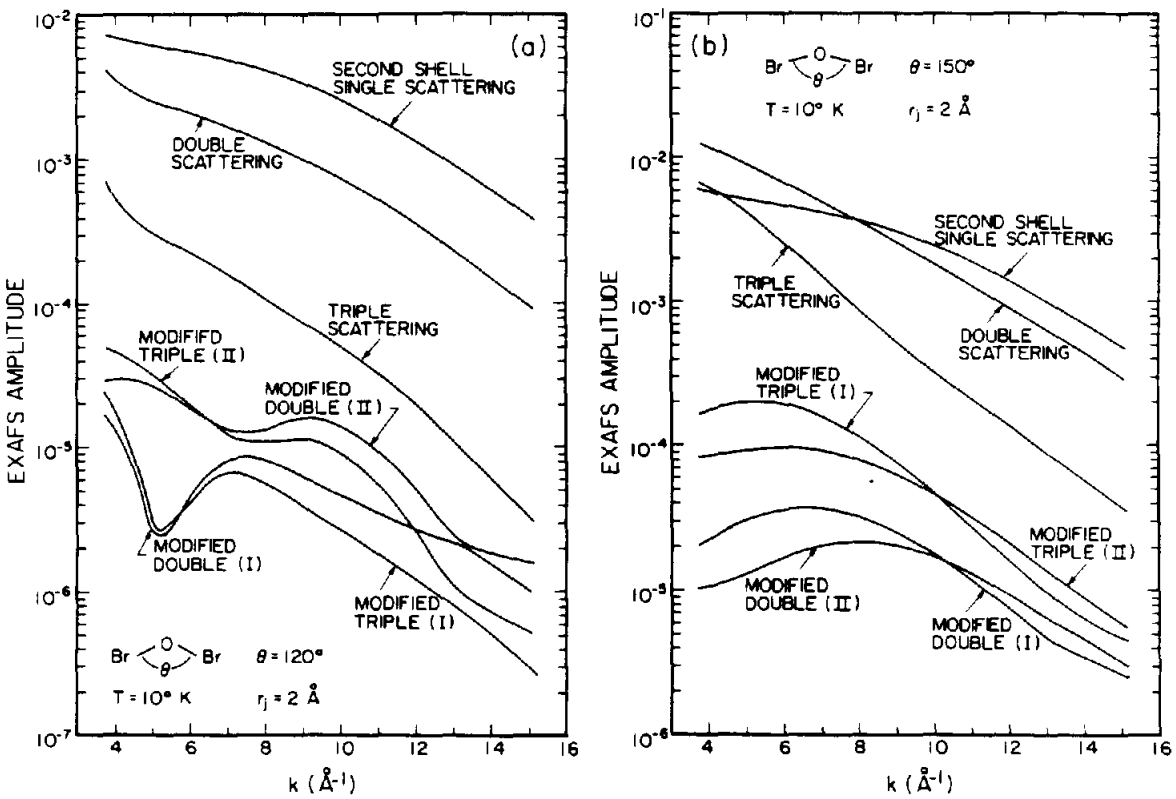

Figure 10.

Amplitude of the individual terms which contribute to the EXAFS of the Br_2O system. All calculations were carried out at 10°K and a bond distance of 2.0 Å. The sign of the modified triple scattering type I and II terms is positive while all other terms are negative. Note that the modified type I terms are to be multiplied by a cosine of the appropriate argument while the type II terms are multiplied by a sine. Amplitudes as a function of k are given for bridging angles of (a) 120°. (b) 150°. (c) 180°.

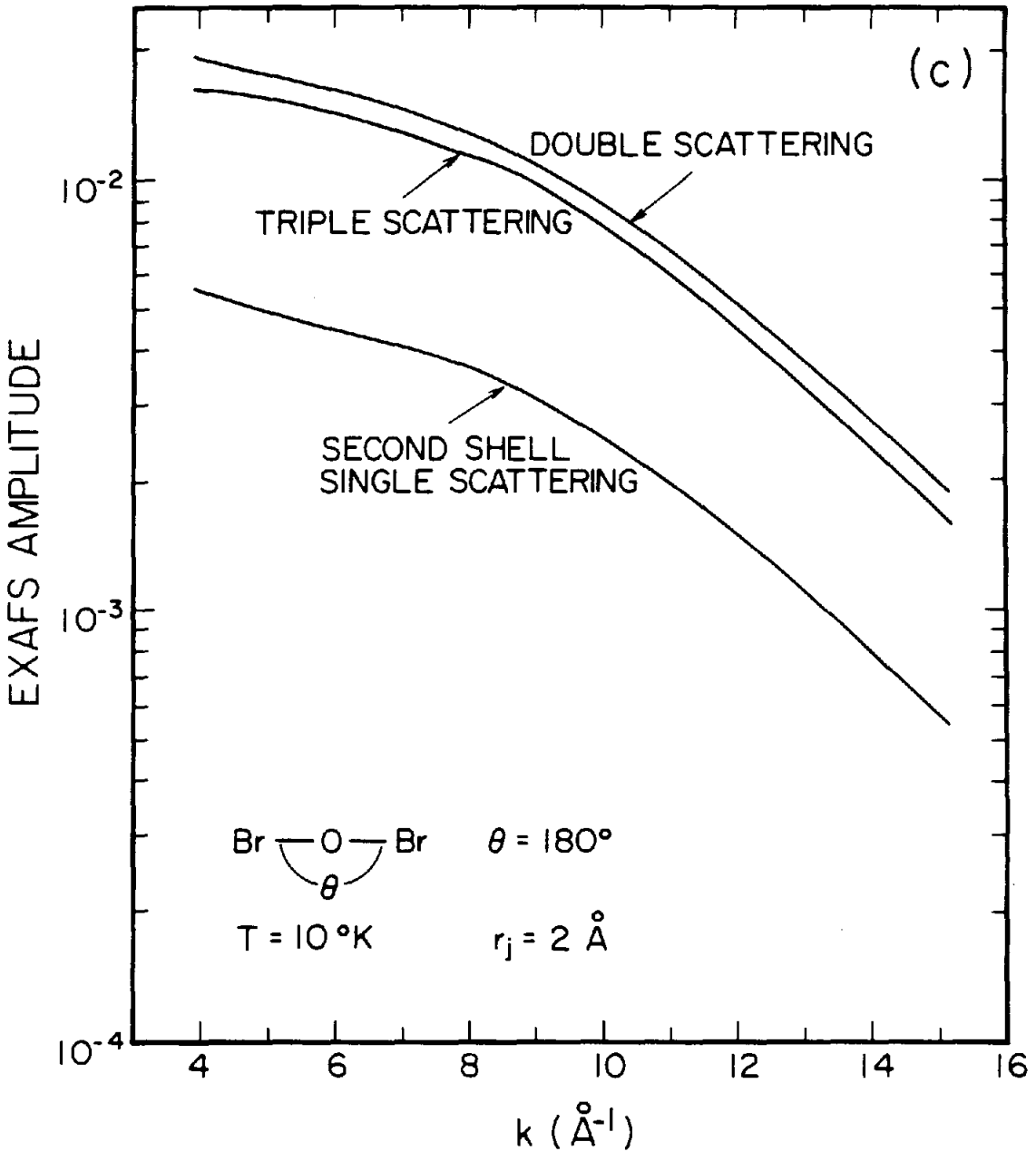

Figure 10, continued.

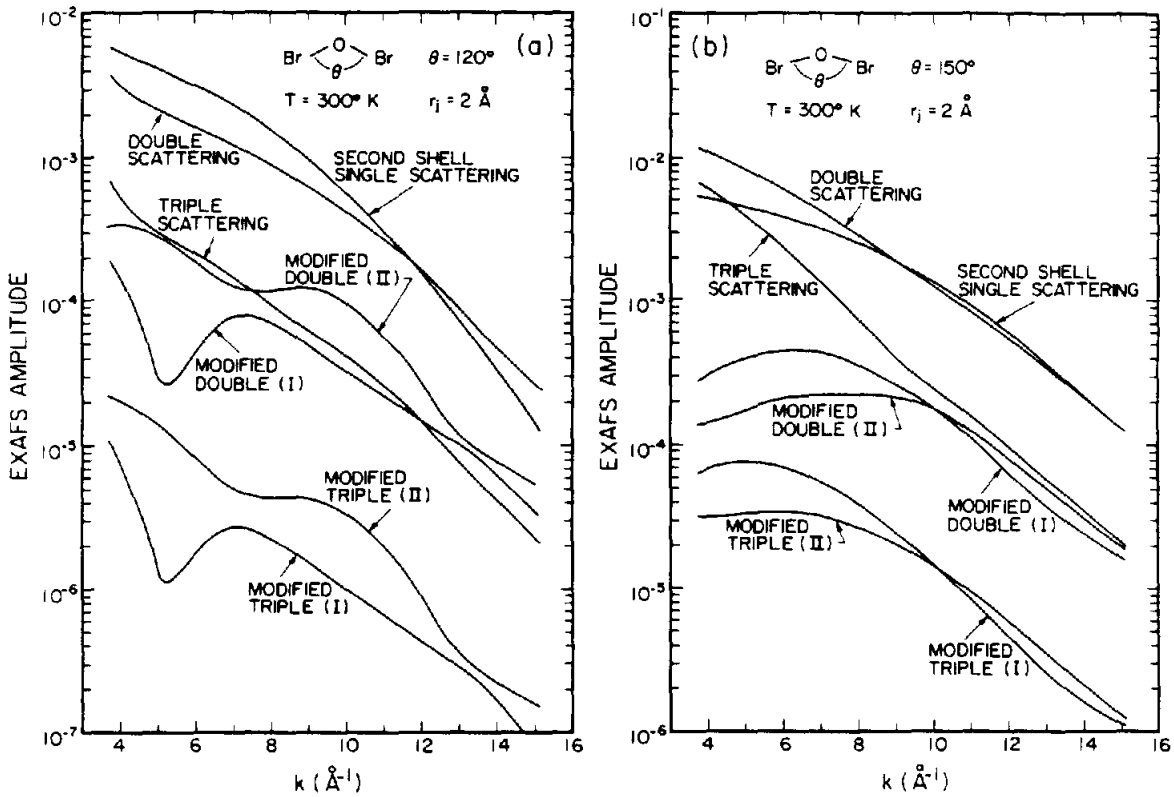

Figure 11.
Same as for Fig. 10 except that all calculations are for a temperature of 300°K.

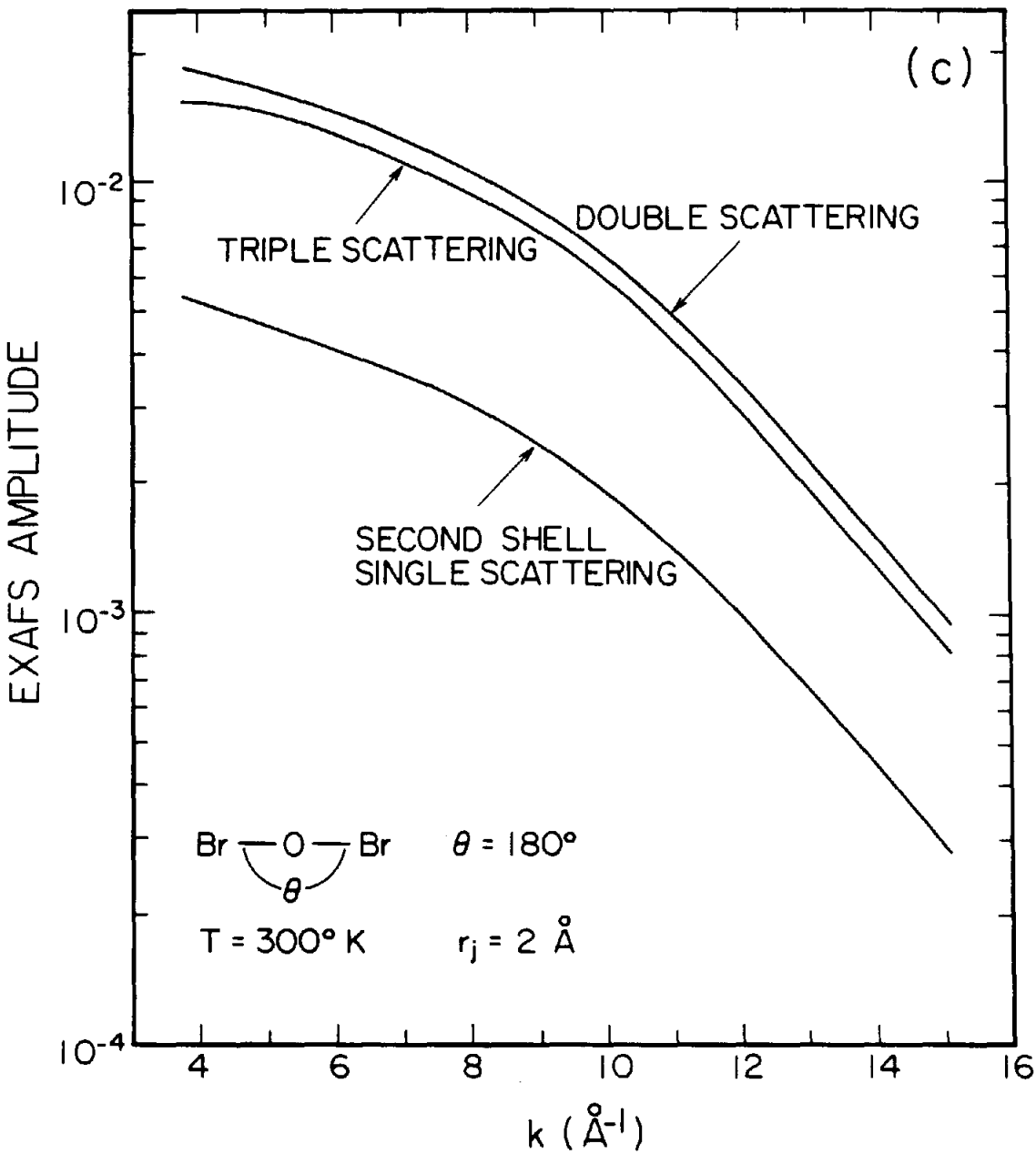

Figure 11, continued.

CHAPTER VI

THE CALTECH LABORATORY EXAFS SPECTROMETER

6.1 Introduction

In recent years extended x-ray absorption fine structure (EXAFS) spectroscopy has been used extensively as a structural tool.[1] Although the existence of this extended structure has been known for many years,[2] the low flux available from conventional sealed tube x-ray sources severely hampered the growth of the technique. Most of the early EXAFS data suffered from poor signal to noise such that early investigators were mainly concerned with the qualitative variations in the data from one material to another.

Much of the present interest in EXAFS is due to the pioneering work of Sayers, Stern and Lytle[3] who introduced a simple parametrization of the fine structure in terms of physically significant quantities. An equally important factor in the development of EXAFS, however, was the emergence of the synchrotron radiation laboratory at Stanford University, which provided large fluxes of highly collimated and polarized x-rays.[4] Together, these advances, combined with the appealing short range nature of the probe, provided a major impetus towards the development of EXAFS as a structural tool.

The subsequent interest in EXAFS, however, placed a considerable burden on the synchrotron facilities, and as a

result, it became difficult to obtain beam time to perform experiments. Even when beam time became available there were considerable time constraints within which each experiment was to be completed. Investigators did not have the luxury of being able to repeat experiments and it was difficult for students to learn under such conditions. Furthermore, the analysis routines developed at these synchrotrons became widely used throughout the EXAFS community and little consideration was given to new methods of analysis.

The laboratory EXAFS spectrometer has developed into an important alternative to the use of synchrotron radiation. Clearly, such a spectrometer cannot compete with a synchrotron facility in terms of flux. What is important, however, is the fact that the investigator has now sufficient time to try out new experimental ideas, ideas which might not have received beam time at a synchrotron facility. In any case, a laboratory EXAFS spectrometer has sufficient flux and resolution to be useful in the study of a large number of materials. This has allowed synchrotron facilities to concentrate on the study of more complex materials which require the large flux and high resolution available at such centers.

In this chapter we shall describe the Caltech laboratory EXAFS spectrometer. The considerations governing the design of the instrument are discussed in detail together with an analysis of the components which make up the spectrometer.

6.2 General Description of the Spectrometer

A schematic of the laboratory spectrometer is shown in Fig 1. The spectrometer is based on the Rowland circle geometry in which the source, monochromator and the exit slits all lie on the circumference of a circle.[5] The radius of the Rowland circle was chosen to be 75 cm which reduces the effects of both vertical divergence and the effective source size as seen by each point on the crystal. Furthermore, this choice of radius increases the resolving capabilities of the spectrometer. Unfortunately, however, the large path lengths in a Rowland circle of this size results in a significant amount of x-ray scattering by air. For 8 KeV x-rays, a 30 cm path length in air reduces the initial intensity of the beam by 50%. To overcome this problem helium beam lines have been employed along the path of the x-rays.

To obtain an EXAFS spectrum both the incident (I_o) and the transmitted (I) intensities must be monitored as a function of the x-ray wavelength λ according to the equation

$$I(\lambda) = I_o(\lambda)\exp[-\mu(\lambda)X] \qquad (6.2.1)$$

where $\mu(\lambda)$ is the linear absorption coefficient, which contains the EXAFS oscillations. Both $I_o(\lambda)$ and $I(\lambda)$ are measured using gas ionization chambers. To scan the x-ray wavelength, λ , the source, the monochromator and the slits must be moved along the circumference of the Rowland circle,

satisfying Bragg's law for diffraction at each point. The distances from the source to the center of the crystal and slits must be equal to insure focusing of the diffracted x-rays onto the exit slits. In this configuration the condition for diffraction of x-rays of wavelength λ is given by:[5]

$$D = n\lambda R/d = 2R \sin\theta_B \qquad (6.2.2)$$

where D and R are the distances from the source to the crystal and the radius of the Rowland circle, respectively.

Since the source is fixed both the monochromator and the exit slits must be moved to satisfy Eq. (6.2.2). This motion is accomplished by mounting both the monochromator and the slits on lead screws, which are in turn, driven by stepping motors. Figure 2 is a scaled drawing of the spectrometer and shows the stepping motors and the positions of the spectrometer components at three different energies. A single stepping motor (known as the θ motor) serves to maintain the correct Bragg angle for diffraction. Two other stepping motors, which lie along the chords of the circle defined by the source, the monochromator and the slits, serve to adjust these chord lengths in accordance with Eq. (6.2.2). A fourth motor (called the 2θ motor) allows one to adjust the position of the detector stage, which contains the exit slits, until the correct scattering angle ($2\theta_B$) is defined.

The positions of three of these stepping motors are

software controlled. The 2θ motor, however, proved too remote from both the source and crystal and we were unable to accurately predict its correct position as a function of x-ray energy. As a result a calibration procedure is necessary in which the three other motors are moved to their appropriate positions for a given energy and then the 2θ motor is scanned until the maximum intensity is registered through the exit slits. This 2θ position is then recorded and the procedure is repeated over the remaining energies of interest. The calibration file which is created remains valid for as long as the experimental parameters are unchanged.

To perform an EXAFS scan, all four motors are initially moved to the position which corresponds to the first energy at which the absorption measurement is required. The intensity of the x-rays passing into the ionization chambers is then registered. After sufficient counts have been accumulated, the stepping motors move the spectrometer components to the next energy setting where the procedure is repeated. The energy difference between subsequent positions of each stepping motor is typically 2 eV. The data are stored on a floppy disk in the form: energy, counts in chamber I_o, counts in chamber I. From these data, $\mu(\lambda)$ may be determined from Eq. (6.2.1).

6.3 X-Ray Source

The x-ray source consists of a commercially available 12 KW Rigaku RU-200 rotating anode x-ray generator.[6] This x-ray source has many advantages over the conventional sealed tube sources. The emission currents in these latter sources are limited by the amount of heat that can be dissipated by the target. In the case of rotating anodes, this heat is spread over a rotating target. Furthermore, rotating anodes may be interchanged, and hence, the output characteristics of the source may be readily varied. These anodes may also be polished so that contaminants, such asthose due to sputtering from the filament, may be removed.

The output of both rotating anode and sealed tube sources consists of a broad continuum of x-ray frequencies superimposed upon which lies a number of sharp characteristic lines.[7] The continuum radiation or Bremsstrahlung originates from the deceleration of the electrons, which are emitted by the filament, as they penetrate the target material. The characteristic lines result from discrete transitions in the target atoms, due to electron impact ionization of various electronic energy levels of these atoms. A sharp high frequency cutoff exists and corresponds to the complete energy gained by the electrons as they are accelerated between the filament and the anode.

In EXAFS studies only the smooth continuum radiation is used. The sharp, intense characteristic lines represent a problem since the detector system responds non-linearly to

the sudden increase in intensity. Accordingly, it is important to have some means of removing the unwanted effects of these lines. One possible solution is the introduction of an attenuation device which reduces the intensity of the beam passing through the exit slits at energies corresponding to these lines. The device itself consists of a lucite wedge which is driven in and out of the beam by a stepping motor. The incident Bremsstrahlung intensity is measured and recorded as a function of energy. The observed intensity is then extrapolated through all of the characteristic lines in the spectrum. In the region of such a line, the wedge position is given by thatwhich reproduces the extrapolated intensity. In this manner a look-up table of wedge positions is generated which ultimately yields a smooth intensity distribution.

As an alternative to this wedge method, it is possible to choose a target material which has no characteristic lines in the energy range of interest. Such a material must also be a good thermal conductor since, most of the energy of the incident electrons is dissipated as heat.[8] Silver proved to be just such a material. Apart from having the highest thermal conductivity of any substance it also has no characteristic lines in the energy region from 2 KeV to 22 KeV.[9] This energy region is sufficiently large to allow EXAFS studies on almost all elements.

There is, however, another source of characteristic lines. The electrons which bombard the target are produced

by thermionic emission from the filament. This emission is described by the Richardson-Dushman equation:[10]

$$J = AT^2 \exp[-E_w/kT] \qquad (6.3.1)$$

where J is the emission current, A is a constant and E_w is the workfunction of the filament material. The filament is heated by passing a current through it and, as a result, electrons are boiled off. Due to the high temperature of the filament, however, atoms from the filament are sputtered onto the anode. Consequently, over a period of time, characteristic lines of the filament material appear in the output of the x-ray source. In the case of tungsten, the most common filament material, a large number of characteristic lines appear between 8 KeV and 12 KeV which is an important energy region for the study of first row transition metal compounds.

To counteract this problem thoriated-tungsten filaments have been constructed. The thorium atoms are believed to reside near the surface and markedly reduce the workfunction of the filament. For a given emission current, the required filament current was observed to be half that required for a pure tungsten filament. The operating temperatures of these new filaments is, therefore, reduced by a factor of four. We have observed experimentally, that only after months of continuous operation does the degree of contamination of the anode become so severe that polishing is necessary.

6.4 Monochromator System

The x-ray monochromator employed in the spectrometer is of the Johansson type shown in Fig. 3. The front surface is ground and polished to the diameter of the Rowland circle. The crystal is then bent to the diameter of the circle such that the polished surface lies on the circumference. In this configuration, all x-rays incident on the crystal from the source, which is a distance D away, are focussed down to a point, the same distance from the crystal, but on the other side of the circle (see Fig. 3). Accordingly, each point on the crystal diffracts x-rays of the same wavelength, which is defined by Eq. (6.2.2). The Johansson arrangement, therefore, results in an intense, fully diffracting monochromator, the intensity of which is some three to four hundred times greater than that of a similar but flat crystal.

The mechanism for bending the crystal is shown in Fig. 4. Note that bending moments are applied at both ends of the crystal with cylindrical couples. Each bending element may be adjusted by a micrometer independently of the other elements. This allows translation of one or both ends of the crystal in addition to bending. This bending mechanism is convenient since several bending geometries are possible (e.g., cylindrical, logarithmic spiral etc.) with the same bender and crystal. There is a trade off involved in the use of bending couples, however. The closer the bending elements of the couple are to each other the better the

approximation to a cylinder, but the greater the strain placed on the crystal. Furthermore, note that the crystal being bent is not uniformly thick, and hence, a perfect cylindrical bend is not possible. Accordingly, bending mechanisms of this type are most appropriate for spectrometers which require a large Rowland circle radius.

As an alternative to the bending mechanism discussed above, it is possible to obtain ground and polished crystals which have been fixed to a backing block of the correct curvature. In this manner large (3 cm x 15 cm) Johansson crystals may be obtained. There are often problems with monochromators of this kind, however, since dust particles or dirt in the epoxy introduce local strain on the crystal, and hence, distort the Bragg planes. Such distortions result in diffuse x-ray scattering and ultimately contribute to an aberration in the focus.

In the case of our laboratory spectrometer, the bending mechanism discussed above is used to bend a thin (0.2 x 2.5 x 5.0 cm) Si(111) crystal, and allows EXAFS data to be obtained in the 6 KeV to 12 KeV energy range. The fixed curvature monochromator consists of a four by one inch Ge(220) crystal which is affixed to an aluminum backing block. This latter crystal is operative in the 13 KeV to 20 KeV energy range.

In choosing a suitable monochromator the question of harmonic generation must be considered. The presence of harmonics in the diffracted beam tends to smear out the

EXAFS oscillations and distorts the amplitude information they contain. The problem of harmonics may be eliminated by operating the x-ray generator at a voltage below the energy of the harmonic. This, however, limits the maximum emission current, due to space charge effects and also reduces the lifetime of the filament. The Si(111) crystal has no second order reflection, and hence, may be used at relatively high voltages. The Ge(220) crystal, on the other hand, reflects in second order, but since it is operative at high energies, this is not a serious restriction.

6.5 X-Ray Detectors

At present, ionization chambers are used to detect both the incident and transmitted x-ray intensities. A schematic of an ionization chamber is shown in Fig. 5. X-rays entering such a chamber, ionize the gas inside, and produce a certain number of electron-ion pairs. The average energy required for the formation of each electron-ion pair is approximately 30 eV and is roughly independent of the nature of the gas.[11] When a bias voltage is applied across the chamber the electron-ion pairs drift apart under the influence of the applied field. The total charge at the collection electrode is dependent on the applied voltage. Ionization chambers operate at a voltage which allows every electron-ion pair produced to be collected at the electrodes. At voltages lower than the ionization chamber voltage, recombination is important while at higher voltages

secondary ionization occurs. The currents obtained from such ionization events are typically in the picoampere range.

It is possible to calculate the degree of absorption in each chamber which provides the best signal to noise ratio.[1] The ionization chamber which detects the intensity should absorb 20% of the beam while the sample absorbs 80% of the remaining intensity. The rear ionization chamber, which detects the intensity of the transmitted beam through the sample, should absorb as much as possible of this intensity. The first ionization chamber has a path length of 7 cm and contains a 20:80 mixture of argon and nitrogen. The rear chamber has a pathlength of 13 cm and contains pure argon. These chambers satisfy the criteria for maximum signal to noise at 8 KeV. At higher energies, however, chambers with longer path lengths or heavier gases are required.

6.6 Spectrometer Performance

The present performance of the EXAFS spectrometer is characterized by a photon flux of 10^7 photons per second and an energy resolution of 5 eV (see Fig. 6). These values are for 8 KeV x-rays using the Si(111) monochromator described earlier. At higher energies the photon flux is greater but the resolution is decreased. There are many factors which influence the spectrometers performance, but in our case, by far the most important of these, is the monochromator system.

The x-rays produced from a rotating anode by electron bombardment are 4π emitted. In what follows, we shall

assume that the energy distribution of photons is the same within each solid of the beam. Such an assumption is well justified in view of the large potential energy of the incident electrons, which tends to make polarization and other effects insignificant.

We shall limit our discussion to the performance of the spectrometer at 8 KeV. At this energy the chord length, D, from the source to the monochromator is 35 cm. The focus on the anode is 1.0 x .05 cm, which when viewed at a 6° take off angle, yields an effective focus width of 50 microns. At a distance of 35 cm, each point on the crystal see intensity within an angular range of 30 seconds of arc. The monochromator crystal may or may not be capable of diffracting intensity within this angular range. The angular range over which a crystal can diffract is called the acceptance angle ω_s of the crystal. From dynamical theory we obtain an expression for ω_s[12]

$$\omega_s = \frac{2e^2}{\pi mc^2} \quad \frac{\lambda^2 |F|}{V \sin 2\theta_B} \tag{6.6.1}$$

where F is the structure factor and θ_B is the Bragg angle for diffraction. Note that ω_s is directly proportional to $|F|$, and hence, the larger the angular range over which the crystal can diffract, the brighter the crystal. Using Eq. (6.6.1) we can calculate the acceptance angle for Si(111). For this crystal, at a Bragg angle $\theta_B = 14.217^{\circ}$, corresponding to copper K_α radiation, we obtain an

acceptance angle of 6.9 seconds of arc. Since our beam has an angular range of 30 seconds of arc, we are in principle, only using one quarter of the beam intensity.

We must also consider the factors which determine the resolution of the spectrometer. From Bragg's law we can readily derive the dispersion relation:

$$\Delta\theta = \Delta\lambda/\lambda \tan \theta_B \qquad (6.6.2)$$

In the limiting case, where the angular spread $\Delta\theta$ corresponds to the acceptance angle, maximum resolution $\Delta\lambda/\lambda$ is obtained and full use is made of incident intensity. In the case of Si(111) using copper K_α radiation we calculate a resolution of 1.06 eV from Eq. (6.6.2).

From the above discussion, however, it is clear that such a resolving power may not be achieved with our spectrometer. Using a beam with an angular spread of 30 seconds of arc we predict an experimental resolution of 4.6 eV. This resolution will be achieved only if the whole system is working perfectly, any misalignments or vibrations will tend to increase this value. Accordingly, the observed resolution of 5 eV (see Fig. 6) indicates that the spectrometer is functioning as well as can be expected. Note, however, we are still using only one quarter of the beam so that if we use a 3^o take off angle the resolution will increase by a factor of two while the flux remains unchanged. This is not entirely feasible, however, since in the case of a rotating anode, even a slight wobble in the

axis of rotation would be critical at such low angles.

6.7 Conclusions

The laboratory EXAFS spectrometer described above, provides both sufficient flux and resolution to perform studies on a wide variety of samples. All the data presented in this thesis have been obtained using this spectrometer. The systems which were studied are relatively simple and probably could not have been studied at a synchrotron facility. However, a careful study of these systems has revealed a hidden wealth of information in EXAFS, information which had not been uncovered in ten years of work using synchrotron sources. The detailed experimental work which was performed using this spectrometer is described in Chapters VII through IX of this thesis.

References

1. P.A. Lee, P.H. Citrin, P. Eisenberger and B.M. Kincaid, Rev. Mod. Phys. **53**, 769 (1981).

2. R.L. Kronig, Z. Phys. **70**, 317 (1931); **75**, 191 (1932).

3. D.E. Sayers, E.A. Stern and F.W. Lytle, Phys. Rev. Lett. **27**, 1204, (1971).

4. A. Bienenstock, EXAFS Spectroscopy, Techniques and Applications, edited by B.K. Teo and D.C. Joy (Plenum Press, New York, 1981).

5. J.W.M. DuMond, D.A. Lind and E.R. Cohen, Rev. Sci. Instrum. **18**, 617 (1947).

6. Rigaku/USA Corporation, Danvers, MASS 01923.

7. A.H. Compton and S.K. Alison, X-rays in Theory and Experiment (Van Nostrand, New York, 1935) p. 80.

8. Reference 7, p .89.

9. Handbook of Chemistry and Physics (CRC press, Cleveland, 1974) 54 th edition, E-197.

10. C. Herring and M.H. Nichols, Rev. Mod. Phys. **21**, 185 (1949).

11. W. Jesse and J. Sadauskis, J. Phys. Rev. **97**, 1668 (1955).

12. R.W. James, The Optical Principles of X-ray Diffraction (Cornell University Press, New York, 1965).

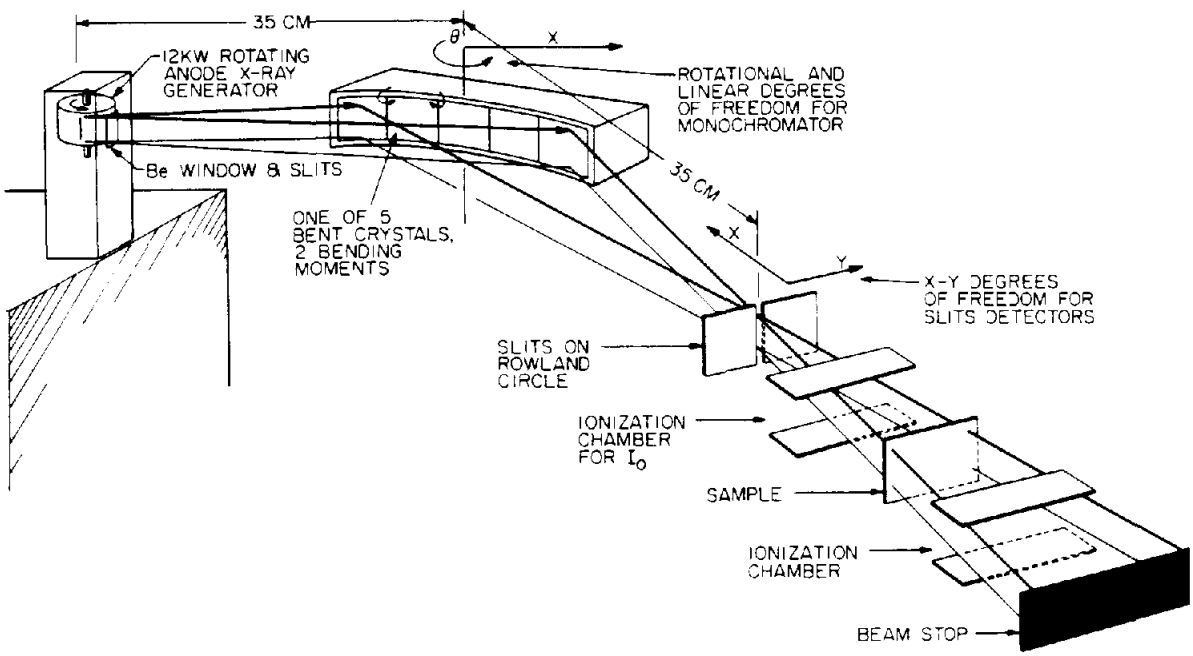

Figure 1.
A schematic of the laboratory EXAFS spectrometer. The distances shown are for diffraction of 8 KeV x-rays.

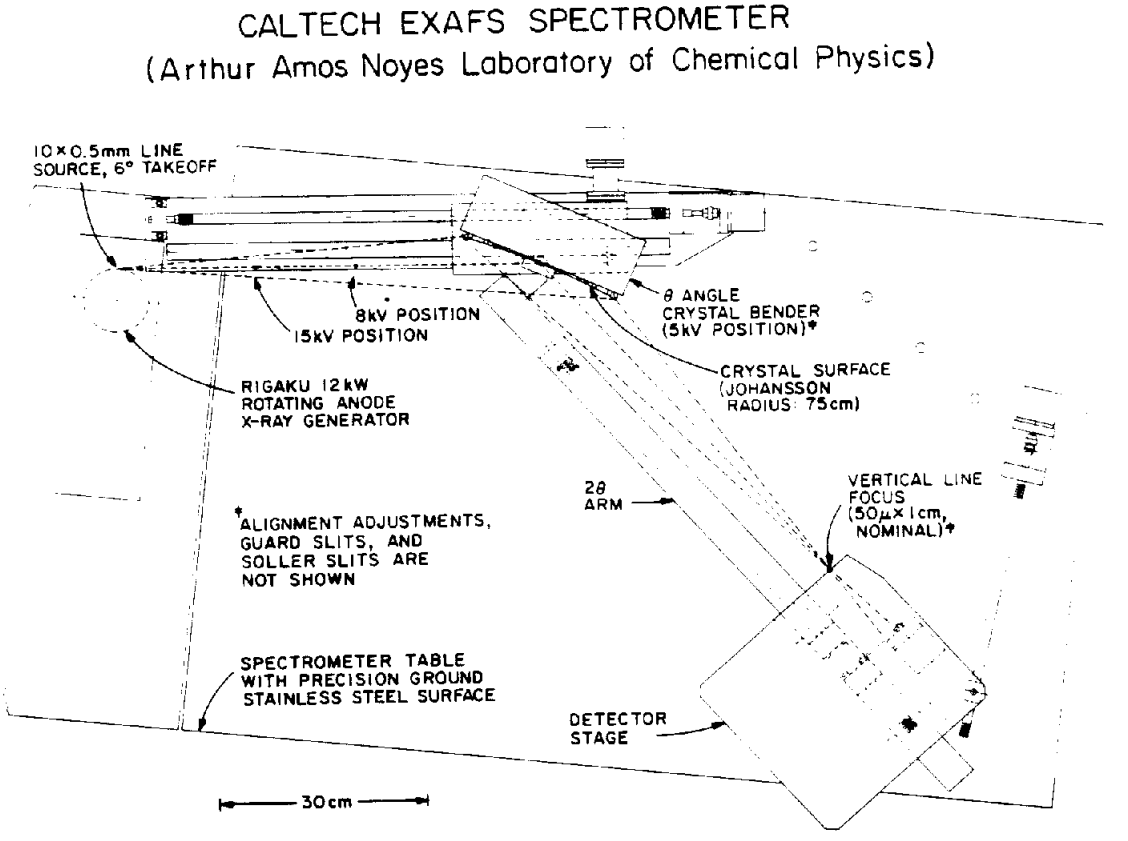

Figure 2.
A scaled drawing of the laboratory spectrometer. The configurations of the spectrometer components required for the diffraction of 5 KeV, 8 KeV and 15 KeV x-ray photons are shown. Note the positions of the four stepping motors which are used to move the components of the spectrometer.

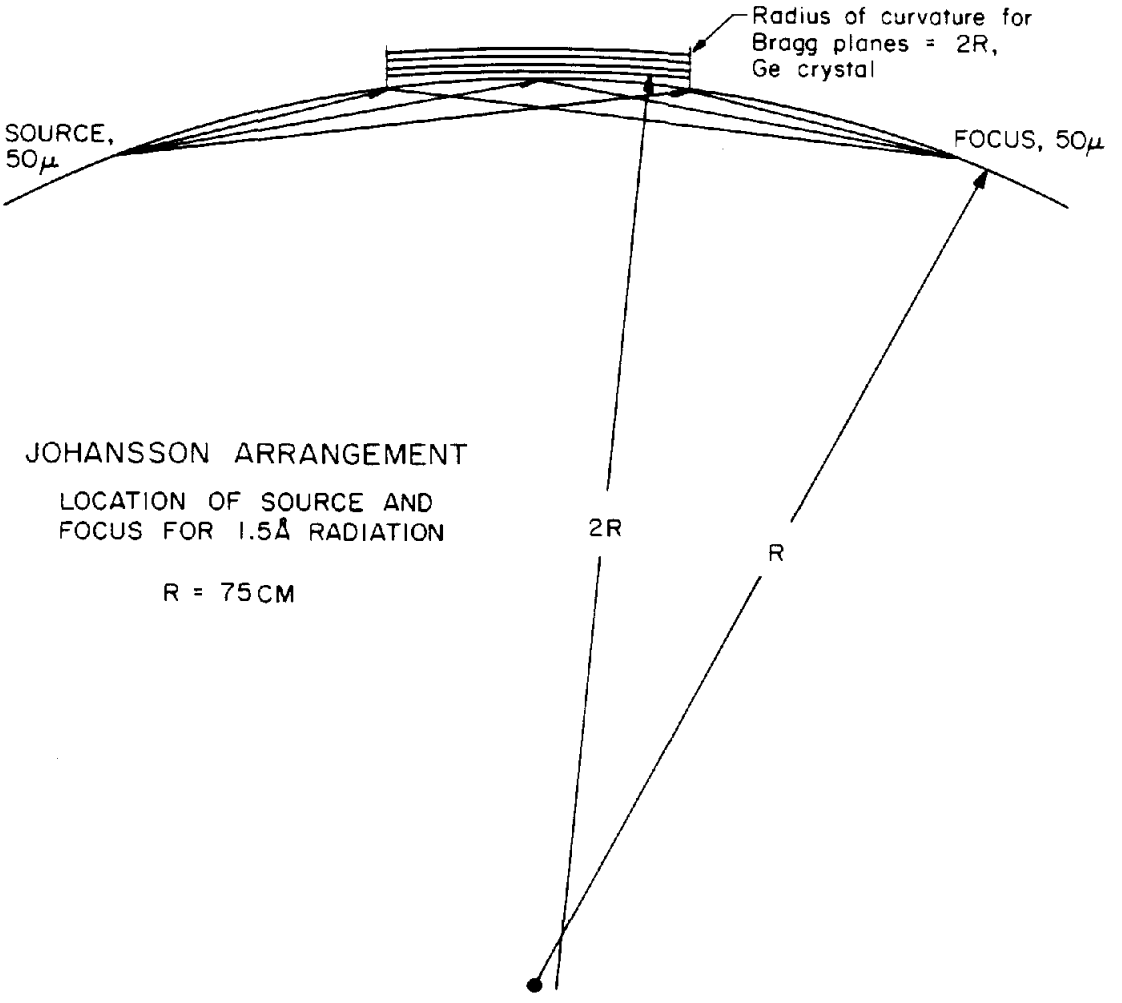

Figure 3.
The Johansson configuration of the monochromator. In this arrangement, x-rays which are incident upon the crystal from one side of the Rowland circle, are focussed onto the other side of the circle.

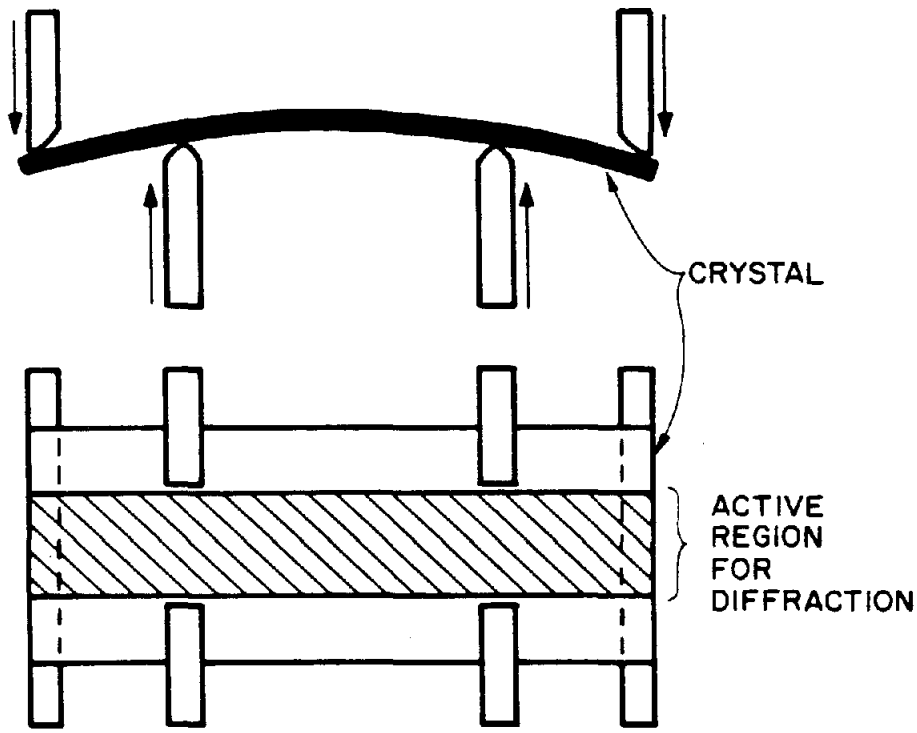

Figure 4.
Crystal bending appartus with two bending moments. The upper drawing shows the bend as seen from the top. The arrows indicate the direction of the force which induces the bend. The lower drawing is a side view, showing the front surface, a portion of which must be left unobstructed for diffraction.

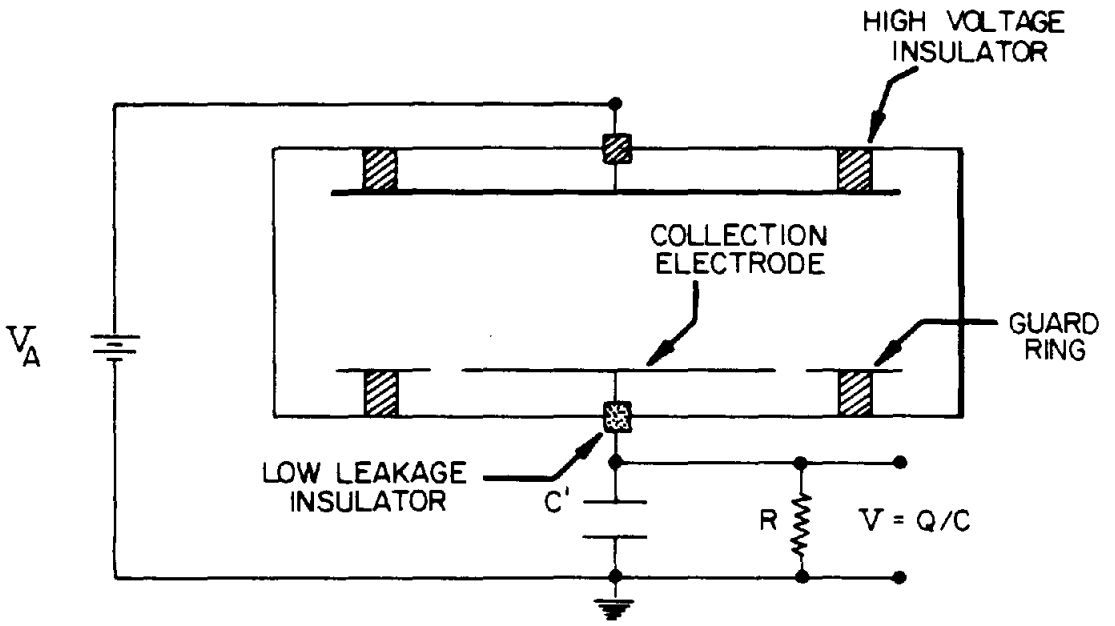

Figure 5.
Schematic of a parallel plate gas ionization chamber. The applied voltage is V_A. If the capacitance of the chamber is C_i, then the total capacitance is $C=C_i+C'$. The output voltage is then Q/C, where Q is the total charge collected during the gas ionization process.

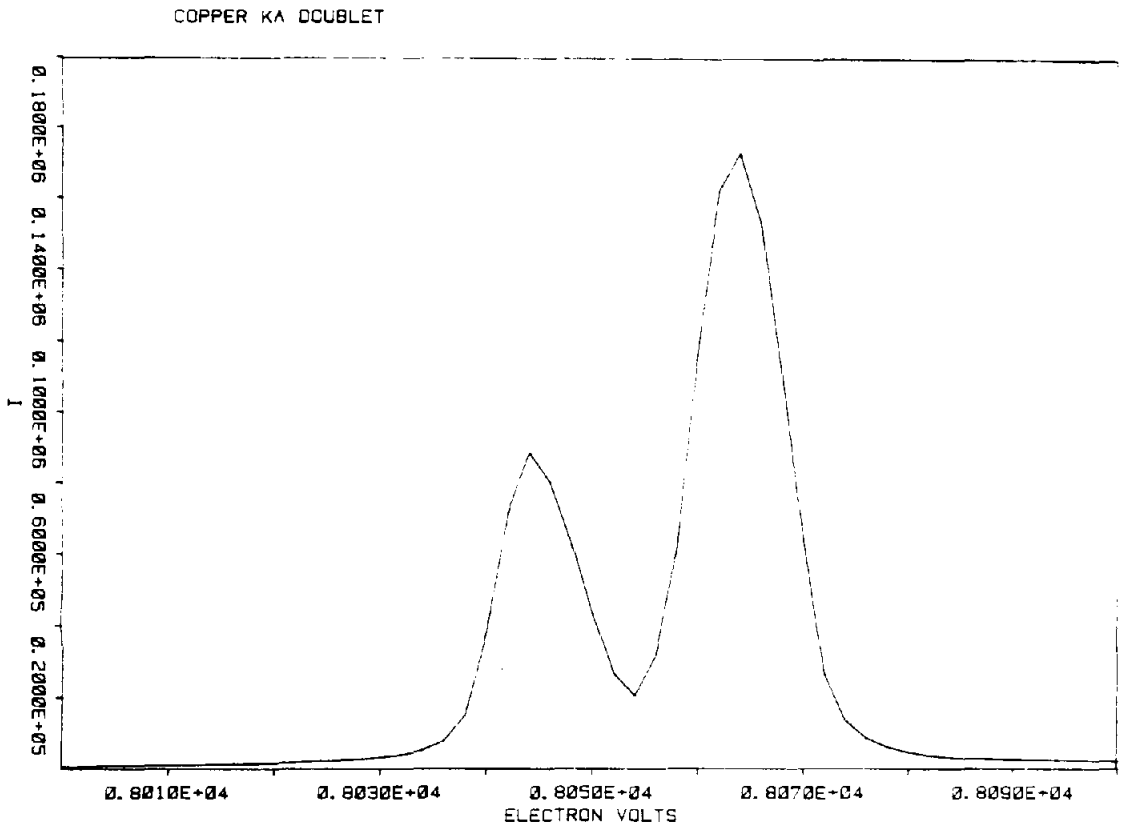

Figure 6.
The copper K_α doublet. The step size is 2 eV so that the observed energy resolution is approximately 5 eV.

CHAPTER VII

DATA ANALYSIS IN EXTENDED X-RAY ABSORPTION FINE STRUCTURE: DETERMINATION OF THE BACKGROUND ABSORPTION AND THE THRESHOLD ENERGY*

7.1 Introduction

Extended X-Ray Absorption Fine Structure (EXAFS) refers to the modulations observed on the high energy side of an x-ray absorption edge. EXAFS has been shown to be sensitive to the local environment of the absorbing atom.[1] An expression for the single scattering EXAFS may be written as:[2]

$$\chi(k) = -\sum_j \frac{N_j |f_j(k,\pi)|}{kR_j^2} e^{-2\sigma_j^2 k^2} e^{-2R_j/d} \times \sin[2kR_j + \delta_j(k)], \tag{7.1.1}$$

where N_j is the number of equivalent scatterers of type j at distance R_j, $f_j(k,\pi)$ is the backscattering function, $\exp(-2k^2\sigma^2)$ is a Debye-Waller factor for thermal fluctuation and static disorder, $e^{-2R_j/d}$ is a term which accounts for inelastic scattering, where d is the photoelectron mean-free path and sin $[2kR_j + \delta_j(k)]$ is the interference term, with $\delta_j(k)$, the composite phase shift function. k is the photoelectron wave number defined by $k = [2m(\hbar\omega - E_o)]^{1/2}/\hbar$, where E_o is the threshold energy and m is the electron mass.

In a transmission experiment, one measures $\mu(k)x = \ln(I_o/I)$, where $\mu(k)$ is the total absorption cross section,

x is the sample thickness, I_o is the incident x-ray beam intensity and I is the intensity after the beam passes through the sample. $\mu(k)$ in Eq. (7.1.1) is actually obtained as:

$$\chi(k)=\frac{\mu_c(k)-\mu_0(k)}{\mu_0(k)}, \qquad (7.1.2)$$

where $\mu_c(k)=\mu(k)-\mu_v(k)$. $\mu_v(k)$ is a correction for absorption of x-rays by electrons other than those of the edge under study. This contribution may be calculated by fitting the pre-edge data to the so called Victoreen formula, $\mu_v=a\lambda^3-b\lambda^4$, where a and b are constants and λ is the x-ray wavelength. A data set of length equal to that of the experiment is generated, using the calculated parameters a and b above, and is subsequently subtracted from the experimental spectrum to give μ_c, the corrected absorption coefficient. $\mu_o(k)$ is the slowly varying background absorption of the absorbing atom in the absence of interfering neighboring atoms for the same sample thickness. It is evident, that in order to compare the theoretical expression for the EXAFS with the experimental data, an accurate estimate of μ_o is essential.

There is no standardized technique for background determination in EXAFS. Since there is no analytical expression for $\mu_o(k)$ that is adequate for all systems, the investigator must judge the points that represent the background absorption. These points, in most cases, are

subsequently subjected to a cubic spline fit to produce a data set of equal length to that of the experimental spectrum.[3] Recently, Cook and Sayers[4] introduced an empirical set of criteria for background removal using the cubic spline method. The above methods, however, are highly flexible and ultimately depend on the discretion of the investigator.

The EXAFS expression, Eq. (7.1.1), is written as a function of the photoelectron wavenumber k. The k range is dependent on the value chosen for the threshold energy E_o. Since E_o is a non-linear function of k, the value of E_o determines the frequency of the data in k space. Various approaches have been applied to the E_o problem. In instances where model compounds are used, the same value of E_o is chosen for both the unknown and the model compounds. Provided the compounds do not differ greatly, this method works reasonably well.[5] An alternative approach has been to vary E_o until the peaks in the real and imaginary parts of the Fourier transform coincide.[6] This latter method, however, requires a knowledge of too many parameters to be useful in a study of unknown compounds. A third approach invokes the concept of phase transferability by assuming that the phase difference between the unknown and model compound is a linear function of k and passes through the origin. The value of E_o is varied until the best fit to such a line is obtained. Another approach has been to numerically differentiate the edge region and locate the

inflection points.[7] In all of these methods, the data are weighted by k^3 to minimize any error in the choice of E_o.

In the present chapter we present two approaches to the problem of background removal in EXAFS. Both methods involve the convolution of the EXAFS spectrum with a Gaussian function, the width of which determines the extent of the damping in the observed spectrum. The first approach originated from the experimental observation that a low resolution EXAFS spectrum results from increasing the spectrometer slit width. In the second method, the EXAFS damping is achieved via the discrete convolution of the spectrum with a calculated Gaussian function. This latter method also gives a unique intersection at the absorption edge which is shown to be a measure of the threshold energy, E_o.

7.2 Experimental Approach

In this approach, two data sets are employed for a given sample, one collected with a narrow slit width (150 μm) while the second set is collected with a larger slit width (1mm) yielding a spectrum of lower resolution. In accordance with Eq. (7.1.1), the EXAFS modulations are damped around μ_o, and the intersection points of the two spectra are then nodal points that lie on the background absorption. This can be illustrated by considering the distribution of energies diffracted by the monochromating crystal [Silicon (111)] around some nominal position. In Fig. 1, this distribution (rocking curve) is shown at 9500 eV. It is

obvious that opening the slit will include more photons of different energies, accounting for the observed damping of the EXAFS.

To illustrate this method of background removal, the analysis of the EXAFS data from a 12.5 μm thick copper foil is presented. All measurements were made at room temperature and in the transmission mode utilizing the Caltech Laboratory EXAFS Spectrometer (which is described in Chapter VI). The energy scale of the spectrometer was calibrated by assigning the energy of the copper K_α emission line the value of 8066 eV. Figure 2 shows a plot of the absorption as a function of energy for copper collected with a slit width of 125 μm. Preliminary data analysis involves removing the absorption due to electrons other than the K-shell of copper. This is accomplished by using the Victoreen formula as discussed earlier, and allows the EXAFS to be normalized as given in Eq. (7.1.1).

Figure 3(a) displays the absorption spectra of copper for slit widths of 125 μm and 1 mm. The first peak above the edge in the high resolution spectrum is washed out when the slit is opened. Beyond this point, however, the two spectra are matched peak for peak, with the amplitude of the low resolution spectrum being noticeably damped.

It is important to note that not all intersection points in a given pair of spectra are true nodal points. This is because there are different frequency components of different amplitudes contributing to the EXAFS at each point

in k space. The true isosbestic points become apparent if an additional spectrum is recorded with a third slit width, as shown in Fig. 3(b), and will become more evident in Section 7.3 below. In practice, however, we have found that the extra intersection points lie symmetrically about the true background and contribute negligible errors if they are included in the smoothing spline fit. The loss of the first peak after the edge is not a serious problem since a typical range for data analysis is from k = 4 to 16 Å^{-1}. To obtain the background absorption a computer program is used to calculate the difference in the absorption of the two spectra in Fig. 3(a). Only those points satisfying the average difference of the two spectra in the smooth high k region are chosen for the calculation. These points are then used to generate the background by means of a cubic spline with a high smoothing factor [a small smoothing factor would make the background follows the data more closely, (see Cook and Sayers[4])]. The Victoreen-generated contribution to the absorption is also subtracted from this background to give μ_o in Eq. (7.1.2).

Figure 4 displays the post-edge absorption of the copper foil sample as a function of k, together with the splined background, calculated as described above. Subtracting this background from the total absorption in Fig. 4 yields the desired EXAFS after dividing the difference by μ_o (Fig. 5). Division by μ_o rather than a constant is necessary if a rigorous comparison to the

theoretical EXAFS expression is to be attempted. This normalization makes the EXAFS amplitude independent of the central atom and effectively weights the data more at higher k values.

The modulus of the Fourier transform of the data shown in Fig. 5 is presented in Fig. 6. The data points were weighted by k^3, which is frequently used to balance out the approximate k^{-2} dependence of the scattering amplitude at high k and the k^{-1} factor in Eqn. (7.1.1). This weighting scheme also makes the choice of E_o less critical.

7.3 Computational Approach

The experimentally observed slit function of the EXAFS spectrometer is approximately Gaussian in shape, with full width at half maximum of about 8eV for a 100 μm slit width (Fig. 1). The observed damping of the EXAFS shown in Fig. 3 is the result of increasing the width of this Gaussian distribution as the slit width of the spectrometer is increased. The observed EXAFS is effectively a convolution of the true spectrum with the experimental slit function. In this section we introduce a background determination scheme, which is similar to that described above, except that the convolution is performed by means of a convolution algorithm.

The convolution of a function f(x) with a function g(x) is defined by the convolution integral

$$h(x) = \int_{-\infty}^{\infty} f(t)g(x-t)dt \qquad (7.3.1)$$

For finite functions, the integration limits are determined as follows: If L_1 and L_2 are the lower non-zero values of the two functions and U_1 and U_2 are their upper non-zero values, then the lower integration limit is chosen as $\max(L_1,L_2)$ and the upper integration limit as $\min(U_1,U_2)$. For large data arrays, the convolution integral is readily calculated by means of the fast Fourier transform (FFT) and the convolution theorem. If F(y) and G(y) are the Fourier transforms of f(x) and g(x), respectively, then the convolution theorem states that, the convolution integral [Eq. (7.3.1)] is the Fourier transform of the product of F(y) and G(y). For details on the convolution process, see Brigham.[8]

For the purpose of background determination, the experimentally obtained EXAFS spectrum of a 12.5 μm thick copper foil (Fig. 2) was convolved with a series of Gaussian functions of different widths. A Gaussian distribution function was chosen in view of the shape of the observed slit function, Fig. 1. Furthermore, the smooth tails of the Gaussian distribution help minimize edge effects in the convolution process. To normalize the results of the convolution to the original data, the area of the slit function is set equal to one.

Figure 7(a) illustrates the effect of convolving the experimental EXAFS (shown as dots) with a series of Gaussian functions of different slit widths. Note that the EXAFS is progressively damped as the width of the Gaussian

function is increased. The intersection points of these spectra are not all unique and do not represent true isobestic points. These results are in complete agreement with the experimental observation made in Section 7.2 above. The effect of this convolution process on the copper absorption edge is shown separately in Fig. 7(b). The sharp rise in the edge is smeared out as the width of the Gaussian function is increased. Note that there is a unique intersection point approximately mid-way through the edge. This intersection point was taken to be the threshold energy E_o [See Section (7.4)]. The rest of the analysis is identical to that discussed in the previous section. Figure 7(c) shows the EXAFS plotted along with the background. Note the difference in the background absorption calculated by the two methods [Fig. 4 and Fig. 7(c)]. The k range is smaller in the computational method compared to that in the experimental method. This is due to the slight edge effect resulting from the convolution of the EXAFS with a wide Gaussian function. The distorted points in the computed convolution at high k were discarded. In addition, the background determined by the computational approach does not bisect the peaks in the low k region (below 4 $\AA^{-1}$). The origin of this difference, is the need to choose a single point that lies on the background in the low k region, where no intersection points occur due to the dominant effect of the absorption edge. This is acceptable, however, as the simple EXAFS expression, Eq. (7.1.1), is not valid beyond

this range. In Fig. 7(d), the modulus of the Fourier transform is shown, and agrees well with results obtained by other investigators.[4,9]

7.4 Discussion

The background determination scheme employed above, takes advantage of the fact that all EXAFS components have much higher frequencies than the background. By successively convolving the observed spectrum with a series of increasingly wider Gaussians, the higher frequency components are gradually removed. Eventually all of the EXAFS will be removed and what remains is simply the low frequency background. This method of background determination is not very useful, since serious edge effects occur, due to the large widths of the Gaussians required to smooth out all of the EXAFS. Fortunately, however, there is a limit to the lowest frequency EXAFS component that can exist and is determined by the smallest distance in the system. When only this lowest frequency component remains, increasing the width of the Gaussian, only serves to further dampen this component. The intersection points of these dampened spectra are unique due to the presence of the single remaining EXAFS component. These points are then used to generate the background. It is important to note that the intersection points are not unique until the Gaussian function is sufficiently wide to eliminate all EXAFS components other than the lowest frequency EXAFS

component.

Improper background removal in EXAFS can cause erroneous interpretation of the Fourier transform results, even for data with a high signal-to-noise ratio. In both the experimental and the computational methods described above, the Fourier transform contains structural information up to the fifth shell of copper. There is a low amplitude peak in the 0-1 Å region of the transform indicating the presence of a spurious low frequency component in the isolated EXAFS. This peak is smaller for the computational method than in the experimental technique. The size and position of this peak, however, does not distort the peaks at higher R values which contain the structural information. While the magnitude of such a peak is a measure of successful background removal, it is not the only criterion which must be satisfied. It is important that the calculated background does not add or subtract frequency components which may distort the true EXAFS. The transforms shown in Figs. 6 and 7(d) satisfy the empirical criteria for background subtraction set by Cook and Sayers.[4]

Other experimental methods of damping the observed EXAFS are also possible. If a variable temperature study is performed over a wide range, the nodal points of these data sets may be used to generate the background absorption curve. The damping, however, is more pronounced at high k making the variable slit method more reliable. In laboratory EXAFS systems it is also possible to vary the

bias voltage on the x-ray tube and change the focus size on the anode. This method is equivalent to the variable slit method due to the symmetry of the Johansson geometry. Frequently, however, the dynamic range of the bias voltage is too small to cause sufficient defocusing.

The computational approach is prefered over the experimental method for various reasons. With the variable slit method, the scattered radiation may present a problem so that the ratio of I/I_o is not the same for all slit widths in a smooth region of the spectrum. Also, the experimental approach to the background removal effectively doubles the time necessary for data acquisition. Although this does not present a serious problem in the case of laboratory EXAFS systems, it may restrict the use of this method when data are collected at synchrotron facilities. Furthermore, the peak positions in the low resolution experimental spectrum may not match those in a high resolution spectrum if the spectrometer slit does not open symmetrically with respect to the beam.

The presence of a unique intersection point in Fig. 7(b) may be understood in terms of the theoretically predicted functional form of the x-ray absorption edge. The absorption edge may be constructed from a series of discrete Lorentzians due to bound state transitions. The contribution to the absorption edge, due to transitions into the continuum, may be described in terms of the integral of a Lorentzian, weighted by the appropriate density of states

function. This integral takes the form of an arctangent function.[10] The absorption edge, therefore, consists of a series of discrete Lorentzian functions superimposed on an arctangent function.[6] The convolution process described above is normalized so that the area under each absorption curve is the same, regardless of the width of the Gaussian slit function used. Since the width of the slit functions are much greater than the width of the Lorentzian peaks describing the bound state transitions, the convolution process is insenitive to these features. The normalization, however, constrains the convoluted spectra to pass through the inflection point of the arctangent curve and thus maintains the same integrated absorption for all slit functions. The existence of a unique intersection point can be demonstrated by considering the convolution of a Gaussian function g(x) of width parameter w and an arctangent function c(x), with a sharpness parameter s. The convolution integral is given by:

$$g(x)*c(x) = \int_{-\infty}^{\infty} \exp[-(x-t)^2/w]\tan^{-1}(t/s)\,dt \qquad (7.4.1)$$

where the asterisk (*) represents the convolution of the two functions. Note that the arctangent function c(x) has an inflection at x=0. From symmetry considerations, the value of the convolution integral Eq. (7.4.1), is zero at this inflection point (x=0) and is independent of the width parameter of the Gaussian slit function. This prediction is in complete agreement with the computationally derived

spectra in Fig. 7(b).

Theoretical studies[10] have shown that the inflection point of the arctangent function is a good measure of the threshold energy E_o. Numerical differentiation techniques have been used to locate this inflection point.[7] In practice, these methods are hampered by the presence of bound state transitions. The convolution process, however, is insensitive to these details and provides a good estimate of E_o. Problems occur, however, when the amplitude and the density of states corresponding to the bound state transitions do not differ appreciably from those of the continuum states. In such instances, the bound states may be included in the summation (integration) over the continuum, and hence, become buried in the arctangent function. The unique intersection point will then occur at smaller energies than the threshold energy. In a series of related compounds, the observed intersection point, may be used as a measure of the relative threshold energy.

Advantage may also be taken of the convolution approach presented above to enhance spectral resolution. If the instrumental line shape or slit function is accurately known, a deconvolution algorithm may be used, for instance, to obtain edge structures from data collected with spectrometers that have insufficient resolving power. This is easily achieved by the use of the convolution theorem. If f(k) and g(k) represent the true EXAFS and the experimental slit function, respectively, then the observed

EXAFS is given by:

$$(S_{EXAFS})_{obs.} = f(k)*g(k) \qquad (7.4.2)$$

If $(S_{EXAFS})_{FT}$, F(r) and G(r) are the Fourier transforms of $(S_{EXAFS})_{obs.}$, f(k) and g(k), respectively, then

$$(S_{EXAFS})_{FT} = F(r).G(r) \qquad (7.4.3)$$

Provided that g(k) is known, the true EXAFS, f(k), can be obtained by the Fourier transformation of $(S_{EXAFS})_{FT}/G(r)$.

The use of the deconvolution approach described above to improve resolution is currently being tested. This treatment would be a great advantage in laboratory EXAFS systems since a laboratory spectrometer in which, for example, a channel-cut arrangement [1] is used to improve the resolution, suffers a loss of flux which leads to a lower signal-to-noise ratio. The deconvolution method would offer an alternative that facilitates data acquisition in a reasonable length of time.

In summary, the convolution approach offers a simple and straightforward method for calculating the background absorption in EXAFS. Furthermore, a unique estimate of the threshold energy E_o is obtained. The deconvolution approach offers the possibility of extracting information with improved resolution from experimental spectra.

References

*This chapter is based on: J.J. Boland, F.G. Halaka and J.D. Baldeschwieler, Phys. Rev. **B 28**, 2921 (1983).

1. See for example P.A. Lee, P.H. Citrin, P. Eisenberger and B.M. Kincaid, Rev. Mod. Phys. **53**, 769 (1981).

2. C.A. Ashley and S. Donaich, Phys. Rev. **B 11**, 1279 (1975); P.A. Lee and J.B. Pendry, Phys. Rev. **B 11**, 2795 (1975).

3. T.K. Eccles, SSRL Report No. 78/01 (1978), unpublished.

4. J.W. Cook and D.E. Sayers, J. Appl. Phys. **52**, 5024 (1981).

5. P.H. Citrin, P. Eisenberger and B.M. Kincaid, Phy. Rev. Lett. **36**, 1346 (1976).

6. P.A. Lee and G. Beni, Phys. Rev. B **15**, 2862 (1977).

7. S.P. Cramer, K.O. Hodgson, E.I. Steifel and W.E. Newton, J. Amer. Chem. Soc. **100**, 2748 (1978).

8. E.O. Brigham, The Fast Fourier Transform, (Prentice Hall, New Jersey, 1974).

9. G. Martens, P. Rabe, N. Schwentner and A. Werner, Phys. Rev. B **17**, 1481 (1978); F.W. Lytle, D.E. Sayers and E.A. Stern, Phys. Rev. **B 11**, 4825 (1975).

10. F.K. Richtmyer, S.W. Barnes and E. Ramberg, Phys. Rev. **46**, 843 (1934).

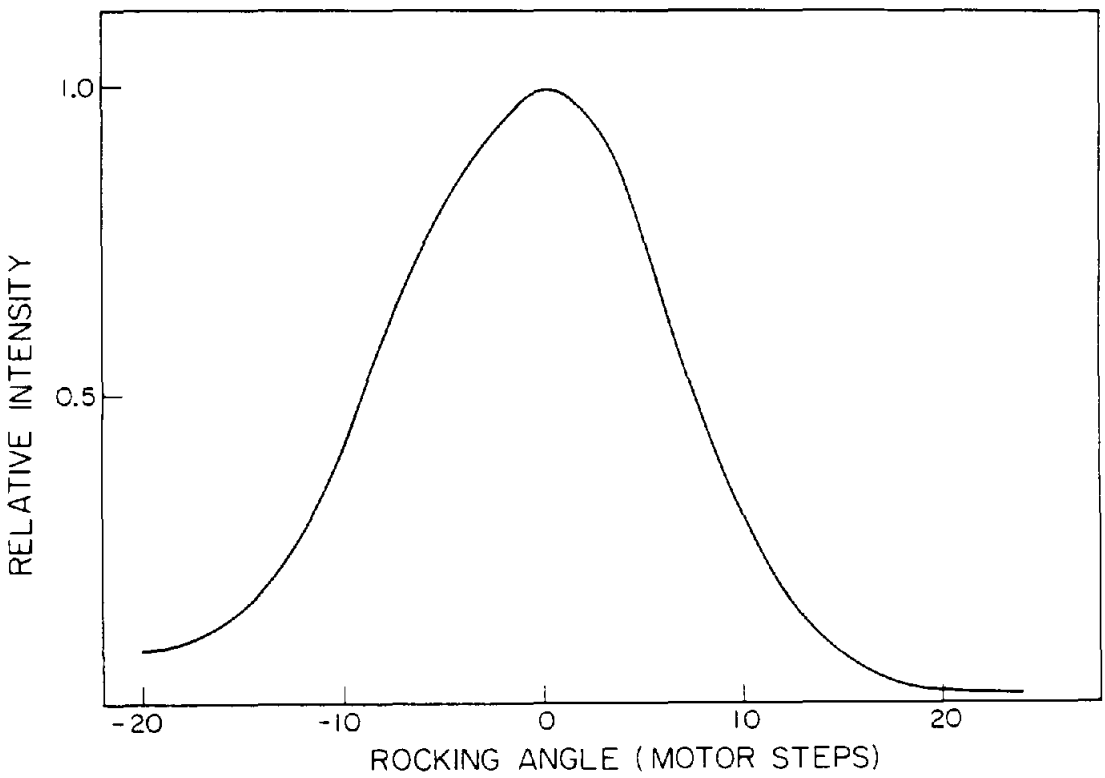

Figure 1.
Spectral distribution of energies diffracted by the monochromator at 9500 eV. This curve was obtained by rocking the Si(111) Johansson crystal about the Bragg angle for diffraction of 9500 eV photons. A narrow slit was used such that the intensity collected from every point on the crystal has a very small angular spread. Note the distribution is slightly asymmetric indicating the increased flux from the source at higher energies (lower Bragg angles).

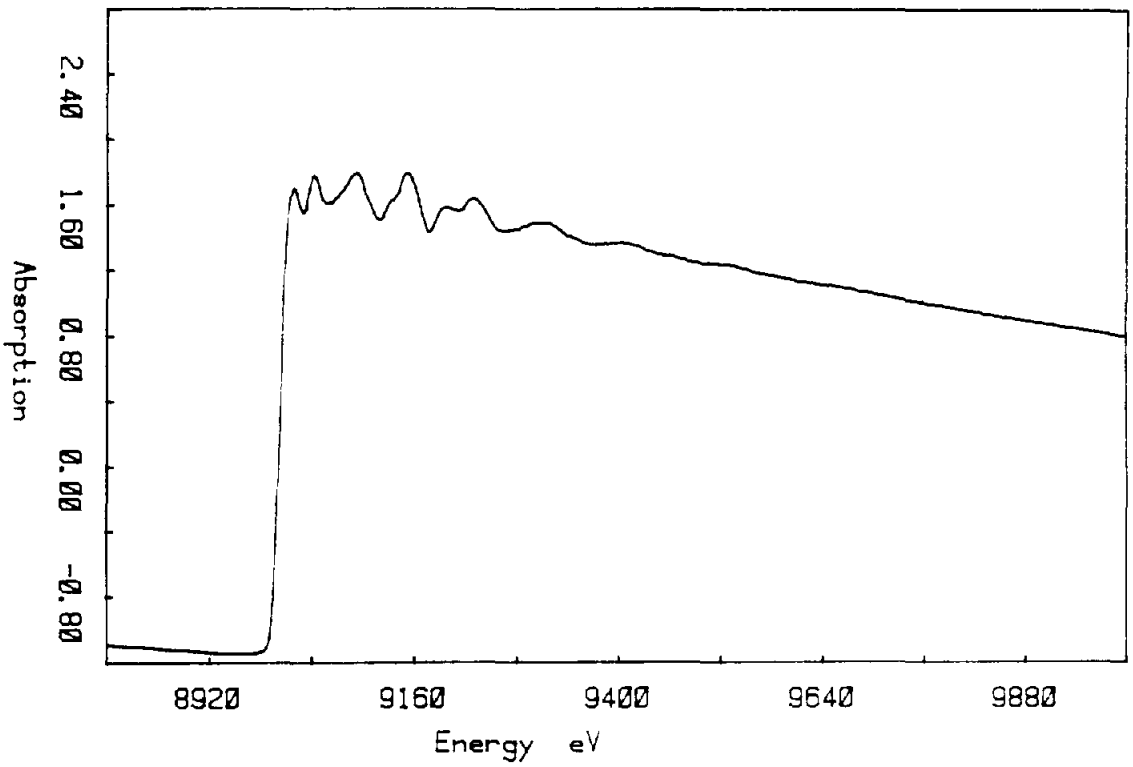

Figure 2.
Plot of the absorption as a function of x-ray energy for a 12.5 micron thick copper foil. The slit width is 125 microns.

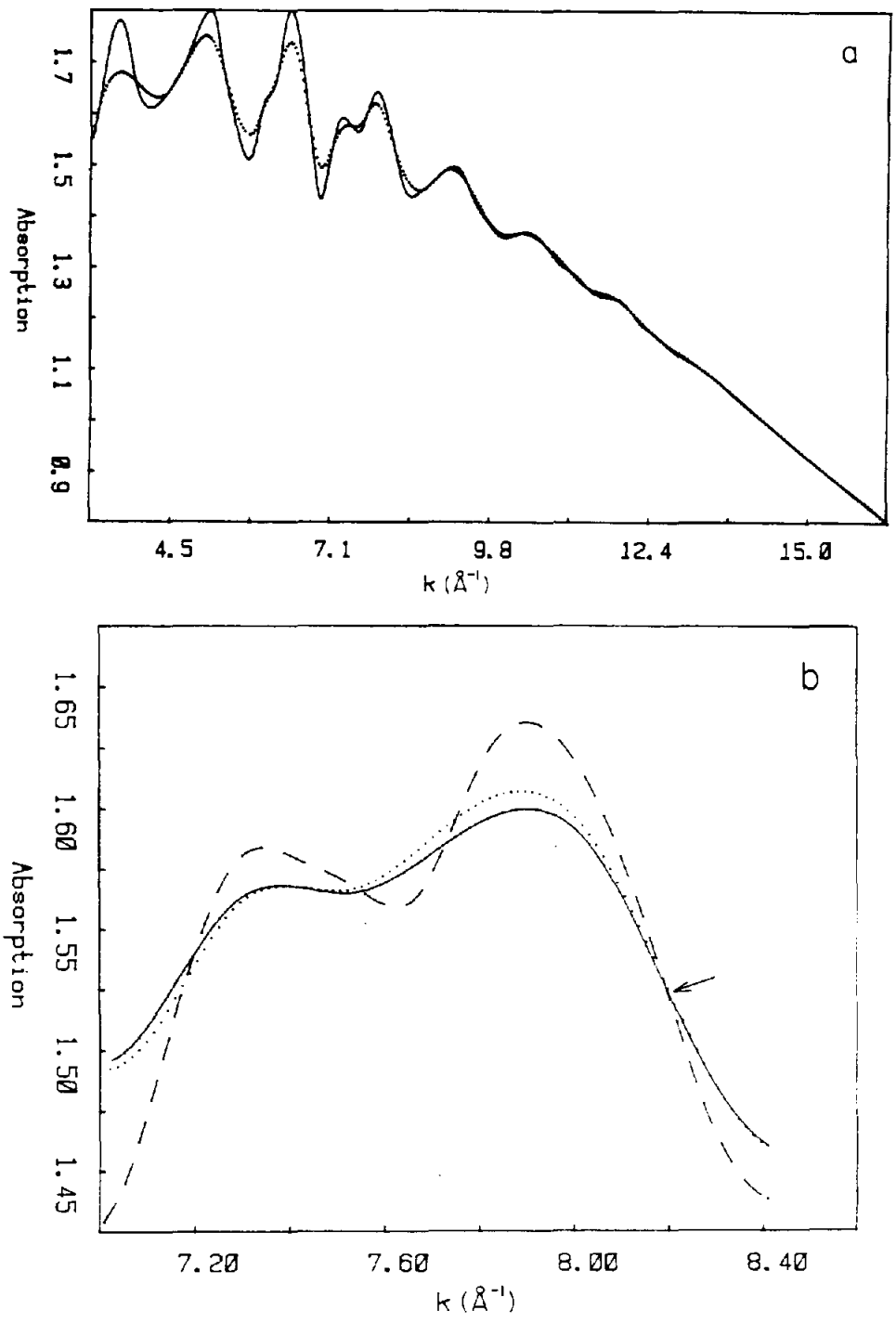

Figure 3.

Plot of the post-edge absorption as a function of the photoelectron wave number. (a) Solid and dashed curves refer to slit widths of 125 microns and 1 mm, respectively. (b) Dashed, dotted and solid curves refer to slit widths of 125 microns, 1 mm and 1.5 mm, respectively. Note that in (b) only one unique intersection point occurs (indicated by the arrow) and represents the only true isosbestic point.

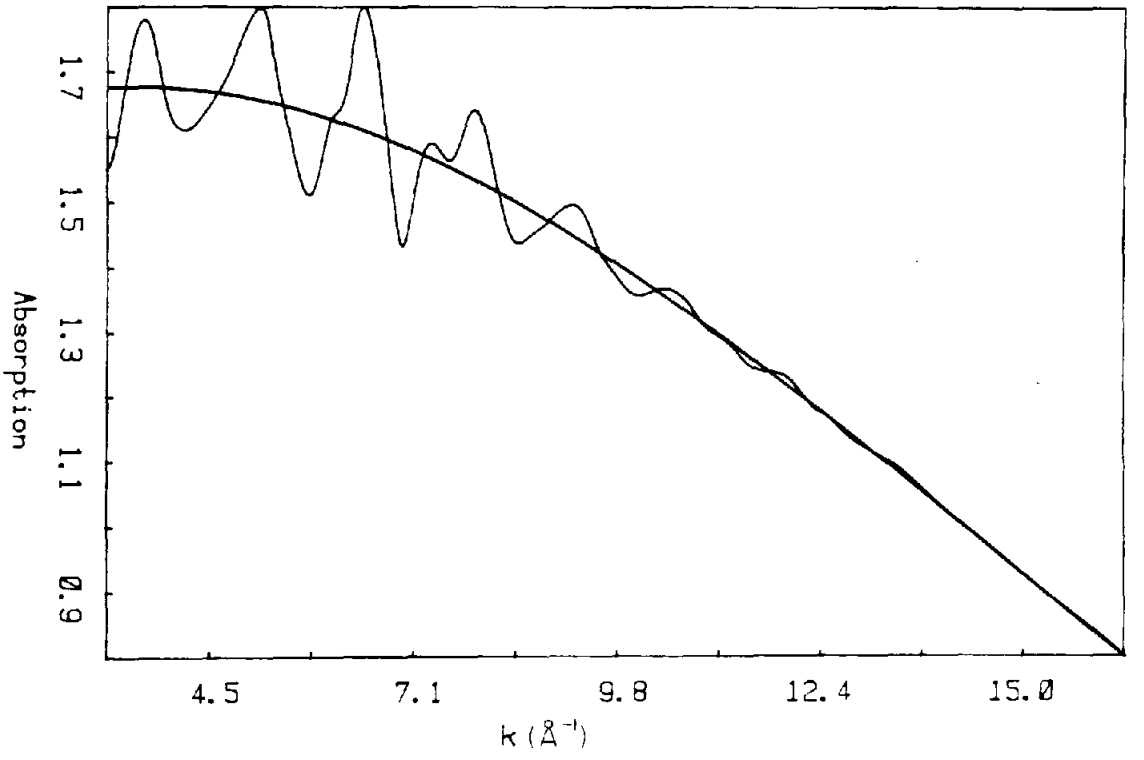

Figure 4.
Plot of the original EXAFS, obtained using a 125 micron slit width, together with the calculated background absorption. The smooth background was obtained by a cubic-spline interpolation of the intersection points of the two curves shown in Fig. 3(a).

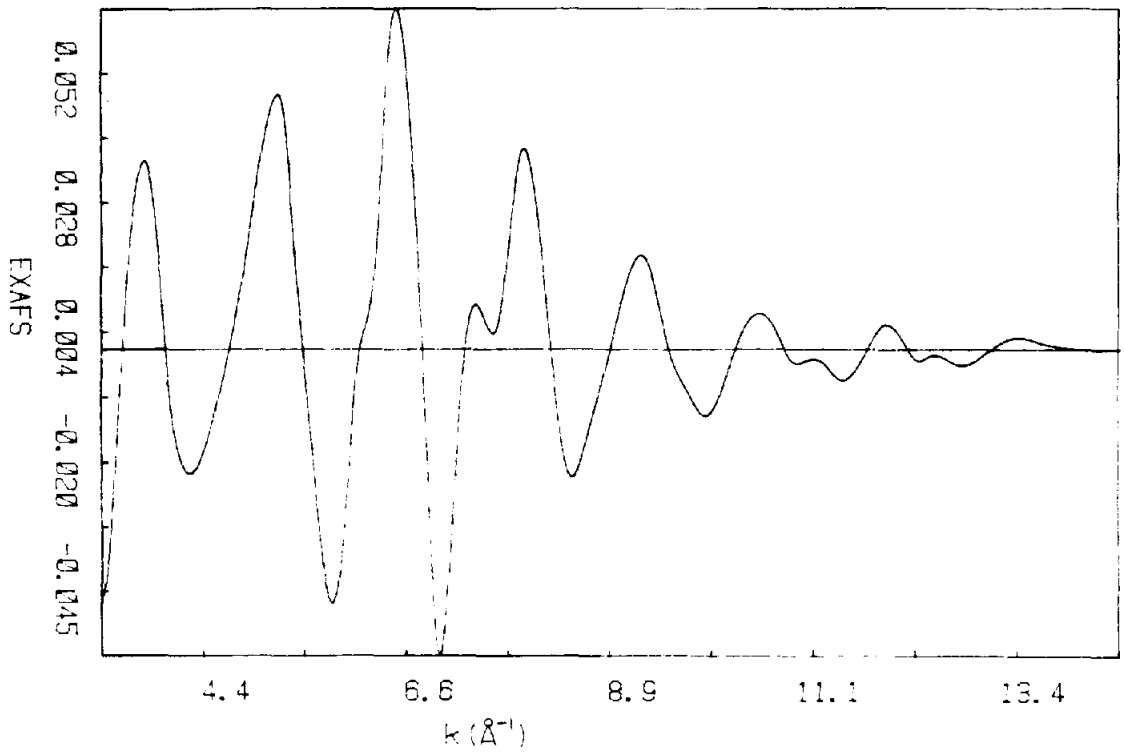

Figure 5.
Plot of the EXAFS as a function of photoelectron wavenumber. The isolated EXAFS was obtained by substracting the two curves shown in Fig.4 and dividing the result by the calculated background.

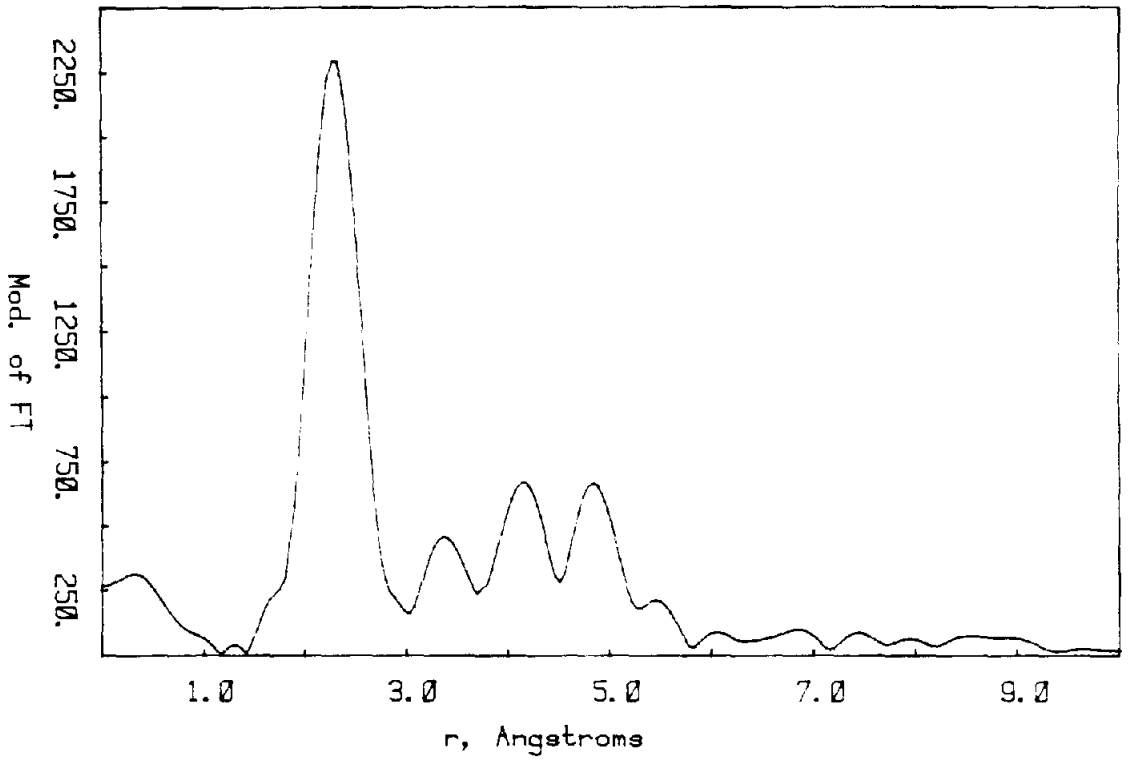

Figure 6.
Modulus of the Fourier transform of the isolated EXAFS from the copper foil sample. The EXAFS was weighted by k^3.

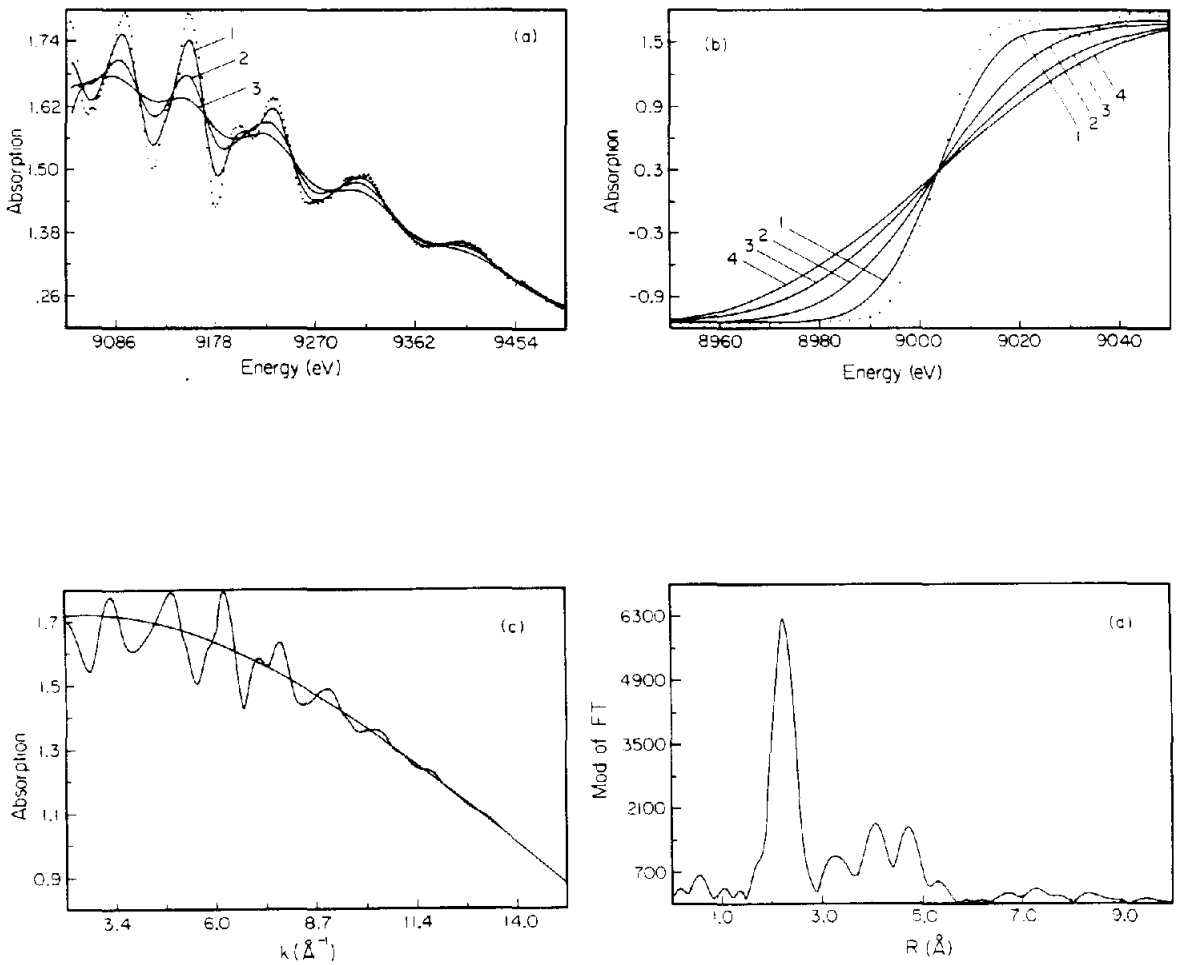

Figure 7.

The background and threshold energy determinations using the computational approach. (a) The experimental EXAFS is shown as dots. Curves 1-3 represent the convolution of the observed EXAFS with Gaussian functions of FWHM of 16, 32, and 48 eV, respectively. (b) The effect of convolution on the absorption edge. Curves 1-4 represent the convolution of the edge with Gaussians functions of FWHM of 16, 32, 48, and 64 eV, respectively. (c) The observed EXAFS together with the calculated background. (d) Modulus of the Fourier transform as determined by the computational method.

CHAPTER VIII

IDENTIFICATION OF NEIGHBORING ATOMS IN EXTENDED X-RAY ABSORPTION FINE STRUCTURE*

8.1 Introduction

Extended X-Ray Absorption Fine Structure (EXAFS) spectroscopy, the modulation in the x-ray absorption coefficient at energies above the absorption edge, has been applied to a wide range of structural problems in recent years. The use of the method is not limited by the physical state of the sample, and hence, it is a valuable tool for determining local structure, in instances where conventional x-ray diffraction methods are not applicable. Such cases include, certain metallo-proteins,[1-3] solutions[4,6] and gases.[7]

The single scattering EXAFS expression may be written as:[8]

$$\chi(k) = -1/k\sum_j A_j \sin[2kr_j + \delta'_j(k)] \qquad (8.1.1)$$

where A_j is the amplitude function. A_j contains the number of atoms of type j, the Debye-Waller factor and the inelastic loss term. k is the photoelectron wavenumber defined by:

$$k = [2m(\hbar\omega - E_o)]^{1/2}/\hbar \qquad (8.1.2)$$

where ω is the frequency of the x-rays and E_o is the threshold energy. $\delta'_j(k)$ is the composite phase shift

function given by:

$$\delta'_j(k) = \delta_a(k) + \delta_j(k) \qquad (8.1.3)$$

$\delta_a(k)$ is the phase change in the photoelectron wave due to the absorbing atom potential and $\delta_j(k)$ is the phase of the scattering amplitude associated with atom j.

Model compounds are used extensively in EXAFS to determine atom types as well as bond distances. Chemical intuition and information available from other techniques usually reduce the number of model compounds that are required. There is usually, however, no independent method to determine the nature of the scattering atom . The backscattering amplitude may exhibit a Ramsauer-Townsend type resonance, and in this manner, the scattering atoms may be identified.[9] These resonances, however, are experimentally observable for heavy scattering atoms only. The identification of light atoms is more difficult since their backscattering amplitudes are small and do not exhibit such structure. A method for distinguishing light atoms (as scatterers) would thus be a valuable addition to EXAFS. For example, differentiating between carbon, nitrogen, or oxygen atoms in metalloproteins or in surface chemistry.

In this chapter, we present a method for identifying scattering atoms by comparing their phases with those of known compounds. We exploit the information contained in the non-linear phases through least squares curve-fitting to show the distinguishability of carbon, nitrogen, and oxygen

in a series of cobalt complexes. Theoretical calculations of the scatterer phases by Teo and Lee[10] clearly demonstrate this point. We now show that such an identification is possible from phases which are properly extracted from EXAFS data. We also introduce a new approach for isolating peaks in R space which minimizes distortion of the phase during the back-transformation process.

8.2 Physical Basis for The Atom Identification Scheme

The total phase of an absorber-scatterer pair in an unknown compound is given by:

$$\phi^{u}_{aj}(k) = 2kr^{u}_{j} + \delta_a(k) + \delta^{u}_{j}(k) \qquad (8.2.1)$$

where the superscript u denotes an unknown, and the subscripts a and j denote an absorbing and scattering atom, respectively. The absorbing atom can easily be identified by its absorption edge, and is assumed to be known. For a known (model) compound with the same absorber,

$$\phi_{aj}(k) = 2kr_j + \delta_a(k) + \delta_j(k) \qquad (8.2.2)$$

We will assume that $\delta_a(k)$ and $\delta_j(k)$ can be expressed as polynomials in k.

$$\begin{aligned} \delta_a(k) &= a_o + a_1k + a_2k^2 + ... \\ \delta_j(k) &= b_o + b_1k + b_2k^2 + ... \end{aligned} \qquad (8.2.3)$$

Substituting $\delta_a(k)$ and $\delta_j(k)$ into Eq. (8.2.2) yields

$$\phi_{aj}(k) = (a_o+b_o) + (2r_j+a_1+b_1)k + (a_2+b_2)k^2 + ... \qquad (8.2.4)$$

or

$$\phi_{aj}(k) = c_o + c_1 k + c_2 k^2 + ... \qquad (8.2.4)$$

Similarily for an unknown compound

$$\phi^u_{aj}(k) = c^u_o + c^u_1 k + c^u_2 k^2 + ... \qquad (8.2.5)$$

Note that the c_1 coefficient contains the distance information.

If the scatterers are the same in both the unknown and model compounds, the corresponding coefficient in Eqs. (8.2.4) and (8.2.5) will be the same provided that the phase isolation is done adequately. In general, the phase difference between neighboring atoms in the Periodic Table is a smooth function of atomic number, the larger the atomic number the more positive the phase. This monotonic behavior is especially true at high k values.[10] Therefore, the scattering phase of, for example, oxygen, is larger at all practical k values than that of carbon.

The method employed in this work, exploits the difference in scattering phase between atoms as a means for their identification. To illustrate this last point, we show in Fig. 1, the calculated scatterer phase functions of Teo and Lee[10] for carbon and oxygen. Note that the curves converge slightly at lower k values. It is apparent that the region of maximum phase separation, and hence the best range for our calculation, is from k = 6 Å^{-1} to k = 13 Å^{-1}. It is also apparent that a least squares fitting method, should give c_o terms that are well separated for carbon and

oxygen, since their scatterer phases are slowly varying. This is the basis for the present work. The value of the c_o coefficient of an unknown compound may be compared to that of a series of model compounds. In this manner the nature of the scattering atom may be established. Note that since c_o is the phase intercept at k = 0 $\AA^{-1}$, this atom identification scheme is insensitive to the absorber-scatterer distance.

8.3 Data Acquisition and Analysis

All EXAFS measurements were made at room temperature and in the transmission made using the Caltech laboratory EXAFS spectrometer (see Chapter VI). The cobalt in the cobalt complexes used in the present study is in the +3 formal oxidation state. All compounds were analytical grade reagents. EXAFS samples were prepared by dissolving a known weight of material in a solvent to make a saturated solution. Another solvent (in which the compound is sparingly soluble) is then added, to precipitate the compound in fine powder form. The powder was filtered, dried, and stored on a polycarbonate membrane. The thickness of the samples was calculated to absorb 70% of the x-ray beam 100 eV above the absorption edge. This method of preparing the sample was found superior, for example, to grinding the sample material to obtain a uniform particle size.

In transmission experiments, the total absorption coefficient $\mu(k)$ is measured as:

$$\mu(k)\ X = \ln(I_o/I) \qquad (8.3.1)$$

where X is the sample thickness, I_o is the incident x-ray beam intensity and I is the intensity after the beam passes through the sample. $\mu(k)$ in Eq. (8.1.1) then calculated as:

$$\mu(k) = [\mu_c(k) - \mu_o(k)]/\mu_o(k) \qquad (8.3.2)$$

where $\mu_c(k)$ is the absorption coefficient corrected for absorption by electrons other than those of the edge under study. This correction is done by using the Victoreen formula:

$$\mu_c(k) = \mu(k) - \mu_v(k) \qquad (8.3.3)$$

where $\mu_v = a\lambda^3 - b\lambda^4$ and a and b are constants and λ is the wavelength of the x-ray photon. $\mu_o(k)$ is the background absorption of the absorbing atom in the absence of ligands for the same sample thickness.

There are several problems that have to be overcome before a successful interpretation of the EXAFS data is possible. It is apparent from Eqs. (8.1.1) and (8.3.2) that a knowledge of μ_o is essential before a comparison may be made between the theoretical expression and the experimental data. It is also evident from the definition of k [Eq. (8.1.2)], that an accurate estimate of E_o is necessary for a correct k scaling. An accurate k scaling is important since the data are typically Fourier transformed to give peaks in R space; the position of these peaks will depend on the

choice of E_o. An incorrect k scale will also hamper attempts to least-squares fit the theoretical expression [Eq. (8.1.1)] to the data. The presence of non-linear phase shifts also complicates the data analysis, and results in a distribution of frequencies in k space. The transformed peaks in R space are thus broad and asymmetric. This non-linearity will also affect the peak positions in R space if different k ranges are taken for transformation. For this reason, data analyses of model compounds and unknowns are typically Fourier transformed with the same k range.

In an earlier communication,[11] we presented a method for the determination of both μ_o and E_o (see Chapter VII). In that method, the raw EXAFS is convoluted with a series of Gaussian functions, resulting in a damped EXAFS spectrum. The intersection points of this series of transformed spectra are used to generate the background absorption. We have also demonstrated that, a unique intersection point exists at the absorption edge, and that this intersection point provides a relative measure of the threshold energy. An example of such an intersection point is shown in Fig. 2 for $Co(acac)_3$. The distortions that occur at the edges of the data arise from the nature of the convolution algorithm.[11] The convolution method represents a straightforward approach for the determination of both μ_o and E_o, and is the method used throughout this present work.

This atom identification scheme requires the measurement of the phase intercept to an accuracy of at

least 0.1 radians (see Fig. 1). The method used to isolate the data range to be transformed should minimize spurious sidelobes in the Fourier transform and keep the phase unchanged. In the forward transform (FT of EXAFS data from k space to R space) this may be accomplished by ensuring that the data begin and end at a node. For the back transform, however, the problem is more difficult because of the presence of side lobes about the base of the peak which is to be isolated. In this case, only the undistorted part of the peak [shaded area in Fig. 4(a)-(e)] is transformed. To avoid distortions which result from applying a window for the isolation, the desired region of the peak is translated down to the distance axis. The rest of the data in R space are set equal to zero. The peak now starts and ends at zero modulus values (nodes in both real and imaginary parts). In practice, this is accomplished by substracting the lowest modulus value in the region to be backtransformed, from the modulus at every point in that region. This can be performed without changing the phase. If we denote the lowest modulus value by A_o, then we require that for each point:

$$A_j = A_i - A_o \tag{8.3.4}$$

where the subscript j denotes a new value and i the old one. Requiring that the phase remains unchanged implies that

$$\phi(k) = \tan^{-1}[(Im_i)/(Re_i)] \tag{8.3.5}$$

is invariant. But since we may write A_i and A_j in the form:

$$A_i = [(Re_i)^2 + (Im_i)^2]^{1/2} \qquad (8.3.6)$$

we can construct an expression for the new real and imaginary parts of the data, in terms of the original amplitude and phase:

$$\begin{aligned} (Im_j) &= \tan\phi(k)\ [(A_j)^2 - (Im_j)^2]^{1/2} \\ (Im_j) &= \pm \{[(A_j)^2 \tan^2\phi]/[\tan^2\phi + 1]\}^{1/2} \end{aligned} \qquad (8.3.7)$$

$$(Re_j) = \pm [(A_j)^2 - (Im_j)^2]^{1/2} \qquad (8.3.8)$$

The signs in Eqs. (8.3.7) and (8.3.8) are chosen such that the original signs of the real and imaginary components remain unchanged. It is evident that the amplitudes will be smaller using this window method. This is not a serious problem in our present goal of identifying atoms from their phases since the phases remain unchanged. In the next section, we shall show that other windowing techniques also change the amplitude.

8.4 Results and Discussion

The isolated EXAFS patterns for the cobalt series of compounds: $Co(acac)_3$, $[Co(en)_3]Cl_3$ and $K_3[Co(CN)_6]$ are shown in Fig. 3. The modulus of the k^3 weighted FT of each of these compounds is presented in Fig. 4. The shaded portion of the first-shell peak in each transform represents the region of R space which was backtransformed into k space using the procedure described in the previous section. The

total phase was extracted from the first-shell EXAFS using the method described by Lee et al.,[12] and was subsequently fitted to a polynomial in k [Eq. (8.2.5)]. The fit was tried for several polynomials with different degrees in k. We have found that a second order polynomial gives an adequate fit. Figure. 5 shows the isolated phase together with the polynomial fit for each of the three compounds. Table I contains the coefficients of the polynomial fit for several fitted ranges of k space.

Table I shows that the constant coefficient in the polynomial fit for each of the three compounds is approximately independent of the fitted k range, provided the minimum k value in the fit is greater than 6.5 Å^{-1}. This observation is in agreement with the calculated phases shown in Fig. 1. Since only high k data are analyzed, the coefficients obtained from the fit are relatively insensitive to the choice of the threshold energy E_o. Furthermore, the small spread in the values of the coefficients in Table I may be attributed to a small higher-order component in the phase. Note that the difference in the phase intercepts between the oxygen and carbon compounds is approximately 0.7 radians. This difference is smaller than that predicted by Fig. 1 but is quite acceptable since the phases of oxygen and carbon converge somewhat at lower k values (Fig. 1). Lee et al.[13] have shown that the composite phase shift may be fitted to the function,

$$\delta'(k) = c_o + c_1 k + c_2 k^2 + c_3/k^3 \qquad (8.4.1)$$

and that the coefficients obtained are linear functions of atomic number over small regions of the Periodic Table. The quadratic form of Eq. (8.2.5), was used instead of Eq. (8.4.1), since the latter function is not defined at the origin. Despite this, we have found that the phase intercept of the nitrogen compound lies approximately in between that of the oxygen and carbon compounds, so that the constant coefficient is still an approximately linear function of atomic number (see Table I). This quadratic function, however, does not accurately describe the scattering phase for heavy atoms especially in the low k region.[13] Since EXAFS data from such heavy scatterers extend out to high k values, it is still possible to use the quadratic form of Eq. (8.2.5) provided only the high k data are fitted. This forms the basis for identification of scattering atoms which are heavier than those discussed here.

It should be noted,[11] however, that the phase can only be calculated to within an arbitrary factor of π. If 3π is added to the phase intercepts for the oxygen and carbon compounds, intercepts of 1.756 and 1.049 radians are obtained, respectively. These intercepts are in good agreement with the values calculated by Lee et al.,[13] especially when the range of the fitted data is considered. A factor of $n\pi$ should, however, be easily identifiable,

since the separation between the phases of carbon and oxygen in Table I (see also Fig. 1) is 0.7 radians, which is small in comparison to π. In practice, we have found that if the same data range is transformed for all compounds, there is no need to add or substract multiples of π.

The ability to distinguish between and identify different scattering atoms is dependent on the manner in which the EXAFS data are treated. The isolated phase extracted from experimental data is sensitive to windowing effects. In the forward transform no window function was used; the data analyzed began and ended at a node. This procedure yields good results provided an accurate background absorption has been determined and subtracted, such that the end points chosen for the analysis are true nodal points.

The isolation of a peak in R space is more difficult, however, since the peak amplitude rarely drops rapidly to zero because of the non-linearity in the phase. Furthermore, the peak usually contains side lobes due to termination errors in the transform. Any isolation procedure results in the data in the inverse space being the convolution of the FT of the isolated data with the FT of the window function. If a high percentage Gaussian window is used, the FT of the isolated peak is convoluted with a narrow Gaussian in k space. In addition, the data in k space also contain much of the information which was present in the side lobes around the base of the peak. To eliminate

this problem, a low percentage Gaussian window may be used. However, the FT of the isolated peak is then convoluted with a wide Gaussian in k space. In principle, it is possible to remove the effects of the window function by a deconvolution process. In practice, however, this procedure introduces noise and suffers from the same problems as those found in the original transform.

As an alternative to the above methods, we have introduced a new isolation procedure. As described in the previous section, the phase information is constrained to be the same as that in the original peak in R space while the amplitude is reduced such that the real and imaginary parts of the transform begin and end at a node. A comparison of this method with other isolation methods is shown in Fig. 6. The data shown in this figure are from the isolated first-shell peak in $[Co(en)_3]Cl_3$. Note the distortions present in the amplitude and phase of the isolated peak when a 20% (dotted curve) and a 5% Gaussian window (dashed curve) are used. As noted by previous investigators the distortion appears to be greatest in the first and last oscillations in k space.[12] This, however, does not guarantee that the data in between are undistorted, since the sides of the peak which are multiplied by a Gaussian window function in R space, receive a contribution to their intensity from all points in k space. The distortion is greatest in the first and last oscillation in k space because the amplitude of the original data is smallest in these regions. The present

method (solid curve) does not introduce such distortions since no window function has been employed. This method, however, does suffer from the usual termination effects due to the finite data range in the discrete transform.

We have found this new peak isolation technique to be superior when an accurate phase measurement is required. Since the atom identification scheme requires an accurate knowledge of the phase intercept, slight distortions in the phase due to the usual windowing procedures are sufficient to make such a measurement impractical. The coefficients obtained from the quadratic fit are moderately sensitive to the width of the peak transformed in R space. This can be explained by considering the nature of the peak shape. Each peak in R space contains, due to phase non-linearity, a distribution of frequencies from k space. The quadratic form used here may contain the most significant terms in such a distribution, but not all of them. It is clear then that FT of peaks in R space with different widths may contain variable contributions of higher-order terms in k. Accordingly, the most reliable phase intercepts are obtained when the peaks in R space are transformed with the same width (base of dashed area in Fig. 4).

To illustrate the quantitative nature of this atom identification scheme, a fourth compound, $[Co(NH_3)_6]Cl_3$, was studied. The isolated EXAFS and the k^3 weighted FT of this compound are shown in Fig. 7. Using the procedure described above, the phase of the first-shell peak was extracted and

fitted to a quadratic function. The coefficients of the fit are shown in Table II for a series of fitted k ranges. Note that the phase intercept for this compound is virtually identical to that obtained for $[Co(en)_3]Cl_3$ (see Table I). Therefore, if $[Co(NH_3)_6]Cl_3$ were an unknown compound, a comparison of its phase intercept with the three model compounds studied earlier would reveal that $[Co(en)_3]Cl_3$ is the appropriate model compound, and that the scattering atom is a nitrogen.

In many instances, however, the first coordination sphere is comprised of different types of atoms. If the separation in distance is greater than 0.4 Å, the FT will distinguish between the different distances, and the above analysis may be applied to each separate peak. Often this is not the case and only one first shell peak is observed in the FT. When this happens, the isolated phase is dependent upon the amplitude of the individual components which make up the peak. Consider a two component first shell consisting of N_A atoms of type A and N_B atoms of type B. Clearly,

$$N_A + N_B = N \tag{8.4.2}$$

where N is the coordination number of the first shell. Let A(k) and B(k) be the EXAFS amplitude of components A and B, respectively. The EXAFS corresponding to the first shell-peak is given by:

$$Z(k) = A(k)\sin\phi_A(k) + B(k)\sin\phi_B(k) \tag{8.4.3}$$

where $\phi_A(k)$ and $\phi_B(k)$ are the total phases of components A and B. If Eq. (8.4.3) is Fourier transformed and only the positive distances are retained, then the back transformed EXAFS may be described by:[12]

$$\begin{aligned}\hat{Z}(k) &= 1/2i[A(k)e^{i\phi_A(k)} + B(k)e^{i\phi_B(k)}] \\ &= |\hat{Z}(k)|e^{i\theta(k)}\end{aligned} \tag{8.4.4}$$

where $\theta(k)$ is the observed total phase which may be expressed as:

$$\theta(k) = \tan^{-1}\left\{\frac{A(k)\sin\phi_A(k) + B(k)\sin\phi_B(k)}{A(k)\cos\phi_A(k) + B(k)\cos\phi_B(k)}\right\} - \pi/2 \tag{8.4.5}$$

A factor of $\pi/2$ is typically added to Eq. (8.4.5) to yield the physically significant phase $\theta'(k)$.[12] If each of the phase functions can be parameterized as follows:

$$\begin{aligned}\phi_A(k) &= a_o + a_1k + a_2k^2 \\ \phi_B(k) &= b_o + b_1k + b_2k^2\end{aligned} \tag{8.4.6}$$

Then the extrapolated value of the phase intercept is given by:

$$\theta'(0) = \tan^{-1}\left\{\frac{A(0)\sin a_o + B(0)\sin b_o}{B(0)\cos a_o + B(0)\cos b_o}\right\} \tag{8.4.7}$$

If the total coordination number is known, and we assume that

$$N_BA(k) = N_AB(k) \tag{8.4.8}$$

then the nature of the coordination sphere may be determined since we have two equations, Eqs. (8.4.2) and (8.4.7), and two unknowns, N_A and N_B. Using the phase intercepts shown in Table I, Eq. (8.4.7) has been plotted in Fig. 8 as a function of N_A and N_B, assuming the approximation in Eq. (8.4.8) to be valid. For any observed phase intercept $\theta'(0)$ in Fig. 8, there are two possible compositions of the first shell. In general, however, only one of these compositions will correspond to an integer number of atoms.

Unfortunately, the approximation in Eq. (8.4.8) is not generally valid. In the worst case of a coordination sphere made up of oxygen and carbon atoms, the scattering amplitude of the oxygen can be approximately 30% greater than that of the carbon.[10] The metal-carbon bond distance, however, is typically shorter than the corresponding oxygen distance, which partially offsets the difference in the scattering amplitudes. In general, Eq. (8.4.8) should be rewritten as:

$$N_B A(k) = N_A B(k)\ X \qquad (8.4.9)$$

where X is a factor, assumed to be constant, which represents the difference between the EXAFS amplitudes of components A and B. Equation (8.4.9) must be substituted into Eq. (8.4.7) to obtain the true dependence of the phase intercept on the number of atoms in each component. If component A is oxygen and component B carbon, then Table III shows the observed phase intercepts for several X values. Note that increasing the value of X shifts the phase

intercept to a more positive value, and hence, weights more strongly the contribution of the oxygen atoms to the observed phase. This shift, however, is small so that even if the EXAFS amplitude due to oxygen is 50% greater than that due to carbon the composition of the shell will still be distinguishable from other possible compositions (see Table III).

It should be noted, however, for this method to yield reliable atom identification, several criteria must be met. The raw data must be of high quality for both the model and unknown systems. The subsequent analyses of the data should be performed in the same manner for all compounds. An incorrect estimation of E_o presents a major problem. The method of determining E_o discussed in Chapter VII should be adequate, provided the compounds do not differ greatly in their edge structure. If a known compound exhibits edge structure which differ from that of the unknown, this compound must be viewed as an unsuitable model compound for the latter.

The identification scheme introduced here represents a contribution to current methods for EXAFS data analyses. The examples shown demonstrate the distinguishability of carbon, nitrogen and oxygen in a series of cobalt complexes. These three atoms represent important scatterers, the identification of which may help to resolve significant structural problems. For example, in metalloproteins, the first-shell metal ligands consist primarily of nitrogen,

oxygen and sulfur from the protein amino acids. Since this approach can be readily extended to other scattering atoms there should be numerous chemical applications of this identification scheme.

References

*This chapter is based on: F.G. Halaka, J.J. Boland and J.D. Baldeschwieler, J. Amer. Chem. Soc. in press (1984).

1. P. Eisenberger, M.Y. Okamura and G. Feher, Biophys. J. **37**, 523 (1982).

2. B. Chance, R. Fischett and L. Powers, Biochemistry **22**, 3820 (1983).

3. L. Powers, Biochem. Biophys. Acts **683**, 1 (1982).

4. T.M. Hayes, J.W. Alen, J. Tauc, B.C. Giessen and J.J. Hauser, Phys. Rev. Lett. **36**, 134 (1975).

5. P. Eisenberger and B.M. Kincaid, Chem. Phys. Lett. **36**, 134 (1975).

6. D.R. Sandstrom, J. Chem. Phys. **71**, 2381 (1979).

7. B.M. Kincaid and P. Eisenberger, Phys. Rev. Lett. **34**, 1361 (1975).

8. D.E. Sayers, F.W. Lytle and E.A. Stern, Advance in X-Ray Analysis **13**, 248 (1970).

9. P.A. Lee and G. Beni, Phys. Rev. Rev. **B15**, 2862 (1977).

10. B.K. Teo and P.A. Lee, J. Amer. Chem. Soc. **101**, 2815 (1979).

11. J.J. Boland, F.G. Halaka and J.D. Baldechwieler, Phys. Rev. **B 28**, 2921 (1983).

12. P.A. Lee, P.H. Citrin, P. Eisenberger and B.M. Kincaid Rev. Mod. Phys. **53**, 769 (1981).

13. P.A. Lee, B.K. Teo and A.L. Simons, J. Amer. Chem. Soc. **99**, 3856 (1977).

14. J.R. Taylor, Scattering Theory (Wiley, New York 1972) p. 181.

15. E.A. Stern, B. Bunker and S.M. Heald, EXAFS Spectroscopy: Techniques and Applications; edited by B.K. Teo and D.C. Joy (Plenum Press, New York 1981).

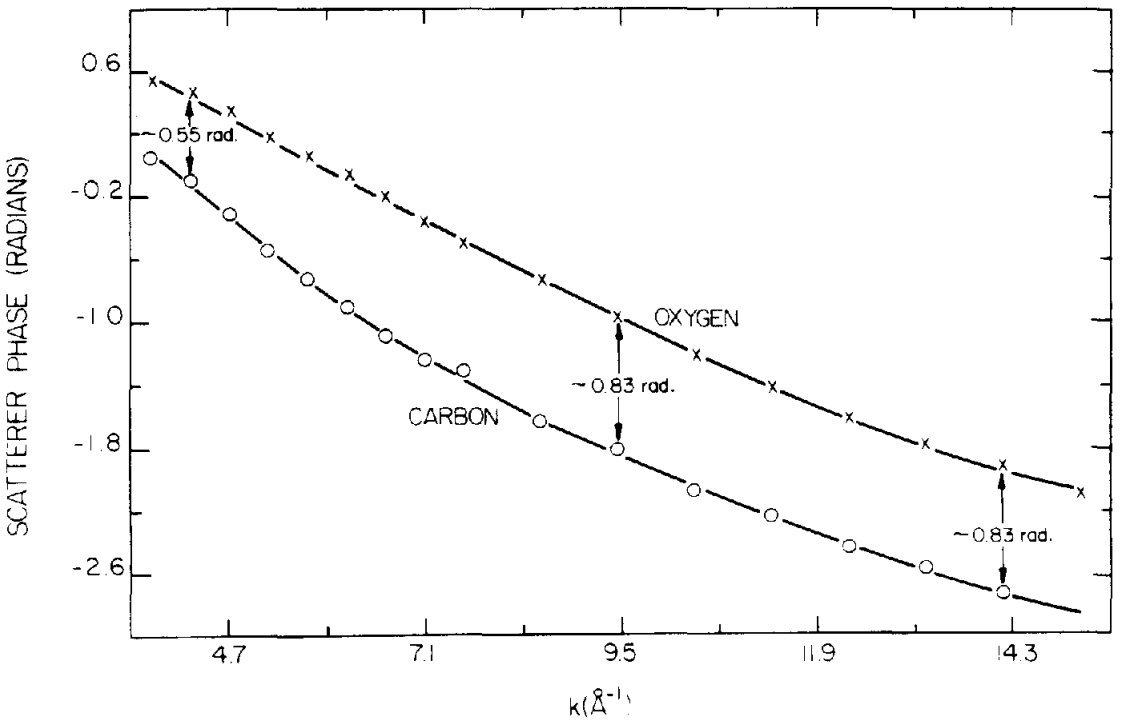

Figure 1.
The scattering phases of carbon (o) and oxygen (X) as calculated by Teo and Lee.[10] The solid curves are spline fits to the calculated data.

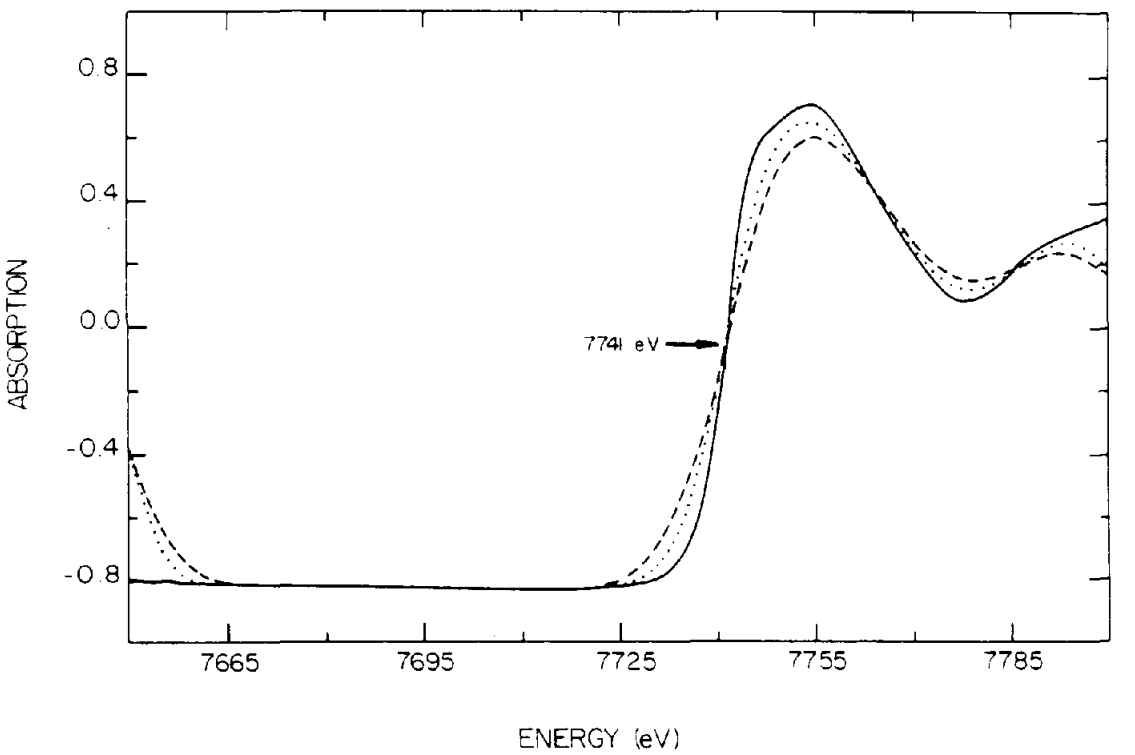

Figure 2.
Determination of the threshold energy (E_o) for $Co(acac)_3$. The solid line is the original data. The dotted and dashed curves correspond to convoluting the data with Gaussian functions of FWHM of 16 eV and 32 eV, respectively. The unique intersection point at the edge corresponds to the E_o used in this work.

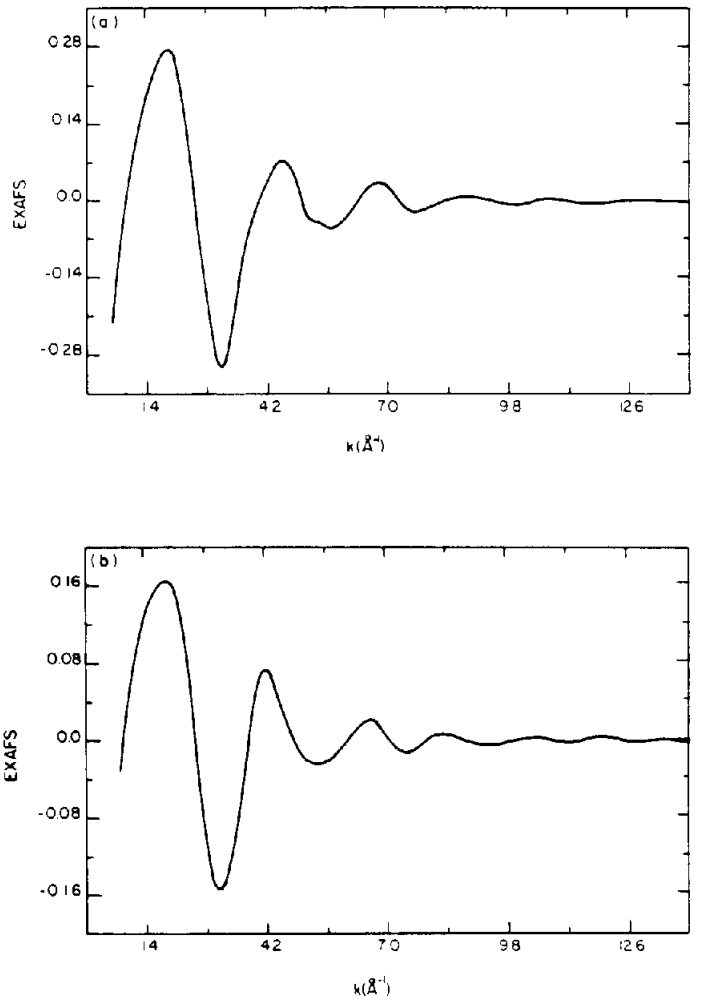

Figure 3.
Isolated EXAFS spectra: (a) $Co(acac)_3$. (b) $[Co(en)_3]Cl_3$. (c) $K_3Co(CN)_6$].

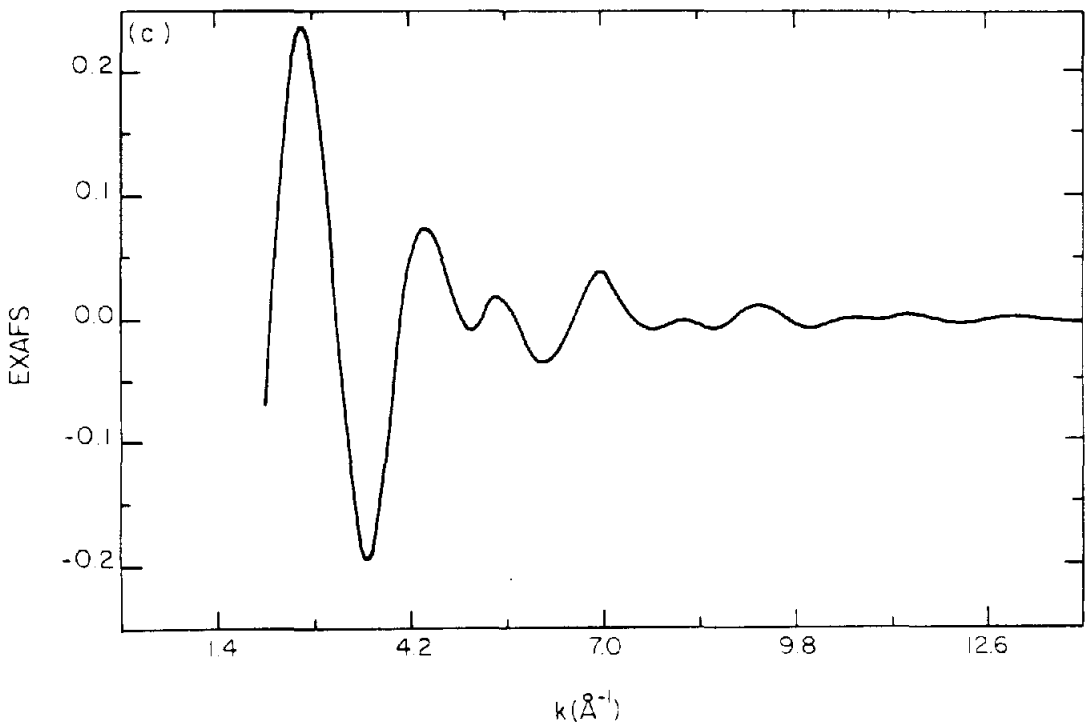

Figure 3, continued.

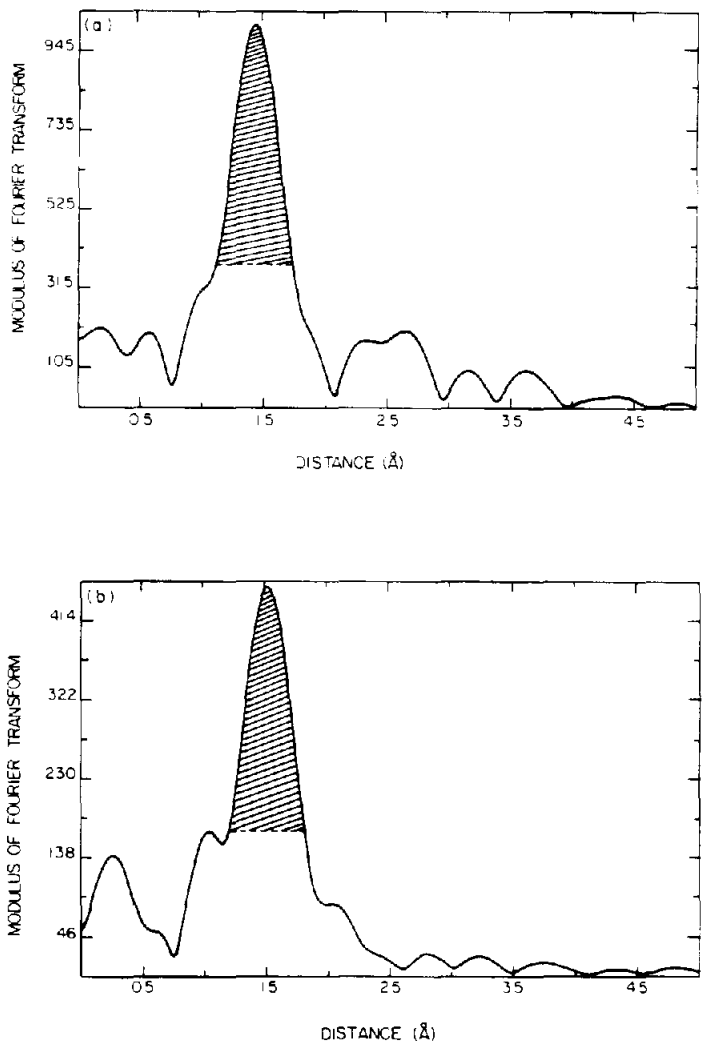

Figure 4.
Modulus of the FT of the k^3 weighted EXAFS. (a) $Co(acac)_3$. (b) $[Co(en)Cl_3]$. (c) $K_3[Co(CN)_6]$. The shaded area in each transform represents the region of R space which was backtransformed into k space using the windowing procedure described in the text.

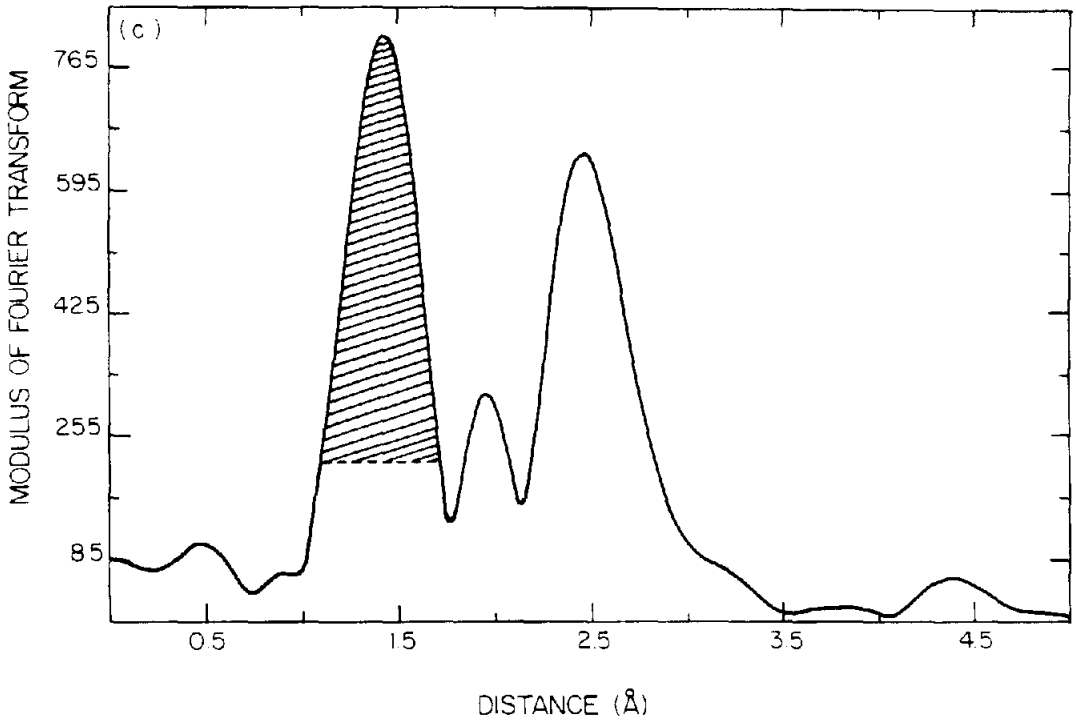

Figure 4, continued.

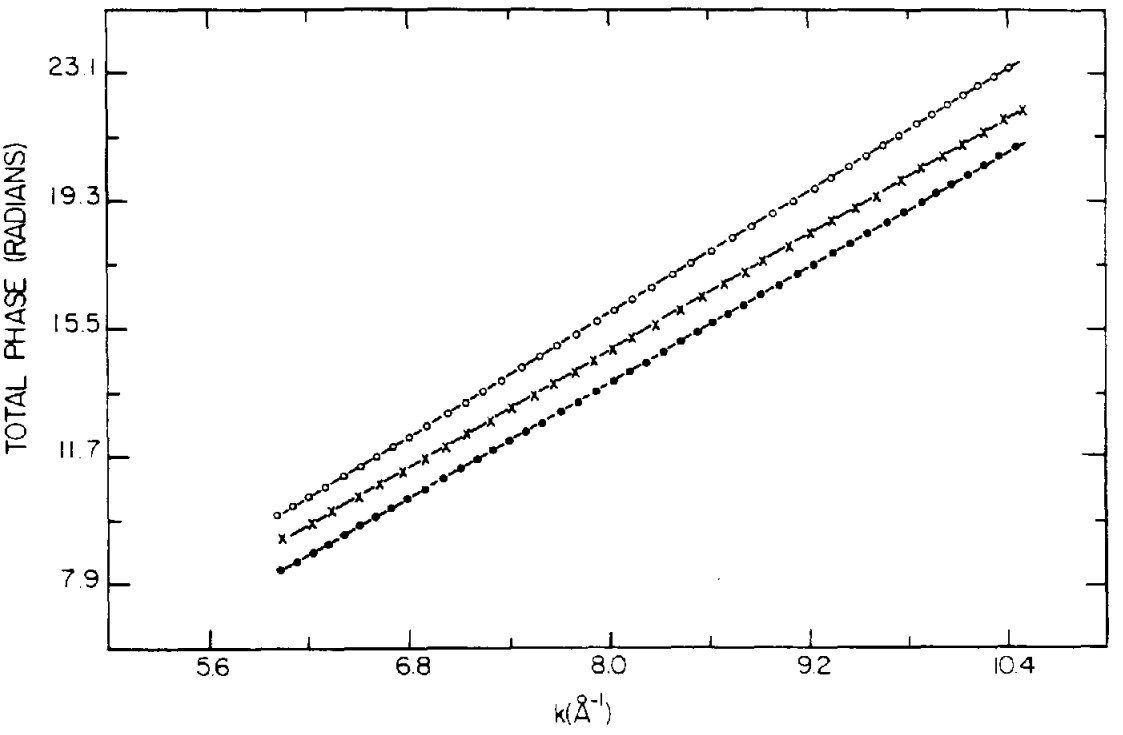

Figure 5.
Total phase isolated from the first-shell peak in $Co(acac)_3$ (X), $[Co(en)_3]Cl_3$ (open circles) and $K_3[C_o(CN)_6]$ (closed circles). The solid curve represents the best fit to a quadratic function. Only every fourth data point is shown.

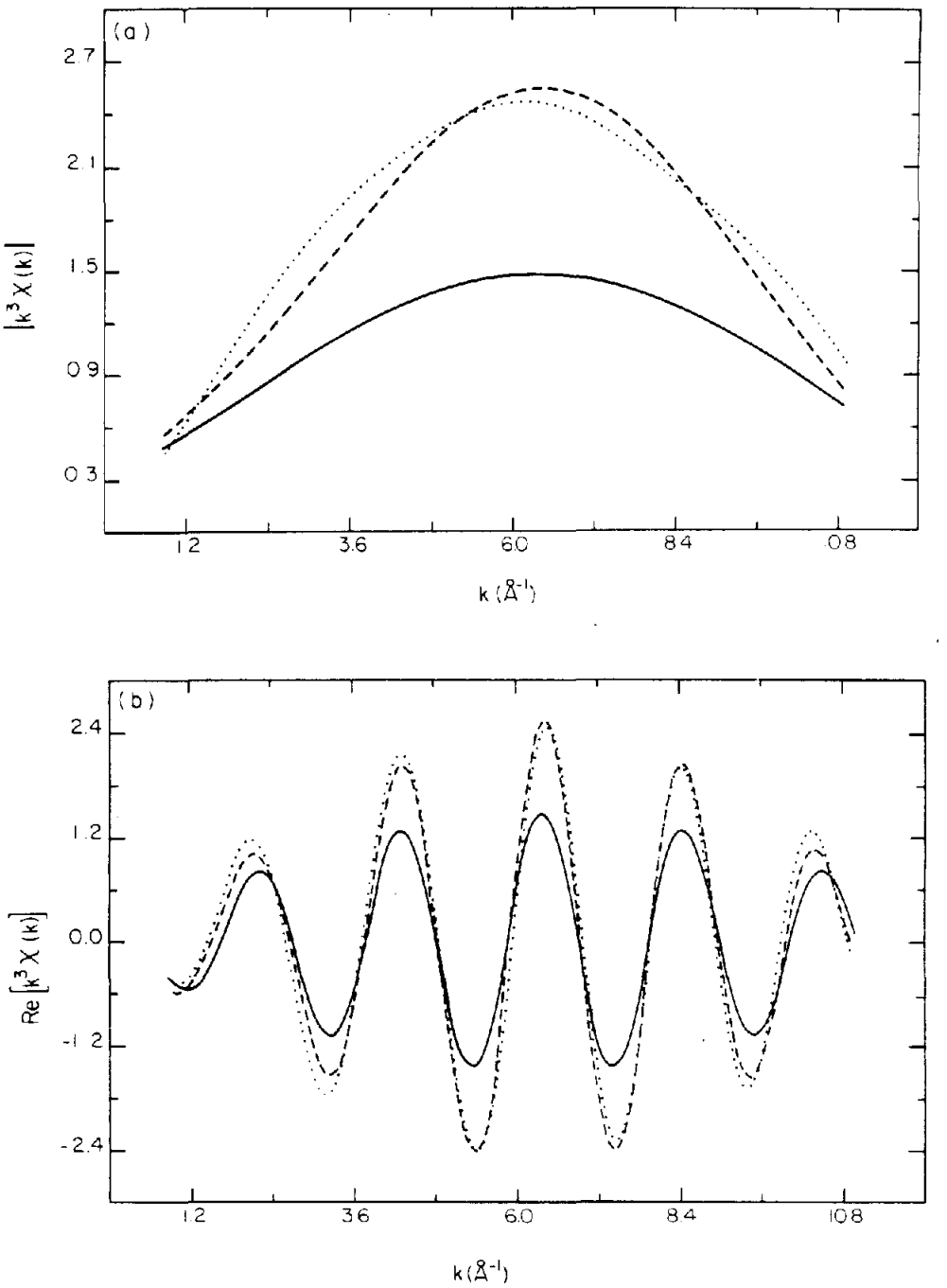

Figure 6.

A comparison of the new windowing procedure with the earlier methods. The first shell peak in the $[Co(en)_3]Cl_3$ compound was isolated using the present method (solid curve), a 20% (dotted curve) and a 5% Gaussian window (dashed curve). (a) Modulus of the k^3 weighted EXAFS. (b) Real component of the k^3 weighted EXAFS.

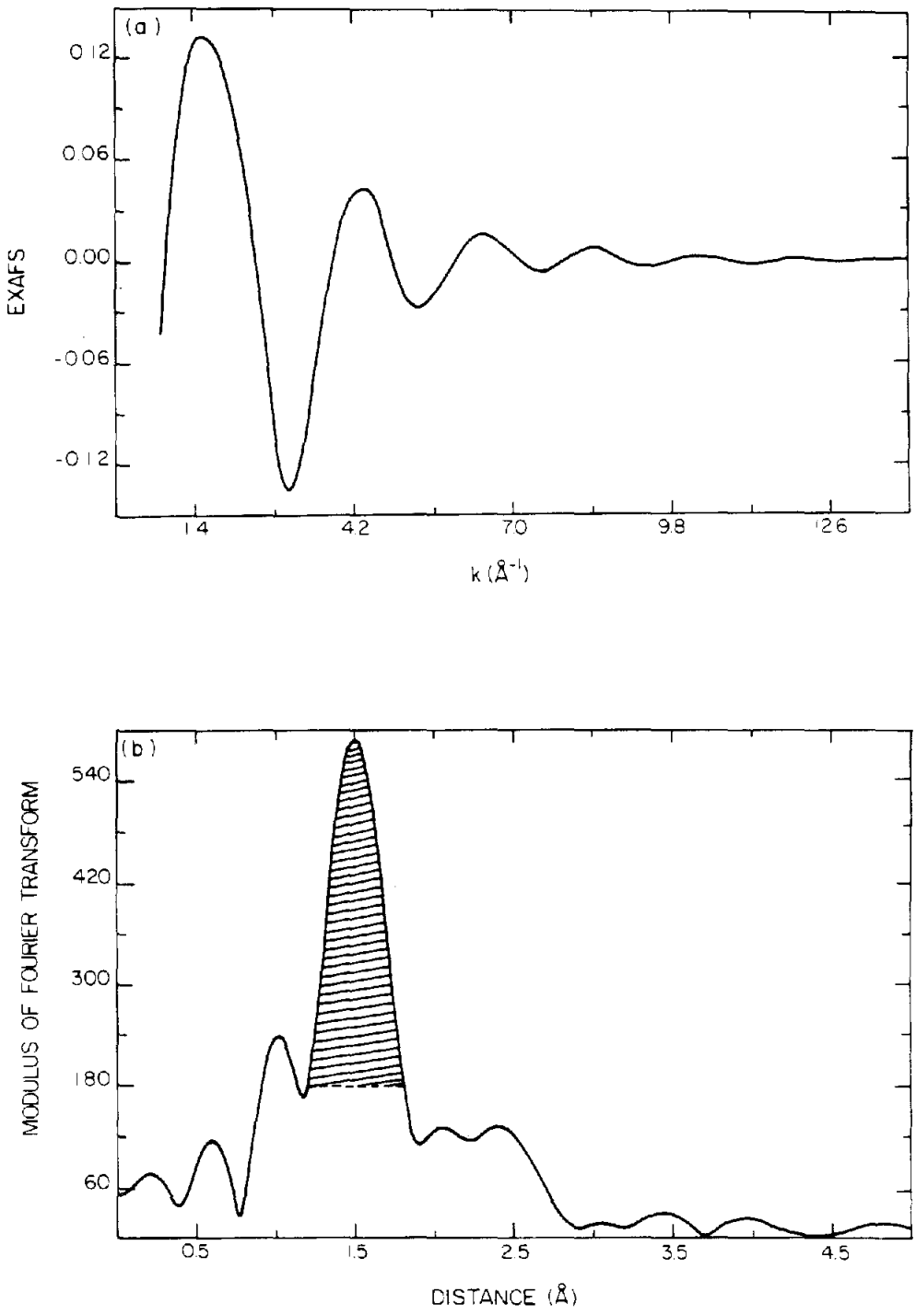

Figure 7.
(a) Isolated EXAFS from the $[Co(NH_3)_6]Cl_3$ compound.
(b) FT of the k^3 weighted EXAFS shown in (a).

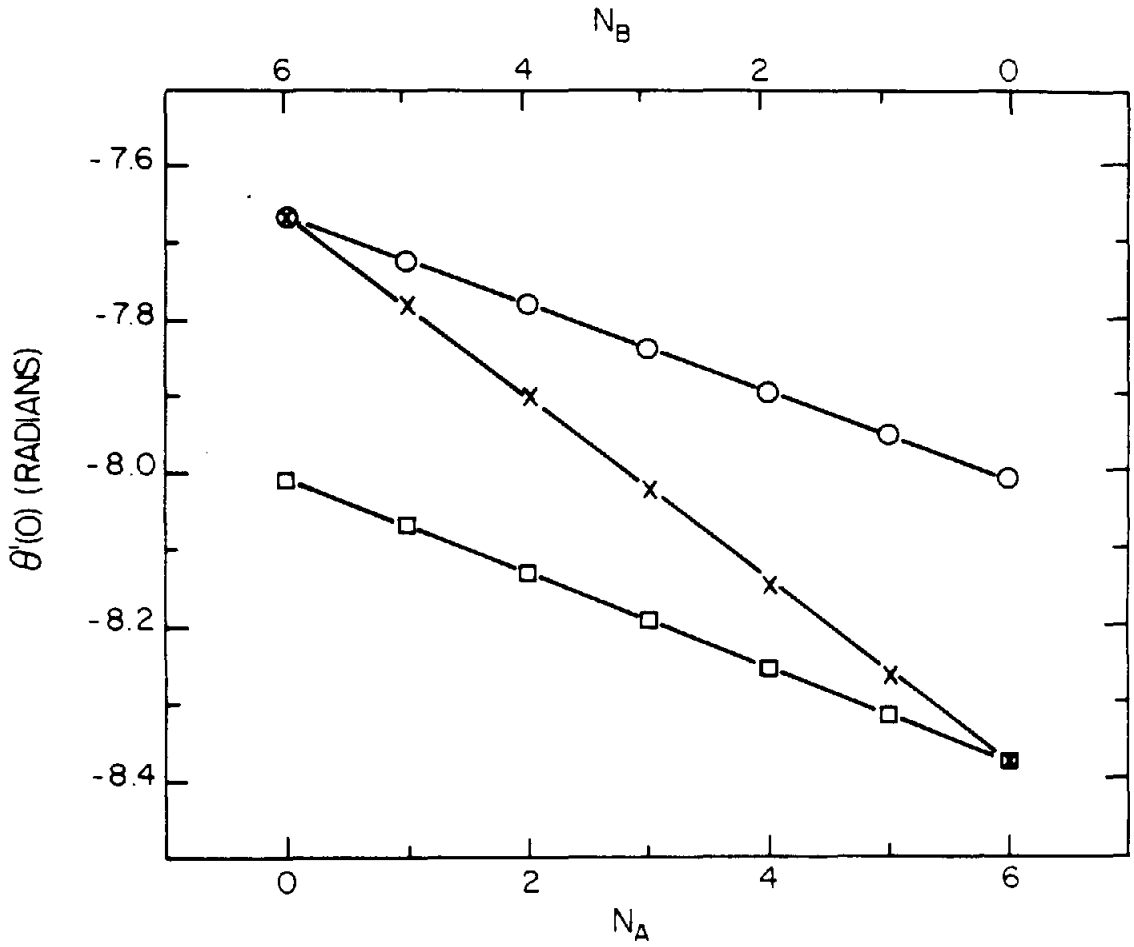

Figure 8.

Phase intercept for a coordination shell of six atoms containing N_A and N_B atoms of types A and B. Component A always refers to the lighter of the two atoms. Nitrogen and oxygen (open circles); carbon and oxygen (X); carbon and nitrogen (open squares). The phase intercepts for the individual pure components were taken to be the average of the values shown in Table I. This figure was generated using Eqs. (8.4.7) and (8.4.8).

Table I. The coefficients from the least-square fit of the total phase to a quadratic equation.

k range ($Å^{-1}$)	Coefficient	$Co(acac)_3$	$[Co(en)_3]Cl_3$	$K_3[Co(CN)_6]$
	c_o	-7.746*	-8.030	-8.517
4.0-10.5	c_1	2.777	2.962	2.767
	c_2	0.0057	0.0041	0.0044
	c_o	-7.722	-8.022	-8.475
5.0-10.5	c_1	2.771	2.960	2.756
	c_2	0.0061	0.043	0.0050
	c_o	-7.682	-8.006	-8.412
6.0-10.5	c_1	2.762	2.956	2.741
	c_2	0.0066	0.0045	0.0059
	c_o	-7.634	-7.976	-8.320
7.0-10.5	c_1	2.751	2.949	2.720
	c_2	0.0073	0.0049	0.0071
	c_o	-7.692	-8.010	-8.393
8.0-10.5	c_1	2.760	2.956	2.736
	c_2	0.0066	0.0045	0.0062

* Typical errors determined by the least-squares fit: $c_o \pm 0.004$, $c_1 \pm 0.001$, $c_2 \pm 5 \times 10^{-5}$

Table II. Coefficients from the least-square fit of the total phase extracted from the amine $[Co(NH_3)_6]Cl_3$ complex to a quadratic function.

k range (A^{o-1})	c_o	c_1	c_2
4.0-10.5	-8.087*	2.957	0.0058
5.0-10.5	-8.065	2.952	0.0054
6.0-10.5	-8.034	2.944	0.0058
7.0-10.5	-7.983	2.932	0.0065
8.0-10.5	-8.041	2.945	0.0058

* Typical errors determined by the least-squares fit $c_o \pm 0.004$, $c_1 \pm 0.001$, $c_2 \pm 5 \times 10^{-5}$

Table III. Calculated phase intercepts for a two component system. Component A is carbon and component B is oxygen.

N_A	N_B	$\theta'(X=1.0)$	$\theta'(X=1.25)$	$\theta'(X=1.5)$
0	6	-7.6690*	-7.6690	-7.6690
1	5	-7.7812	-7.7613	-7.7474
2	4	-7.8998	-7.8654	-7.8398
3	3	-8.0220	-7.9811	-7.9484
4	2	-8.1442	-8.1068	-8.0746
5	1	-8.2629	-8.2396	-8.2178
6	0	-8.3750	-8.3750	-8.3750

* Phases for the pure components are the average of those shown in Table I.

CHAPTER IX

POSSIBILITY OF BOND-LENGTH DETERMINATION IN EXAFS WITHOUT THE USE OF MODEL COMPOUNDS OR CALCULATED PHASES*

9.1 Introduction

Extended X-Ray Absorption Fine Structure (EXAFS) refers to the modulation observed on the high frequency side of an x-ray absorption edge. The origin of this structure is due to an interference phenomenon in which the final state photoelectron is scattered by neighboring atoms. Thus the phase difference between the scattered and unperturbed photoelectron waves is given by the product of the photoelectron wavenumber and the path difference together with any phase changes which occur during the scattering process. The normalized oscillatory component of the absorption coefficient is given by[1]

$$\chi(k) = -\sum_i \frac{N_i |f_i(\pi,k)| e^{-2\sigma_i^2 k^2}}{k\, r_i^2} \sin(2kr_i + \theta_i(k)) \qquad (9.1.1)$$

where N_i is the number of equivalent scatters of type i at a distance r_i from the absorbing atom. $f_i(\pi,k)$ is the back-scattering function and σ_i is a Debye-Waller factor which accounts for thermal vibrations and static disorder. The argument of the sine term represents the total phase difference between the scattered and unscattered photoelectron waves where $\theta_i(k)$ is the composite phase shift function.

The Fourier transform (FT) of Eq. (9.1.1) is a form of

radial distribution function (RDF) in which the absorbing atom is located at the origin. The position of each peak in the RDF does not coincide with the true interatomic distance due to the presence of the phase function $\theta_i(k)$ in the sine argument. The correct distance is usually obtained by using a known (model) compound with the same absorber-scatterer pair. The phase function is assumed to be transferable from the model compound to the unknown.[2] Calculated phase shift functions are also used for this purpose. In this case, it is assumed that these phases can be accurately calculated and that the plane wave approximation inherent in these calculations is justified.[3] Chemical binding effects are assumed to be unimportant in each case. Furthermore, each of the proposed methods for determining the distance assume an a priori knowledge of the scattering atom (the absorbing atom may be always identified by the observed energy of the absorption edge).

In this chapter we present a method of determining bond distances in EXAFS which does not rely on model compounds or theoretical phase shifts. In addition, there is no assumption concerning the nature of the scattering atom; in fact, during the distance determination process, the observed phase intercept is a measure of the type of scattering atom involved (see Chapter VIII).

9.2 Physical Basis for The Method

The physical basis for this scheme is the absence of a linear term in the phase function $\theta_i(k)$. This fact is

expressed by Levinson's Theorem[4] which states:

$$\delta_L(0) - \delta_L(\infty) = n_L \pi \qquad (9.2.1)$$

where n_L is the number of bound states of angular momentum L and $\delta_L(k)$ is the L^{th} partial wave phase shift. Levinson's Theorem is an expression of the fact that each partial wave phase shift is bounded, and thus, every atom has a finite scattering power. Since the scatterer phase may be expressed as a sum of partial waves, the total phase function $\theta_i(k)$ must also be bounded. The presence of a linear term would cause the phase to diverge as k approaches infinity; and hence violate Levinson's Theorem. There is no reason why the phase, in a finite k range, cannot be parameterized by an equation containing a linear term as discussed by the Lee et al.[5] However, it must be realized that the parameterization does not represent the true functional form of the phase. If the phase does not contain a linear term, why then do the peaks in the FT occur at shorter distances than the true interatomic distances? The observed peak position is a reflection of the fact that the FT is a linear integral transform. The FT attempts to linearize the data but since the phase $\theta_i(k)$ is a non-linear, decreasing function of k, the result is a peak which is shifted to smaller distances. The intrinsic non-linear nature of the phase, however, is evident from the peak shapes, which are broad and asymmetric.

To exploit the absence of linear terms in the phase

$\theta_i(k)$ let us write the total phase function $\Phi_i(k)$ as:

$$\Phi_i(k) = 2kr_i + \theta_i(k) \tag{9.2.2}$$

where r_i is the true interatomic distance. We may now define a function $g_i(k)$ such that:

$$g_i(k) \equiv \frac{\partial \phi_i(k)}{\partial k} - \frac{\phi_i(k)}{k} \tag{9.2.3}$$

where the subscript i is a shell index. Since $\theta_i(k)$ is non-linear there is no loss of phase information in constructing $g_i(k)$. The linear term in Eq. (9.2.2), however, is completely absent from $g_i(k)$. Thus $g_i(k)$ is essentially a differential equation in the phase $\theta_i(k)$

$$g_i(k) \equiv \frac{\partial \theta_i(k)}{\partial k} - \frac{\theta_i(k)}{k} \tag{9.2.4}$$

The general solution of a differential equation of this kind is given by:

$$\theta_i(k) = k[K + \int g_i(k)/k \, dk] \tag{9.2.5}$$

where K is the constant of integration. Since the phase $\theta_i(k)$ is bounded by Levinson's Theorem, the constant of integration must be zero since otherwise the phase will diverge at large k. We may thus solve Eq. (9.2.4) for $\theta_i(k)$, substitute into Eq. (9.2.2) and obtain the true distance r_i.

To solve Eq. (9.2.4) we must find a functional form for $\theta_i(k)$ which satisfies the criteria outlined above. It is important to note that for K-edge EXAFS, $\theta_i(k)$ is comprised

of the L = 1 partial wave phase shift, $2\delta_1$, due to the central atom potential, together with the phase of the scattering amplitude, $\psi_i(k)$, associated with the i^{th} shell of atoms. At sufficiently high energies each partial wave phase shift may be approximated by:

$$\delta_L(k) \approx -2mk/(\hbar^2) \int j_L(kr)\ V(r)\ j_L(kr)\ r^2 dr \qquad (9.2.6)$$

where $j_L(kr)$ is a spherical Bessel function and V(r) is the scattering potential. Equation (9.2.6) is the Born approximation for the phase shift, in which the radial solution of the full Schrodinger equation is replaced by the free radial solution $j_L(kr)$. It may be shown that, for any potential V(r), the partial wave phase shift varies as the inverse of the photoelectron wavenumber at high energies. We shall demonstrate this fact for the simple case of a square well potential.

$$V(r) = \begin{cases} V_o & 0 < r < a \\ 0 & r > a \end{cases} \qquad (9.2.7)$$

At sufficiently high energies the spherical Bessel function may be written as:

$$j_L(kr) \approx 1/kr \sin(kr - L\pi/2) \qquad (9.2.8)$$

Substituting Eqs. (9.2.7) and (9.2.8) into Eq. (9.2.6) it may be shown, by elementary integration, that to lowest order, the phase shift for any L is given by:

$$\delta_L(k) = mV_o a/(\hbar^2 k) + O(1/k^2) \qquad (9.2.9)$$

Therefore, the central atom phase shift approaches zero as 1/k, when k tends to infinity.

We must still calculate the asymptotic behaviour of the phase of the scattering amplitude. Assuming the phase shifts are real, $\psi_i(k)$ may be written as:

$$\psi_i(k) = \tan^{-1}\left[\frac{\sum_L (2L+1)\,2\sin^2\delta_L\, P_L(\cos\pi)}{\sum_L (2L+1)\sin 2\delta_L\, P_L(\cos\pi)}\right] \qquad (9.2.10)$$

Since δ_L is small for large k and independent of L, the sine terms in Eq. (9.2.10), may be replaced by their arguments. Furthermore, the partial wave phase shifts may be removed from both summations. Using Eq. (9.2.9) the scatterer phase may then be expressed as:

$$\psi_i(k) = \tan^{-1}[mV_o a/(\hbar^2 k)] \qquad (9.2.11)$$

For large k, the argument of the tangent is small and maybe used to approximate the tangent itself. The scatterer phase varies as 1/k and, therefore, the composite phase shift function, $\theta_i(k)$, also approaches zero like 1/k as k tends to infinity.

A functional form which satisfies the above criteria is:

$$\theta_i(k) = A + B\exp(-Ck) \qquad (9.2.12)$$

This function may be expanded in a Taylor series to demonstrate its approximate 1/k behaviour at large k. If the composite phase is of the form shown in Eq. (9.2.12)

then the function $g_i(k)$ takes the form:

$$g_i(k) = -A/k - (BC + B/k) \exp(-Ck) \qquad (9.2.13)$$

where A, B and C are now adjustable parameters in the fit of Eq. (9.2.13) to the experimentally determined function $g_i(k)$. When these parameters are determined, the phase function may be calculated from Eq. (9.2.12) and the distance from Eq. (9.2.2).

9.3 Application to Model Systems

To illustrate the ability of this scheme to determine accurate bond distances, a series of cobalt complexes were studied. In this chapter, however, we will discuss just one of these complexes, $Co(acac)_3$. A more detailed description of this technique, together with the manner in which accurate phase information may be extracted from EXAFS data, will be presented in a later publication. The $Co(acac)_3$ sample used in this study was prepared from analytical grade reagent. The EXAFS measurement was made at room temperature, in the transmission mode, using the Caltech Laboratory EXAFS Spectrometer (described in Chapter VI). The background absorption and the threshold energy were determined using the convolution method introduced earlier.[6] The first-shell peak in the transform, corresponding to the cobalt-oxygen distance was isolated using the peak isolation scheme discussed previously.[7] The total phase was determined using a scheme due to Lee et al.[1] and the

function $g_1(k)$ was constructed. Figure 1 shows a plot of the total phase together with the function $g_1(k)$. Table I shows the parameters of the fit of $g_1(k)$ to the functional form shown in Eq. (9.2.12) for several fitted data ranges. Using these parameters, the phase function $\theta_1(k)$ was generated and the cobalt-oxygen bond distance was determined from Eq. (9.2.2)

The observed bond distance is dependent on the data range used in the fit. The largest deviations from the true distance occur when exclusively high k data is analyzed. It is possible, however, to determine which data should be used in the distance analysis. The derivative of the total phase $\phi_i(k)$, is simply the derivative of the scattering phase function together with a constant $(2r_i)$. If the exponential form in Eq. (9.2.12) is to describe the scattering phase function, then any deviations from this functional form may readily be seen from the derivative of the total phase. At high k values this derivative is often seen to differ markedly from that of a simple exponential function. Therefore, it not surprising that the distances obtained from an exclusive analysis of such data are wrong, since Eq. (9.2.12) is not a valid description of the scattering phases in this region. The origin of these deviations, however, is more likely to be due poor quality data rather than additional structure in the scattering phase at high k values.

An accurate estimation of the threshold energy, E_o, is

also required for this method. It is important to note that an error in E_o cannot contribute to an error in the k scale which varies linearly with k. This may readily be seen from a binomial expansion of the free electron dispersion relation which relates the x-ray energy to the photoelectron wavenumber by this quantity E_o. Changing E_o by ΔE_o will change a given k value into a new value k' defined by:

$$\begin{aligned} k' &= [k^2 - 2\Delta E_o/7.62]^{1/2} \\ &\approx k[1 - \Delta E_o/(7.62\ k^2)] \end{aligned} \qquad (9.3.1)$$

Clearly, an error in E_o cannot produce a linear change in k, and therefore, such an error will persist in the differential equation Eq. (9.2.4). The present approach is to accept this uncertainity in E_o and to correct for it in the latter part of the analysis. The manner in which such an analysis may be performed will be discussed in detail in a forthcoming publication.

The phase intercept has been shown to be a quantitative means of determining the nature of the scattering atom.[7] In this case, the intercept is given by the sum of the A and B coefficient. Therefore, it is possible to simultaneously derermine the bond distance and the type of neighboring atom involved. The observed phase intercept for oxygen with cobalt as the absorbing atom agrees with the value previously reported.[7]

9.4 Discussion

In conclusion, this method may be used to determine bond distances from EXAFS data to within 1% (for single shell systems), without resorting to model compounds or calculations. No assumption is made concerning the nature of the scattering atom; indeed, it is possible to identify such atoms from the observed phase intercept.

References

*This chapter is based on: J.J Boland, F.G. Halaka and J.D. Baldeschwieler, J. Amer. Chem. Soc. in press (1984).

1. P.A. Lee, P.H. Citrin, P. Eisenberger and B.M. Kincaid, Rev. Mod. Phys. **53**, 769 (1981).

2. P.H. Citrin, P. Eisenberger and B.M. Kincaid, Phys. Rev. **B 28**, 2921 (1983).

3. B.K. Teo and P.A. Lee, J. Amer. Chem. Soc. **101**, 2815 (1979).

4. M.L. Goldberger and K.M. Watson, Collision Theory, (Wiley and Sons, New York, 1964) p. 284.

5. P.A. Lee, B.K. Teo and A.L. Simons, J. Amer. Chem. Soc. **99**, 3856 (1977).

6. J.J. Boland, F.G. Halaka and J.D. Baldeschwieler, Phys. Rev. **B 28**, 2921 (1983).

7. F.G. Halaka, J.J. Boland and J.D. Baldeschwieler, J. Amer. Chem. Soc. in press (1983).

8. G.J. Kruger and E.C. Reynhardt, Acta Cryst. **B 30**, 822 (1974).

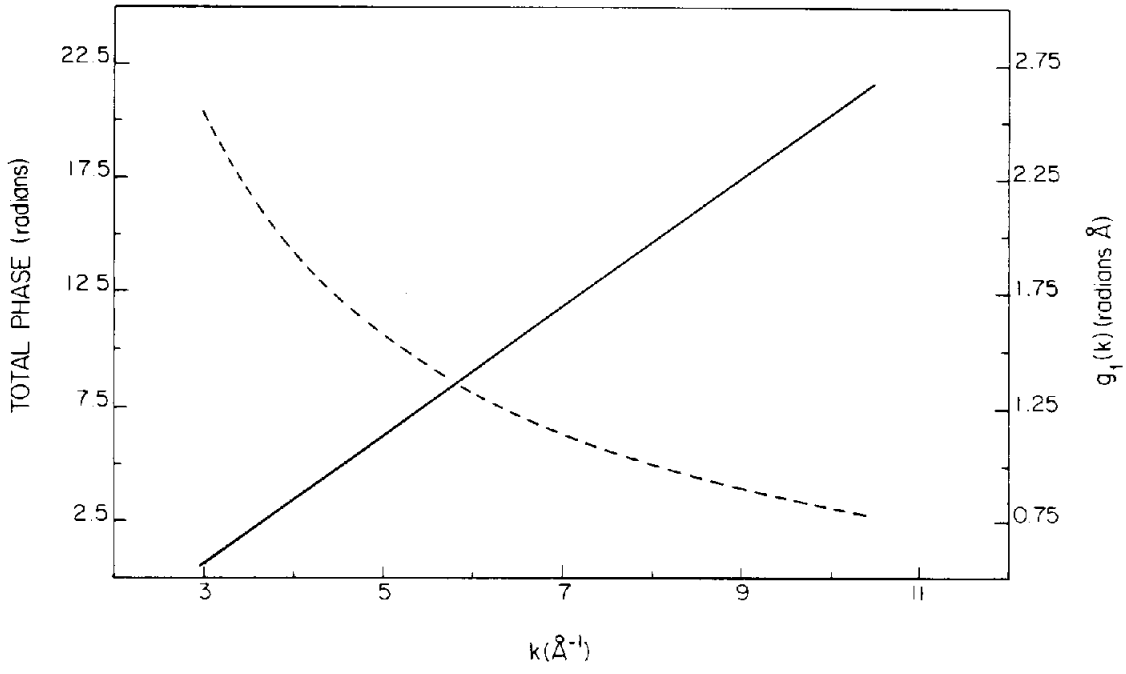

Figure 1.
Plot of the total phase (solid curve) and the function $g_1(k)$as a function of k. These data are for the $Co(acac)_3$ complex. Note that the total phase <u>appears</u> linear due to the dominant $2kr_1$ term.

Table I. The parameters obtained in the fit of Eq. (9.2.3) to the function $q_1(k)$ which is calculated from the total phase of the first shell peak in the $Co(acac)_3$ complex.

Fitted k Range	A	B	C	r_1(Å)*
3.1 - 10.4	-82.896	75.158	0.0131	1.879
3.1 - 5.5	-83.870	76.130	0.0133	1.891
5.0 - 10.4	-82.262	74.551	0.0136	1.889
7.0 - 10.4	-83.908	76.233	0.0153	1.917

*R(Co-O) = 1.888 Å determined by x-ray diffraction.[8]